Hadron production in 10.8 A·GeV/c Au+Au collisions

by

Roger Lacasse

A thesis submitted
to the Faculty of Graduate Studies and Research
in partial fulfillment of the requirements
of the degree of

Doctor of Philosophy
in Physics

Foster Radiation Laboratory,
Physics Department, McGill University, Montréal, Canada.

To my loving wife and kids.

—I found the meaning of life. It's in the eyes of my wife and kids.

1995.

Abstract

Hadron production in relativistic 10.8 A·GeV/c Au+Au collisions is studied at forward rapidities using the E877 experimental setup at the AGS. The details of the design, assembly, testing, calibration and performance of the E877 spectrometer time-of-flight hodoscope are presented. The analysis steps necessary to produce the measured double differential multiplicities $1/\mathrm{m}_\mathrm{t}^2 \cdot d^2N/d\mathrm{m}_\mathrm{t}d\mathrm{y}$ for pions, kaons and protons are discussed. Rapidity distributions $dN/d\mathrm{y}$ are studied for pions and protons. The results are compared to calculations from the RQMD 1.08 model. The general characteristics of the measured transverse mass spectra are shown to be well reproduced by the model while small systematic discrepancies remain. In the case of protons, the model seems to predict an insufficient amount of collective transverse flow. The measured ratios of pion transverse mass spectra are shown to exhibit a significant rapidity-dependent charge asymmetry at low m_t. A model of the final-state Coulomb interaction is developed to demonstrate that pion charge-asymmetry m_t and y dependences can be attributed to an effective Coulomb potential. The magnitude of this effective potential is estimated and is shown to be consistent with the measured rapidity dependence of the ratio of $dN/d\mathrm{y}$ of the two types of pions.

Résumé

La production de hadron dans les collisions relativistes Au+Au à 10.8 A·GeV/c est étudiée aux rapidités avant en utilisant les instruments de l'expérience E877 à l'AGS. Les détails de la conception, de l'assemblage, des vérifications, de la calibration ainsi que la performance de l'hodoscope de temps-de-vol du spectromètre E877 sont présentés. L'analyse menant à l'obtention de spectres différentiels doubles $1/\mathrm{m}_\mathrm{t}^2 \cdot d^2N/d\mathrm{m}_\mathrm{t}dy$ de pions, de kaons et de protons est exposée. Les distributions en rapidité dN/dy sont étudiées pour les protons et les pions. Les résultats expérimentaux sont comparés avec ceux provenant du modèle RQMD 1.08. Le modèle reproduit les caractéristiques générales des spectres en masse transverse malgré la présence de petites différences systématiques. Pour les protons, le modèle semble prédire une composante de flux transverse moins importante que celle qui est observée dans les données. Le rapport des spectres de pions mesurés en masse transverse présente une asymétrie de charge significative aux petites valeurs de m_t et qui dépend de la rapidité. Un modèle de l'interaction coulombienne dans l'état finale est élaboré pour démontrer que la dépendance de l'asymétrie de charge en m_t ainsi qu'en y peut être attribuée à l'effet d'un potentiel coulombien effectif. La valeur de ce potentiel effectif est estimée. Il est également démontré qu'elle est consistente avec la dépendance mesurée en rapidité du rapport des distributions dN/dy des deux types de pions.

Figure 0.1: *Dirty pants and large smiles!* This picture was taken just after the completion of the hodoscope wall. The TOFU is viewed from the downstream side, from left to right: Gang Wang, myself and my advisor Professor Jean Barrette.

Contents

List of Figures

List of Tables

Acknowledgments

This work would not have been possible without the unconditional support from my parents. Their love and guidance have allowed me to fulfill this work. I want to thank my wife for the courage she showed during my numerous and extended trips to Long Island, NY. She sometimes had a difficult time to understand why I was studying physics, but always loved me for who I am. She and, in recent years, my kids have provided me with an incredible amount of joy and happiness which helped me complete this work.

Claude Pruneau initialized the design of the time-of-flight hodoscope. He held my hand in the first stages of the design and data analysis, always showing patience with my numerous questions. To this day, he remains a close friend of mine. I want to thank the people that put their shoulder to the wheel during the long, and often tedious assembly days and during the operation of the hodoscope, namely: Sylvain Gilbert, Yujin Qi, Tarek Saab and Nikolai Starinski and Gang Wang. Marzia Rosati helped me a great deal with software writing. I will always miss our "little" late-afternoon chats. Yi Dai gave me a more than welcomed hand at the times of calibration and acceptance calculations. Kirill Filimonov helped me more than I deserved, especially with the proofreading of this text.

At several occasions, I had the privilege of discussing, and learning some physics at the same time, with Dr. Peter Braun-Munzinger, Prof. Johanna Stachel and Prof.

Thomas K. Hemmick. I keep good memories of the discussions I had with Prof. S. K. Mark "Tommy". His knowledge of the *who's who* of physics still amazes me. I learned the basics of thermal models from Prof. Subal Das Gupta and had several interesting discussions with Prof. Charles Gale. Althought their work is mainly in a different energy domain, they both showed genuine interest whenever I needed to clarify a concept.

I made many friends amongst the people that formed the E814 and E877 collaborations (listed below) and I want to thank them all here. The effervescence that reigned during the data taking runs was one of the most stimulating experiences of my still very short scientific career. It also gave me great opportunities to learn about cultures from around the world and travel to some very interesting places. One thing is clear, I will miss the "official E877 midnight poker games" and the 3 am Silicon Graphics flight simulator dogfight challenges.

I learned a lot about the nitty-gritty details of detector building from the Foster Radiation Laboratory staff. Leo Nikkinen always answered my numerous questions about this, and my thousand-and-one little side projects with enthusiasm. I learned everything I know about machining from Steve Kecani. He never thought twice before putting the extra hours of work when they were most needed or when I had this one last little thing to finish in the machine shop. The technical staff of the Brookhaven National Laboratory physics department and Alternate Gradient Synchrotron were always ready to lend a hand to this grad-student from up-north who they barely knew.

Finally, I want to express my most sincere gratitude to my advisor, professor Jean Barrette, who first guided me through an M.Sc. degree [1]. I thank him for offering me the exceptional privilege of actually building an operating, from start to finish, a nuclear physics apparatus of considerable size and importance. Unfortunately, in the fast expanding ultra-relativistic heavy-ion field, this is an opportunity that fewer and fewer graduate students are getting. Because of that, I am all the more thankful. He also allowed me to present our work at several important conferences where I met and learned from the world experts in the field of relativistic heavy-ions. To this day, his formidable insight keeps amazing me. He has an ability to show up and resolve problems, on which I had been working for days, in just a few minutes. His integrity, devotion to his graduate students, enthusiasm for the field of relativistic heavy-ions and to physics in general are examples for all of us to follow.

The E814/E877 collaboration: J. Barrette[5], R. Bellwied[11], S. Bennett[11], R. Bersch[7], P. Braun-Munzinger[7], W. C. Chang[7], W. E. Cleland[9], M. Clemen[9], J. D. Cole[4†], T. M. Cormier[11], Y. Dai[5†], N. C. daSilva[10*], G. David[1], J. Dee[7*], G.E. Diebold[12*], O. Dietzsch[10], M. W. Drigert[4†], M. Fatyga[1*], K. Filimonov[5†], D. Fox[3*], A. French[11†], J.V. Germany[12*], S. Gilbert[5*], S.V. Greene[12*], J. R. Hall[11], T. K. Hemmick[7], N. Herrmann[2], B. Hong[7], K. Jayananda[9*], D. Kraus[9*], C. L. Jiang[7], S. C. Johnson[7†], Y. Kwon[7†], B. Shiva Kumar[12*], R. Lacasse[5], A. Lukaszew[11†], Q. Li[11], D. Lissauer[1*], W.J. Llope[7*], T. W. Ludlam[1], S. McCorkle[1], R. Majka[12*], S. K. Mark[5], R. Matheus[11], J.D. Mitchell[12*], M. Muthsuwamy[7*], D. Miśkowiec[7], J. Murgatroyd[11†], E. O'Brien[1], S. Panitkin[7], P. Paul[7†], T. Piazza[7†], M. Pollack[7†], C. Pruneau[11], Y. Qi[5], M. N. Rao[7], M. Rosati[1], F. Rotondo[12*], J. Sandweiss[12*], N. C. daSilva[5], J. Simon-Gillo[8*], J. Sullivan[3*], S. Sedykh[7], J. Sheen[11†], U. Sonnadara[9], J. Stachel[7], N. Starinski[5†], J. Sullivan[3*], H. Takai[1*], E. M. Takagui[10], M. Trzaska[7], T. G. Throwe[1*], L. Waters[7*], C. Winter[12*], S. Voloshin[9], T. Vongpaseuth[7†], G. Wang[5], J. P. Wessels[7†], K. L. Wolfe[8*], D. Wolfe[6*], C. L. Woody[1], N. Xu[7], Y. Zhang[7], Z. Z. Zhang[9], C. M. Zou[7] - [1]BNL - [2]GSI - [3*]LANL - [4†]Idaho Nat. Eng. Lab. - [5]McGill Univ. - [6*]Univ. of New Mexico - [7]SUNY, Stony Brook - [8*]Texas A&M Univ. - [9]Univ. of Pittsburgh - [10]Univ. of São Paulo, Brazil - [11]Wayne State Univ. - [12*]Yale Univ., [*]E814 only, [†]E877 only.

Preface

During warm summer evenings, I still enjoy lying down on the ground and staring at a dark countryside sky for hours. This is a frightening experience at times. It always makes me realize how small we are and how little we know about the *real* questions: *Where do we come from? How did all of this come to exist? Why this, rather than something else?* In my early teens, as an amateur astronomer, I quickly became interested in knowing more about the origin of the Universe [2].

The discovery of the expansion of the Universe led to the idea that it must have originated from a much denser state than at present: the Big Bang theory. It is believed that the Universe originated from a cosmic singularity some 15 to 20 billion years ago. At first, the Universe would have been formed of pure energy. The subsequent expansion and cooling allowed the quarks and gluons to bind into hadrons (around $T \sim 200$ MeV or 2.4×10^{13} °K, $t \sim 10^{-5}$ s [3]). As the temperature further decreased (starting at $T \sim 0.1$ MeV or 1.2×10^{10} °K, $t \sim 100$ s when the Universe had a radius of $R \sim 10$ km [3]), these hadrons formed, through primordial nucleosynthesis, the original distribution of elements still observable today.

I started my bachelor degree with the intention of learning more about astronomy, nuclear and particle physics. When I learned that there was such a thing as relativistic heavy-ion physics, a field that is at the junction of the three subjects that brought me to physics, I signed up right away.

Chapter 1

Introduction

1.1 Relativistic heavy-ions, the quark-gluon plasma and the origin of the Universe

As we dissect matter to finer and finer scales, we find out that it is made of yet fewer and smaller constituents. First, there are the molecules ($\sim 10^{-10}$ m), then the atoms ($\sim 10^{-11}$ m), the hadrons like the protons and neutrons ($\sim 10^{-15}$ m), and finally the quarks ($\sim 10^{-16}$ m). The quarks were originally proposed as a way to put some order into the observed multiplicity of baryons, mesons and their reactions [4, 5]. The existence of quarks is now well established and, along with leptons, are the Standard Model basic building blocks of matter [6]. So far, quarks have only been observed inside hadrons. Mesons and baryons are made of two and three quarks respectively, bound together by gluons, the strong nuclear force carriers. It is postulated that quarks exist only in a confined state. The interaction between quarks is such that its strength increases with distance. Quarks can be separated only up to the point where there is sufficient potential energy to allow the creation of a quark-antiquark pair, thereby preventing the emission and observation of single quarks.

One of the proposed methods of studying effectively deconfined quarks consists in *crushing* the boundaries of the hadrons inside which they are normally confined. Using accelerators to collide nuclei, it is already possible to excite the nuclear medium so that its constituents behave as an hadronic gas mainly made of nucleons and pions. Further increase in density and temperature will lead to a point where the hadrons significantly overlap. At that point, the quarks and gluons should lose their allegiance to specific hadrons. This would create a new phase of strongly interacting matter, namely, the *Quark-Gluon Plasma* (QGP). The quarks and gluons would remain confined by the boundaries of the QGP but not to the dimensions of a hadron. If such a QGP was formed, it would be as close as one can presently get to recreating, in the laboratory, the conditions that prevailed in the earliest stages of the Universe formation.

The phase diagram of nuclear matter, as expected from Quantum Chromodynamics [7] (QCD) calculations, is schematically drawn in figure 1.1. Nuclear matter in its normal state is found at $\rho/\rho_\circ = 1$. The results from QCD calculations predict that a QGP would be formed in an experiment if temperatures of about $T \sim 150$ to 200 MeV or if energy densities of $\rho > 1$ GeV/fm^3 could be reached ($\rho_\circ \approx 0.17$ GeV/fm^3). The highly excited nuclear matter would remain in the QGP phase for expected lifetimes of the order of $t \sim 10^{-23}$ s [8].

The early Universe hadronized through the high temperature and low density part of the nuclear matter phase diagram. Witten [9] was the first to suggest that a first order QGP phase transition could have created inhomogeneities in the initial baryon distributions, thus affecting the nucleosynthesis [10]. The study of the behavior of nuclear matter under high temperature and densities might therefore tell us about the laws of physics that governed the early Universe. Neutron stars are at the other extreme with their relatively cold temperature ($T \sim 1-100$ KeV) and large densities ($\rho \sim 10 \times \rho_\circ$) [11]. The study of the dynamics of the interior of neutron stars is a

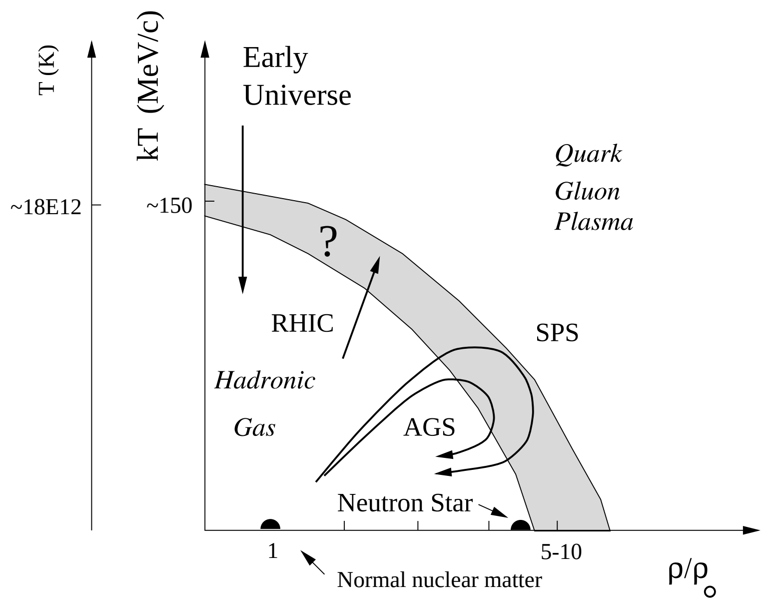

Figure 1.1: Nuclear matter phase diagram. The trajectories followed by matter during the early Universe cool down and in experiments at the AGS, SPS and RHIC are schematically shown. The shaded area represents the expected phase transition boundaries.

potential source of information on the behavior of large volume dense nuclear matter.

The physics of Relativistic-Heavy-Ions (RHI) is the subject of intense scientific activity throughout the world. It is now assumed that large volumes of highly-excited baryon-rich nuclear matter are being formed at the Alternate Gradient Synchrotron (AGS) and at the Super Proton Synchrotron (SPS). Central collisions at the Relativistic-Heavy-Ion Collider (RHIC) and at the Large Hadron Collider (LHC), scheduled for 1999 and $\approx$ 2005 respectively, are expected to create high temperature and low-density baryon-free volumes of nuclear matter.

It is now believed that the most central collisions in the Au+Au fixed target experiments at the AGS reach densities as high as 5 to 10 $\times \rho_\circ$ [12, 13]. These densities are possibly sufficient to form a mixed-phase of normal and QGP matter, at least in some of the most violent collisions [14]. Relativistic heavy-ion experiments at the AGS are, therefore, in an excellent position to learn more about the behavior of nuclear matter under high pressure, density and temperature on the way to the study of the QGP.

1.2 Physics issues

The Relativistic-Heavy-Ion experimental program at the AGS is now more than 10 years old. Since then, much has been learned about the dynamics of RHI collisions [15, 16, 17]. In order to produce a medium suitable for the formation of a QGP, sufficient energy needs to be deposited inside the interaction region. Thus, the feasibility of creating large extremely hot and dense lumps of nuclear matter had to be established first. Experimentally measured transverse energy spectra have demonstrated that, at the AGS, a large degree of stopping is achieved in collisions with light beams [18, 19] and, recently, in the Au+Au system [12]. A measure of the dimensions of the created system can be extracted from particle correlations. Typical fireball radii of 3 to 4 fm are found in the Si+Al system [20], 4 to 5 fm in S+Ag [21], whereas in the Au+Au system values as large as 5 to 6 fm are measured [22, 23]. The shape of the produced particle distributions contains information on the amount of thermalization that is achieved during the collisions [24]. Thermal models have a long history of successful applications to RHI [25, 26]. The systems that are created at both AGS and SPS are found to be close to thermal and chemical equilibrium [14]. However, particle decay contributions distort the shapes of the produced spectra [27, 28, 29] and complicate their interpretation. Additionally, the existence of collective effects has been recently demonstrated. Evidence of collective longitudinal, transverse [30] and directed [31, 32] flow effects has been reported. Theoretical models that qualitatively reproduce the observed particle distributions suggest that densities as high as 8 to 10 times that of normal nuclear matter are achieved in Au+Au collisions [33, 34, 35]. Large volumes of baryon-rich hot and dense nuclear matter are indeed produced at the AGS.

One of the main experimental RHI challenges consists in identifying QGP signatures in collisions that are dominated by hadronic reaction backgrounds [36]. Several experimental QGP signatures have been postulated to exist, based on our understanding of the reaction processes. Comparisons made between the data measured in the A+A systems to that in p+p and p+A emphasize the effects that are due to the larger number of participant particles. Effects like the enhancement of strangeness production [37], J/ψ suppression [38, 39] relative to simple superposition of p+p collisions have already been observed. Enhancements of strange particle production like kaons [40, 41, 42] and ϕ [43, 44] have been measured whereas suppression of the production of $\bar{\mathrm{p}}$ [45, 46] have also been observed. But currently, no single unambiguous signature of the formation of a QGP has been observed. A better understanding and a more detailed characterization of the reaction dynamics are needed to rule out all but the more exotic phenomena, like the QGP.

The present work intends to characterize hadron production in 10.8 A·GeV/c Au+Au collisions, specifically for π, K and p. The hadron yields are studied as a function of transverse mass, rapidity and centrality. The structures that deviate from purely thermal spectra are analyzed to pinpoint their origin. The Coulomb field generated by the large amount of charge that is assembled inside relatively small volumes in central Au+Au collisions is then studied to determine whether it can explain the measured shapes of some the particle spectra.

1.3 A magnetic spectrometer for Au+Au

The E814 collaboration extensively studied relativistic heavy-ion collisions at the AGS [47]. The E814 experimental setup was designed to study reactions produced by a relatively light silicon beam accelerated at 14.8 A·GeV/c using a nearly 4π calorimeter coverage around the target and a forward spectrometer. The collaboration produced several important results on transverse energy production and stopping [18], charged particle multiplicities [48, 49], p, K, π [50], $\bar{p}$ [46], Δ [29], strangelet production [51] and particle correlations [52]. With *truly heavy* gold beams becoming available at the AGS in 1993, important spectrometer upgrades were needed to study the large number of particles that are produced in Au+Au collisions, hence, the E877 collaboration was formed [53]. The existing spectrometer tracking system was upgraded by modifying the drift chambers and adding four multi-wire proportional chambers. My personal involvement in this upgrade consisted in building and operating a high-granularity and resolution time-of-flight hodoscope to the existing spectrometer time-of-flight system. This system is therefore throughly discussed in the present work.

1.4 Outline

An overview the complete E877 experimental setup is presented in the next chapter. The details of the design, construction, testing and performance of the time-of-flight hodoscope are the subject of chapter 3. The analysis steps that are necessary to produce identified particle spectra from the quantities that are measured with the spectrometer detectors are described in chapter 4. The results are discussed in chapters 5 and 6. To help interpret the data, results from a theoretical model are compared to the measurements throughout chapter 6. Conclusions and summary of the results are given last.

Chapter 2

Experimental setup

The data presented here were obtained using the experimental setup shown in figure 2.1 located at the Brookhaven National Laboratory (BNL) on Long Island NY. The E877 experimental setup is divided into two main groups of detectors: the target region (insert of figure 2.1) and the forward spectrometer. One of the main features of the apparatus is the almost complete 4π calorimetric coverage in the target region. The forward spectrometer is designed to handle the large particle multiplicities produced in relativistic heavy-ion collisions.

The systems located in the target region are presented first. The forward spectrometer detectors, including a succinct description of the time-of-flight system, are given in section 2.2. An exhaustive presentation of the time-of-flight system is the object of chapter 3.

2.1 Target region

The target region is subdivided into two groups of detectors: the calorimeters and multiplicity detectors and the beam definition detectors. The beam definition detectors are located upstream of the target. They are used for triggering and interaction

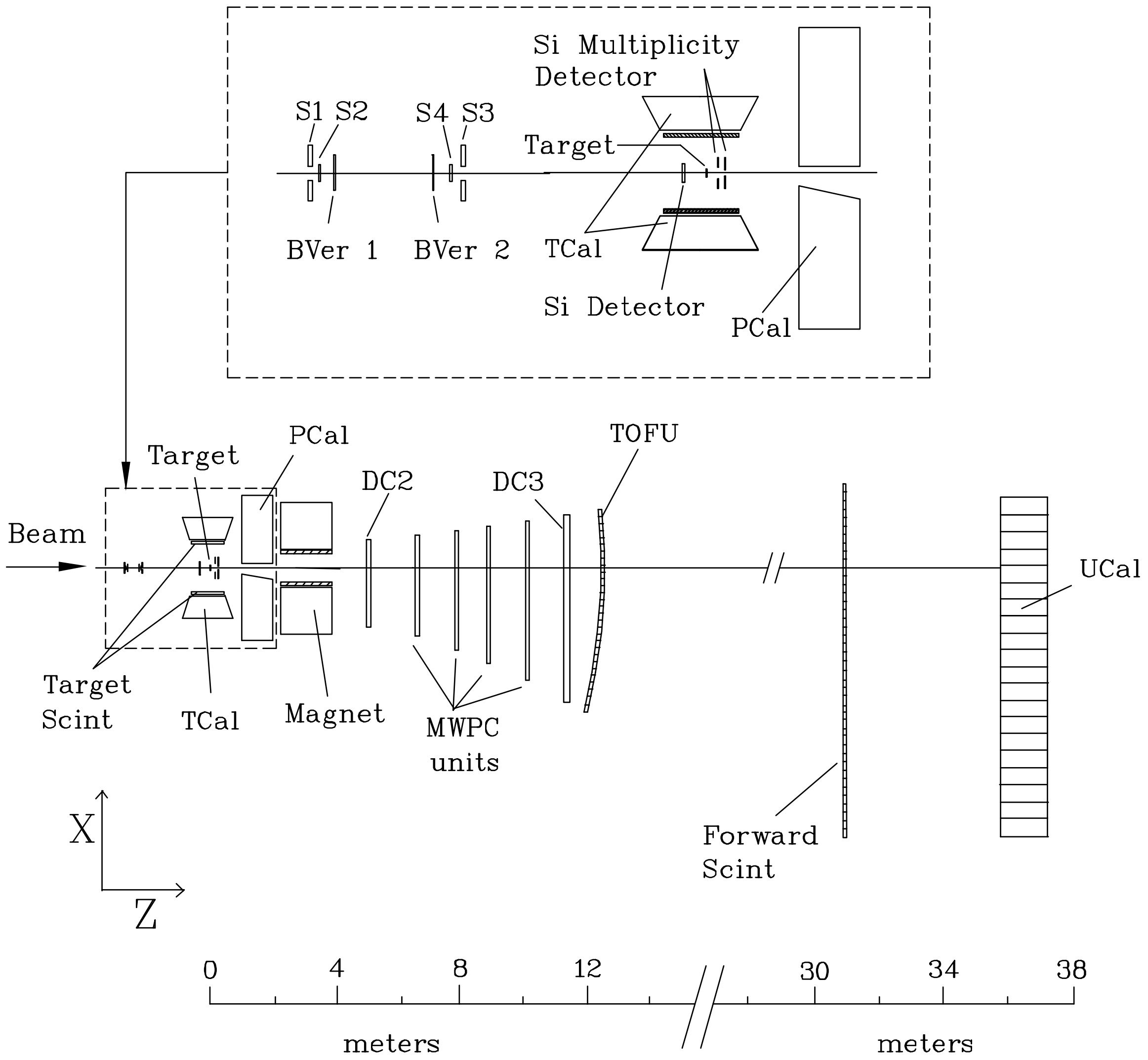

Figure 2.1: The E877 experimental setup

position determination. The calorimeters and particle multiplicity detectors are used to measure global event properties like transverse energy production [54, 55, 56] and collective directed flow [57].

It is convenient to define a common coordinate system for the setup. In the present case, we place the origin of the right handed coordinate system at the center of the target. The longitudinal z axis is defined along the beam trajectory while the transverse x direction is vertical in figure 2.1.

2.1.1 Beam scintillators

The experimental start signal is generated by measuring the arrival of the beam particle on the target using the scintillators S2 and S4. Additionally, a coarse and fast collimation of the beam is desirable to eliminate stray particles at the pretrigger level. This is achieved by using two large veto scintillators (S1 and S3) with center holes. The S2 and S4 scintillators are slightly larger than these holes. A good particle is then defined as one satisfying $\bar{S1} \cdot S2 \cdot \bar{S3} \cdot S4$. The beam scintillators and their performance are described in detail in subsection 3.1.1 since they are part of the time-of-flight system.

2.1.2 Beam vertex detectors

The trajectory of each beam particle in the xz plane is measured using the Beam Vertex (BVer) detectors. The beam angle and position at the target are inferred from the x positions measured by the two 25.4×25.4 mm^2 300 μm thick microstrip silicon detectors etched on 7.6 cm (3 inches) Si wafers. Each detector is segmented into 320 strips spaced by 50 μm. The detectors are placed at -2.8 m and -5.8 m upstream of the target, leading to the beam position and angle resolutions of 70 μm and 12 μrad at the target, respectively. The signals from the BVer detectors are processed by a

LeCroy PCOS discriminators and readout system.

2.1.3 Upstream silicon detector

A 100 μm thick and 1 cm in diameter Silicon (Si Detector) surface barrier detector, mounted about 5 cm upstream from the target, is used to insure of the charge integrity of the beam. The dE/dx measurement is used online to veto most of the beam particles that have interacted upstream of the target.

2.1.4 Target

The data were taken with 540 mg/cm^2 and 980 mg/cm^2 thick Au targets. For a ^{197}Au projectile, they correspond to approximately $\sim 1\%$ and $\sim 1.8\%$ of a nuclear interaction length. The 3 cm diameter discs are mounted on a remotely controlled wheel along with a cross hair and various other targets.

2.1.5 Silicon multiplicity

During the 1993 data taking run, a set of two identical silicon pad detectors was placed just downstream of the target. The first one is located at a distance 3.37 cm and the second one at 8.17 cm. They are made from 300 μm thick silicon discs, approximately 7.6 cm (3 inches) in diameter. Each of them is segmented into 512 pads which are read out with ADC's. Their active regions cover respectively $0.87 < \eta < 1.61$ and $1.61 < \eta < 2.46$ in pseudorapidity[1]. The δ rays originating from the passage of the Au ions through the target were suppressed using 3 mm thick aluminum absorbers placed just upstream of each detector. The Si Multiplicity detectors were used to study charged-particle pseudorapidity distributions [58] and their correlation with transverse energy production [59].

[1] pseudorapidity is defined as $\eta = -\ln[\tan(\theta/2)]$

2.1.6 Target calorimeter

The particles emitted at angles larger than $\theta \approx 45^\circ$ are detected by the Target Calorimeter (TCal). It is an electromagnetic calorimeter that is sensitive to neutrals, charged particles and gamma rays.

The TCal consists of 992 NaI 13.8 cm long crystals corresponding to 5.3 radiation lengths, or 0.34 hadronic interaction lengths [18]. All the crystals are identical but for a single row where they were truncated to allow for a quasi-projective geometry. The crystals are divided into 5 modules called walls: 4 side walls parallel to the beam (only two are shown on figure 2.1), placed at approximately 30 cm from the target along the ϕ coordinate. A fifth module that covers the backward angles (not shown on figure 2.1) was not used in 1993. The TCal angular coverage is $48^\circ < \theta < 135^\circ$, or $-0.5 < \eta < 0.8$ in pseudorapidity.

The light produced by each crystal is detected by directly-coupled vacuum photodiodes. The energy calibration is performed using cosmic rays over a period of several weeks. Details of the performance and calibration can be found in [54]. The average noise in a channel is of $\sigma_E = 1.7$ MeV, of which about 1 MeV is correlated in all channels. The TCal high segmentation and intrinsic gain stability of the photodiodes make it an ideal detector for triggering on the produced transverse energy (E_t). It is, therefore, used in the present work to perform the event selection. Additionally, it allows for the study of energy emission asymmetries near target rapidities $y = 0$ on an event-by-event basis.

2.1.7 Participant calorimeter

Located at 0.8 m downstream from the target, the Participant Calorimeter (PCal) is designed to study transverse energy distributions and energy flow at the AGS [31]. As its name implies, it covers the forward angles $0.83 < \eta < 4.7$ where the reaction participants are preferentially emitted.

The PCal is a sampling calorimeter made of lead, iron and scintillator plates read-out with fiber optics. It consists of 4 identical quadrants that can be arranged to maintain near ϕ symmetry around a central opening. It has a radius of approximately 84 cm and a depth of 4 nuclear interaction lengths. The PCal is divided longitudinally into 4 depth segments, 2 electromagnetic and 2 hadronic. Each quadrant is further segmented according to an azimuthal pattern allowing a complementary E_t measurement to the TCal. A detailed description of the PCal can be found in [55, 60, 61]. The Pcal is well suited for the study of transverse energy production and directed flow effects [32].

2.2 Forward spectrometer

The particles emitted in a forward cone of $\sim 8°$ are sampled using the forward spectrometer. The spectrometer is designed to identify particles and study their emission spectra at small transverse momentum (p_t) values including $p_t = 0$ GeV/c.

The spectrometer collimator is installed at the center of the PCal and defines the geometrical acceptance of the spectrometer. Its rectangular opening is precisely defined with 4 steel pieces shaped to project back to the target. The collimator opening for the 1993 data taking was set to $1° < \theta < -7°$ in the xz plane and $-1° < \theta < +1°$ in the yz plane, or $-126.6 < \theta < 15.1$ mrad and $-10.7 < \theta < 10.7$ mrad, respectively. The opening is asymmetric relative to the incident beam axis to maximize the acceptance in p_t.

The first element of the spectrometer is the analyzing dipole magnet positioned at 3 m downstream of the target. Its field is perpendicular to the spectrometer plane and can be inverted to selectively favor negatively or positively charged particles. The magnet generates a maximum field of ~ 2.2 T and has an effective length of

1.045283 m [62]. A field value of 0.262 T was used for the data presented here.

The charged particle identification is done by simultaneously measuring the charge, the momentum and velocity to reconstruct the mass of particles such as π, p, K, $\bar{\mathrm{p}}$, d [63, 64] and even heavier fragments [65]. The particle deflections (and thus momenta) are measured with the tracking system [62] composed of drift chambers (DC's) and multiwire proportional chambers (MWPC's). The particles velocities are deduced from the time-of-flights ($1/\beta = c/v$) that are measured with the TOFU hodoscope. The spectrometer allows a 2.5 σ separation of π from p to momenta up to 8.8 GeV/c. The detectors from the tracking and time-of-flight systems are discussed separately below with the exception of the forward scintillators and UCal which are not used in the present analysis.

2.2.1 Tracking system

The E877 tracking system is designed to simultaneously measure the trajectories of many charged particles. The tracking system is divided into two sub units: drift chambers (DC's) and multiwire proportional chambers (MWPC's). The DC's provide a high resolution position measurements whereas the four MWPC's are used to discriminate between multiple track reconstruction solutions.

Drift chambers

The two drift chambers (DC2 and DC3) are the main elements of the tracking system. They are located at 5.4 m and 11.5 m downstream from the target. They are both built in similar fashion, DC3 being twice as large as DC2. Each detector has 6 wire planes of vertical anode wires spaced by 6.35 mm and 12.7 mm for DC2 and DC3, respectively. The downstream side of each chambers is closed by a segmented cathode plane.

As particles go through the detector, they liberate electrons within the gas. The free electrons then follow the field lines and drift toward the nearest anode wire with drift velocities of about $v \sim 50$ μm/ns. The increased field gradient close to the wire causes the electrons to generate avalanches. The electron drift time is then used to deduce the incident particle x position with a resolution of $\sigma_x \sim 300\mu$m [50]. The localized ion cloud on the last wire plane induces an image charge distribution on the cathode plane by capacitive coupling. The E877 drift chambers cathode planes are segmented in chevron shaped pads [66, 67, 68, 69]. The image charge spans several cathode plane pads. A y position measurement is interpolated from the sharing of the imaged charge with a resolution of $\sigma_y \sim 1$ mm [63].

Multi-wire proportional chambers

Four Multi-Wire Proportional Chambers (MWPC1-MWPC4) help track recognition by confirming the trajectories found with the drift chambers. The MWPC's are positioned at regular ~ 120 cm intervals between the two drift chambers. They are all built with vertical anode wires spaced by ~ 5 mm and readout using LeCroy PCOS III system. This provides a bit pattern that is used for track confirmation off-line or for simple on-line tracking reconstruction. A detailed description of their construction can be found in [64].

2.2.2 Time-of-flight system

Particle velocities are measured with the TOFU (Time-Of-Flight Upgrade) hodoscope. It is located at 12 m from the target and has an overall TOF resolution of $\sigma_{\mathrm{TOF}} \sim$ 85 ps. The hodoscope comprises about 150 counters, each viewed by two photomultipliers. A vertical position measurement is obtained from measured time differences with a resolution of $\sigma_y \sim 1.8$ cm. The particle energy loss in the scintillators (dE/dx)

is used to determine the charge of the particle, to correct for the time-walk effect and to eliminate multiple hits. Since I have been personally involved in all stages of the construction and operation of this detector system, its design, assembly and performance are discussed in detail in the following chapter.

2.2.3 Spectrometer acceptance

The relevant active dimensions of the spectrometer detectors are listed in Table 2.1 along with the corresponding z positions. The dynamic ranges of the tracking detectors are insufficient to allow a simultaneous measurement of minimum ionizing particles (MIP's) and fully stripped gold ions without causing breakdowns. Therefore, the regions of the tracking detectors through which beam particles and large fragments are going, are deadened by reducing the bias on the anode wires. Data were taken with two opposite magnet polarity settings, respectively called A (0.262 T, pointing along the y axis direction) and B (-0.262 T, pointing opposite to the y axis direction), thus sending the beam into two different regions of the detectors. The precise positions of these regions are summarized in table 2.2.

The E877 spectrometer acceptance coverages for positively (negatively) charged particles for the 1993 data taking run are shown in figure 2.2 for each of the two magnetic field polarities. Acceptance coverages for π, K and p begin at rapidities of 2.4, 1.4 and 1.0 respectively and are determined by the detector edges and the magnetic field strength[2].

The maximization of the spectrometer transverse momentum acceptance implies that at a given magnetic field setting, the spectrometer acceptance will slightly favor either positively or negatively charged particles.

The detector dead sections introduce dead bands into the A (B) field in the lower

[2] rapidity is defined as y $= 1/2 \cdot \ln[(E+p_z)/(E-p_z)]$

Table 2.1: Spectrometer components active dimensions and positions. The numbers for TOFU are given only as indications. The numbers in italic do not influence the acceptance and are given only as indications. All numbers are in cm.

Detector	z	x_{min}	x_{max}	y_{min}	y_{max}
S2	-627.4	—	—	—	—
BVer1	-585.6	—	—	—	—
BVer2	-279.9	—	—	—	—
S4	-200.3	—	—	—	—
Coll. Front	73.37	-8.3594	1.16	-0.6402	0.7684
Coll. Back	154.65	-19.690	2.33	-1.58	1.73
Magnet Front	263.60	-40.31	4.78	*-7.62*	*7.62*
Magnet Back	355.95	-40.31	4.78	*-7.62*	*7.62*
DC2	538.00	-61.2757	20.3218	*-15.*	*15.*
MWPC1	663.26	-81.161	35.619	*-16.5*	*16.5*
MWPC2	784.06	-99.509	35.619	*-19.35*	*19.35*
MWPC3	908.69	-111.941	47.571	*-22.25*	*22.25*
MWPC4	1031.72	-126.148	56.748	*-25.1*	*25.1*
DC3	1154.5875	-142.4478	66.4672	*-30.*	*30.*
TOFU	~123.0	-146.982	68.50	*-30.*	*30.*

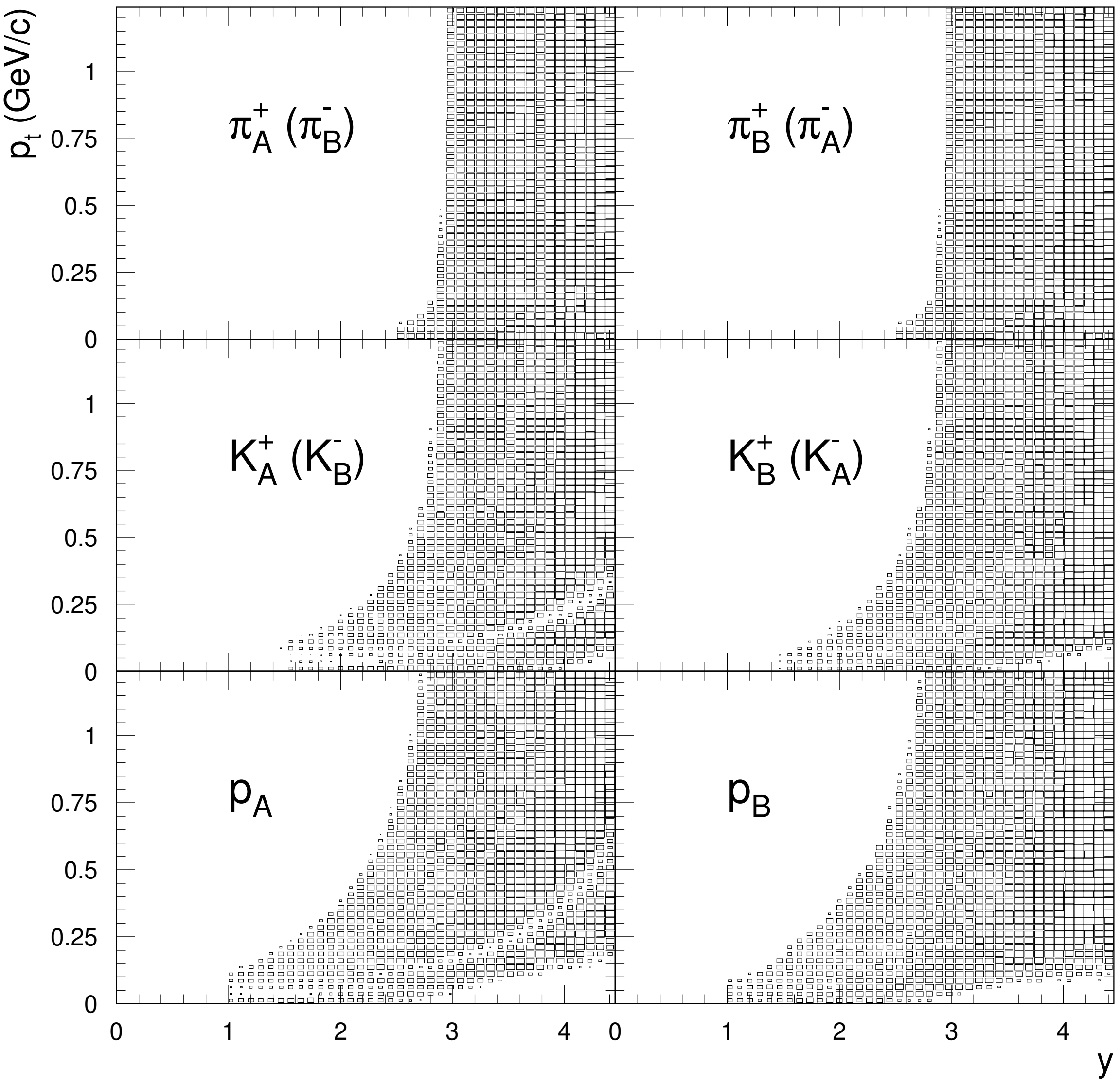

Figure 2.2: Spectrometer acceptance. The acceptance is plotted as a function of transverse momentum versus rapidity for both magnetic field polarities (A and B). Nearly equivalent negative particle acceptances are indicated in parenthesis.

Table 2.2: Tracking detector dead sections. All numbers are in cm

Detector	*Field A*		*Field B*	
	x_{min}	x_{max}	x_{min}	x_{max}
DC2	-3.3833	1.8187	-5.000	0.3000
MWPC1	-3.1015	3.3030	-3.6742	0.9201
MWPC2	-3.3515	3.1015	-5.9121	0.6613
MWPC3	-2.8297	4.0818	-6.5130	0.7060
MWPC3	-2.3326	4.6055	-7.1520	0.0980
DC3	-3.3833	6.5715	-10.6440	0.4800

transverse momentum region of positive (negative) particle acceptance. Thus, the regions that include $p_t = 0$ GeV/c is better covered by the B (A) field setting for positive (negative) particles. At the highest rapidities, the detector dead sections eventually cut into the lowest p_t acceptances of the heavier kaons and protons in both polarities.

Chapter 3

Time-of-flight hodoscope

A new Time-Of-Flight (TOF) hodoscope named TOFU (Time-Of-Flight Upgrade) was built as part of an upgrade to the E814 experimental setup in order to study Au+Au collisions [53, 70]. The E814 spectrometer had two TOF hodoscopes, with the main one located at 30 m downstream of the target as shown in figure 2.1. A secondary hodoscope, located at 12 m from the target, was covering only the larger angles at the edges of the spectrometer (see [48, 71, 72] for descriptions of the E814 spectrometer). In particular, this system was not well suited to study kaons. A large portion of them decayed before reaching the main hodoscope. It was thus decided to replace the hodoscope located at 12 m by a wall of scintillators covering the full aperture of the spectrometer. The shorter flight path allows more than two thirds of the produced kaons to be detected before they decay. The new hodoscope was designed to handle the large particle multiplicities created at forward angles in Au+Au collisions and to significantly improve on the TOF resolution of $\sigma_{\text{TOF}} = 200$ ps achieved with the previous hodoscope.

All TOF systems are composed of start and stop subsystems. Several constraints dictate the basic design of each subsystem. The characteristics of the studied particles

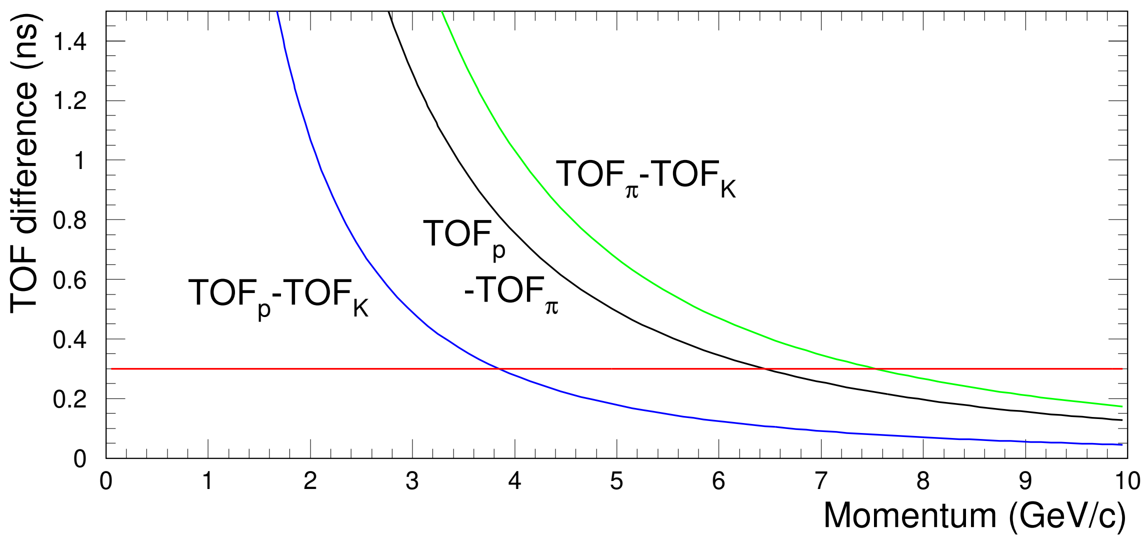

Figure 3.1: Time-of-flight difference between pions, kaons and protons for a 12 m flight path as a function of momentum. The horizontal line at 300 ps corresponds to $3 \times \sigma_{\mathrm{TOF}} = 100$ ps.

determine the required performance of the overall system. The maximum momentum at which particles could be identified by the E814 spectrometer was limited by the time-of-flight resolution. An identification of particles with momenta of up to a minimum of 4 GeV/c was desired in order for the E877 spectrometer to be truly complementary to the other AGS experiments [53]. The time-of-flight differences between pions, kaons and protons, after a flight distance of 12 m, is plotted as function of momentum in figure 3.1. From the K-p curves of figure 3.1 we deduce that an overall time-of-flight resolution of $\sigma_{\mathrm{TOF}} < 100$ ps is required in order to achieve a 3σ identification of 4 GeV/c kaons, as shown by the horizontal line in figure 3.1.

The details the start and stop systems are discussed in the following section. A detailed description of the assembly, physical layout and testing of the stop subsystem follows. The calibration procedure is then explained and the overall performance of the detector system is analyzed.

3.1 Specifications

The design choices that were made are discussed in the next two subsections. We will spend more time on the TOF hodoscope since this is the E877 spectrometer detector system for which I was responsible.

3.1.1 Beam scintillators

During the 1993 data taking, the arrival time of the beam particles was measured with the beam scintillators. The beam counters consist of four scintillator counters mounted in pairs S1-S2 and S3-S4. They provide the start to the time-of-flight system and are also used to derive the gates for all the detectors of the experiments.

The overall mechanical arrangements are schematically shown in figure 3.2. S1

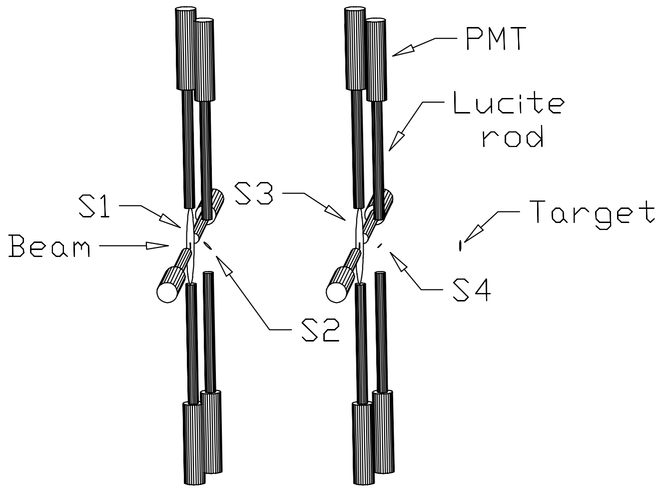

Figure 3.2: Beam scintillators artist's view. The distances between components along the beam axis are scaled down by a factor of $\times 10$.

and S3 are 6.35 mm thick scintillators with outer diameters of 190.5 mm and center hole diameters of 15 mm and 6 mm, respectively. They are each read out by four photomultiplier tubes (EMI 9954B) mounted radially 90° apart around each disk outside of the vacuum. Four 3.4 cm 12 cm long lucite rods carry the light from the outer edges of the scintillators to the outside. Good beam particles must pass through the center holes of both S1 and S3 which are sensitive to Z=1 particles thereby vetoing stray beam particles and upstream interactions. The S2 and S4 scintillators are placed along the beam trajectory inside a vacuum enclosure. S2 and S4 are ellipses with dimensions which give projected disk diameters of 18 and 9 mm when tilted at 45°, thus overlapping the holes of S1 and S3. They are made of Bicron BC422 [73] with a thickness of 0.5 mm. They are installed at an angle of 45° relative to the PMT axis so that the measurement is performed on *direct light*. This minimizes the time spread that would otherwise be introduced by multiple internal reflections of the photons inside the scintillators. The light emitted by the S2 and S4 scintillators is collected and transported outside the vacuum with 12 cm long, 25.4 mm diameter lucite cylinders. The light is then shone into the central part of the PMT photocathodes, to further reduce the electron transit time spread. The rest of the photocathodes were baffled to eliminate stray light from reflections.

Because the S2 and S4 scintillators sit in the beam trajectory, they have to be as thin as possible in order to limit the amount of beam interactions upstream of the target. The mean energy loss rate of fully stripped Au ions is so large that the strength of the signal was not of concern. A thickness of 0.5 mm was chosen as it provides enough structural strength to allow for machining and ease of manipulation. The inorganic scintillator BC422 was selected for its ultrafast timing characteristics [73].

The small number of time channels (4 total) which need a good time resolution allows the use of more expensive PhotoMultiplier Tubes (PMT). The Hamamatsu R2083 50.8 mm (2 inches) 8-stage PMT was selected for its subnanosecond rise time of 0.7 ns, its small electron transit time of 16 ns and transit time spread of 0.37 ns [74]. The complete system produced Au ion signal pulse-heights at the phototube outputs of at least 2 V. This PMT was shown to have a time resolution better than 35 ps by the E802 collaboration [75]. The photomultipliers were part of H2431, PMT and voltage dividing base assembly.

3.1.2 Time-of-flight hodoscope

Several criteria guided the design of the hodoscope, the first one being the optimal number of channels to build. To maximize the tracking power of the spectrometer, it is important that the granularity of TOFU at least matches that of other spectrometer components. The tracking detector placed just upstream of the hodoscope (DC3) has a wire spacing of 12.7 mm and thus an effective granularity of $\delta x_{\mathrm{DC3}} = 25$ mm. Additionally, the granularity of the hodoscope has to be as fine as possible to minimize the occupancy. Budgetary constraints limit the number of channels that can actually be built. For central Au+Au collisions, the mean spectrometer occupancy is $\approx$7 to 8 charged particles per event. The occupancy is highly position dependent along the bend plane of the spectrometer. It peaks in the region that surrounds the beam trajectory, where it reaches $\sim$20% per drift chamber sense wire and decreases smoothly to $\sim$5% at the edge of the detector (see figure 4.7).

The allocated budget allowed for a total of $\approx$150 scintillators to cover a distance of ~ 2.2 m. This allowed for granularity of $\delta x_{\mathrm{TOFU}} = 17$ mm that is well matched to that of DC3 and does not limit the tracking power of the spectrometer. In order to reduce the occupancy around the beam region, a 38 cm long section of the wall was made of 39 counters with granularity of $\delta x_{\mathrm{TOFU}} = 10$ mm. The detector system was designed around 160 virtual scintillators of which 148 were actually built. This allowed for some flexibility in assembly and also provided some spare electronic channels in case of malfunctions.

With momenta of the order of 1 to 5 GeV/c, the energy loss rate of forward produced particles is close to a minimum. They therefore produce the lowest amount of light per unit distance (dE/dx) in the scintillator. They are often referred to as Minimum Ionizing Particles (MIP) [76]. The larger the initial signals are, the easier it is to minimize the effects of detector and electronic noises. The inorganic plastic scintillator BC404 from Bicron has a maximum emission at a wavelength of 408 nm [73] and a fast decay constant of 1.8 ns. It was selected because it has the largest light output of all of Bicron scintillators at the wavelengths corresponding to the PMT maximum sensitivity.

A simple way to further improve on the light output consists in increasing the thickness of scintillating material. A thickness of 15 mm ($\sim$4% of a nuclear interaction length) was selected since it represented a good compromise between maximized signal strength, dE/dx measurement and allowable material thickness before the downstream detectors of the spectrometer.

The R2076 8-stage Hamamatsu photomultiplier was chosen for its fast rise time of 1.3 ns, its small transit time 14 ns and transit time spread of 0.36 ns and for its compactness [74]. A similar PMT, the R3478, was shown to yield 55 ps time resolution by the NA44 collaboration at CERN [77]. The small diameter of its photocathode 19.3 mm is well matched to the scintillator dimensions. It has a sensitivity in the near UV from 160 to 650 nm, peaking at 410 nm close to that of the scintillating material. The photomultipliers were bought as part of the H5010 MOD package that included the base assembly. The package also included a magnetic shield with an outside diameter of 21.5 mm and 3 m long output signals and high voltage cables.

Stacking

Various scintillator stacking alternatives were considered, of which some are described in figure 3.3 and in [78]. Different stacking options are sketched for the wide (a,b) and narrow (c,d,e) scintillators. The relatively narrow widths of the scintillators implied that a simple side-by-side stacking (figure 3.3a and c), with a typical 1 mm gap for

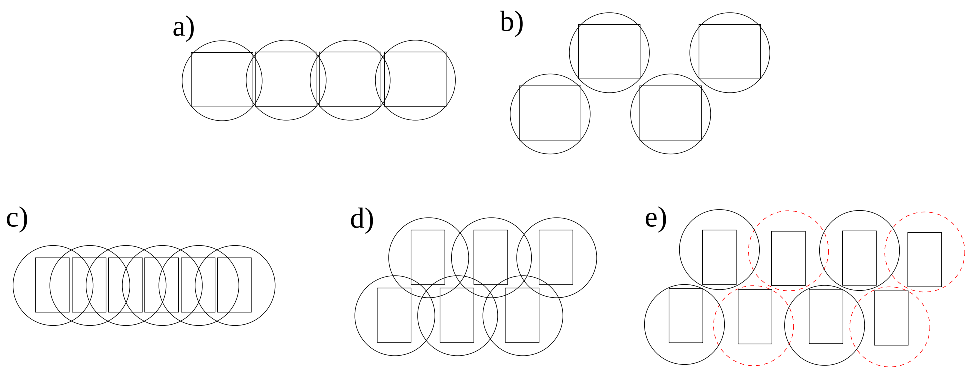

Figure 3.3: Plan view of the wide (a,b) and narrow (c,d,e) hodoscope counters. Scintillators are represented by rectangles, and PMT's by circles.

wrapping would create a 6 to 10% loss in efficiency for normal incident particles. Additionally, the interference of the PMT magnetic shields obliged the usage of light guides or bending of the scintillators.

Instead, staggered patterns (figure 3.3b and d) were adopted that are similar to what is presented in [79]. With this pattern, the potential overlaps and need of light guides are avoided by separating the front and back layers by 2 mm (figure 3.3b). Eliminating the need for light guides minimizes light collection inefficiencies [80]. To eliminate any possible gaps in the scintillator coverage, while keeping to a minimum the fraction of particles that are hitting more than one detector, a small 0.25 mm lateral overlap was included between the front and back layers of counters.

The narrow scintillators that form the high granularity section of the hodoscope presented a special challenge (figure 3.3c). The simple staggered pattern used for the wider detectors can not be used since the PMT's would interfere with each other (figure 3.3d). The strong front to back interference was removed by displacing the PMT's from the scintillator axis by 2 mm (figure 3.3e). The PMT side-to-side interference was resolved by adding a single 150 mm long light guide on one of the extremities of each of the narrower scintillators. This single light guide allows the vertical staggering of the PMT's by mounting the counters with the light guide alternatively at the bottom and top of the scintillator (solid and dashed PMT's in figure 3.3e).

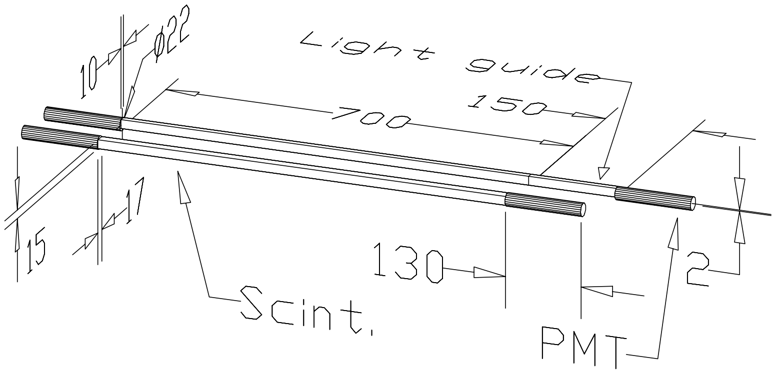

Figure 3.4: Counter dimensions (mm).

The mechanical specifications of both the low and high granularity sections scintillators are summarized in figure 3.4. All the scintillators are 70 cm long and 15 mm thick. They have widths of 17 mm and 10 mm for the low and high granularity sections, respectively. The 15 cm long light guides mounted at one end of the narrow counters are made of UV transparent lucite. The ends of the scintillators and light guides facing PMT's are machined on a lathe using a diamond tip tool into a conical shape (not shown on the sketch) and polished for better light collection [81] and to allow for ease of wrapping. The components, scintillators, light guides and PMT's, are all glued together using BC600 optical cement.

An artist view of the relative positions of the scintillators, light guides and PMT's around the high granularity section is presented in figure 3.5. The scintillator part of the two types of counters is positioned at the same height throughout the hodoscope. In the high granularity section, the light guides allow the separation of the PMT's into two different vertical layers. A smooth transition is provided between the two layer staggered pattern of the high granularity section to the simple staggered pattern of the lower granularity section.

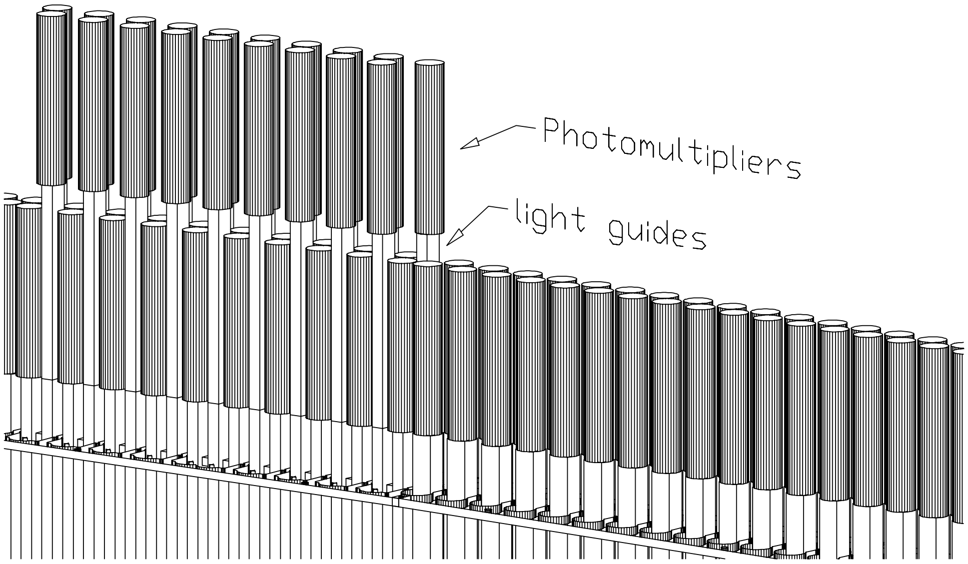

Figure 3.5: An artist view of the counter layout. The scintillators and PMT's are represented by rectangles and cylinders, respectively.

Optical fiber coupling

The need for detector testing and for troubleshooting the large number of channels mandated a test source that mimicked the passage of a particle through each counter. A N_2 dye laser ($\lambda = 460$ nm) was used to pulse the photomultipliers [82, 83]. The light was split and brought to each detector through 250 μm diameter silica optical fibers [84, 85]. For the hodoscope counters, the fibers were coupled to the center of the scintillators using small $3 \times 3 \times 4$ mm UV transparent lucite prisms backed by aluminized mylar as sketched in figures 3.6, in similar fashion to what is done in [86]. Optical fibers were installed in front of each PMT of the start system to pulse them directly. The relative lengths of the fibers were adjusted so that the laser pulses satisfied the timings and gates of the electronics. For the electronics, a *laser event* therefore looked like an event where all the PMT of the hodoscope fired. This system allowed for rapid diagnostics of malfunctions even during downtimes.

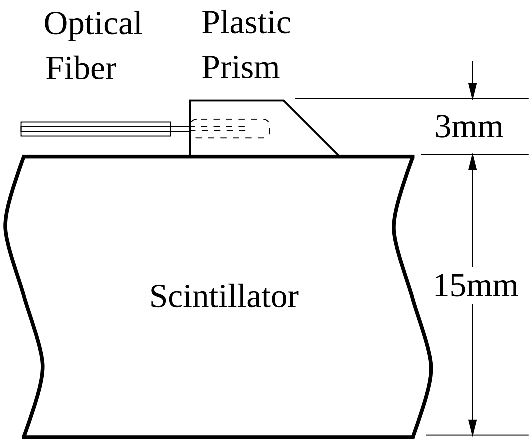

Figure 3.6: Optical fiber coupling to the scintillators. A small piece of aluminized mylar is glued to the back of the prism 45° side.

Wrapping

Precise alignment of the counters is required because of the small dimensions of the scintillators and of the selected hodoscope geometry. A uniform wrapping procedure was developed that minimized the amount and variations in wrapping material. A trilaminated wrapping material made of black plastic, aluminum and clear plastic (total thickness of 250 μm) was selected. It combines into a single layer the usually separate reflecting and opaque wrapping materials. Our tests showed that it resulted in the same light collection efficiency as aluminized mylar, which itself was found to be better than aluminum foil.

The procedure is essentially the same for both sizes of detectors, only the dimensions are different. A sketch of the detector wrapping is shown in figure 3.7. The wrapping procedure was as follows:

1. The plastic was cut to the required dimensions using an aluminum pattern. A 6.4 mm wide double sided tape was affixed along one of the sides of the plastic. The tape was such that, once the second side was removed, only a thin layer of

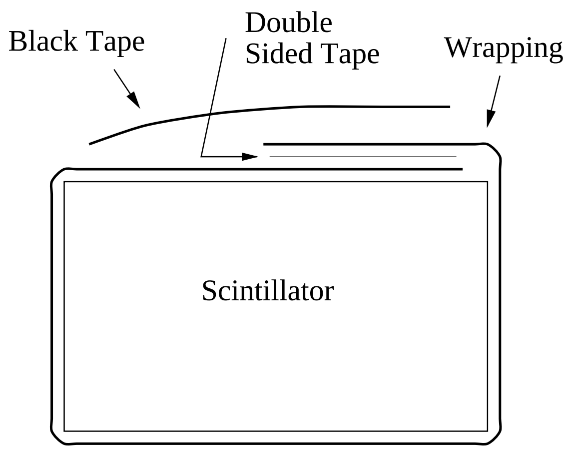

Figure 3.7: Cross section view of the scintillator wrapping.

glue was left. It was used later into the procedure to relieve the stress from the wrapping material.

2. The folds were marked using a grooved plate and a triangular section wheel. The plastic was then hand folded and heat treated (ironed) so as to form permanent 90° creases.

3. The scintillator and wrapping material were cleaned with isopropyl alcohol to remove any residual grease.

4. The plastic wrapping, with the scintillator inside, was inserted inside a grooved bar that maintained three out of the fourth sides of the wrapping in position. The double sided tape was then used to mechanically hold the two flaps of the fourth side into position.

5. A single layer of 3M 33+ black *electrical* tape was applied over the seam to obtain light tightness. The extremities were closed using a layer of 51 mm wide black electrical tape applied perpendicular to the scintillators axis.

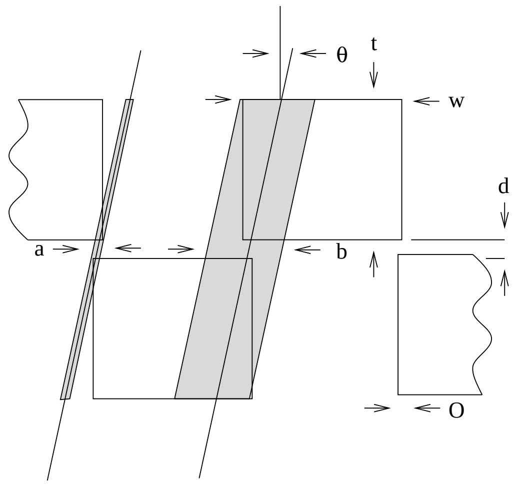

Figure 3.8: Cross section view of the scintillator coverage overlaps. The areas where an incident particle at angle θ hits two detectors are shaded.

6. The light seal around the optical fiber was obtained by applying black silicon rubber generously over 2 cm, at the point where the fiber comes out of the wrapping.

This method lends three surfaces on which the thickness of the wrapping is well known (250 μm) and that can be used for references. The counters were periodically checked for the onset of light leaks over a three-year period. The wrapping was found to be very reliable as no light leaks were found that were attributable to a wrapping defect.

Support structures

Because of the staggered stacking pattern that was selected, a simple flat wall configuration is not optimal for the hodoscope. In a staggered pattern hodoscope, the probability that a particle hits 2 detectors proportionally increases the effective occupancy. For a scintillator of width w (see figure 3.8), thickness t, an overlapping staggered pattern with small overlaps O and short distance between rows d; the fraction of incident particles (coming at angle θ from the perpendicular) that hit two detectors is given by equation 3.1.

$$\mathrm{D}(\theta) = \frac{\mathrm{O} + \mathrm{t}\tan\theta}{\mathrm{w} - \mathrm{O}} \tag{3.1}$$

The fraction D is independent of d since the effective occupancy increase on the large overlap is canceled by the decrease on the small overlap. Because of the large thickness t (15 mm) of the scintillators relative to their width w (10 and 17 mm), the probability of hitting two detectors increases rapidly with incident particle angle. Particle trajectories that are normal to the wall $\theta = 0°$ have a D = 3% chance of hitting two of the wide counters. A straight wall hodoscope configuration (located $\delta z = 9$ m of the magnet downstream opening and perpendicular to the beam axis) would mean that the incident angle value would be of $\theta = 9.5°$, at the outer edge ($x = -1.5$ m). The fraction of particles with an incident angle of $\theta = 9°$ that go through two detectors is calculated to be 33%. A straight wall configuration would thus introduce unacceptable increases in effective counter occupancy. The average incident particle angle is thus minimized by mounting the counters along an arc centered at the magnet with a radius of 9.5 m.

A simple but precise scheme had to be developed to hold the numerous counters into position along this 9.5 m radius arc. In case of malfunctions, it was also desirable that the counters remain individually accessible, even while the hodoscope is in operation. The simplest solution that was found was to use two arcs made of plates with *keyholes* (technical drawings are given in appendix B).

Two types of plates were manufactured, one for each type of counters, and are each partially sketched in figure 3.9. Each aluminum 40 cm long plate defines a section, with the high granularity counters occupying one full section. Once assembled, the sections form two arcs, one above and one other below (60 cm apart) the fiduciary

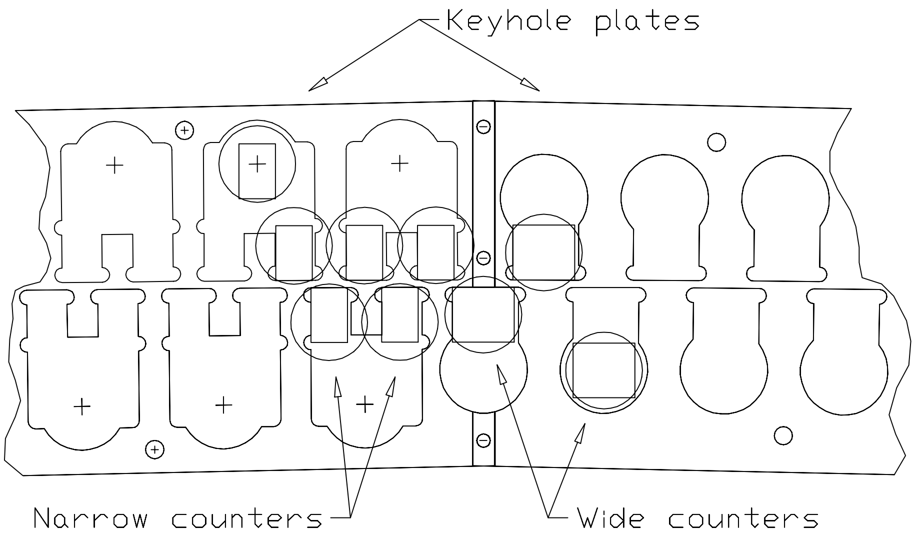

Figure 3.9: Plan view of keyhole plates. The junction between the two types of keyhole plates is sketched, while cross section views of the narrow and large counters are overlaid (rectangles correspond to scintillators, circles to PMT's). Two counters are shown in their removal/insertion position.

scintillator area. The counters are inserted and removed from above, through the larger portion of the keyholes, as sketched by the two recessed counters in figure 3.9. Two sides of the square portion of the keyholes are used as reference. Shims hold the counters into the correct position. The main advantage of this method is that the positioning is done directly on the scintillators. The relative positions of the sensitive areas are therefore well known. Counters can also be easily moved around individually or in sections, while preserving the overall alignment.

A sketch of the scintillator hodoscope and support structure is shown in figure 3.10. It is viewed from upstream on the right side of the beam. The hodoscope wall is about 96 cm high by 240 cm long. The bottom PMT are supported using a single arc made of Bakelite plates for the wide counters. Two Bakelite plates are needed to support the two levels of narrow counters. The arc relative positions are

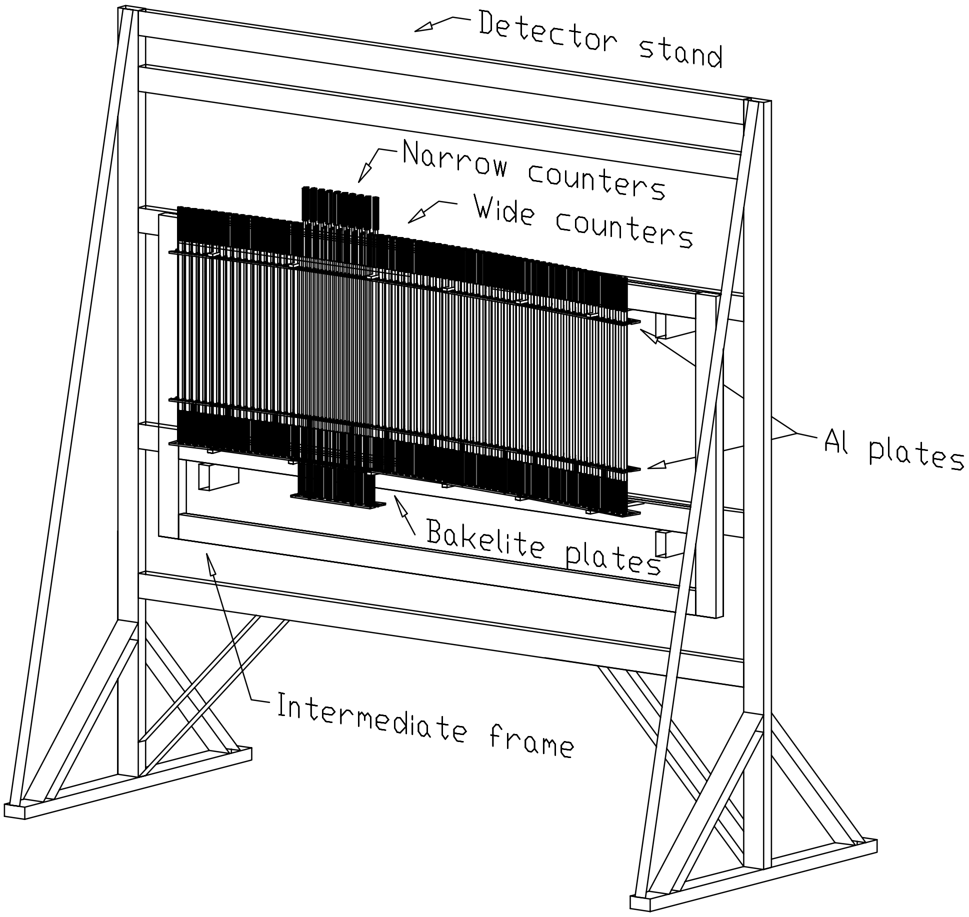

Figure 3.10: An artist's upstream view of the TOFU hodoscope wall and support structures.

held by an intermediate rectangular frame that allows for the fine tunning of the entire wall position. The intermediate frame is attached at four points to the detector stand. The first level of electronics and cable patch panels are placed on a platform located just behind the wall (not shown). This platform allowed for easy installation and maintenance of the hodoscope and also relieved the stress of the readout cables from the detector.

3.2 Bench tests

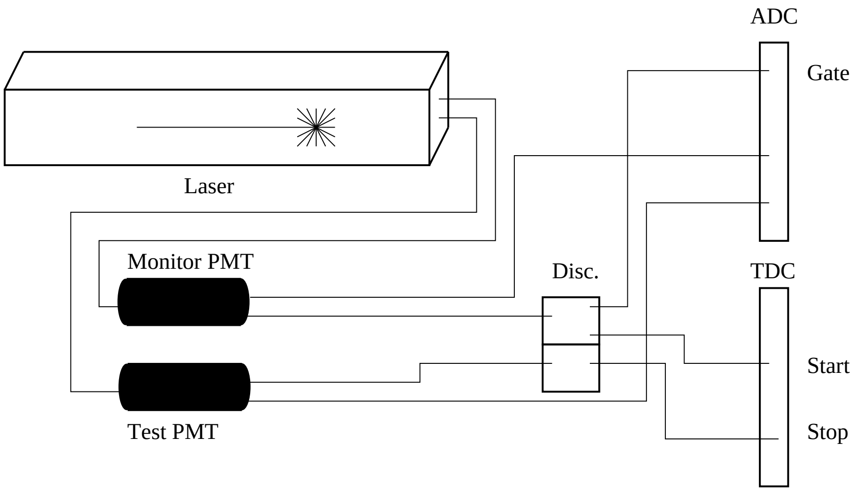

Figure 3.11: PMT bench test setup.

Prior to assembly, the photomultipliers were ordered by time resolution and pulse-height response using the setup schematically shown in figure 3.11. Light pulses from an N_2 dye laser (LN120 from Photochemical Research Associates Inc.) were split and sent through optical fibers to a reference monitor PMT and to the PMT being tested. The time resolution of the photomultiplier being tested was inferred from the width of the time difference distributions measured between the test and reference PMT's using a Phillips 7186 CAMAC Time-to-Digital Converter (TDC) with 25 ps time resolution. The relative gain of each PMT was measured against a single reference photomultiplier (monitor PMT) using a LeCroy 2249A CAMAC charge Analog-to-Digital Converter (ADC).

The photomultipliers were paired according to their measured time resolutions and glued to a scintillator. Once assembled, the complete units were tested using the setup shown in figure 3.12. This flexible configuration allowed to selectively trigger on the test laser, a radioactive ^{207}Bi source or on background. In order to optimize

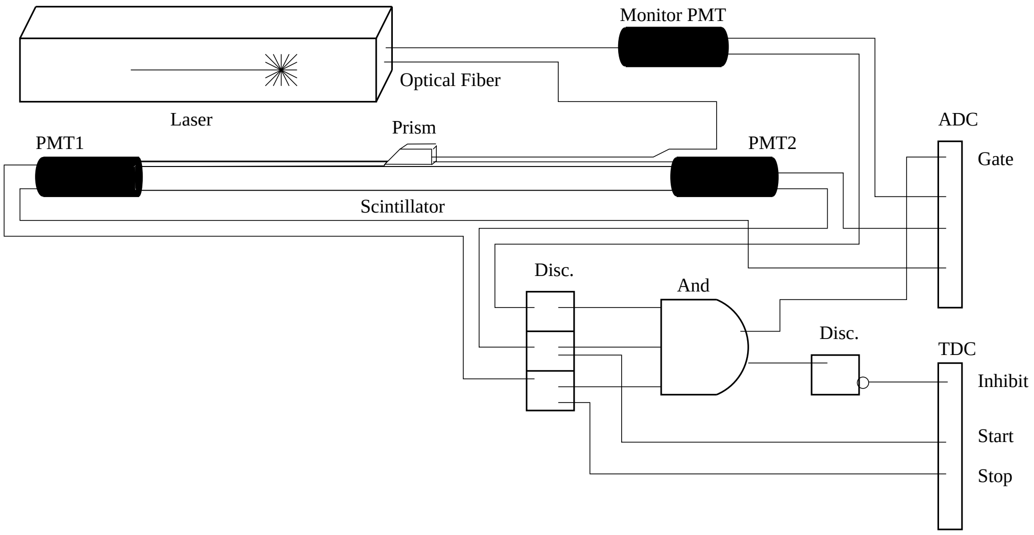

Figure 3.12: Final counter assembly test setup.

particle identification, counters with the best expected time resolution were mounted in the hodoscope closer to the spectrometer axis where the particles with the highest momenta are deflected (*i.e.* highest velocity). Since most of these studies are better performed (and more relevant) on the actual measured particles, the results of only some of them are described below.

3.2.1 Optimal level for discrimination

The effect of time jitters introduced by electronic noise can be minimized by discriminating on the part of the signal with the largest slope. Two other constraints limit the available discrimination level range: the discriminator level can not be set so low as to trigger on noise or so high that it will miss the smaller signals. The discriminator level dependence of the time peak width (σ of a Gaussian fit) for two PMT's is shown in figure 3.13. The time peak width is found to be relatively independent of discriminator level or decrease slightly until about 0.3 or 0.4. At higher discriminator levels, the time peak width is observed to increase. The optimal discriminator level

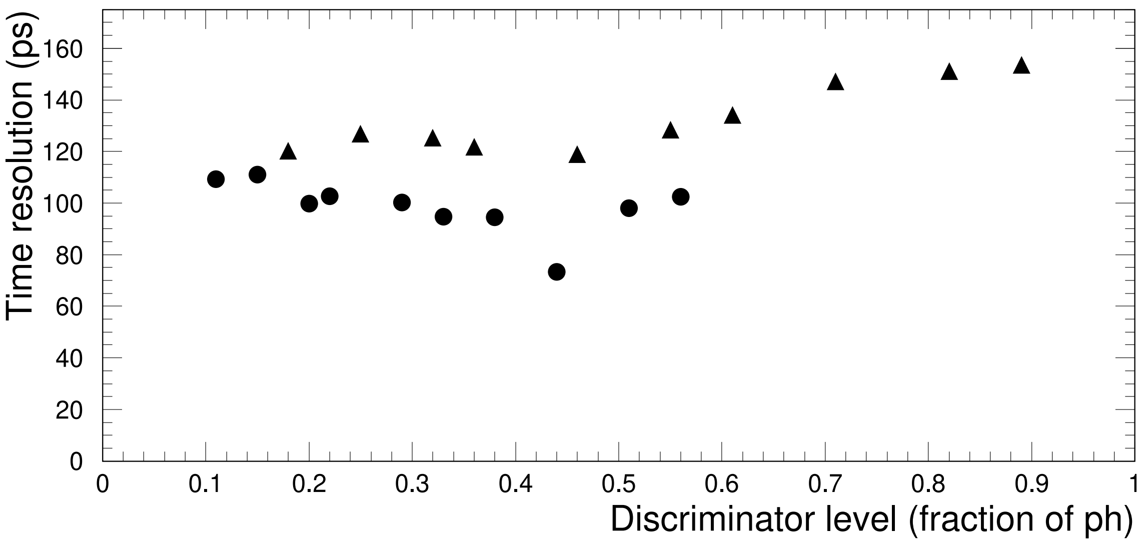

Figure 3.13: Time resolution as a function of discriminator level.

for a given signal pulse-height is therefore found to be around ~0.3–0.4 of the signal pulse-height.

3.2.2 Effective signal velocity and attenuation length

The pulse-height and time dependence on source position was measured at 10 cm intervals along some of the scintillator bars. The results from one of these tests are given in figure 3.14. The measurements were made at regular distance intervals using a ^{207}Bi source while triggering on the coincidences between the counter PMT's.

The effective speed of light $\langle v \rangle$ can be expressed in terms of a length δx

$$\langle v \rangle = \frac{2\delta x}{\delta(t_{x2} - t_{x1})} \tag{3.2}$$

[87] and is obtained by a linear fit to data as is done at the top of figure 3.14. The fitted slope value of 0.15 ns/cm corresponds to an effective signal velocity of 13 cm/ns or 0.44 of c[1].

[1] These values are not corrected for time-walk. See section 3.4.2

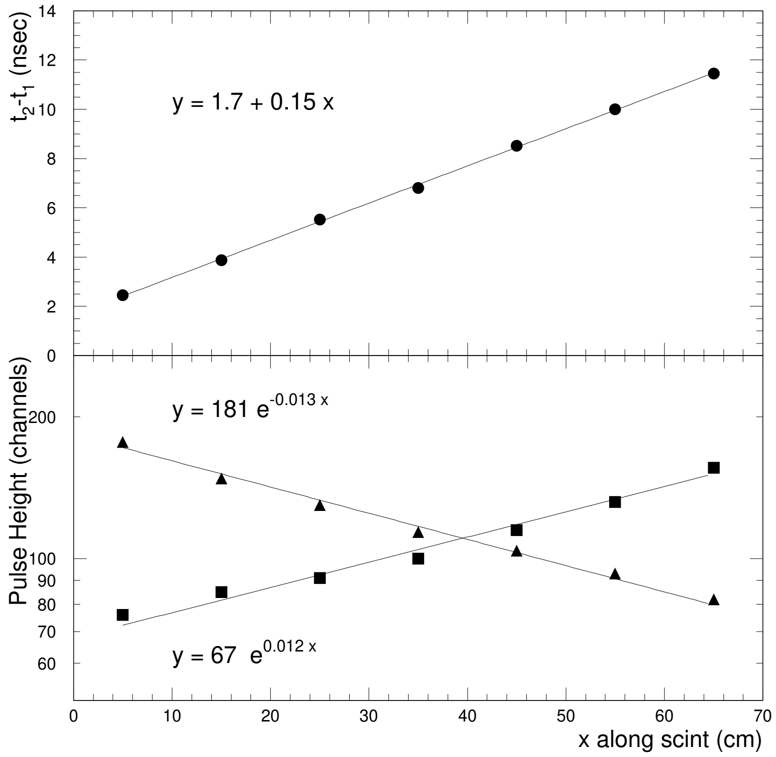

Figure 3.14: Measured time difference (top) and pulse-heights (bottom) as a function of the source position along the scintillator. The lines are linear (top plot) exponential (bottom plot) fits to the data.

The effective scintillator signal velocity $\langle v \rangle$ is related to the speed of light in the scintillator $v_\circ$, the mean angle of refraction $\langle \cos\theta \rangle$ and the index of refraction n by the following relations:

$$\langle v \rangle = \frac{v_\circ}{\langle \cos\theta \rangle} = \frac{c}{n\langle \cos\theta \rangle} \tag{3.3}$$

The index of refraction n of the B404 scintillating plastic being of n =1.58 leads to an average propagation angle of 45°.

The pulse-heights measured as a function of the source position along the scintillator are plotted on a semi-logarithmic scale for each of the two counter PMT's at the bottom of figure 3.14. The observed pulse-height position dependence is well described by the exponential function of the source to PMT distance x

$$\mathrm{PH} = \mathrm{PH}_\circ \cdot \exp \frac{x}{l} \tag{3.4}$$

where l is the attenuation length and $\mathrm{PH}_\circ$, the pulse height at $x = 0$ cm. The exponential functions that are fitted to the data shown at the bottom of figure 3.14 correspond to attenuation length of approximatively $l \approx 80$ cm.

3.2.3 pulse-height dependence on bias voltage

The response of the photomultiplier bases to the applied bias was studied over a large range of voltages. A ^{207}Bi source was placed at the center of each counter being tested and the pulse-heights (PH) were measured at several high voltage settings. The results for four PMT's from two typical counters are plotted on a semi-logarithmic scale in figure 3.15. The four PH gain distribution are well described by exponential

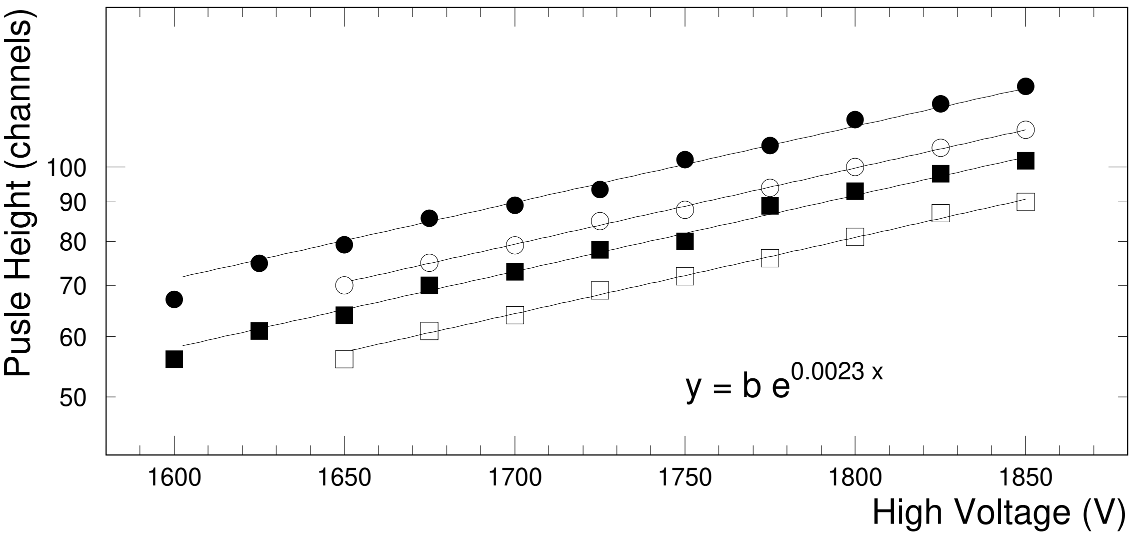

Figure 3.15: Measured pulse-height as a function of applied high voltage. The lines are exponentials with inverse slopes of 435 V.

functions of applied high voltage with a inverse slopes of 435 V, as is shown by the four lines that are overlaid on the data. The common exponential relation provides a convenient way to determine the amount δHV by which the high voltage has to be adjusted to get to a target pulse-height PH, since

$$\delta \mathrm{HV} = \frac{1}{m} \cdot \ln\left(\mathrm{PH}_\circ/\mathrm{PH}_2\right) \tag{3.5}$$

where m is the exponential slope. As a rule of thumb, a 25% increase in measured PH is obtained with an increase of about ~100 V in bias voltage.

3.3 Time-of-flight electronics

The time-of-flight electronics chains used in the E877 setup are described in the two following subsections. Different electronics, are used for the start and stop systems pulse-height measurements. But the two systems share the same TDC's for the time measurements.

3.3.1 Beam counter electronics

A sketch of the beam counter electronics is shown in figure 3.16. The first level of electronics is located at about 20 meters from the detectors while the elements in the dashed box are located inside the central experimental electronics room (counting house). The signal from all the BSci PMT's are brought to the first level electronics through fast RG-8/U foam core cables. They are resistively split into 1/3 for the PH measurement and 2/3 for the timing measurement. The time portion of the S2 and S4 signals is discriminated using Phillips 704 discriminators at approximately 1/10 of the beam particle maximum amplitude and fanned-out. One of each of the fanned-out pulses is used for the event pre-trigger. The logic pulse from one of the PMT's of S4 (called S4-1) is used to define the time of the $\bar{S}1 \cdot S2 \cdot \bar{S}3 \cdot S4$ coincidence which is then used to generate the starts and gates of the data acquisition. The 4

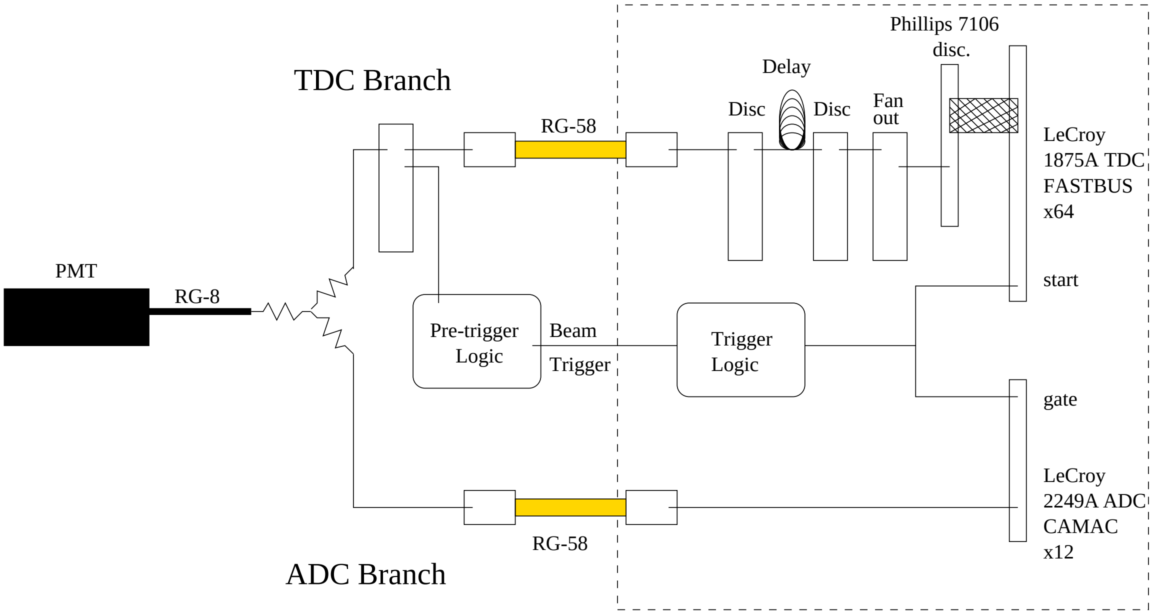

Figure 3.16: Beam counter electronics. The elements in the dashed box are located inside the counting house.

digital time signals from the BSci are sent to the counting house, rediscriminated, and further delayed to fall within the TDC ranges. They are then fanned-out and redundantly fed to each of the 5 TDC modules used in the stop electronics (see below). This over-digitization allows for the individual time-of-flight measurements to be calculated with start and stop information that come from within the same TDC module, thereby eliminating possible cross-module noise sources. The other 1/3 portions of the PMT signals are sent to the data acquisition through RG-58 cables and digitized using a LeCroy 2249A ADC.

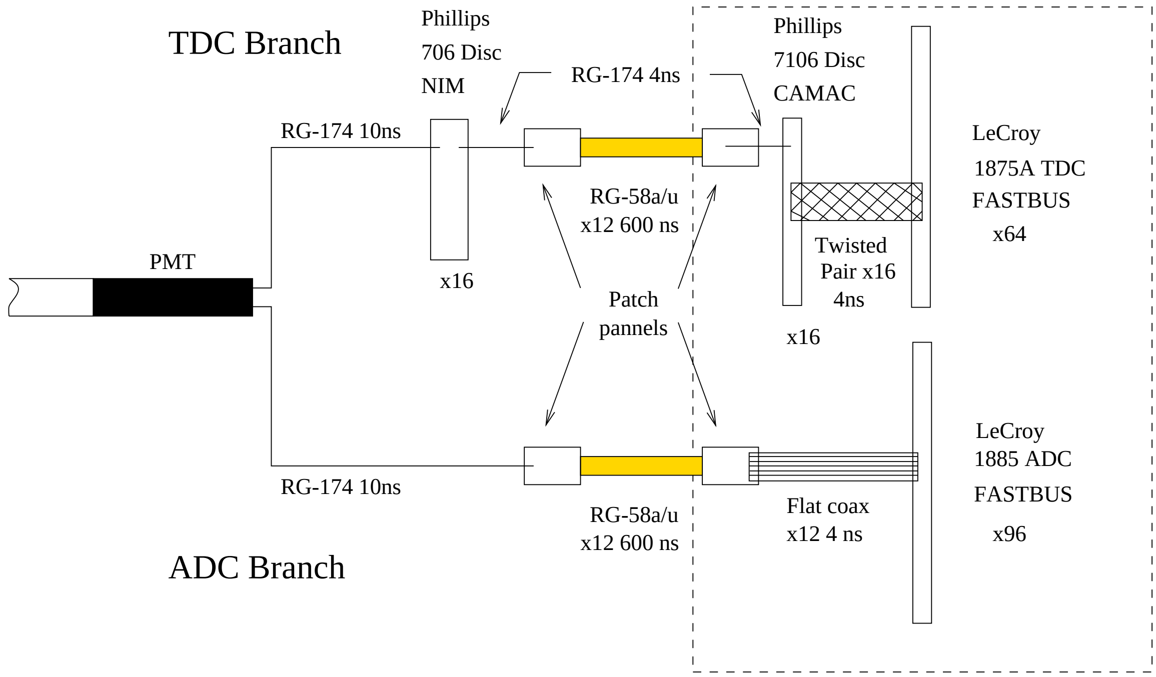

Figure 3.17: Hodoscope electronics. The elements in the dashed box are located inside the counting house. The number of channels per units is indicated where it is greater than one.

3.3.2 Stop electronics

The electronics and cabling used for the hodoscope are schematically shown in figure 3.17. The signal from the photomultiplier cathode is resistively split in two equal outputs inside the PMT base. The signals are carried out on 3 m long RG-174 cables one is used for the time measurement, and the other is used for the pulse-height measurement.

TDC branch

The time signal is discriminated as close to the PMT as possible to limit signal attenuation and possible noise pickup. This is accomplished with 16 channels Phillips 706 NIM discriminator modules. During normal operation, the thresholds on these discriminators were set to 40 mV, *i.e.* ~10% of the average amplitude of the signal of a Z=1 particle. The discriminator digital signal outputs are then sent through ~25 bundles of twelve 600 ns long RG-58 A/U low loss foam coax cables. This signal delay is necessary to allow enough time for a trigger decision to be made. After this long cable delay, the signals are attenuated and deformed. The signals are reshaped and converted to ECL using 32 channels Phillips 7106 CAMAC discriminator modules. The arrivals of the time signals are digitized using five 64 channels LeCroy 1875A FASTBUS TDC's. These 12 bit TDC's have a 100 ns range (25 ps/channel resolution).

ADC branch

The second half of the PMT signals is sent through 600 ns long RG-58 A/U cables to 96 channels LeCroy 1885 FASTBUS ADC's for amplitude measurement. The long delay is necessary for the signals to fall inside the gates that are generated by the data acquisition. The high density of the ADC's imposed the use of 16 flat 50 Ω flat coaxial cable bundles. This also insures the integrity of the impedance and eliminates potential loss and signal reflections.

3.4 Calibration

The TOF system calibration is divided into two stages. First, the pulse-height pedestals are subtracted and the PH gains are equalized. Once minimum ionizing particles can be selected and tracked, the measured time-of-flight and the vertical hit position are then calibrated using identified particles.

Calibration files are generated at regular intervals to account for the observed shifts in gain and time. The largest part of the time shifts is due to the radiation damage suffered by the S2 and S4 BSci scintillators that changes their signal amplitudes. The variation in room temperature, among other factors, changes the gains of all the PMT's, which in turn introduces counter to counter variations in timing and pulse-height.

The calibration procedures of the start and stop signals are almost identical and were mostly done in parallel. The main differences reside in the fact that no position calibration was needed for the start counters.

3.4.1 Pulse-height calibration

The amount of light measured by a photomultiplier after the passage of charged particles through scintillators will depend on many factors, like the charge and the velocity of the particle. Additionally, the amount of energy deposited in a thin scintillator by a minimum ionizing particle follows a fairly broad *Landau* distribution. As is demonstrated in section 3.2.2, the initial amount of light emitted by the scintillator is attenuated exponentially with distance as it travels toward the PMT's. Since the pulse-height is measured at both ends of the scintillators, the initial amount of light or pulse-height (PH) produced can be inferred from:

$$\mathrm{PH} = \mathrm{c}^{j}_{\mathrm{ADC}} \cdot \sqrt{(ph_1 \cdot ph_2)} \tag{3.6}$$

where j is the scintillator slat number and c^{j}_{ADC} is the pulse-height normalization or gain constant that, in the present analysis, is adjusted so that the Z=1 minimum ionizing peak occurs at PH=1. The individual PMT pulse-heights ph_i are obtained from the ADC after subtracting the ADC pedestal and correcting for 60 Hz noise that is picked up from the power grid:

$$\mathrm{ph}^{\mathrm{j}}_{\mathrm{i}} = (\mathrm{ADC}^{j}_{i} - \mathrm{Ped}^{j}_{i} - 60\mathrm{HZ}(\phi)^{j}_{i}). \tag{3.7}$$

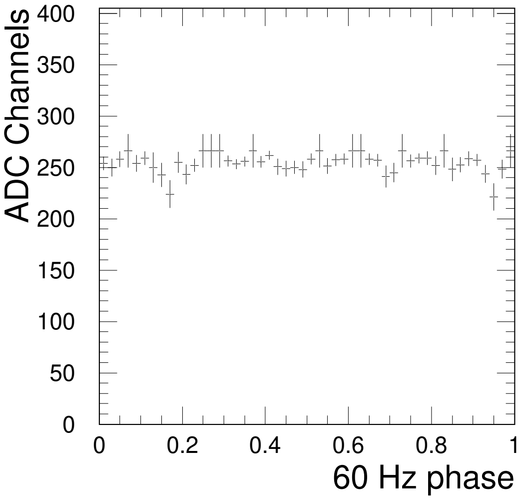

Figure 3.18: Pedestal 60 Hz noise correlation. The pedestal mean (crosses) and variance (vertical error bars) are plotted as a function of 60 Hz phase.

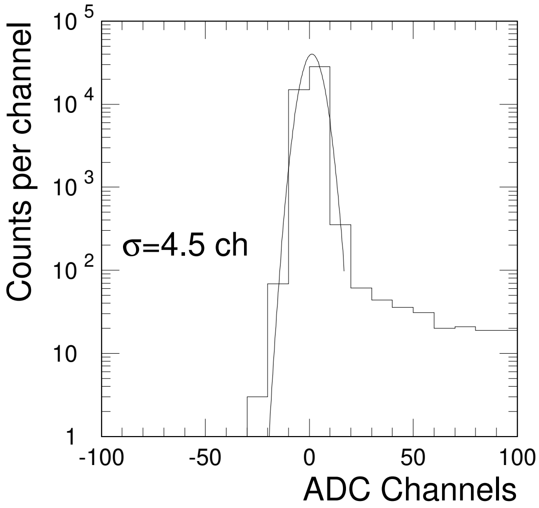

Figure 3.19: 60 Hz corrected ADC pedestals.

Pedestal subtraction

The values measured by each ADC channel in the absence of particles in the spectrometer, called pedestals, are accumulated by expressely triggering the data acquisition system when no beam is present. The pedestal values are histogramed as a function of their relative phase to the power grid 60 Hz as shown in figure 3.18. The phase averaged pedestal value Ped_i^j is then calculated and defines the zero. The variation around the mean value of the pedestal provides a ϕ phase dependent 60 Hz correction $60\mathrm{HZ}(\phi)_i^j$ of equation 3.7. Once the pedestal is subtracted and the 60 Hz is noise corrected, the pedestal width is found to be of the order of 5 ADC channels as shown in figure 3.19.

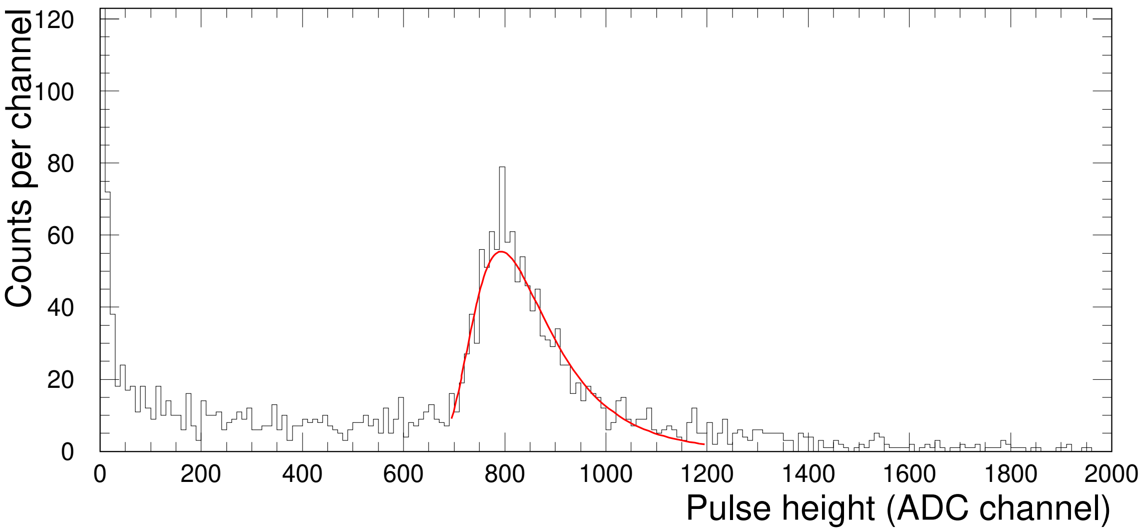

Figure 3.20: Single-counter pedestal-subtracted pulse-height distribution.

Gain calibration

The light collection efficiency and the PMT gain variations lead to variations of the measured signal strengths. In order to be able to combine the measurement from all the counters, their responses are normalized on the most probable PH measured for minimum ionizing particles.

To determine the gain calibration constant c^j_{ADC} of equation 3.6, the pedestal subtracted and 60 Hz corrected data are histogramed as in figure 3.20. The pedestal is seen at PH=0 channels with a clear MIP peak around channel 800 in this example. The value of the gain calibration constant is obtained by fitting the function

$$f(ph) = A \cdot \exp\left(-\frac{1}{2} \cdot \frac{ph - ph_\circ}{w} + \exp\left(-1 \cdot \frac{ph - ph_\circ}{w}\right)\right) \tag{3.8}$$

to the experimental spectra, where $ph_\circ$ is the position of the most probable value, w is related to the width of the distribution. The data in the interval between 0.75 and 1.75 times the position of the maximum are used to perform the fit. A typical fit result is drawn in figure 3.20. The calibration constant is then given by $c^j_{\mathrm{ADC}} = 1/ph^j_\circ$, which places the MIP peak at 1. The resulting calibrated typical spectrum is shown in figure 3.21. This spectrum is obtained in coincidence with spectrometer hits in a

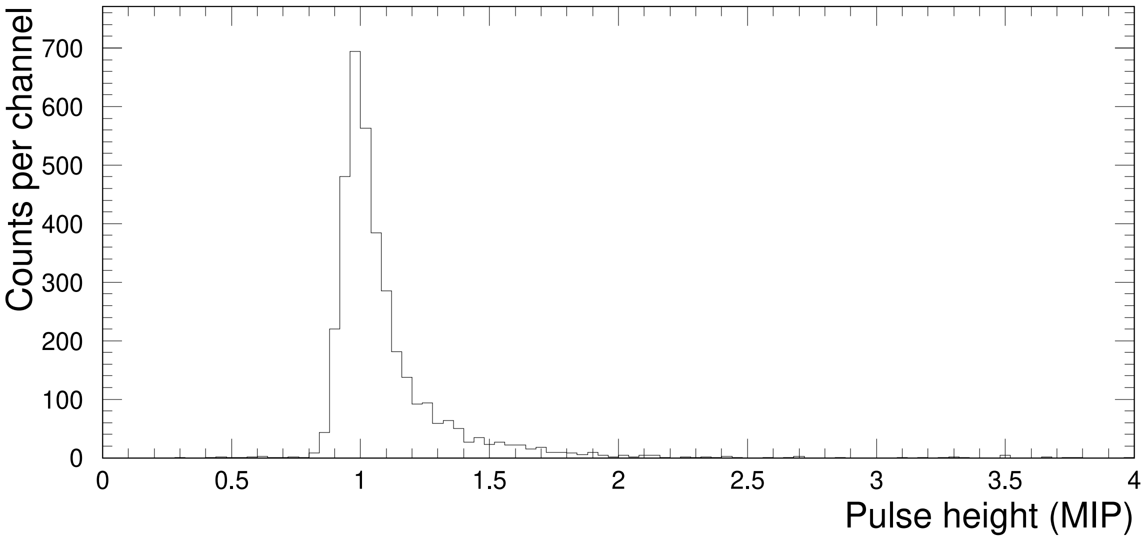

Figure 3.21: Single-counter calibrated pulse-height distribution.

region dominated by Z=1 particles and, consequently, does not exhibit a pedestal. The minimum ionizing peak is relatively narrow with a full width at half maximum of $\sim 16\%$.

3.4.2 Time-of-flight calibration

Each step of the time calibration is discussed after defining the time-of-flight formula. The time-of-flight of particles from the target to an hodoscope counter is expressed as:

$$\mathrm{TOF} = \frac{(\mathrm{t}_1^{\mathrm{stop}} + \mathrm{t}_2^{\mathrm{stop}})}{2} - \frac{(\mathrm{t}_1^{\mathrm{start}} + \mathrm{t}_2^{\mathrm{start}})}{2} - T_\circ^{\mathrm{stop}} \tag{3.9}$$

where t_i^j is the time measured by individual PMT's, and $T_\circ^{\mathrm{stop}}$ is the time offset of the counter. The individual PMT times are obtained from the TDC values TDC_i^j according to the expression:

$$\mathrm{t}_i^j = c_i^j \cdot \mathrm{TDC}_i^j - \frac{b_i^j}{\sqrt{ph_i^j}} \tag{3.10}$$

The TDC internal time gains are calibrated by the time calibration constant c_i^j. Because of the PMT signal finite rise-times, the use of constant level discriminators generates a pulse-height dependency *time-walk* that is assumed to be inversely proportional to the square root of the measured pulse-height ph_i^j (see section 3.4.2). and that is corrected with the time-walk constant b_i^j [88, 89].

Because the time-walk effect is directly related to the signal shape seen by the discriminator, the correction is calculated using the pedestal subtracted pulse-height only. As discussed in the above section 3.4.1, the ph_i^j term of equation 3.10 therefore expands into

$$\mathrm{t}_i^j = c_i^j \cdot \mathrm{TDC}_i^j - \frac{b_i^j}{\sqrt{\mathrm{ADC}_i^j - \mathrm{Ped}_i^j - 60\mathrm{Hz}(\phi)_i^j}}. \tag{3.11}$$

The full expansion of the TOF formula is given in equation 3.12.

$$\begin{aligned}\mathrm{TOF} \;=\; & \frac{(c_1^{\mathrm{stop}} \cdot \mathrm{TDC}_1^{\mathrm{stop}} - \frac{\mathrm{b}_1^{\mathrm{stop}}}{\sqrt{\mathrm{ADC}_1^{\mathrm{stop}} - \mathrm{Ped}_1^{\mathrm{stop}} - 60\mathrm{Hz}_1^{\mathrm{stop}}}})}{2} \\ & + \frac{(c_2^{\mathrm{stop}} \cdot \mathrm{TDC}_2^{\mathrm{stop}} - \frac{\mathrm{b}_2^{\mathrm{stop}}}{\sqrt{\mathrm{ADC}_2^{\mathrm{stop}} - \mathrm{Ped}_2^{\mathrm{stop}} - 60\mathrm{Hz}_2^{\mathrm{stop}}}})}{2} \\ & - \frac{(c_1^{\mathrm{start}} \cdot \mathrm{TDC}_1^{\mathrm{start}} - \frac{\mathrm{b}_1^{\mathrm{start}}}{\sqrt{\mathrm{ADC}_1^{\mathrm{start}} - \mathrm{Ped}_1^{\mathrm{start}} - 60\mathrm{Hz}_1^{\mathrm{start}}}})}{2} \\ & - \frac{(c_2^{\mathrm{start}} \cdot \mathrm{TDC}_2^{\mathrm{start}} - \frac{\mathrm{b}_2^{\mathrm{start}}}{\sqrt{\mathrm{ADC}_2^{\mathrm{start}} - \mathrm{Ped}_2^{\mathrm{start}} - 60\mathrm{Hz}_2^{\mathrm{start}}}})}{2} \\ & - x_{\mathrm{start}} \cdot \mathrm{c_x} \\ & - T_\circ \end{aligned} \tag{3.12}$$

The $x_{\mathrm{start}} \cdot \mathrm{c_x}$ term accounts for a slight start time position dependence that is leftover after calibration (see section 3.4.2) and $T_\circ$ is an overall offset. The determination of the values of each of the constants is done in parallel for the BSci and TOFU systems as described below.

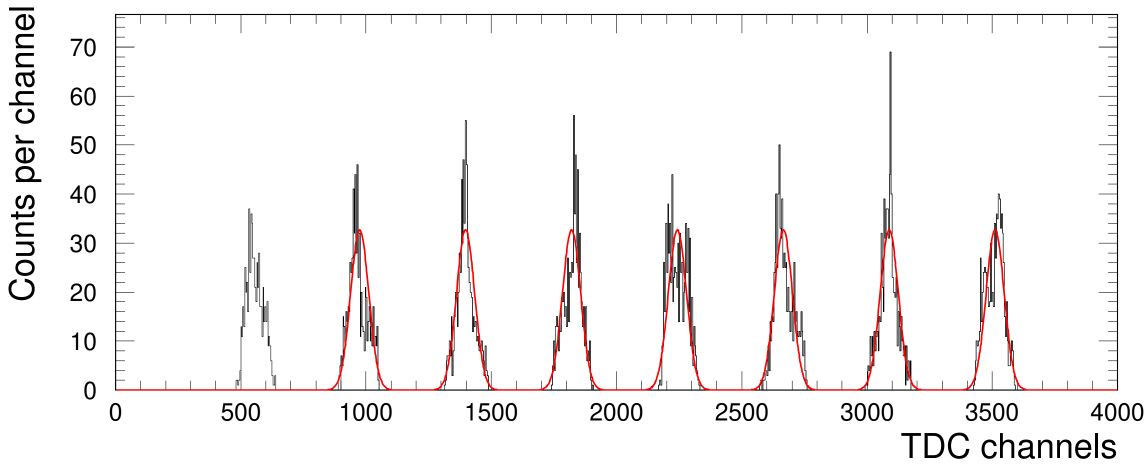

Figure 3.22: TDC time calibration spectrum. Seven gaussians with identical widths and spacing are fitted to the spectrum (solid curve).

TDC time calibration

The 462 Ortec time calibrator NIM module [90] is used to measure the TDC time calibration constants c_i^j values. The time calibrator generates starts and stops logical signals with 8 different intervals at ± 25 ps precision in 10 ns increments. The resulting peaks, for the 1993 data set, measured with a typical TDC channel are plotted in figure 3.22. The peaks are found to be much wider than the quoted precision of the time calibrator. This was traced to a time-delay generator module that introduced a large time spread in the electronics calibration chain. The problem was corrected for the subsequent running periods (1994 and 1995). The first peak is in the non-linear first 30 ns of the TDC range and is therefore not included in the calibration procedure. The remaining peaks are fitted with 7 gaussians of identical widths, amplitudes and spacings δt (in TDC channels), as is shown in figure 3.22. The TDC channel time calibration constant is then given by $c_i^j = 10000/\delta t$ ps/channel.

The TDC non-linearity is studied using the peak position deviations from the linear fit where the peaks are individually fitted by a Gaussian distribution. The

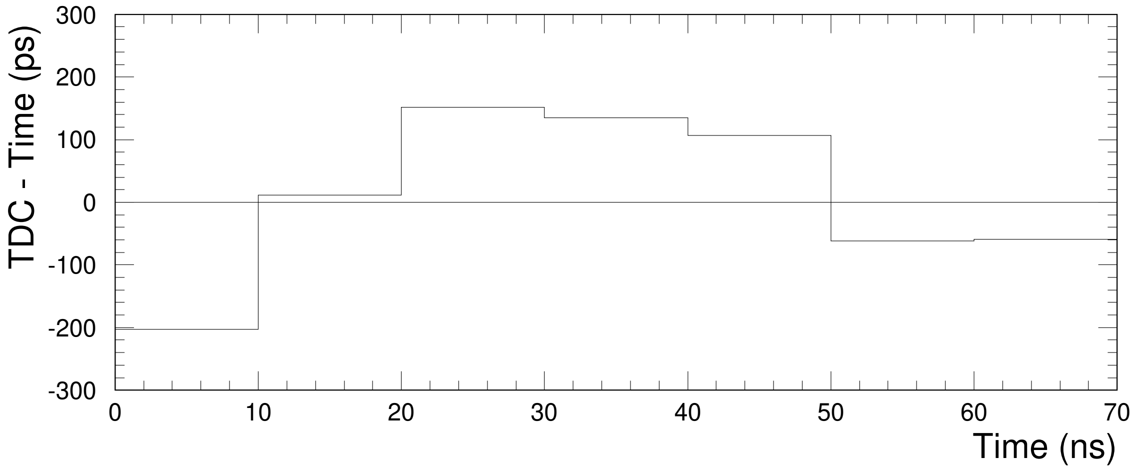

Figure 3.23: TDC non-linearity. Measured time deviations from the time calibration fit as a function of TDC delay.

resulting large scale differential non-linearity for a typical TDC channel is plotted in figure 3.23. The TDC's are found to have non-linearities of the order of ± 175 ps over 70 ns. This is consistent with the value quoted by LeCroy of plus-minus 0.25% of the fitted range [91]. Since the time-of-flight difference needed to separate the different types of particles is of the order of 10 ns, the maximum contribution from non-linearity to TOF error is of the order of 20 to 25 ps.

The first 30 ns and last 10 ns of the range of some of the TDC channels were found to have significantly larger non-linearities than what is shown here [92]. Some are as large as 2.5% of the fitted range. The usable TDC range window of 60 ns remains large enough for our purposes. Special care was taken during the cabling to ensure that the signals were within these windows.

Time-walk correction

The fixed level discriminators used for time measurements of the finite rise-time PMT signals introduce a pulse-height dependency of the measured time, an effect known as *time-walk*. As shown in figure 3.24, two signals that are emitted at the same time,

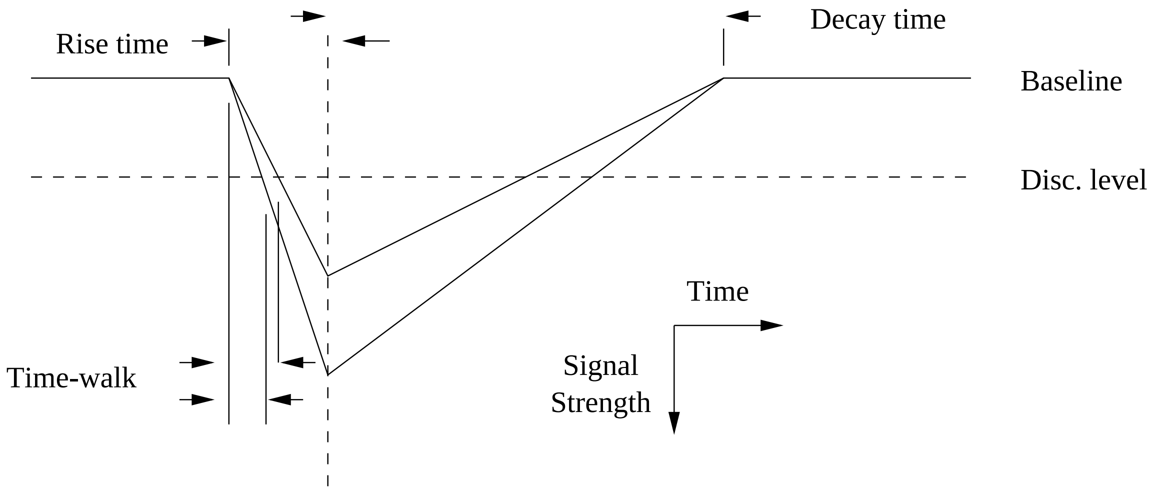

Figure 3.24: Sketch of the time-walk effect on two signals emitted at the same time but with different pulse-heights.

that have identical rise times but different pulse-heights will cross the discriminator threshold at different times. The time of arrival that is measured with a constant level discriminator is therefore a function of the signal pulse-height. Assuming that the pulse leading edge shape is linear, as in sketched in figure 3.24, the time at which the signal crosses the discriminator threshold is then inversely proportional to the pulse-height. If the PMT signal shape is rather approximated to a parabola, the time-walk effect is then inversely proportional to the square root of the ADC measurement. Similarly to what is done in [78], the time-walk correction is therefore assumed to be of the form

$$t_i^j = t_i^j - \frac{b_i^j}{\sqrt{ph_i^j}}, \tag{3.13}$$

where b_i^j is the time-walk correction parameter.

The pulse-heights measured by each tube of a counter are strongly correlated. The optimum values for the time-walk correction must therefore be determined simultaneously for both tubes of the counter. The time-walk parameter values are determined by minizing the width of the difference between the measured and calculated time difference distributions $\mathrm{TOF} - \mathrm{TOF}_{\mathrm{calc}}$ by varying both b_i^j parameters.

Assuming the mass m of a particle, $\mathrm{TOF}_{\mathrm{calc}}$ is obtained from its momentum and path length l measured with the spectrometer tracking system, and is given by

$$\mathrm{TOF}_{\mathrm{calc}} = \frac{l\sqrt{m^2 + p^2/c^2}}{p}. \tag{3.14}$$

For the calibration, particles are identified by roughly cutting on their measured momentum and TOF. The distribution of particles species across the hodoscope varies considerably from one end to the other. Negative pions are used where they are dominant. Protons are used in the area immediately adjacent to the beam. Positive pions are also used for the end of the hodoscope where no negative pions are present.

To minimize the width of the time difference distribution, the values of the time-walk correction parameter b_i^j are scanned in steps of 5 from 10 to 80 $\sqrt{\mathrm{ADC}}/\mathrm{ns}$. A Gaussian distribution is fitted to each of the resulting $\mathrm{TOF} - \mathrm{TOF}_{\mathrm{calc}}$ distributions. The fit results for a typical counter are shown in figure 3.25. The time difference width is observed to be $\sim$ 100 ps for zero b_1 and b_2. The minimum time difference width is obtained, for this particular counter, with parameter values of $b_1 = 55$ and $b_2 = 30$ $\sqrt{\mathrm{ADC}}/\mathrm{ns}$. In general, there is a fairly large area of the matrix over which the value of the distribution width does not vary by more than 5 ps from the minimum. The geometrical center of this area determines the selected values of b_1^j and b_2^j.

An example of the time resolution improvement obtained after the time-walk correction, is presented in figure 3.26. The measured time difference is plotted as a function of the inverse of the square root of the pulse-height at the top-left corner of figure 3.26. The figure is done using identified π^-, that fall within ± 10 cm from the center of a typical counter. The horizontal axis is the projected difference between the measured TOF and the TOF value calculated using the particle momenta obtained with the tracking detectors. Although the pulse-height range of minimum ionizing

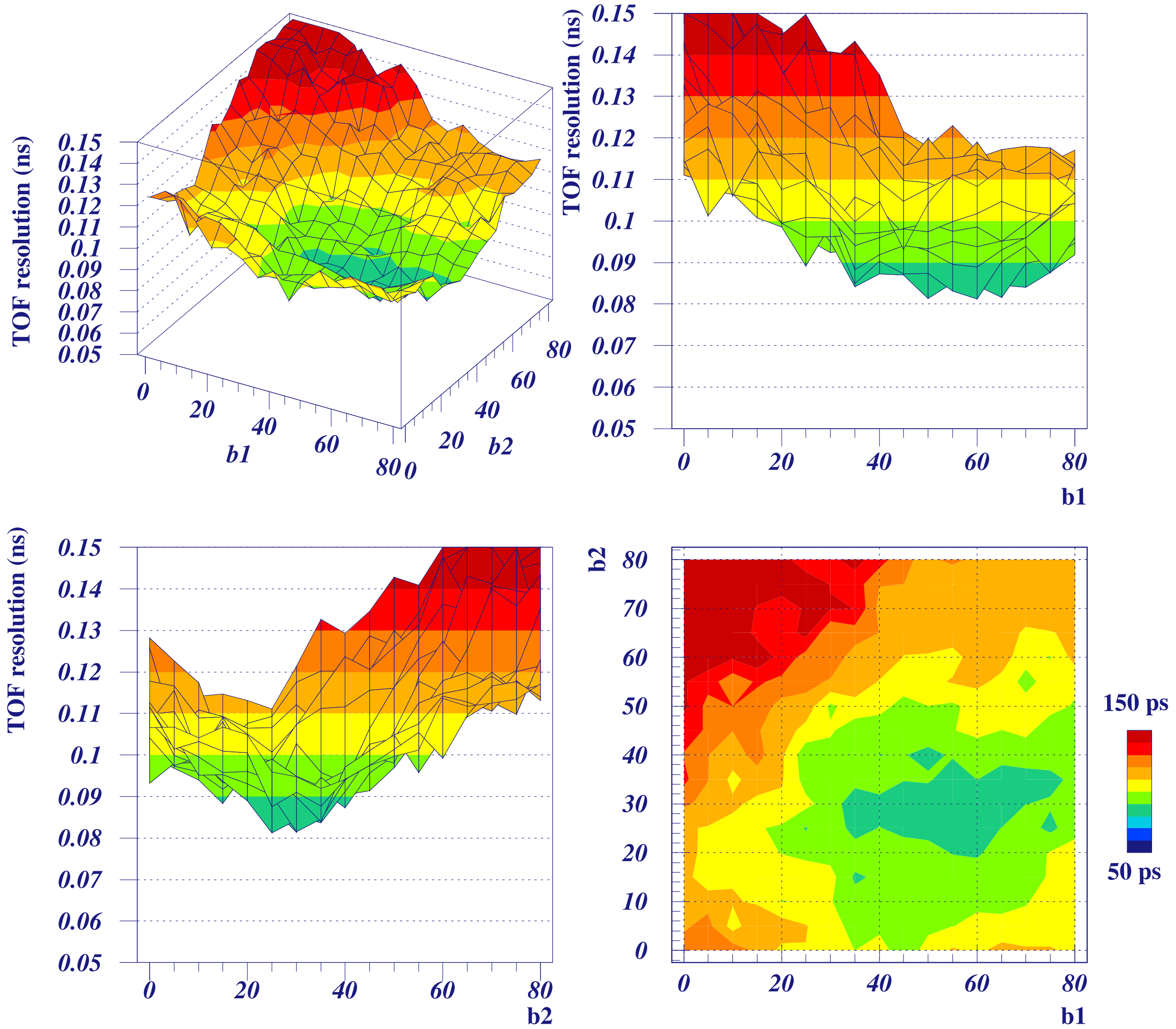

Figure 3.25: Time resolution as a function of time-walk correction parameter values. The width of the TOF − $\mathrm{TOF_{calc}}$ distribution is plotted as a function of b_1^{stop} and b_2^{stop}. The same distribution is plotted from four different angles: a tridimensional view, projections on the b_1 and b_2 axis and a plan view.

particles is relatively small, the pulse-height dependence is well described by a $1/\sqrt{ph}$ parametrization. As shown by the projections on the time axis (bottom of figure 3.26),

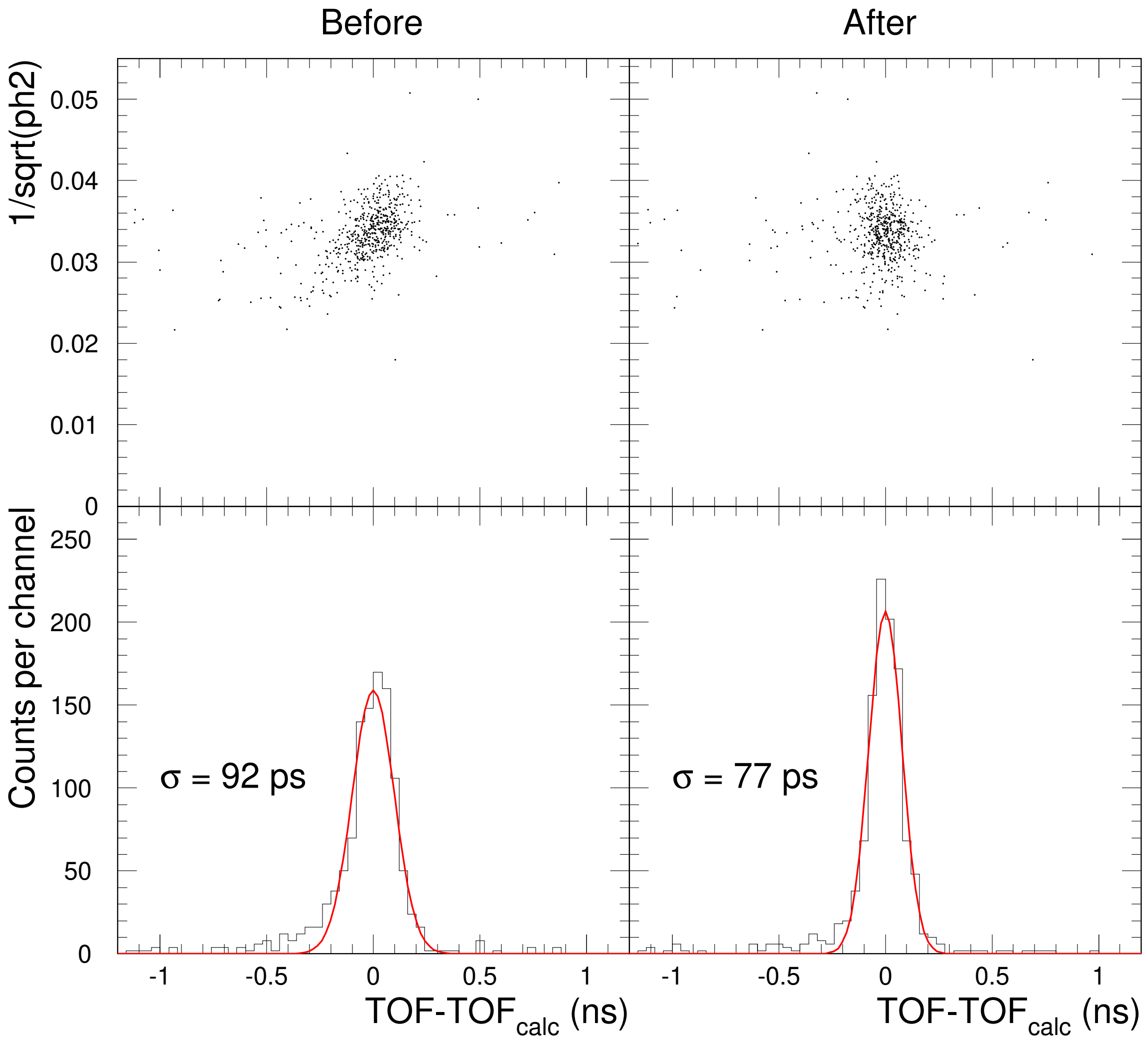

Figure 3.26: TOF-difference pulse-height correlation, before (left) and after (right) time-walk correction are plotted at the top. Corresponding time-difference distributions and resolutions are shown at the bottom.

the time-walk correction results in a sizable improvement in time resolution with a final value 77 ps.

Start-time position dependence

After performing the time-walk correction, a slight start time position dependence remains as shown in figure 3.27. The TOF of the beam particles between S2 and S4

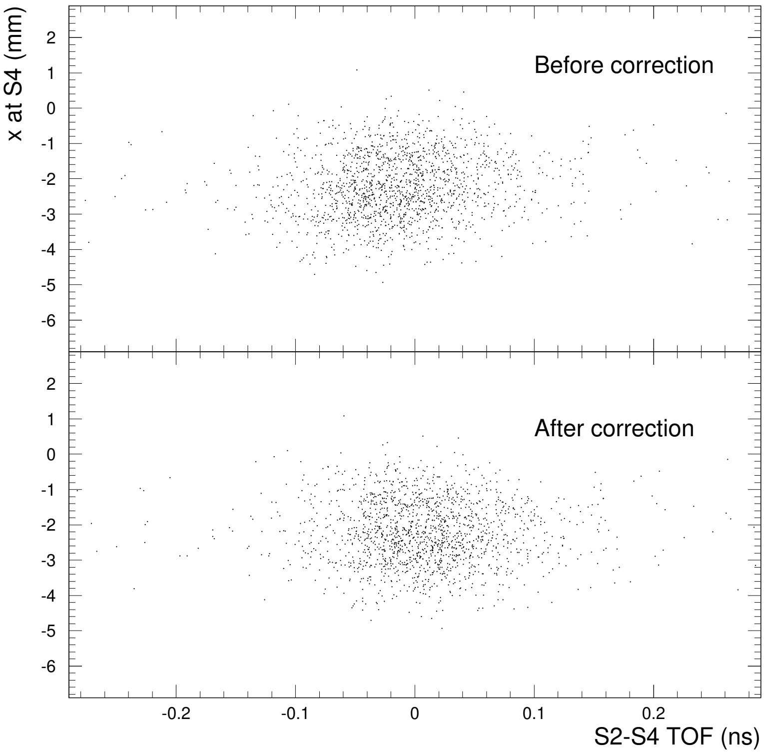

Figure 3.27: Start-time position dependence. The TOF of beam particles between S2 and S4 is plotted as a function of the beam particles positions at S4 before and after the position dependence correction.

is plotted as a function of the extrapolated beam particle positions at S4 as measured by the BVer. The position dependence is parameterized with the linear function

$$\delta t_x^{\mathrm{start}} = x_{\mathrm{start}} \cdot \mathrm{c_x}. \tag{3.15}$$

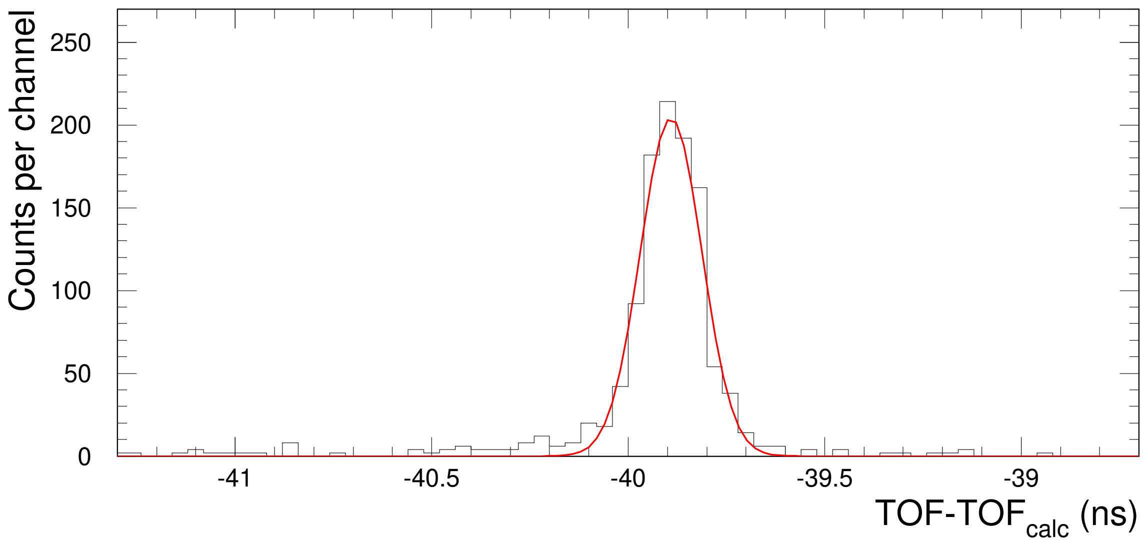

Figure 3.28: Single-counter time-difference distribution used for $T_\circ$ determination.

The magnitude of the correction ($c_x \sim 0.01$ ns/mm) is consistent with the 45° tilt angle of the beam scintillator relative to the beam axis.

Time-of-flight alignment

The last step of the TOF calibration consists in determining the $T_\circ$ time offset values. The $T_\circ$ constant is defined as

$$T_\circ = \langle \mathrm{TOF} - \mathrm{TOF}_{\mathrm{calc}} \rangle. \tag{3.16}$$

Once all other corrections are performed, the $\mathrm{TOF} - \mathrm{TOF}_{\mathrm{calc}}$ distribution is fitted with a Gaussian distribution as is shown in figure 3.28. The $T_\circ$ value is set by the mean value of the Gaussian distribution whereas the width of the distribution is a measure of the time-of-flight resolution.

The $T_\circ$ constants account for all of the small cable lengths differences, flight path variations and varying electronics timing. Over a period of a few hours, the pulse-height degradation due to the radiation damage of the start counter causes the $T_\circ$

constants to change in a correlated fashion. The room temperature variations cause cables lengths to change, thereby generating counter-to-counter variations. All the calibration constants are therefore carefully monitored and readjusted periodically.

3.4.3 Vertical position calibration

Although the TOFU hodoscope is mainly used for charge and TOF measurement, it can also be used to provide a vertical position measurement that is useful in tracking. The spectrometer tracking system was shown to have a vertical position resolution of the order of a few millimeters [93]. Therefore, the hodoscope vertical position can be directly calibrated and the vertical position measured by comparison with the positions extrapolated from the tracking system.

The particle position along a counter is obtained from the time difference between the PMT signals according to the expression

$$y = v_{\mathrm{eff}} \cdot \frac{t_1^{\mathrm{stop}} - t_2^{\mathrm{stop}}}{2} - y_\circ \tag{3.17}$$

where v_{eff} is the effective signal velocity in the scintillator and $y_\circ$ is the position offset correction. The effective signal velocity in each counter is obtained by minimizing the width of the $y_{\mathrm{meas}} - y_{\mathrm{calc}}$ distribution. The calculated vertical position y_{calc} is defined as

$$y_{\mathrm{calc}} = cl\sin(\phi) \tag{3.18}$$

where ϕ is the trajectory angle in the yz plane and l is the track length as measured with the tracking system.

3.4.4 Counter signal velocity

The counter effective signal velocity distribution is plotted in figure 3.29 for the entire hodoscope. The v_{eff} values are obtained by minimizing the widths of the vertical po-

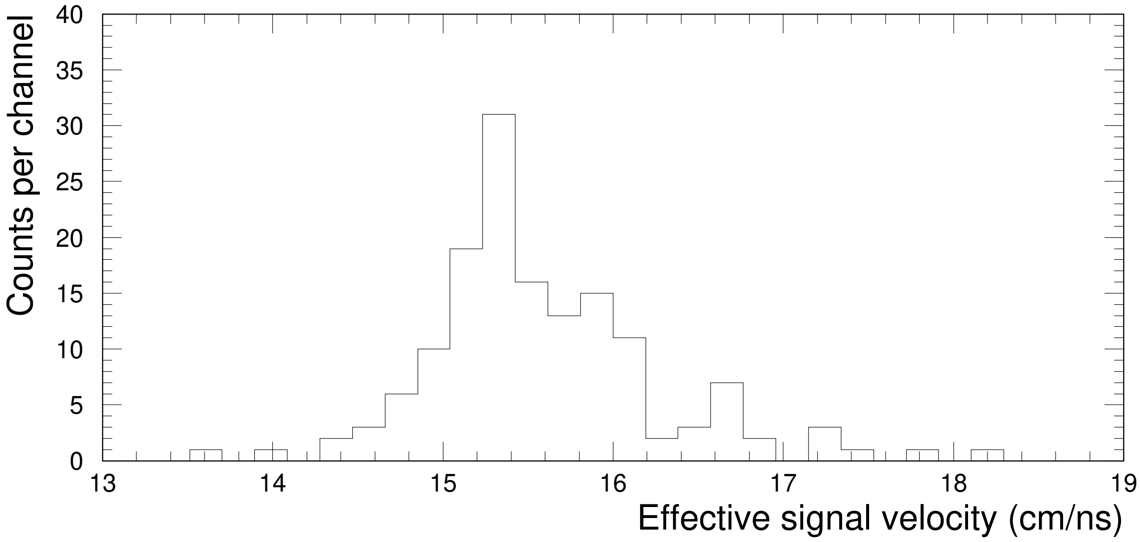

Figure 3.29: Hodoscope counter effective signal velocity distribution.

sition difference $y - y_{\rm calc}$ distributions for each hodoscope counter. The distribution is plotted from vertical position measurement y of Z=1 particles and $y_{\rm calc}$ is extrapolated from the spectrometer tracking measurement (as discussed in subsection 3.4.3). The measured effective signal velocity values range from 14 to 18 cm/ns with a mean value of about $\langle v_{\rm eff} \rangle = 15.7$ cm/ns. Because the time measurements are now corrected for time-walk, the present signal velocity values are larger than the ones that were measured on the test bench (section 3.2).

The average effective signal velocity is ~ 15.4 cm/ns for the wide counters and 16.0 cm/ns for the narrow ones, hence the double peak structure of the distribution shown in figure 3.29. With an index of refraction of $n = 1.58$ one can deduce that the average angle of the light reaching the PMT's is of about $\langle \theta \rangle \approx 36°$ and $\approx 32°$, respectively. The shallower angle of the narrow scintillator is attributed to the larger number of internal reflections that the light has to undergo, and increased attenuation of large angle components, before reaching the PMT [94].

Once the effective speeds of light are determined, the mean values of the fitted gaussian distributions define the vertical position offset $y_\circ = y_{\mathrm{meas}} - y_{\mathrm{calc}}$. A typical calibrated measured and calculated vertical position difference distribution is presented in figure 3.30. The width of the distribution is a measure of the vertical

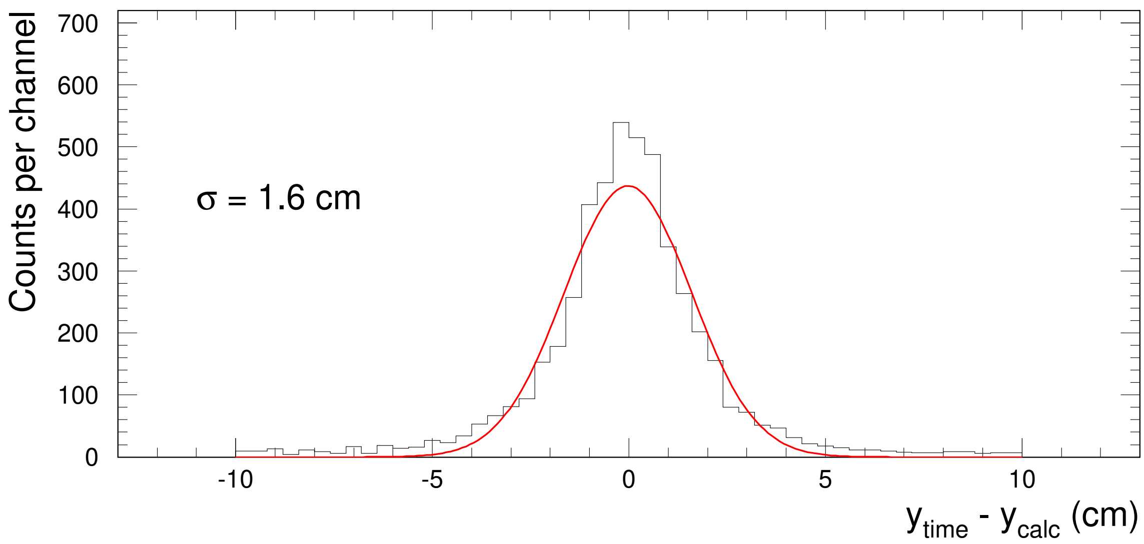

Figure 3.30: Vertical position difference distribution.

position resolution. The best counters are found to have a vertical position resolution of about 1.0 cm. Similarly to the $T_\circ$ time offset constants, the vertical position offsets $y_\circ$ account for differences in cable lengths and timing that come from a variety of sources. The $y_\circ$ constants slowly drift over time and are monitored accordingly.

3.5 Time-of-flight system performance

In this section, we evaluate the performance of the TOFU hodoscope in terms of pulse-height, position and time-of-flight resolutions.

3.5.1 Charge separation

In order to achieve short risetimes and get the better time resolution, most of the photomultipliers are operated near or slightly above the maximum recommended voltage of 1800 V. This leads to an average signal amplitude at the PMT's of about $\sim$ 0.5 V for Z=1 particles. The drawback is that the PMT base response is not linear with the light that is collected by the photocathode. The response of a typical counter situated near beam particle trajectories is shown in figure 3.31. Besides the

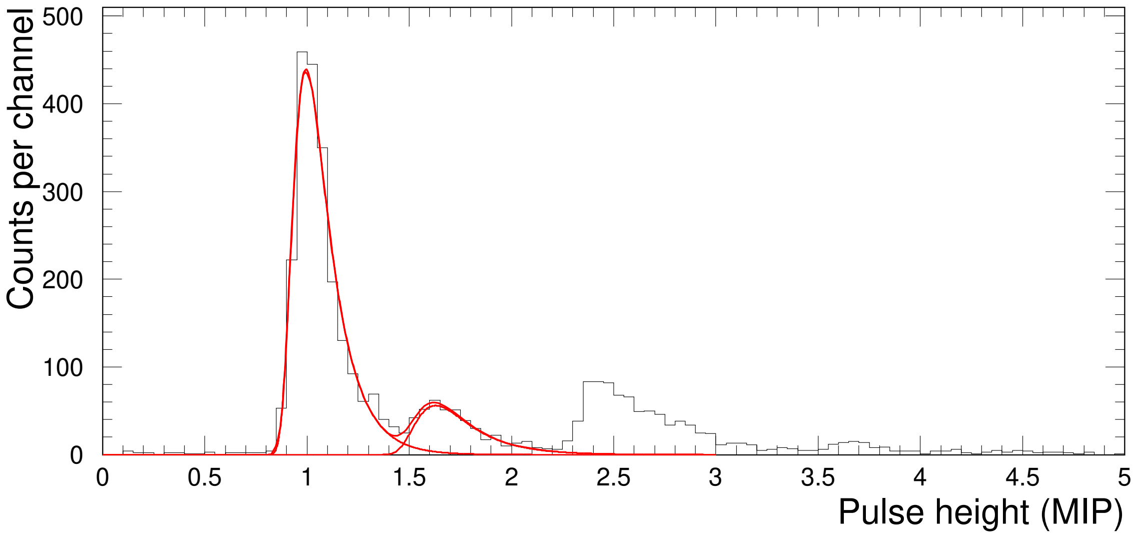

Figure 3.31: Counter pulse-height distribution measured near beam-particle trajectories.

main peak corresponding to the detection of a single Z=1 minimum ionizing particle, one observes a peak at 1.6 corresponding to the pile-up of two Z=1 particles and a peak at 2.4 MIP corresponding to the passage of Z=2 particles. The ionized particles energy loss per unit of length (dE/dx) is described by the Bethe-Bloch formula [95]. It is proportional to

$$\frac{dE}{dx} \propto \frac{z^2}{\beta^2}. \tag{3.19}$$

If the PMT response was linear, one would expect to find the events with two $Z = 1$ particles close to 2 MIP and $Z = 2$ particles at 4 MIP [2]. To determine the extent of the non-linearity, the 1 and 2 MIP peaks were simultaneously fitted by the function

$$\begin{aligned} f_2(\mathrm{PH}) \;=\;& A_1 \cdot \exp\left(-\frac{1}{2} \cdot \frac{\mathrm{PH}-\mathrm{PH}_{1\circ}}{w_1} + \exp\left(-1 \cdot \frac{\mathrm{PH}-\mathrm{PH}_{1\circ}}{w_1}\right)\right) \\ &+ A_2 \cdot \exp\left(-\frac{1}{2} \cdot \frac{\mathrm{PH}-\mathrm{PH}_{2\circ}}{w_2} + \exp\left(-1 \cdot \frac{\mathrm{PH}-\mathrm{PH}_{2\circ}}{w_2}\right)\right). \end{aligned} \tag{3.20}$$

which is the addition of two peaks as described by equation 3.8. In the present analysis, a $Z = 1$ particle is defined as one for which the measured pulse-height falls in the $0.8 < \mathrm{PH} < 1.5$ interval. The pulse-height non-linearity does not represent a problem for the present analysis. However, it should be taken into consideration for the study of multiply charged fragments like ^{3}He or α.

3.5.2 Pulse-height cut efficiency

The pulse-height distribution of single minimum ionizing particles has a tail that extends well beyond the two Z=1 particle pile-up peak. A Z=1 pulse-height selection cut will inevitably reject some Z=1 particles. An estimate of the fraction of minimum ionizing particles that are rejected with the selected PH interval can be obtained from a *clean* area of the hodoscope. This *clean* region is defined as one where the occupancy, the number of double hits and alpha particles are negligible. If one then assumes that all the observed particles have a Z=1 charge, the pulse-height cut efficiency minimum value is then obtained by calculating the proportion of the total counts that fall inside the selected pulse-height window. The pulse-height distribution measured by 10 counters located in a *clean* portion of the hodoscope (counters 20 to 29, B-field running) is shown in figure 3.32. The measured PH distribution is plotted on a

[2] even if quenching effects to be at play, *i.e.* $dE/dx \propto z^{1.8}/\beta^2$, one would expect the Z=2 peak to be near 3.5 MIP

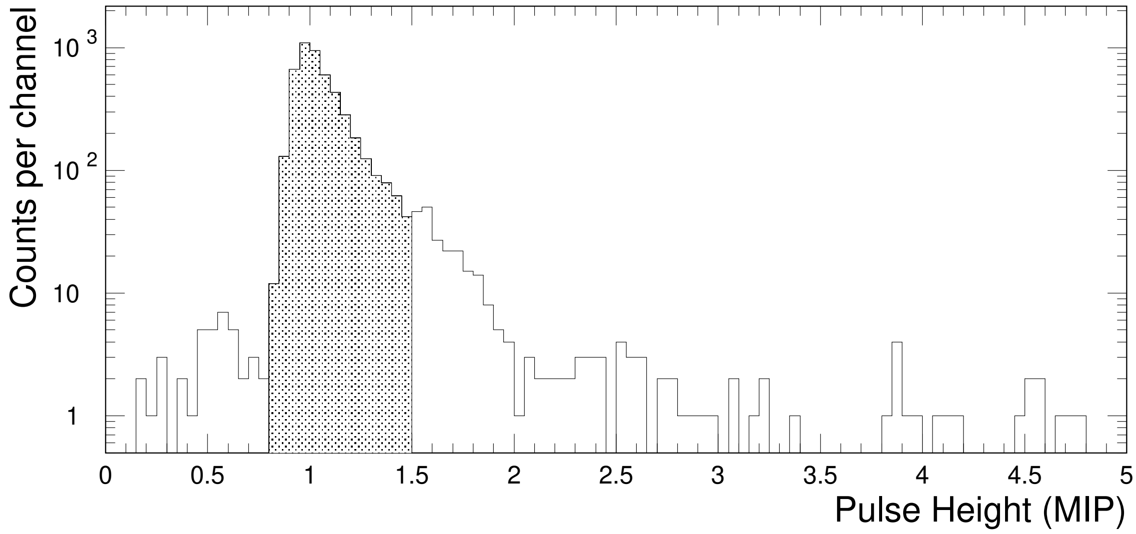

Figure 3.32: Pulse-height distribution measured by counters located in a *clean* portion of the hodoscope used for the Z=1 selection cut efficiency calculation. The shaded area corresponds to a $0.8 < \mathrm{PH} < 1.5$, Z=1 particle selection window.

logarithmic scale to better display the counts on either side of the Z=1 peak. The shaded area corresponds to the $0.8 < \mathrm{PH} < 1.5$ Z=1 particle pulse-height selection window used in the present analysis. The shaded area integrates to 94% of the total number of counts. This test, done over several parts of the hodoscope, reveals that the PH cut efficiency value varies by at most 1% from counter to counter.

A small pile-up peak is visible near 1.6 MIP and contributes in making the PH cut efficiency estimate pessimistic. By fitting the function of equation 3.20 to the PH distribution of figure 3.32, one finds that the two Z=1 particles peak contributes for about 2% of the total number of counts. However, equation 3.8 is only a crude description of the MIP peak shape and actually falls down faster at large PH's than what is observed. It is thus clear that the value of 2% is an upper limit to the two Z=1 particles contribution. The pile-up corrected, pulse-height cut efficiency value for the $0.8 < \mathrm{PH} < 1.5$ window is therefore taken to be of $95\pm1\%$. A summary of

Table 3.1: Minimum pulse-height cut efficiency.

PH cut	*Efficiency*
$0.8 < \mathrm{PH} < 1.5$	$95 \pm 1\%$
$0.8 < \mathrm{PH} < 1.4$	$93 \pm 1\%$
$0.8 < \mathrm{PH} < 1.3$	$89 \pm 1\%$
$0.8 < \mathrm{PH} < 1.2$	$83 \pm 1\%$

the pulse-height cut efficiency minimum values is given in table 3.1 for several PH windows.

3.5.3 Pulse-height particle-velocity dependence

The PH distributions measured in 4 different velocity intervals are shown in figure 3.33. According to equation 3.19, the mean of the pulse-height distribution should increase for slower particles (smaller values of β). But, because of the base saturation, the most probable PH is not quite proportional to $1/\beta^2$. Only a small fraction of the slow particles ($\beta < 0.9$) generate pulse-heights that are higher than PH > 1.5 MIP. The $0.8 <$ PH < 1.5 PH cut window is therefore wide enough to accommodate the velocity dependence and does not introduce sizable velocity dependent inefficiencies.

3.5.4 Time-of-flight resolution

The time-of-flight resolution can be expressed in terms of its two main components, the start resolution σ_{start} and the stop resolution σ_{stop}, as:

$$\sigma^2_{\mathrm{TOF}} = \sigma^2_{\mathrm{start}} + \sigma^2_{\mathrm{stop}} \tag{3.21}$$

where the BSci beam counters are used to generate the start, while the stops are measured with the hodoscope. Since the two subsystems equally contribute to the

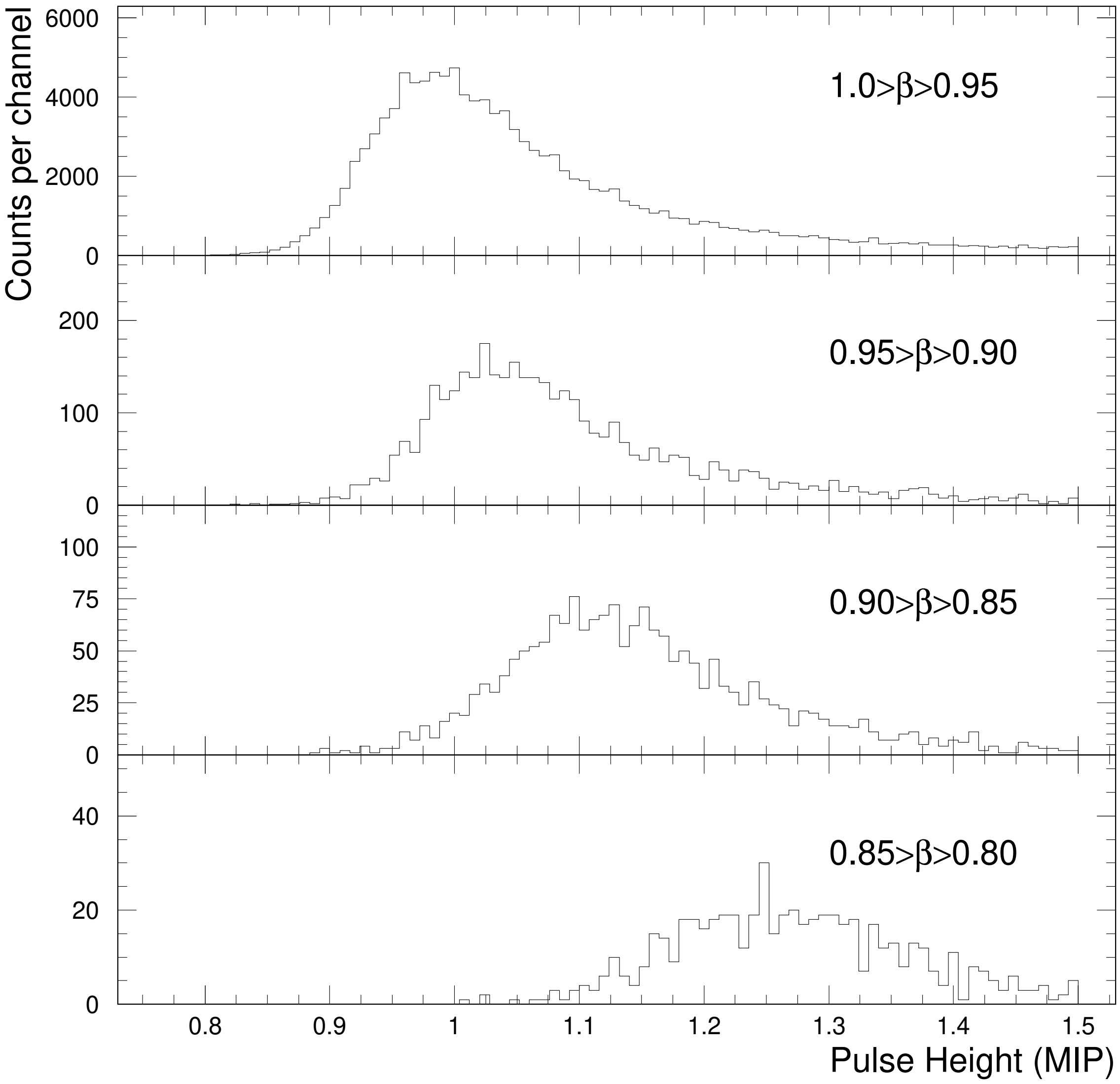

Figure 3.33: Measured pulse-height particle velocity dependence. The pulse-height distribution measured over the hodoscope is plotted for 4 particle velocity intervals.

overall TOF resolution, it is important to minimize the BSci contribution, hopefully to the point where it is negligible compared to that of the hodoscope.

The TDC time resolution is discussed first. The time resolution of the start system is then analyzed to determine its contribution to the overall TOF resolution, which is discussed last.

TDC resolution

The time measurement is performed using five LeCroy 1875A TDC FASTBUS modules. According to the manufacturer, these TDC's have a time segmentation of ~ 25 ps per channel and a maximum RMS noiseof 2 channels [91]. To verify that the TDC's are operating within the manufacturer's specifications we take advantage of the fact that the signal from the first S4 PMT (S4-1) is used to generate the TDC starts and is redundantly fed as stop signal to every TDC. The resulting distributions are given in figure 3.34 for each of the five TDC modules. The measured widths are found to vary from $\sigma = 2.1$ to 2.9 channels, which corresponds to values of 3 to 4 channels RMS. The difference between the manufacturer's claim and the measured values is attributed to jitters introduced by the decision making electronics that is located between the original S4 signal and the TDC start.

Beam TOF resolution

The BSci S2 and S4 counters each provide independent measurements of the beam particle arrival time. The TOF start time resolution can thus be inferred from the measured beam particle time-of-flight between these two counters. The beam particles TOF between S2 and S4 is expressed as

$$\mathrm{TOF_{beam}} = \frac{t_1^{\mathrm{S4}} + t_2^{\mathrm{S4}}}{2} - \frac{t_1^{\mathrm{S2}} + t_2^{\mathrm{S2}}}{2} - \mathrm{t_{offset}} \qquad (3.22)$$

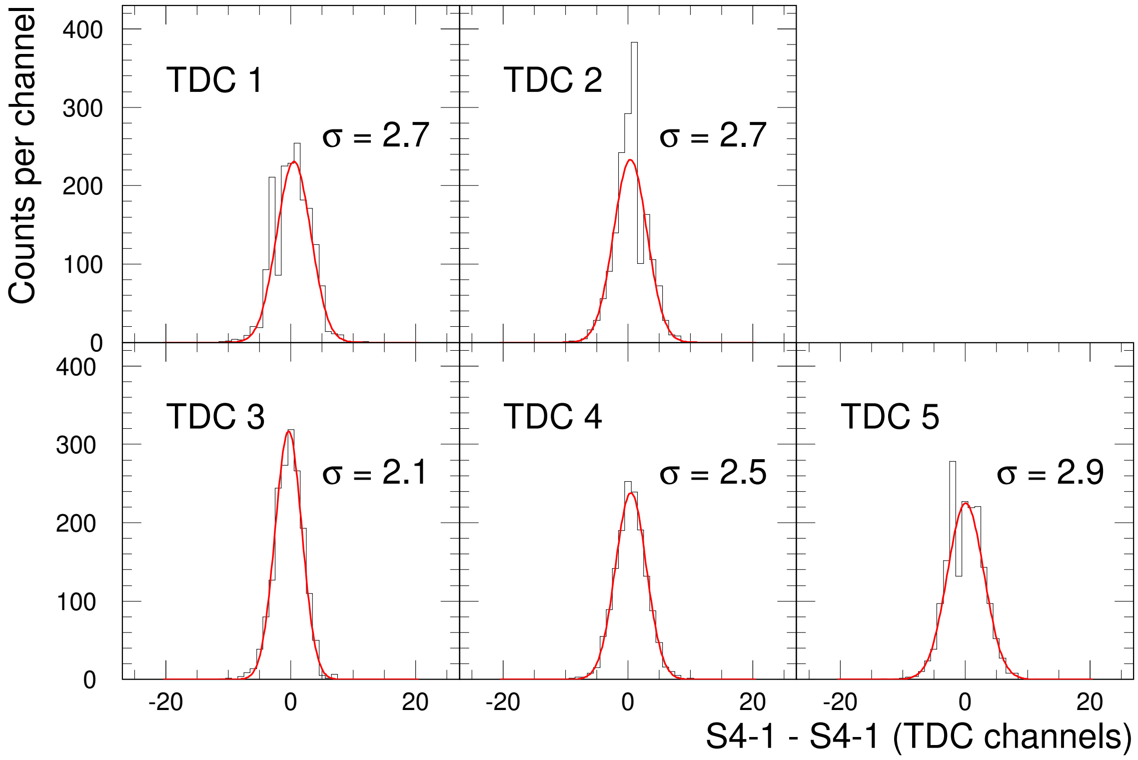

Figure 3.34: Measured time distribution of the S4-1 signal that is used to start and stop a single channel in each of the five TDC's.

where t_i^j is the time obtained from each PMT of S2 and S4 after time-walk correction. A typical TOF distribution measured with AGS gold beam is shown in figure 3.35. A Gaussian fitted to the TOF_{Beam} distribution has an overall width of 55 ps. The beam counters were used up to a rate of 3×10^5 particles/s without any sizable degradation of the time resolution.

Each scintillator of the start subsystem is viewed by two photomultipliers leading to a total of six possible PMT time-measurement pair combinations. Since the system is overdetermined and assuming that each of these time measurement is independent, each PMT time resolution can be estimated. The results from such an analysis are shown in table 3.2 and lead to an average value of 36 ps for the two S2 PMT's and

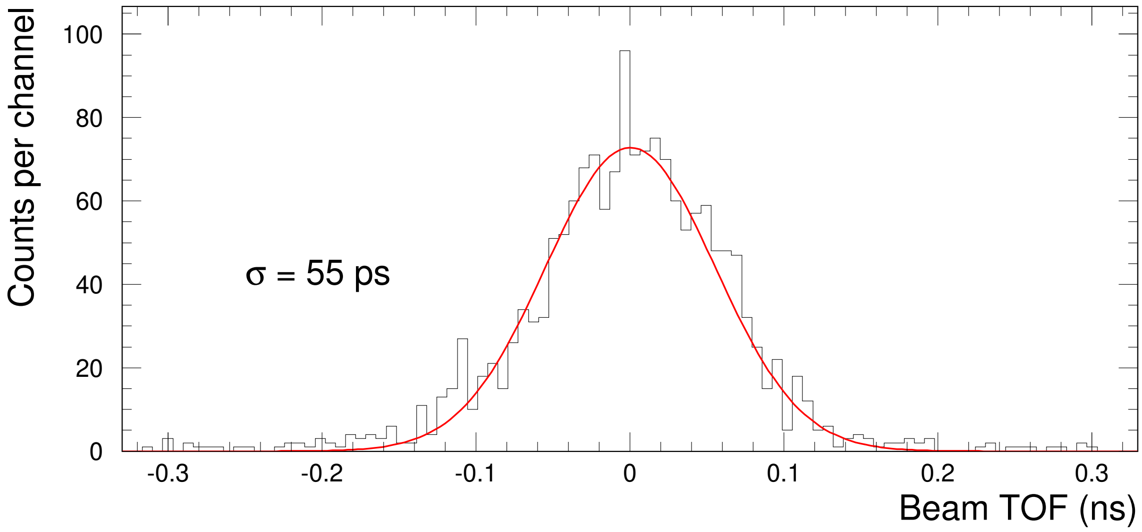

Figure 3.35: Beam particle time-of-flight distribution measured between the S2 and S4 BSci counters.

Table 3.2: Start counters resolutions

PMT	1	2
S2	37 ps	34 ps
S4	57 ps	49 ps

53 ps for the S4 PMT's. The resolution of the S2 PMT's being significantly better than that of S4, the geometrical average between the two S2 PMT's defines the TOF start time t_{start} for the present data analysis. Assuming that the two S2 PMT time measurements are independent and can be added quadratically leads to an estimated combined start subsystem resolution of 25 ps.

Overall time-of-flight resolution

The overall time-of-flight resolution is determined by measuring the width of the identified particle $TOF - TOF_{\mathrm{calc}}$ distribution in each counter. The distribution of

TOF resolutions obtained with π^- particles is shown in figure 3.36. Single-counter

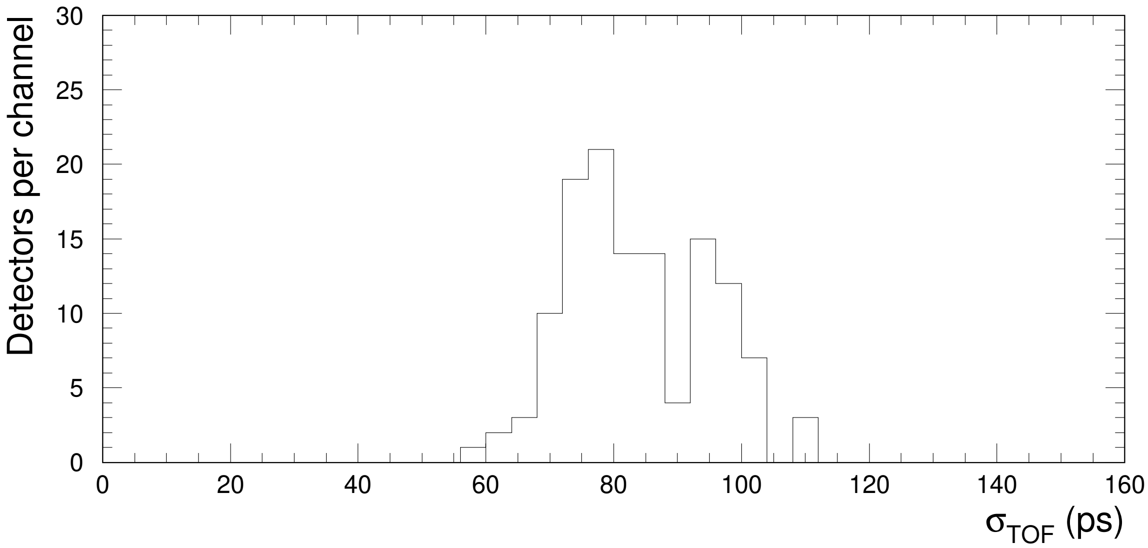

Figure 3.36: Hodoscope counter time-of-flight resolution distribution.

TOF resolutions as good as 60 to 70 ps are observed, while an average of 85 ps is obtained over the entire hodoscope. Assuming that the start and stop are independent and that their resolutions add quadratically, an average stop counter time resolution of 81 ps is obtained.

3.5.5 Vertical position resolution

There are two ways to measure the hit position along scintillator bars. The first uses the signal arrival time difference between the two PMT's as is described in subsection 3.4.3. The exponential attenuation suffered by the light while it travels through the scintillator provides a second method of measuring the incident particle position. Since the amplitude decays exponentially with the distance traveled inside the scintillators, as was shown in figure 3.14, the hit position is then obtained with the pulse-height difference measured between the two counter PMT's according to the expression

$$y_{\mathrm{PH}} = \ln\left(\frac{\mathrm{PH}_1}{\mathrm{PH}_2}\right) \cdot \frac{a}{2} - y_\circ \qquad (3.23)$$

where the attenuation length a is obtained by minimizing the vertical position difference $y_{\mathrm{PH}} - y_{\mathrm{calc}}$ distribution width. The PH vertical position difference $y_{\mathrm{PH}} - y_{\mathrm{calc}}$ distribution for one of the best hodoscope counters is plotted at the top of figure 3.37. A Gaussian distribution fit lends a PH vertical-position resolution of $\sigma = 2.3$ cm for

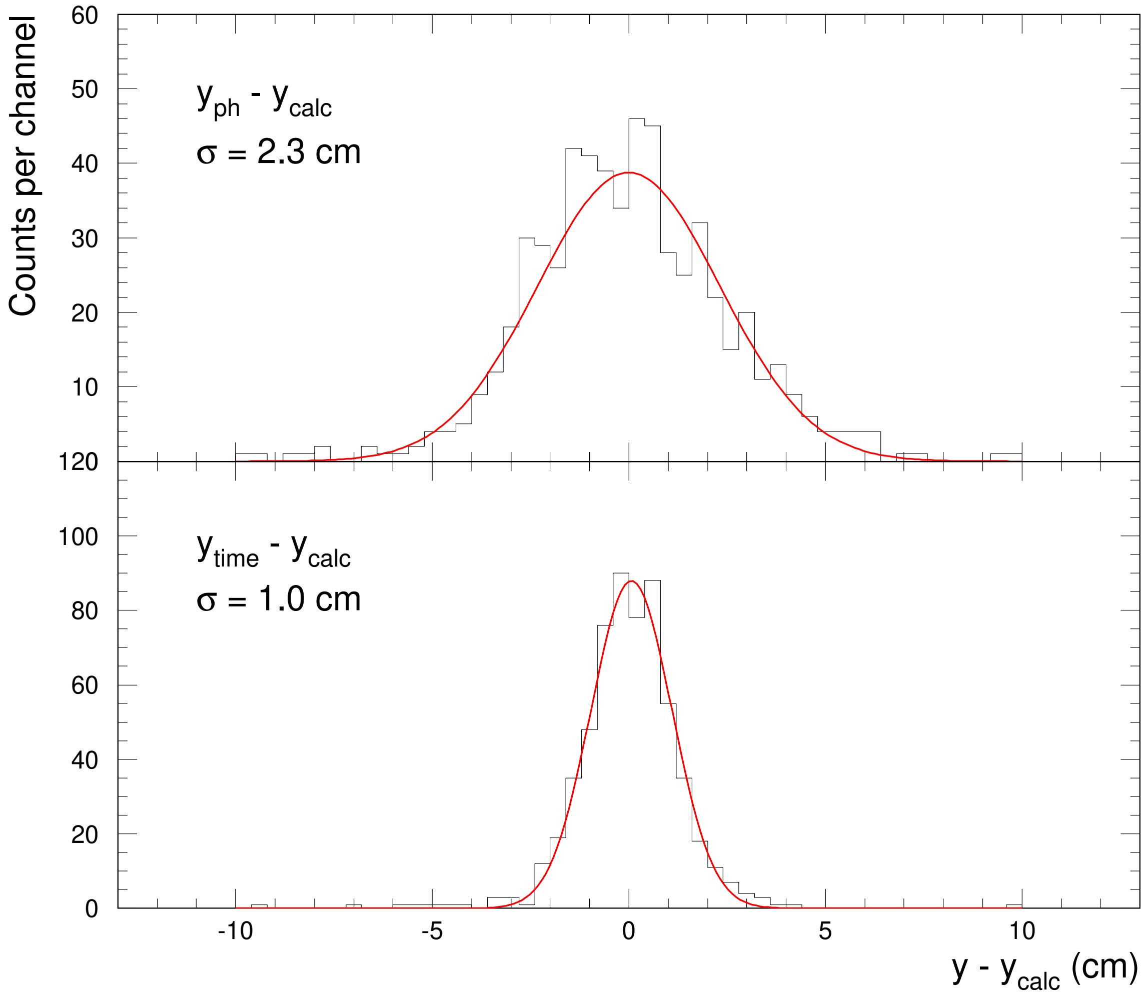

Figure 3.37: Vertical position difference distributions are plotted from pulse-height (top) and time (bottom) information obtained from the same hodoscope counter.

this particular counter. The time vertical-position difference distribution is plotted at the bottom of figure 3.37 for the same hodoscope counter. A much better position resolution of $\sigma = 1.0$ cm is then obtained. For data analysis purposes, the vertical position obtained from the PMT time difference is used since it has a much better resolution than that obtained from the pulse-height information.

An overall vertical position difference $y_{\rm time} - y_{\rm calc}$ distribution done over the entire hodoscope for Z=1 particles is shown in figure 3.38. An overall vertical position

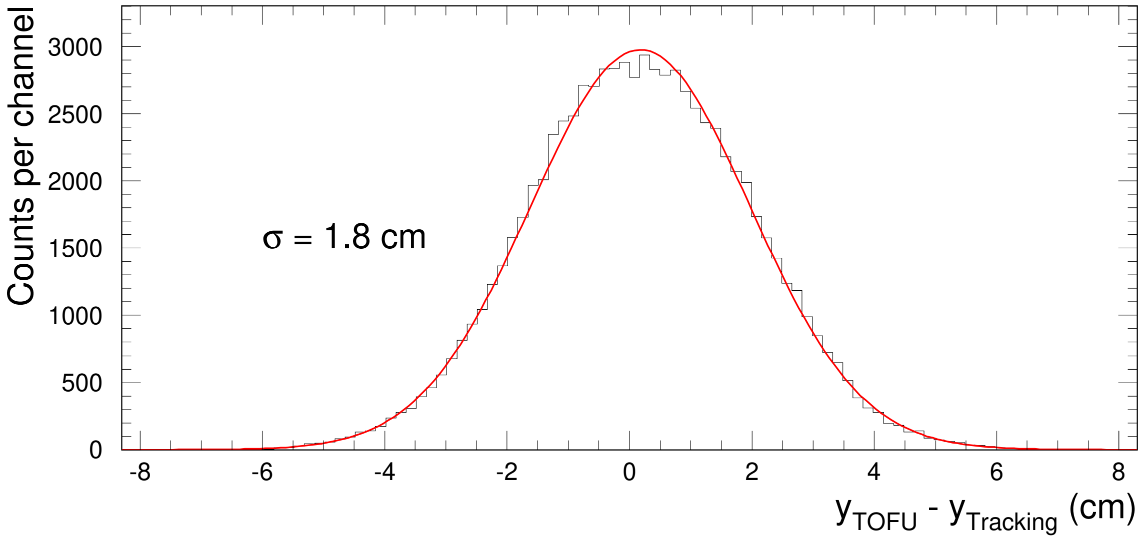

Figure 3.38: Hodoscope vertical position difference distribution obtained from time information.

resolution of 1.8 cm is observed, which is consistent with what is expected from the mean TOF resolution. It is interesting to note that the measured resolution is of the same order as the hodoscope horizontal granularity *i.e.* ± 1.7 and ± 1.0 cm.

The overall time difference vertical position resolution can be compared with that expected from the overall counter time resolution since

$$\sigma_y = \frac{1}{2} v_{\rm eff} \cdot \sqrt{\sigma_{t_1}^2 + \sigma_{t_2}^2}. \tag{3.24}$$

Table 3.3: Time-of-flight performance summary.

Quantity	*Performance*
PH cut efficiency $0.8 < \text{PH} < 1.5$	$95 \pm 1\%$
Overall vertical position resolution	18 mm
horizontal position resolution	10 or 17 mm
Start time resolution	25 ps
Stop time resolution	81 ps
Overall Time-of-flight resolution	85 ps

Using the measured average hodoscope counter time resolution value of $\sigma = 81$ ps and average signal velocity $v_{\text{eff}} = 15.7$ cm/ns, one finds an expected vertical resolution of $\sigma_y = 1.3$ cm that is comparable to the measured value of 1.8 cm.

3.5.6 TOFU performance summary

The performance and characteristics of the TOFU are summarized in table 3.3. The Z=1 charge particle selection can be done with an efficiency of 90 to 95% depending on the pulse-height cut selected. The hodoscope provides a vertical position measurement with a resolution of 18 mm that is complementary to the one obtained from the tracking. An overall TOF resolution of 85 ps which is 15 ps better than the original design value.

Chapter 4

Data analysis

It is mainly by studying the rapidity and transverse momentum phase space particle distributions that we hope to get information on the physics of relativistic heavy-ions. In this chapter, we discuss the steps involved in extracting particle spectra from the quantities that are measured by the detectors. The centrality determination and event selection are first discussed. The track reconstruction algorithm and terminology are then briefly described. The close track resolution performance of the spectrometer is studied and a position dependent occupancy correction is developed. A description of the geometrical acceptance calculations is followed by a summary of the corrections that are applied to the measured data. The particle identification procedures for kaons, pions and protons are discussed and typical measured transverse momentum spectra are given.

4.1 The 1993 data set

The data presented here were taken in September 1993, using a 10.8 A·GeV/c Au beam accelerated by the AGS [62]. The slowly extracted beam was delivered on the target in 1 s long spills at intervals of 3 to 4 s at rate of about 50 000 particles per spill. The data were accumulated over a period of three weeks producing a total of about 10 000 000 recorded events. These events were selected using centrality triggers set at three different levels and each account for about 30% of the events. The data taking was divided equally between two opposite spectrometer magnetic field polarity settings called A and B, to maximize the acceptance for positive and negative particles. For normalization purposes, scaled-down minimum-bias beam trigger events were also recorded, as well as empty target events.

4.2 Centrality determination

If a new state of nuclear matter exists, it will most likely be produced during the most central collisions where the largest energy densities are expected to be produced. The centrality of a reaction is correlated with the impact parameter: the smaller the impact parameter, the more overlap there is between projectile and target nuclei. Since the impact parameter can not be directly measured, it has to be inferred from other measurable quantities such as transverse energy ($\mathrm{E_t}$) [12, 96, 97, 98]. In the present analysis, the data are divided into centrality intervals that are determined using the TCal.

The total transverse energy produced in an event is usually defined as the summation of all particle energies E_i weighted by the sines of the angles θ_i between their trajectories and that of the beam according to

$$\mathrm{E_t} = \sum_i E_i \cdot \sin\theta_i. \tag{4.1}$$

The TCal is a calorimeter and as such, does not provide particle identification. The partial $\mathrm{E_t}$ measured with this highly segmented calorimeter is thus operationally redefined as being the summation of the energies E_i measured by each of its elements and weighted by their angles (θ_i) relative to the beam trajectory. To illustrate the

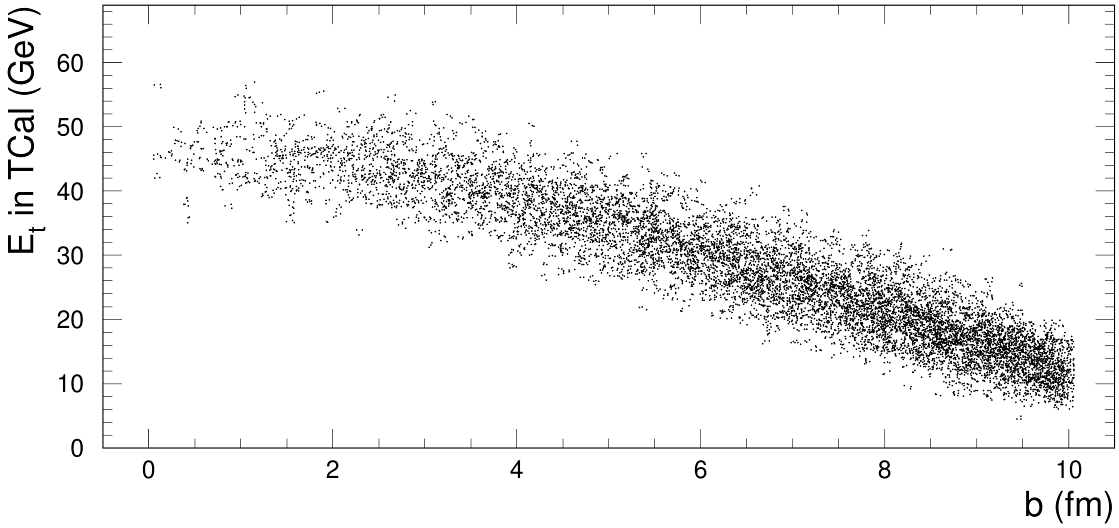

Figure 4.1: Impact parameter and TCal transverse energy relation according to RQMD 1.08.

relation between the event impact parameter and the part of the E_t measured by the TCal, the result from an RQMD 1.08 calculation (see subsection 6.1.1) is presented in figure 4.1. The calculation accounts for the detector response to all relevant types of particle (see subsection 6.1.2) but does not account for leakage. The event impact parameter is strongly anti-correlated with transverse energy deposited in the TCal. At large impact parameters, very little of the initial momentum is transferred into the transverse direction and most of the particles travel along the beam trajectory so that the measured E_t is small. As the impact parameter decreases, the collisions become more and more violent and larger fractions of the available momentum and energy are transferred into the transverse direction. The correlation is found to somewhat saturate for impact parameters below $b < 2.5$ fm. Fluctuations in the amount of energy that is produced at the backward angles contribute to the broadening of the correlation between the impact parameter and measured TCal E_t.

The centrality of the collisions can be inferred using the ratio

$$\sigma = \sigma_{\rm top}({\rm E_t})/\sigma_{\rm geom}. \tag{4.2}$$

where $\sigma_{\rm top}({\rm E_t})$ is defined as:

$$\sigma_{top}({\rm E_t}) = \int_{\rm E_t}^{\infty} \frac{d\sigma}{d{\rm E_t}} \cdot d{\rm E_t}, \tag{4.3}$$

and the geometrical cross section $\sigma_{\rm geom}$ is given by:

$$\sigma_{\rm geom} = \pi(R_{\rm beam} + R_{\rm target})^2 \tag{4.4}$$

with

$$R_i = 1.2A^{1/3}. \tag{4.5}$$

With a nucleus radius of $R_{\rm Au} = 6.98$ fm, the Au+Au collision geometrical cross section is $\sigma_{\rm geom} = 6.12$ barns.

The Au+Au experimental differential transverse energy cross section $d\sigma/d{\rm E_t}$ obtained with the TCal is plotted in figure 4.2. Typical centrality intervals used in the present work are shown by the hashed areas. They correspond to the most central 4 and 10% collisions or events with a minimum measured TCal $\rm E_t$ of 18, and 15.5 GeV, respectively.

4.3 Momentum measurement

4.3.1 Track reconstruction

The particle trajectories in the spectrometer are reconstructed using a tree-climbing algorithm [99]. The tracking software is only briefly described here. More details are given in [50, 63, 71].

Wire hits in the drift sections of the chambers (DC2 and DC3) are first combined into (x) *elements*. Wire hits are required in at least 3 out of 6 wire planes to constitute

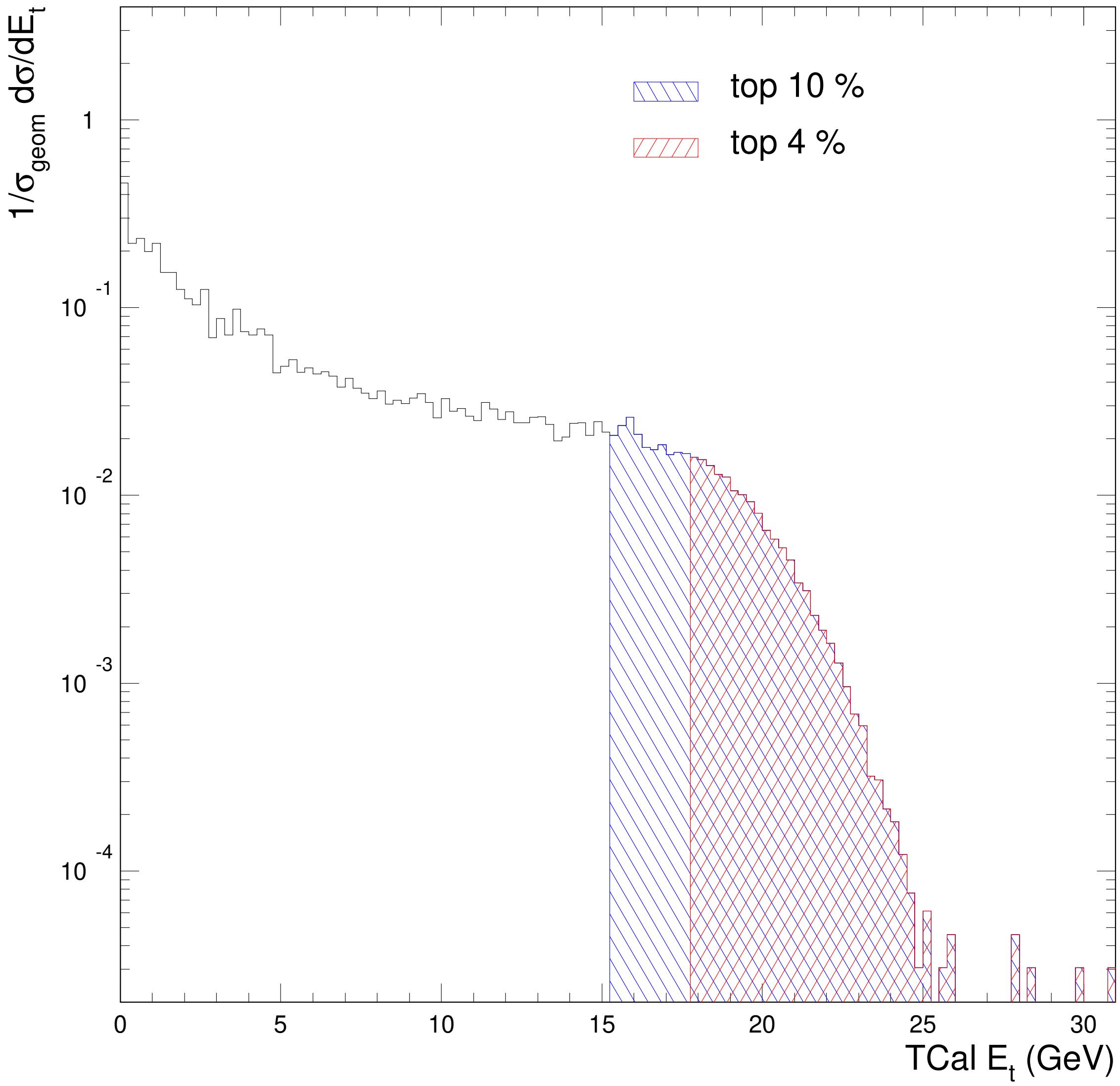

Figure 4.2: Transverse energy distribution for Au+Au as measured with the TCal.

a valid element. The pads of the segmented cathode are scanned for hits. For each group of pad hits, a pulse height weighted centroid is computed to determine the (y) position of the *clusters*. The clusters are then assigned to the corresponding wire plane elements.

The elements from each of the two drift chambers are linked to one another to form *segments*. The segments are then checked to see if they point toward the magnet opening and that they satisfy loose geometrical cuts. The segments are then assigned momenta to become *candidates*. The momenta are recursively calculated assuming that the candidates come from the target. An effective magnetic field length accounts for fringe field effects [62]. The precise interaction position at the target as measured with the BVers is used to compute the track momentum. Once the momenta have been calculated, the *candidates* that share hits in the drift chambers are eliminated. Finally, candidates graduate to *tracks* once they have been confirmed by hits in 3 out of the 4 MWPC's along their trajectories.

The time-of-flight information for each track is obtained by extrapolating the measured trajectory down to the TOFU hodoscope. The closest hit that lay within a single scintillator width and three times the vertical resolution σ_y is assigned to the corresponding track.

A plan view of a typical event, as produced by the E877 event display program, is shown in figure 4.3 to illustrate the track reconstruction power of the algorithm. The pad planes of the drift chambers and TOFU are flipped on there sides to display their vertical information. In this particular event, 8 tracks were found and confirmed by the MWPC's. The vertical positions measured by TOFU and DC3 are nicely correlated. Tentative particle species have been assigned to each of the tracks (6 protons and 2 pions) using loose particle identification windows by combining the momentum and time-of-flight information as discussed in section 4.4.

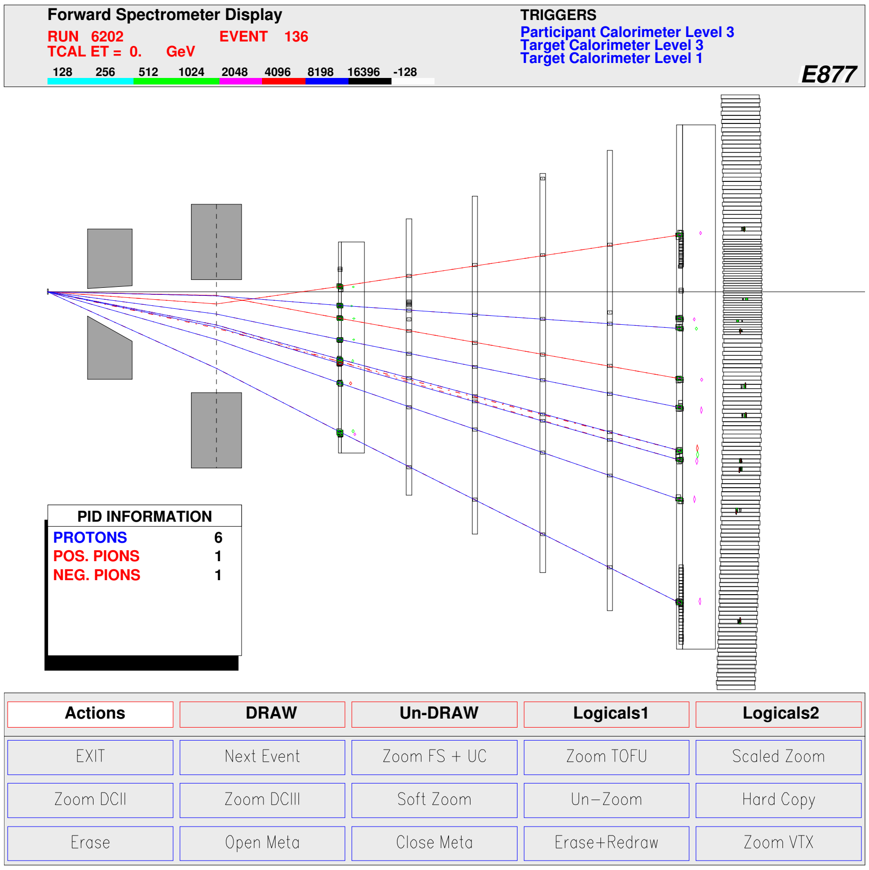

Figure 4.3: Printout of the E877 event display program for a typical central Au+Au spectrometer event. Schematically shown from left to right are the collimator, magnet, DC2, MWPC's, DC3 and TOFU.

4.3.2 Momentum resolution

The momentum resolution achieved with the tracking system was extensively studied [100]. The results of three different calculations are compared in figure 4.4, a simple Monte-Carlo model (solid lines), an analytical calculation (dashed lines) and Gaussian fits performed on particles tracked after propagation in a detailed model of the spectrometer using GEANT (dots). The three results are found to be quite consistent and show that the resolution is mainly determined by the multiple scat-

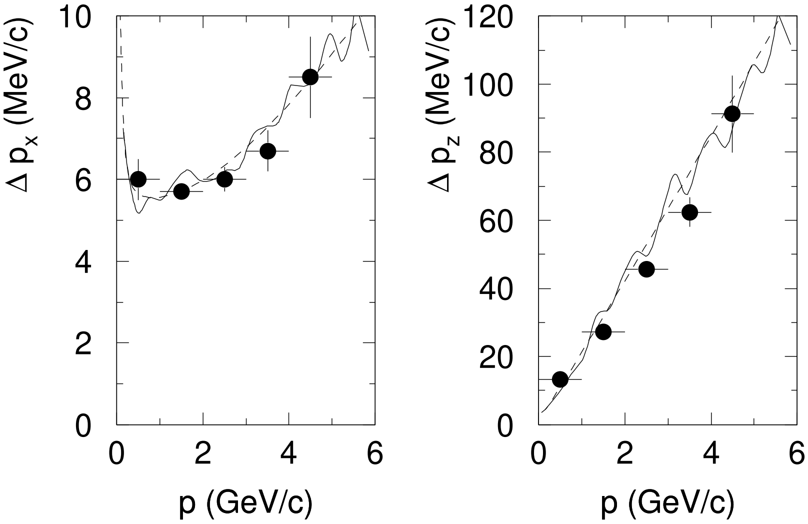

Figure 4.4: Spectrometer momentum resolution. The momentum resolution in p_x and p_z are plotted as a function of total momentum for pions. Figure taken from [100].

tering in the spectrometer material. The transverse momentum resolution is found to be approximately constant with particle momentum at $\Delta \mathrm{p_x} \sim 6$ MeV/c. The longitudinal momentum resolution varies from $\Delta p_z/p \sim 0.02$ to 0.04 depending on particle type.

4.4 Particle identification

In the E877 spectrometer, particle identification proceeds by mass reconstruction from the measured momentum and time-of-flight. A scatter plot of the distribution of tracks with charge $Z = 1$ as a function of inverse momentum (1/p) and velocity ($1/\beta$) is plotted in figure 4.5. The particles are distributed along their *mass lines* according to the relation

$$\frac{1}{\mathrm{p}} = \frac{1}{m}\sqrt{\frac{\beta^2}{1} - 1}. \tag{4.6}$$

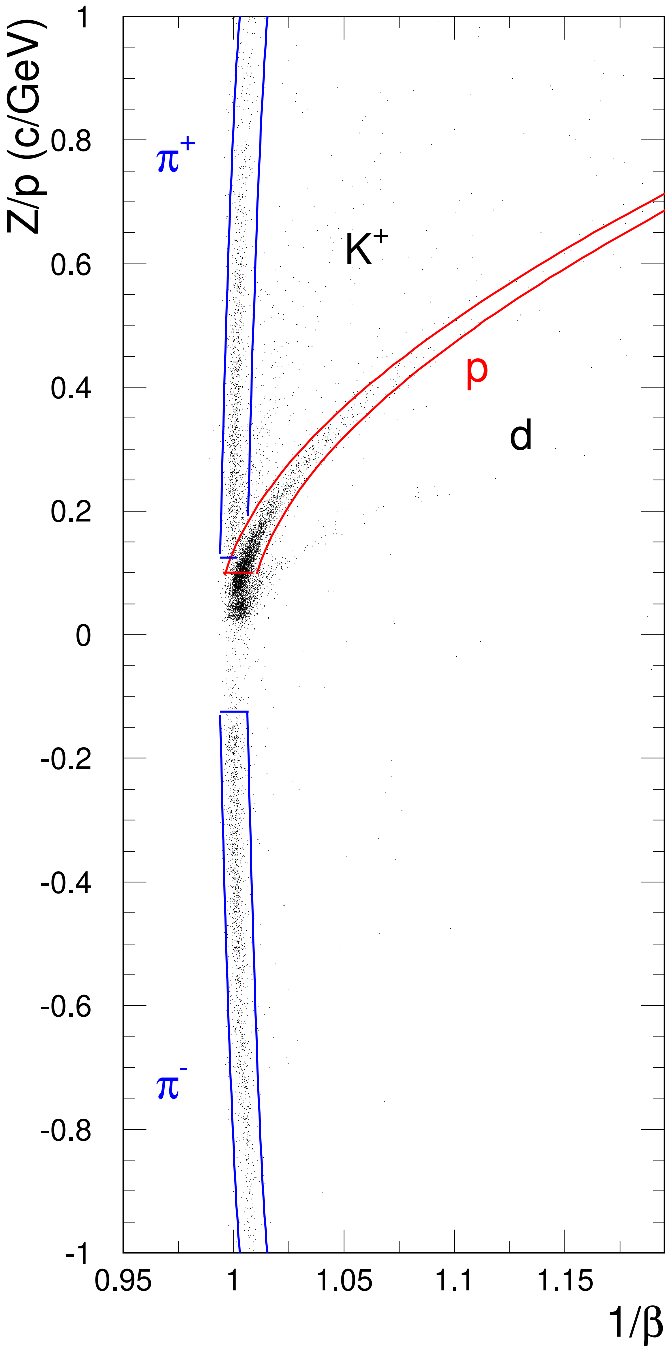

Figure 4.5: Particle identification inverse momentum and velocity distribution for $Z = 1$ particles. The lines are the particle selection windows for protons and pions.

The scatter around these lines is due to the finite momentum and TOF resolutions. In the present analysis, the pions and protons are selected using a particle identification (PID) window $\pm 3\sigma$ wide on either side of their mass line (see figure 4.5). The width of the distribution in inverse momentum is measured by fitting slices taken from the plot of figure 4.5 with a Gaussian, whereas the inverse velocity width is calculated from the measured TOF resolution. To avoid ambiguous particle identification, only protons with $p < 10$ GeV/c ($1/p > 0.1$ $(GeV/c)^{-1}$) and pions with $p < 8$ GeV/c ($1/p > 0.125$ $(GeV/c)^{-1}$) are included in the PID windows. The positive pion window is truncated on the larger TOF side for inverse momentum value interval of $0.125 <$ 1/p < 0.175 c/GeV to reduce the contamination from the proton distribution tail. The fraction of pions that are truncated is calculated using fits made to the adjacent *clean* (proton-free) region of the pion distribution. The weights of the pions that fall in this part of the PID window are then proportionally increased.

The pion and proton yields are large compared to the kaon yield. The tails of the pion and proton distributions and tracking errors result in a relatively smooth background under the kaon distributions that mandates a careful subtraction of the background. The kaon identification procedure is described in details in chapter 5.

4.5 Tracking efficiency and occupancy correction

The efficiency with which particle trajectories are reconstructed depends on several factors of which spectrometer occupancy is the most important. As shown in figure 4.6, the mean number of tracks in the acceptance of the spectrometer per *central event* ($\sigma_{\rm top}/\sigma_{\rm geom} \sim 10\%$) is about 7 particle per event and the distribution has a tail that extends up to 17 particle per event. Furthermore, the distribution of particles across the spectrometer is not uniform. The occupancies in the three main detectors of the spectrometer are plotted in figure 4.7 as a function of horizontal x positions.

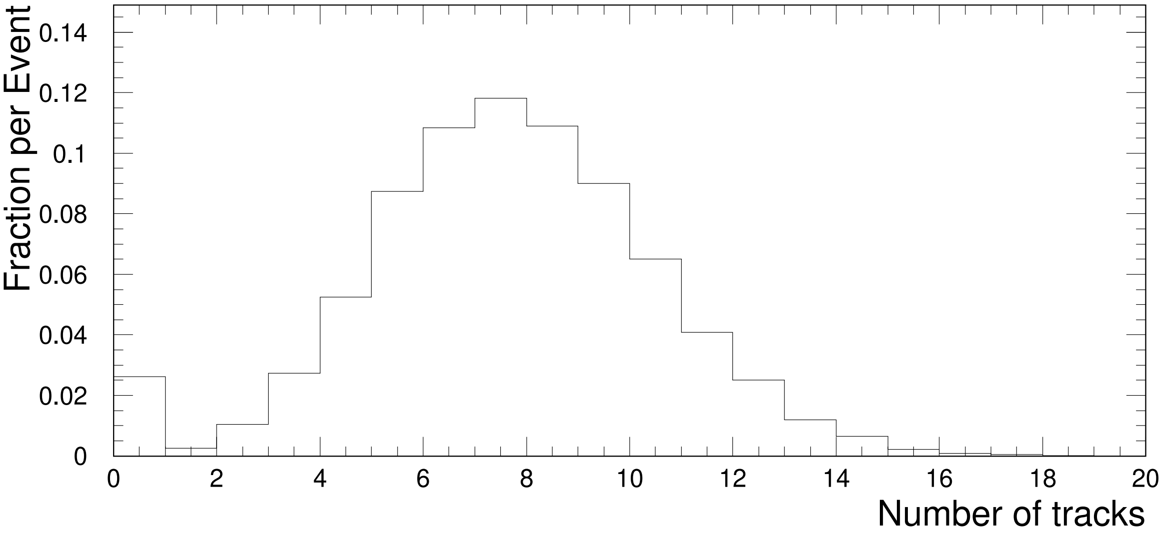

Figure 4.6: Spectrometer track multiplicity distribution for central Au+Au events ($\sigma_{\rm top}/\sigma_{\rm geom} = 10\%$).

As expected, the particle multiplicity is the highest around the beam trajectory ($x \approx$ -2 to -5 cm). The holes at $x \approx 0$ cm correspond to the detector dead sections. The spectrometer track occupancy varies greatly, from as low as 1%, at the edges of the detectors, to as high as 20% near the beam trajectory. The large occupancy in the beam region effectively limits the centrality of the collisions that can be studied with the spectrometer to $\sigma_{\rm top}/\sigma_{\rm geom} \sim 10\%$.

Particle with higher momenta and larger masses are less deflected by the magnet and tend to concentrate close to the beam trajectory. On the other hand, slower and lighter particles are distributed more evenly across the spectrometer. Consequently, all occupancy related detector inefficiencies introduce momentum dependent distortions. Besides that, all detectors have finite granularities which result in limited ability at resolving close hits. As two particles get sufficiently close to each other, the probability that their tracks will be resolved by a given detector has to eventually decrease. The spectrometer detector responses to close hits are plotted as a function

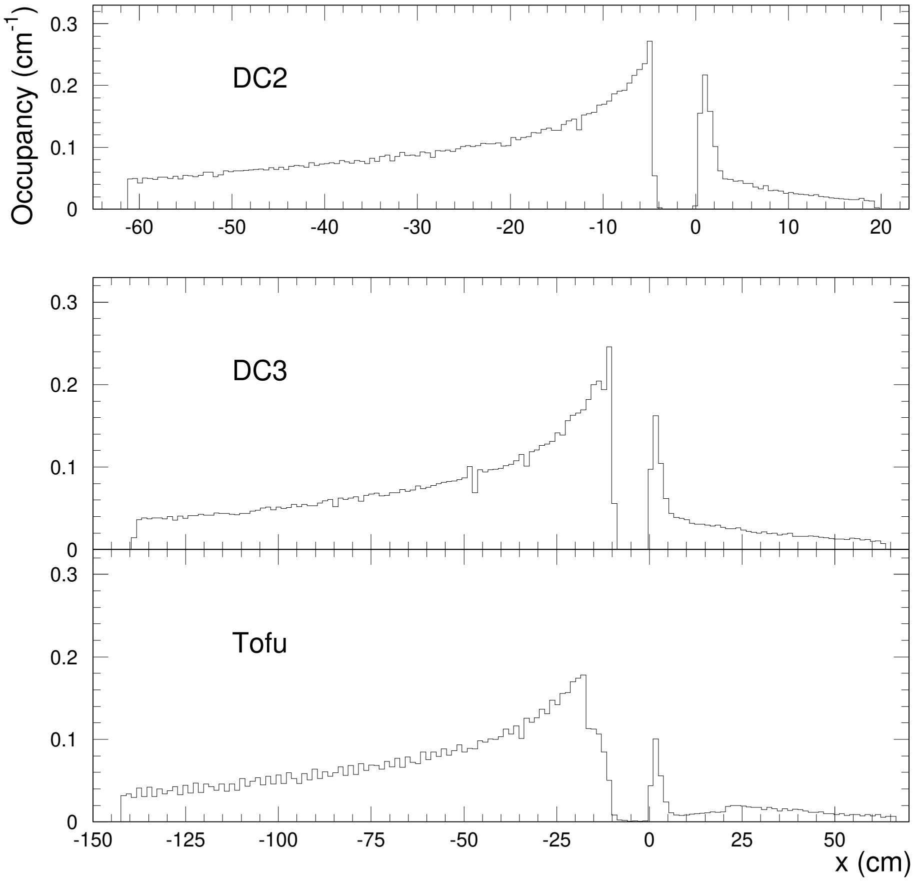

Figure 4.7: Spectrometer detector occupancy as a function of x position in DC2, DC3 and TOFU for B polarity.

of hit separation in figure 4.8. For a given track, the probability of finding another element at distance $-\delta x$ cm away, normalized by the occupancy at $-\delta x$ cm is plotted as a function of the distance δx between the track and the element. To avoid boundary effects that would introduce a large δx deficit resulting in an overall slope, the histograms are computed for portions of the detectors that are at least 10 cm away from the physical detector boundaries. The efficiency to resolve close elements increases with increasing δx until it reaches a plateau. The width of the close element efficiency is characterized by the *confusion length* $\delta x = l_i$ that we define as being the

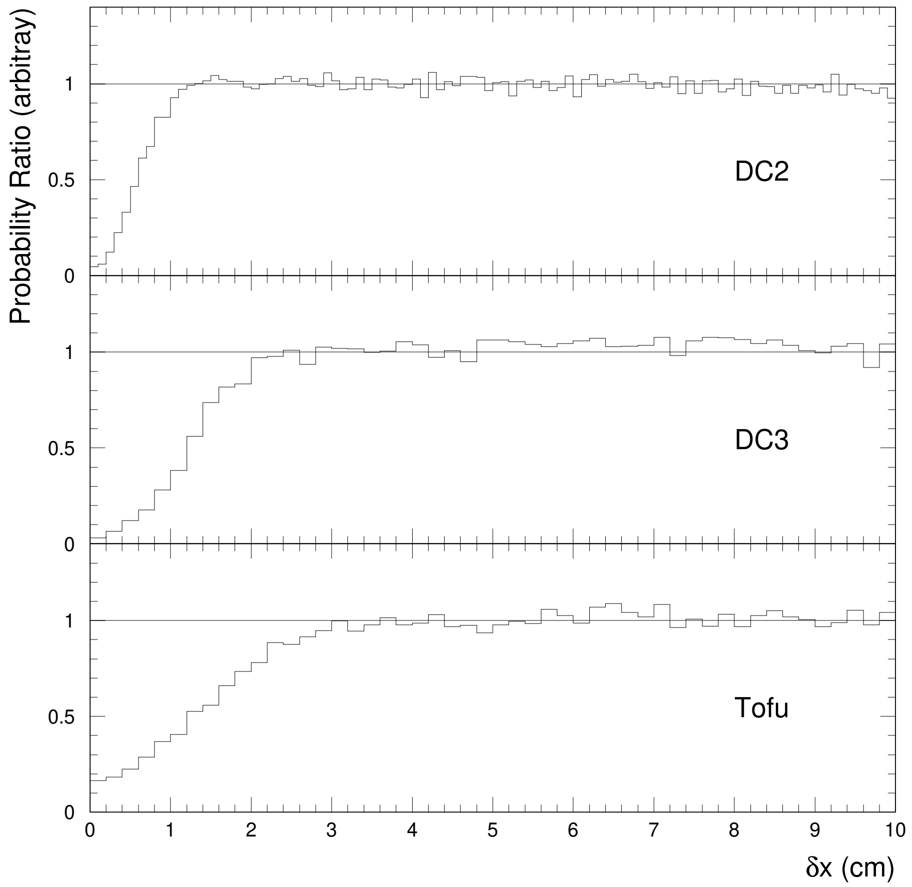

Figure 4.8: Close element reconstruction probability as function of their separation. The flat portions of the histograms are arbitrarily renormalized to 1.

distance at which half of the plateau value is reached. It is interesting to note that, in the DC's, the confusion length is approximately equal to the cell sizes (6.35 mm for DC2, 12.7 mm for DC3). Wire hits in the DC's have a left-right ambiguity that effectively doubles the cell size. The efficiency plateau is therefore not reached until twice the confusion length. Each of the TOFU hodoscope scintillators is physically independent. Its maximum confusion length is therefore equivalent to half of the detector width. The larger confusion length found in figure 4.8 is due to the high correlation of the horizontal positions of the missed tracks between DC3 and TOFU.

Upon understanding the origin of the close tracks inefficiencies, we have developed a data correction procedure. For a detector i and probability ε of detecting an element at a distance δx from a track, $(1-\varepsilon_i)$ is the probability of missing an element at δx. The total number of missed elements N_i^{elements} around a given track is obtained by integrating over the detector the δx dependent probability of missing an element multiplied by the position dependent element occupancy O

$$N_i^{\text{elements}} = \int_{-\infty}^{\infty} O_i(1-\varepsilon_i)dx_i. \tag{4.7}$$

Since the inefficiency affects only the tracks that are closer than $2l_i$, the integration can be performed on the corresponding range. The position dependent probability that an element forms a track, or single track reconstruction efficiency, is given by the ratio of the track distribution T_i across the detector to the element distribution O_i. Assuming that this ratio varies slowly at the confusion length scale, the total number of missed tracks N_i^{tracks} around a given track is then given by

$$N_i^{\text{tracks}} = \frac{T_i}{O_i} N_i^{\text{elements}} = \int_{-2l_i}^{2l_i} \frac{T_i}{O_i} O_i \cdot (1-\varepsilon_i)dx_i = \int_{-2l_i}^{2l_i} T_i \cdot (1-\varepsilon_i)dx_i. \tag{4.8}$$

The occupancy correction W_i for a single detector is therefore written as

$$W_i = 1 + \int_{-2l_i}^{2l_i} T_i \cdot (1-\varepsilon_i)dx_i. \tag{4.9}$$

W_i is used to weight the tracks, and accounts for the ones that are lost due to the presence of the ones that are seen.

In order to avoid overcorrecting in multiple detector systems, one has to account for correlated misses, *i.e.* tracks can only be missed once. Considering a two detector system and a track at position x_1 in detector 1 and x_2 in detector 2, the number of tracks missed in detector 2 that were already missed in detector 1 is given by

$$S_{1\times 2} = \int_{-2l_2}^{2l_2} C_{12} \cdot (1-\varepsilon_2)dx_2 \tag{4.10}$$

where C_{12} is the distribution of positions x_2 in detector 2 for tracks at x_1 in detector 1, or x_1 *vs* x_2.

The detectors required to reconstruct a track in the E877 spectrometer are the DC2 and DC3 only. However, the time information from the TOFU hodoscope is ultimately needed to perform the particle identification and must therefore be included in the correction procedure. The overall occupancy correction for the spectrometer is therefore written as

$$\begin{aligned} W &= [1 + N^{\mathrm{tracks}}_{\mathrm{DC2}}] \\ &\cdot[1 + N^{\mathrm{tracks}}_{\mathrm{DC3}} - S_{\mathrm{DC2\times DC3}}] \\ &\cdot[1 + N^{\mathrm{tracks}}_{\mathrm{TOFU}} - S_{\mathrm{DC2\times TOFU}} - S_{\mathrm{DC3\times TOFU}} + S_{\mathrm{DC2\times DC3\times TOFU}}] \end{aligned} \tag{4.11}$$

The δx dependence of the probability ε is readily obtained from the distributions in figure 4.8. Assuming that the track occupancy T_i is approximately constant over $2l_i$ on either side of the track at x_i, T_i can be taken out of the integral of equation 4.8. The correction is then integrated and the number of missed tracks is obtained by multiplying the track occupancy T_i by the number of missed elements. Correlated misses $S_{i\times j}$ are integrated from 4.10 in a similar fashion by assuming that the x_1 *vs* x_2 correlation is approximately constant over $2l_2$ on either side of the element at x_2.

The occupancy correction for protons is shown in figure 4.9 as a function of transverse momenta. The ratio of the proton $1/\mathrm{p_t} \cdot dN/d\mathrm{p_t}dy$ spectra with and without the occupancy correction are plotted for three rapidity intervals. As expected the effect of the correction is $\mathrm{p_t}$ dependent. It is more important at low $\mathrm{p_t}$ where it reaches values of up to 30%. The low $\mathrm{p_t}$ high rapidity tracks tend to concentrate around the beam trajectory in the higher occupancy region of the spectrometer. This results in a higher probability that tracks will be close and proportionally reduces the tracking efficiency. At larger $\mathrm{p_t}$ values, the correction saturates to about 10% which is mainly determined by the spectrometer single track reconstruction efficiency T_i/O_i.

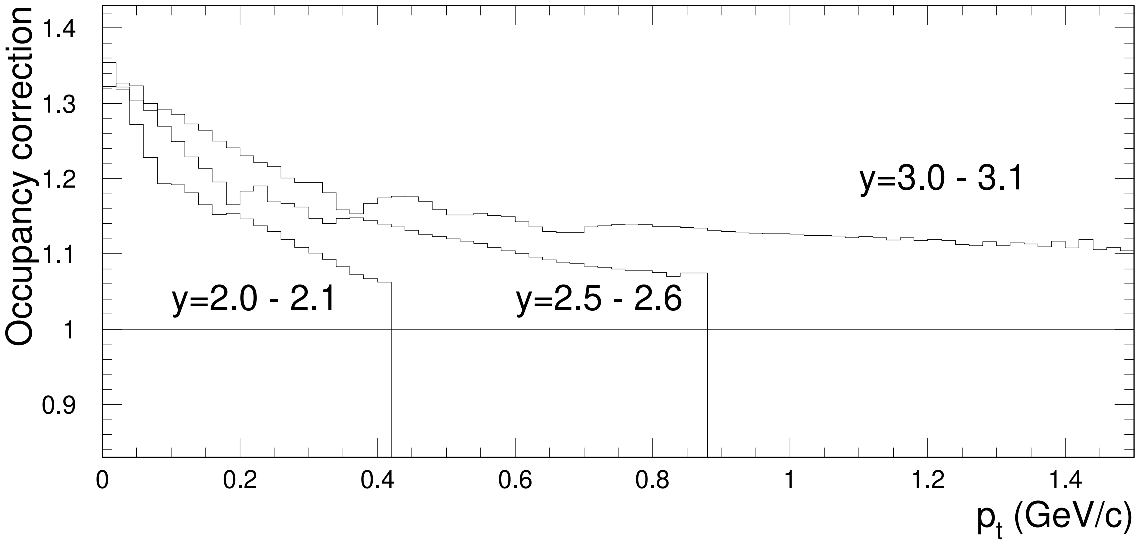

Figure 4.9: Magnitude of the occupancy correction as a function of transverse momentum and rapidity.

Two other occupancy corrections were developed in parallel to the one described above. The first method rejects all pairs of tracks that failed a minimum separation cut [101]. The effect of this cut is calculated by adding single virtual tracks to *real* events and computing the probability that the virtual tracks fail the minimum separation cuts. The results are then integrated into the acceptance calculation. The second method consists in removing all the tracks that fall inside a minimum separation cut and replacing them by doubling the weight of the tracks that fall inside a minimum separation window which is twice as large [102]. The three methods are found to give the same correction values with maximum differences of 5%. The corrections were also compared to results from a GEANT [103] calculations done using an exhaustive software model of the spectrometer. From events generated with the RQMD model, it was shown that the second type of correction could reproduce the original particle spectra to within 5%.

The occupation correction that we have developed has the advantage of keeping all the tracks that are reconstructed. It replaces missed tracks by increasing the weight of tracks that fall in the same region of the detectors and have, therefore, similar characteristics. This method undercorrects for the cases when 2 tracks are closer than $2l_i$ but one of them is successfully reconstructed. It also neglects triple track overlaps and higher order effects.

4.6 Acceptance calculations

Hundreds of particles are produced in every central collision but the spectrometer detects roughly ten of them. The particles that are detected by the spectrometer correspond thus to a limited sample of the produced particles. The size of the sample is determined by the geometrical acceptance of the spectrometer. Additionally, the detectors have dead sections and bad channels that introduce transverse momentum and rapidity dependent inefficiencies.

The geometrical acceptance is computed by randomly generating particles over a p_t and y phase space larger than that covered by the spectrometer. The simulated particles are propagated through a software model of the spectrometer that accounts for the physical boundaries of the detectors and their dead sections[1]. For each particle that is accepted, a phase space histogram is incremented at the corresponding (p_t, y) bin. Finally, the distributions are normalized by the number of particles that were generated. The resulting phase space acceptance diagrams for pions, kaons and protons are shown in figure 2.2. The results of the calculation for positive (negative) particles are presented for both field polarity settings (since they are roughly equivalent). With a center of mass rapidity of 1.57 and a beam rapidity of 3.14 the acceptance of the spectrometer is quite forward with smallest usable rapidity values of about y = 2.2, 2.0 and 2.8 for p, K and π, respectively (see also figure 2.2). The

[1]their precise positions are summarized in tables 2.1 and 2.2.

lower limits in rapidity are determined by the geometry whereas the magnitude of the magnetic field determines the rapidity at which large transverse momentum particles are accepted. The deadened sections of the tracking detectors introduce y dependent dead bands for positive (negative) particles in the A (B) field setting. The dead section of DC2 limits the extent of the $p_t = 0$ acceptance coverage for the highest rapidity values, especially for the heavier particles like protons.

A better understanding of the acceptance is obtained from the study of its p_t dependence. Rapidity slices of the acceptance phase space distribution are shown in figure 4.10. Acceptances are presented for protons and each charge state of pions and kaons in both roughly equivalent magnet polarities. The acceptance is found to vary rapidly over the first three bins from ~ 0.4 to ~ 0.08. This is due to the rectangular shape of the collimator. For positive (negative) particles in the A (roughly equivalent to B) polarity setting, the dead section of DC3 creates a hole in the acceptance at low p_t (0.1 to 0.15 GeV/c). The acceptance then flattens out to values around ~ 0.04 at medium p_t values until falling again rapidly at the largest p_t's. The structures that are found throughout the acceptance distribution originate from individual detector dead regions.

In order to improve the size of the statistical sample and the acceptance coverage at both ends of the p_t spectrum, the data accumulated with the two polarity settings have been combined. At high p_t, the data are kept up to the point where the acceptance falls abruptly. The data that fall on either sides of the acceptance holes are also removed, up until the bin-to-bin variation is smaller than a factor of two. For positive (negative) particles, this is done by keeping only the data that are on either sides of the hole of the A (B) field setting acceptance. Kaons were treated differently due to the background subtracting procedure described in section 5.2 where only the data taken in the acceptance hole-free polarity setting are analyzed.

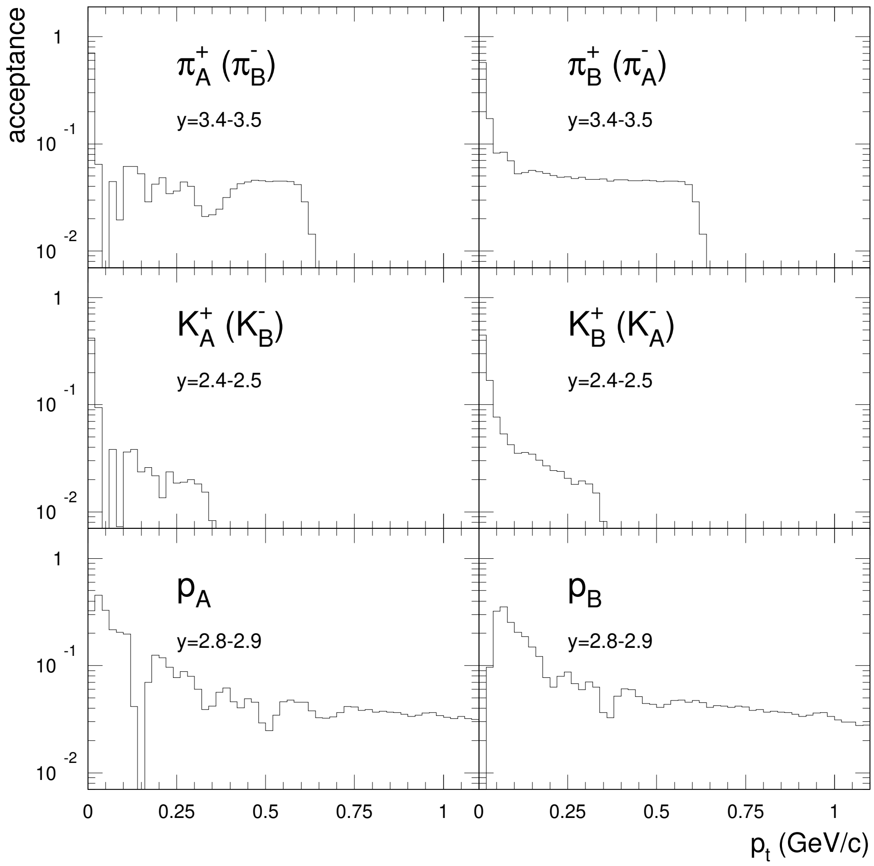

Figure 4.10: Spectrometer acceptance in transverse momentum for both magnetic field polarities (A and B) for typical rapidity slices. Nearly equivalent negative particle acceptances are indicated in parenthesis.

4.6.1 Summary of the corrections

As mentioned above, the measured data represent only a sample of the particles that are produced. To reconstruct the particle production in the covered phase space, the measured data needs to be corrected for the spectrometer acceptance and the PH cut efficiency and multiplied by the occupancy correction. The large momentum pion spectrum is also corrected for the pions cut in the PID matrix. Each of these corrections introduces its corresponding uncertainty.

The spectrometer acceptance varies from values 0.4 to 0.01. The data presented in this work are obtained from the region where the acceptance varies slowly. These regions of phase space are the more reliably modeled and, consequently, the acceptance calculation uncertainty is evaluated to be of the order of 5%.

The tracking efficiency and occupancy corrections has values that range from 1.1 to 1.3. Considering the agreements between the three correction methods that were developed independently and the GEANT simulation the combined efficiency and occupancy correction systematic uncertainties are estimated to be of less than 10%.

The efficiency of the pulse height cut that is used to select Z=1 charge particles is of 0.95 and therefore, is small compared to other corrections. The uncertainty on the pulse height cut efficiency was evaluated to be of approximately $\sim 1\%$ (see section 3.5.2). The pion truncation correction applies only to pions of high momentum. Its value varies from 1.0 to 0.5. The error of this correction is estimated from the quality of the width of the pion mass line to be of at most 5%. The combined overall systematic uncertainty of all corrections is estimated to be of the order of 15%.

4.7 Particle spectra

The fact that the measured particle yields should be independent of the spectrometer field polarity can be used to evaluate the consistency of the data corrections. The ratios of negative pion transverse momentum spectra measured in each of the two spectrometer magnetic field settings for nine different rapidity slices are plotted in figure 4.11. The ratios are consistent with unity (dashed line) with maximum systematic discrepancy of the order of $\approx 10\%$.

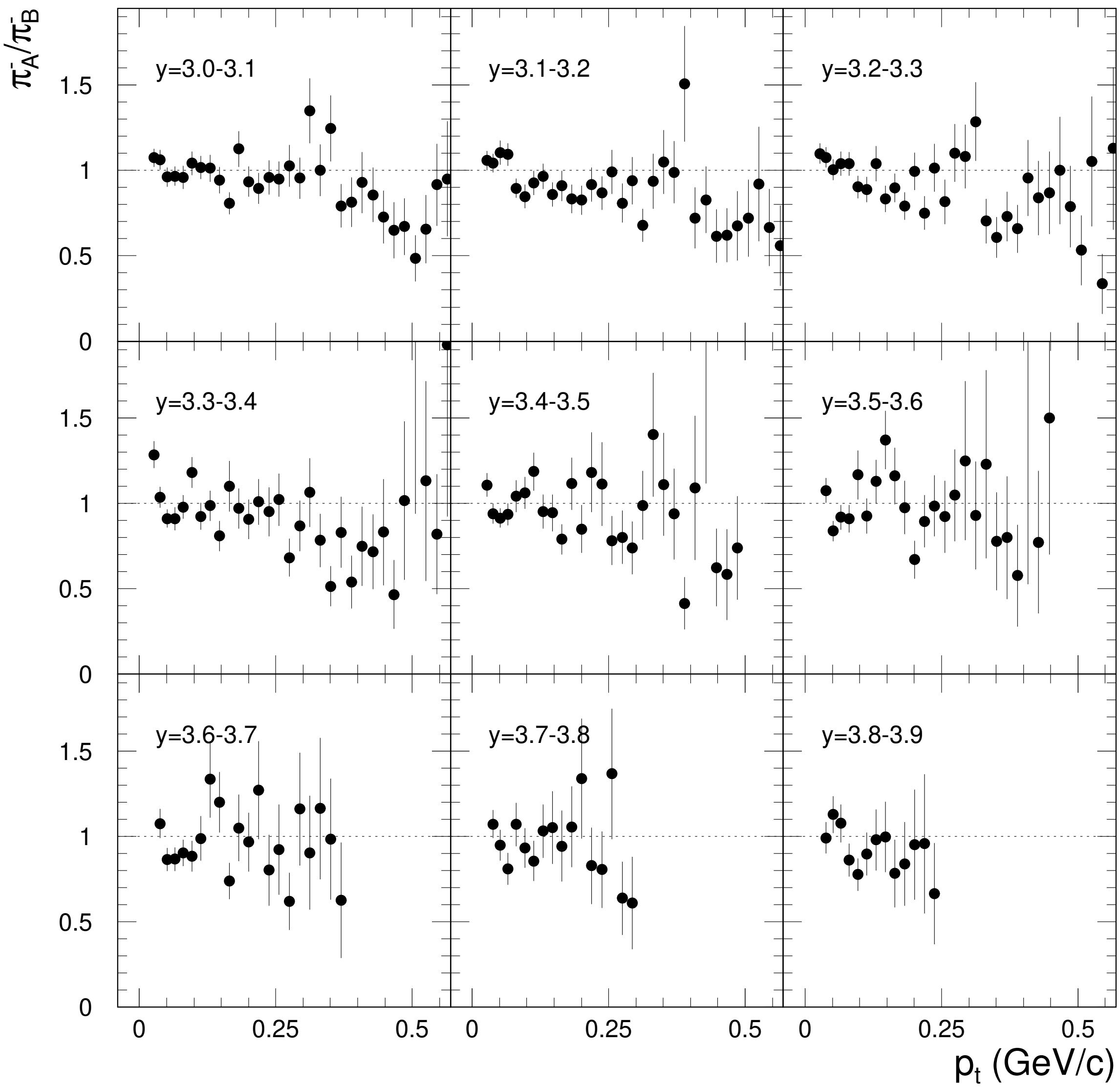

Figure 4.11: Ratios of negative pion yields measured in each of the two spectrometer field settings (A and B) for central Au+Au collisions ($\sigma_{\rm top}/\sigma_{\rm geom}$=0.04)

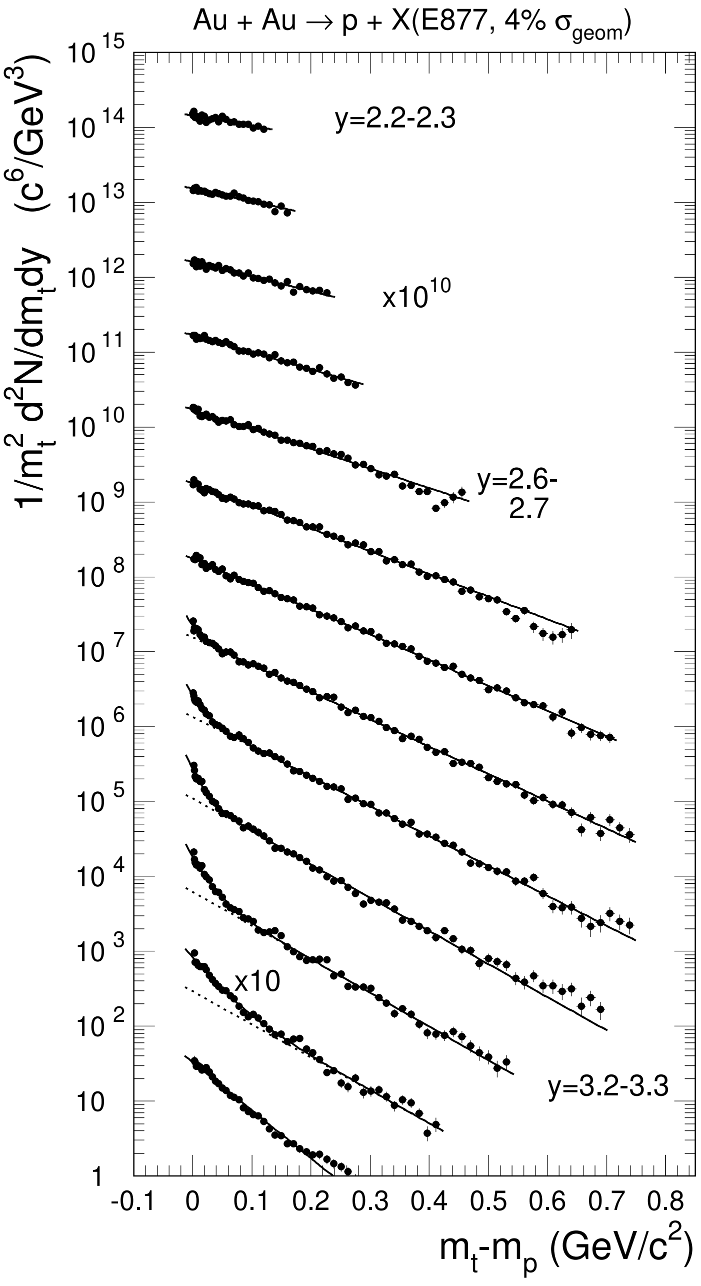

Figure 4.12: Proton transverse mass spectra measured in central Au+Au collisions ($\sigma_{\mathrm{top}}/\sigma_{\mathrm{geom}}$=0.04). Beginning with rapidity bin y = 3.3 − 3.4, spectra have been multiplied by successively increasing powers of ten.

4.7.1 Proton spectra

The proton transverse mass spectra for the most central $\sigma_{top}/\sigma_{geom} = 0.04$ data as measured in Au+Au collisions are shown in figure 4.12. The vertical axis $1/\mathrm{m_t}^2 \cdot d^2N/d\mathrm{m_t}dy$ is the representation in which a Boltzmann (or thermal) distribution is a pure exponential in $\mathrm{m_t}$ ($\mathrm{m_t} = \sqrt{\mathrm{p_t}^2 + \mathrm{m}^2}$) [72]. The data are divided into constant $\mathrm{p_t}$ bins of 20 Mev plotted on an $\mathrm{m_t} - \mathrm{m_p}$ scale and y bins of 0.1 units of rapidity. The spectra have thermal shapes with increasing inverse slope parameter when approaching mid-rapidity. A steeper component is seen at the lowest values of transverse mass of $\mathrm{m_t} - \mathrm{m_p} < 0.2$ GeV/c^2, for the rapidities near $\mathrm{y_{beam}} = 3.14$. This colder low transverse momentum component was already observed in the Si+Pb system and is attributed to spectator protons coming from the projectile [72].

Also plotted are the results of two-component Boltzmann fits to the data (solid lines). The dashed lines near beam rapidity show the contribution from the component with the larger inverse slope that is attributed to the *fireball.* This component always dominates at $\mathrm{m_t}$ larger than 0.1 GeV/c^2. It is used to extrapolate the proton production at large $\mathrm{p_t}$ values when calculating the rapidity distributions.

4.7.2 Pion spectra

Typical π^+ and π^- transverse mass spectra are presented in figure 4.13 for the $\sigma_{top}/\sigma_{geom} = 0.04$ centrality. The data are divided into constant $\mathrm{p_t}$ bins of 20 MeV plotted on an $\mathrm{m_t} - \mathrm{m_\pi}$ scale and y bins of 0.1 units of rapidity.

The transverse mass spectra are exponential with slopes decreasing with increasing rapidity. A clear enhancement above a pure exponential is observed for $\mathrm{m_t} - \mathrm{m_\pi} < 0.2$ GeV/c^2. A similar effect was already observed for the Si+Pb system and was explained by the contribution from decay pions of Δ resonances [29]. The enhancement is systematically increasing as one goes toward $\mathrm{y_{cm}}$. It is found to be

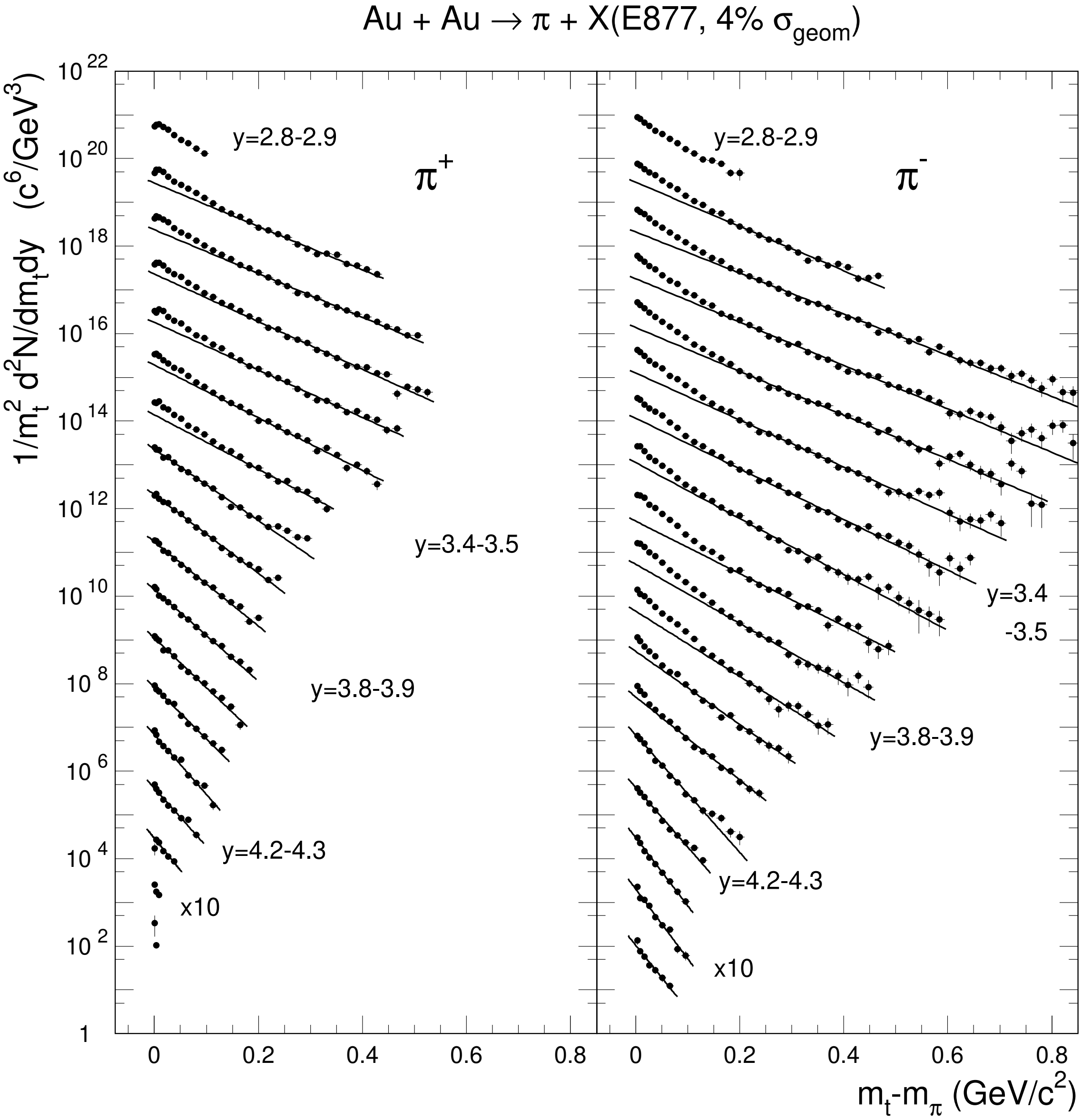

Figure 4.13: Pion transverse mass spectra for central ($\sigma_{\rm top}/\sigma_{\rm geom} = 0.04$) Au+Au collisions. Beginning with y=4.4-4.5, the spectra in each successively lower y bin have been multiplied by increasing powers of ten.

larger for the π^- than π^+ where it decreases in the lowest m_t bins. The solid lines are the results of Boltzmann fits to the data. The fits are performed in the interval $m_t - m_\pi > 175$ MeV/c^2 for the rapidity intervals below $y = 3.5 - 3.6$ and $y = 4.5 - 4.6$

for π^+ and π^-, respectively. For the other rapidity intervals the fits are performed to all of the available data which are dominated by resonance decay pions. A more detailed discussion of these proton and pion data is presented in chapter 6.

Chapter 5

Kaon production

The study of kaon production and other strange particles provides information on the level of chemical equilibrium achieved in heavy-ion reactions. It is also relevant to determine whether chiral restoration is achieved. Data from Au+Au collisions were awaited with great anticipation following the unexpected observation reported earlier for the Si+Pb system [64, 104]. Although of limited coverage in transverse momentum, the Si+Pb spectra exhibited a large enhancement at $m_t \approx 0.$ GeV/c^2 and unexpectedly low inverse slope parameters. These spectra were characterized by inverse slope parameters about one order of magnitude lower than those measured at larger values of m_t by other experiments [41, 105]. These data could not be explained by conventional models such as RQMD [106] (see section 6.1.1). Instead, exotic effects like density isomers [107] and collective cooling [108] had to be introduced. The soft component of the kaon spectra was even labeled as possibly being the first observed signature of chiral symmetry restoration in the laboratory [108].

Preliminary Au+Au kaon data, shown in figure 5.1, were presented at the Quark Matter '95 conference [31]. These K^+ spectra present an overall thermal behavior as shown by the exponential fits to the data (dashed lines). However, below $m_t -$

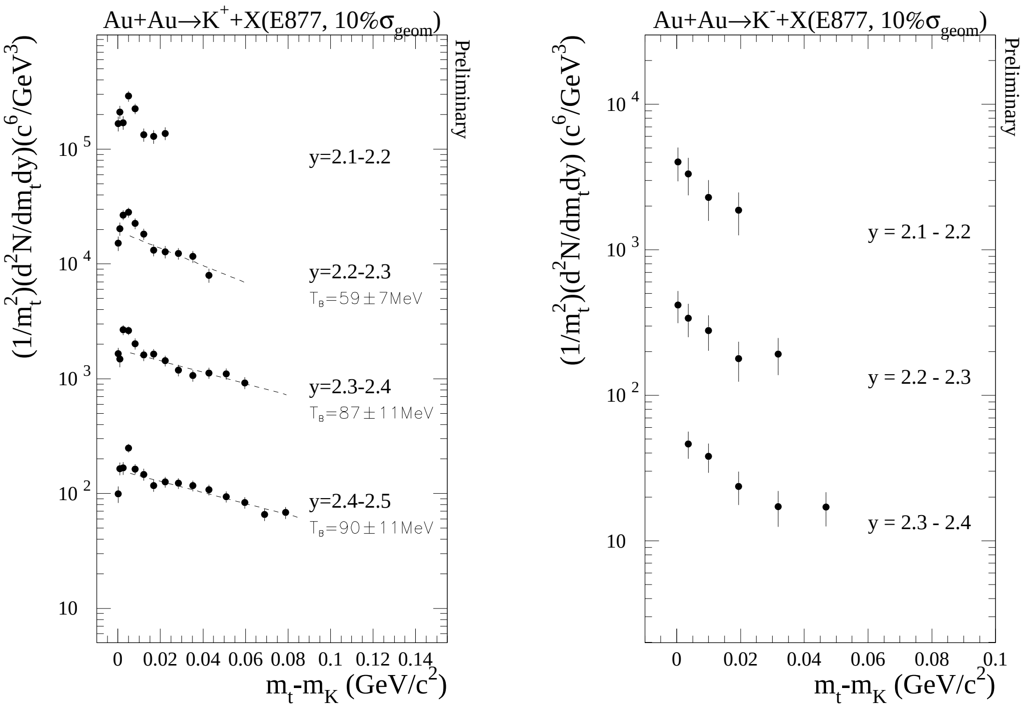

Figure 5.1: Left: Experimental K^+ spectra. The dashed lines are exponential fits to the data above $m_t - m_K = 0.02$ GeV/c^2. Right: Experimental K^- spectra. In each panel, the bottom spectrum is absolutely normalized. Spectra at lower rapidities are multiplied by an increasing factor of 10. Figures taken from [104].

$m_K = 0.020$ GeV/c^2 a sharp enhancement is observed which is consistent with the preliminary data on kaon production in Si+Pb collisions reported at [104]. A steep component at low m_t was also seen in the preliminary K^- spectra (right side of figure 5.1). Furthermore, the measured K^+ spectra presented a very narrow dip at $m_t - m_K = 0$ GeV/c^2.

In this chapter we discuss the re-analysis of the data presented at the Quark Matter '95 conference. The origin of the low p_t structure is traced to a source of beam rapidity protons located at the upstream edges of the spectrometer's collimator (inside the PCal). The origin of this K^+ background is discussed in the following subsection. The procedures to subtract the backgrounds from the K^- and K^+ are described next, and finally, the resulting spectra are presented.

5.1 Collimator albedo

To better evaluate the background contribution to the kaon yield for each rapidity bin, we plot a mass spectrum for each of the p_t bins of the m_t spectra. This procedure is similar to that used by B. Hong [64]. The number of kaons is then obtained by fitting a gaussian over an exponential background that accounts for the tail of the pion peak. In this analysis, the data from the region of the K^+ spectra below $p_t < 0.200$ GeV/c are carefully inspected for an additional source of background that could create the observed structure.

The measured mass distributions of positive particles for the first 8 bins in p_t are plotted at the top of figure 5.2 for the kaon rapidity interval of $y = 2.2 - 2.3$. Although the 1993 data set statistical sample is relatively limited, the measured mass distributions contain indications of a smoothly moving background peak (shaded histogram) located between the π^+ and p in bins 2 and 3 and between the π^+ and K^+ peaks in bins 6 and 7. The smooth variation of the background peak position with p_t hints that it is first located under the p peak in bin 1, below the K peak in bins 4 and 5 and finally under the π^+ peak for bin 8 and higher.

In an effort to pinpoint the physical origin of the background, the spatial distributions of tracks that fall in a *kaon mass* window defined here as $0.4 < m < 0.5$ GeV/c^2 are plotted at the DC3 location (top plot) and at the collimator downstream edge position (bottom plot) in figure 5.3 (solid line histogram). The kaon particles are found to be smoothly distributed over about half of the available horizontal acceptance of DC3 (see table 2.1). Backtracking to the collimator downstream edge, the *kaon* trajectories slightly diverge and occupy an even larger fraction of the available

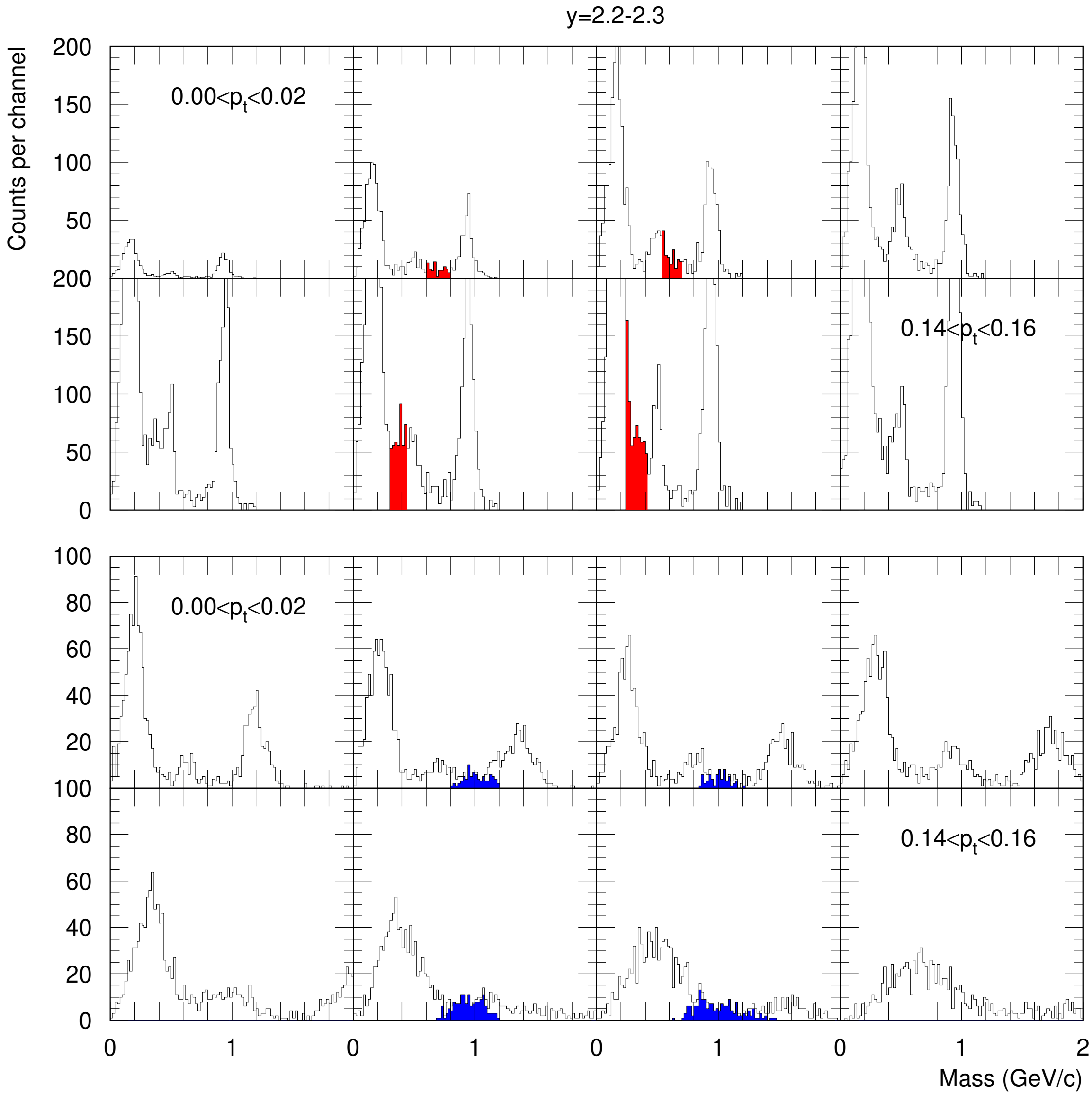

Figure 5.2: Measured mass distributions of positive particles for the first eight p_t bins of the kaon rapidity slice $y = 2.2 - 2.3$, assuming the particle source to be at the target (top plots) and the collimator upstream edge (bottom plots). A moving background is highlighted (shaded histograms).

space. The spatial distribution of tracks that fall in the *background* window defined by the shaded histograms of figure 5.2 are overlaid in figure 5.3 (shaded histogram).

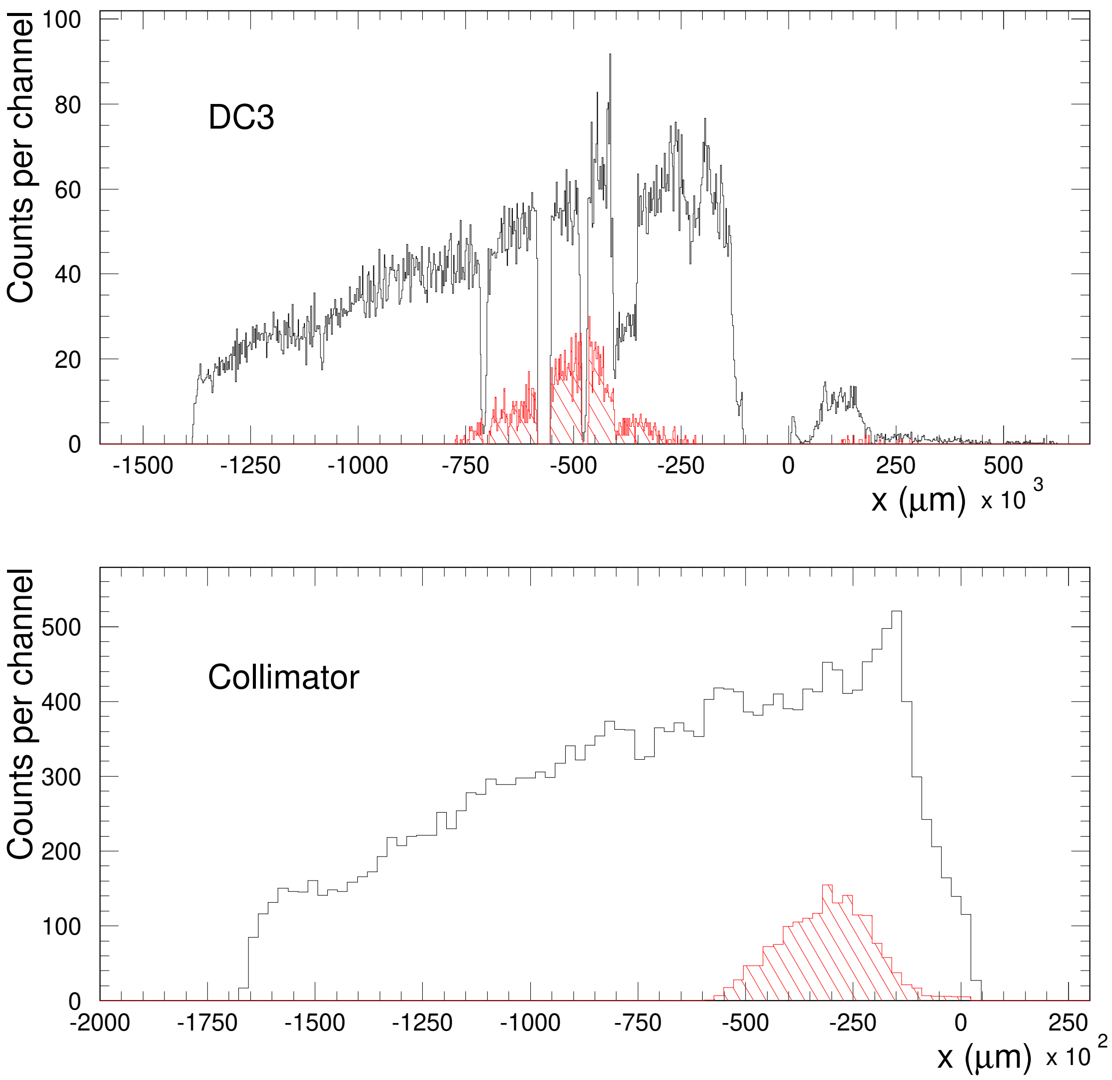

Figure 5.3: K^+ and moving background horizontal x distributions at DC3 (top) and collimator downstream opening (bottom).

At DC3, the background tracks fall in the central portion of the spectrometer. At the collimator, the background trajectories are not spread out as much as the kaons but are rather found to focus near the edge closest to the beam trajectory. This suggests that the background particles might be originating from a source that would be located at the upstream edge of the collimator that is closest to the beam trajectory.

The tentative background source location can be tested by modifying the tracking algorithm. The mass spectra shown at the bottom of figure 5.2 were obtained by assuming that all the tracks originate from a point that is at the middle of the upstream vertical edge of the collimator rather than from the target. The modified measured mass values are calculated using path lengths that account for the travel from the target to the collimator edge point. The overlaid shaded histograms correspond to the tracks that fall in the background windows defined in the corresponding plots at the top of figure 5.2. The background tracks are now consistently reconstructed as particles that have mass that is consistent with protons, in all $\mathrm{p_t}$ bins and rapidity slices. On the other hand, this procedure results in $\mathrm{p_t}$ dependent mass for particles that do originate from the target.

In 1993, the collimator was installed off-axis with one edge close to the spectrometer neutral axis in order to increase the $\mathrm{p_t}$ acceptance. The origin of the moving background can therefore be understood as being due to an albedo source of mid-rapidity protons (since at $\mathrm{p_t} \approx 0$ GeV/c, $\mathrm{p} \approx \mathrm{p_z}$, $\sinh \mathrm{y_p} \approx m_{\mathrm{K}}/m_p \cdot \sinh \mathrm{y_K}$ so for $\mathrm{y_K} = 2.2$, $\mathrm{y_p} \approx 1.6$) located near the upstream edges of the collimator that are closest to the beam. Since, in 1993, no tracking detector was installed upstream of the spectrometer magnet, the track reconstruction algorithm has to assume that all particles come from the target. The background particles are, therefore, reconstructed as protons when the error on their reconstructed trajectories is small *i.e.* when $\mathrm{p_t} = 0$. As the reconstructed $\mathrm{p_t}$ increases, the error on the real trajectory proportionally increases, resulting in lighter reconstructed masses for these albedo protons.

5.2 Kaon background subtraction

In order to extract the K^+ and K^- spectra, two separate procedures are used. The K^- spectra are obtained in a way that is similar to that developed by B. Hong [64]. This method consists in fitting the measured mass distribution of each y and p_t bin with the summation of a Gaussian and an exponential distribution. The original method is modified to include a second pion Gaussian distribution to better account for the pions peak tail. The mean position and width of the kaon mass peak are fixed while all other parameters are allowed to vary freely. The integral of the kaon Gaussian distribution yields the magnitude of the kaon signal in each p_t bin. Typical fit results are shown in figure 5.4 for the $y = 2.4 - 2.5$ rapidity window. The relatively small yield of negative kaons coupled with a smooth but important background contribution explain the large uncertainties in the measured spectra.

The collimator albedo background that affects the K^+ signal requires a slightly different treatment from what was done previously [64]. The albedo significantly contributes to the background in the first eight bins ($0 < p_t < 0.160$ GeV/c) of each K^+ transverse momentum spectra. In these bins, the background is subtracted from the kaon signal in two steps. First, the sum of two Gaussian distributions (one for the moving background and one for the kaon peak) and an exponential distribution (corresponding to the smooth background) are fitted to the measured mass distributions. The width and mean position of the kaon Gaussian are fixed. The position of the background peak and its width are measured by allowing the parameters of the moving background Gaussian distribution to vary. The values are then smoothed over all rapidity windows, leading to a smooth p_t dependent moving background *effective mass* and *width*. A second round of fitting is done using these values of *effective mass* and *width* to fix the background Gaussian. Typical fits are shown in figure 5.5. The measured yield for each p_t bin is then obtained by integrating

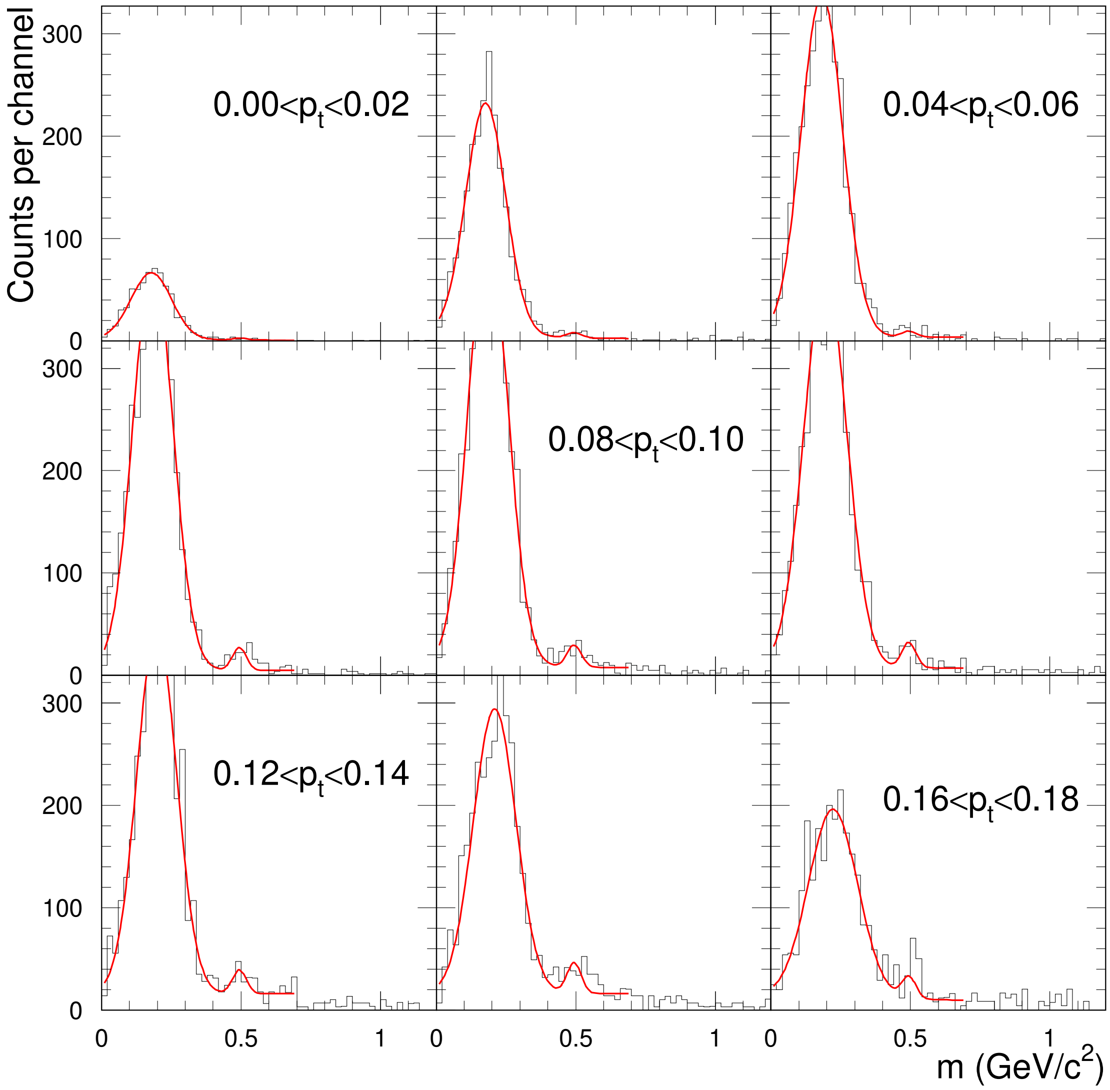

Figure 5.4: Negative particle measured mass distribution for the first nine 20 MeV p_t bins of the kaon rapidity interval $y = 2.4 - 2.5$. Two Gaussian distributions and an exponential background are fitted (solid line) to the data.

the kaon Gaussian. The albedo background subtraction is not possible in the the 4^{th} p_t bin $0.060 < p_t < 0.080$ GeV/c since the background lies right below the K^+ mass peak. Therefore, no measurements are given for that particular p_t bin. At p_t

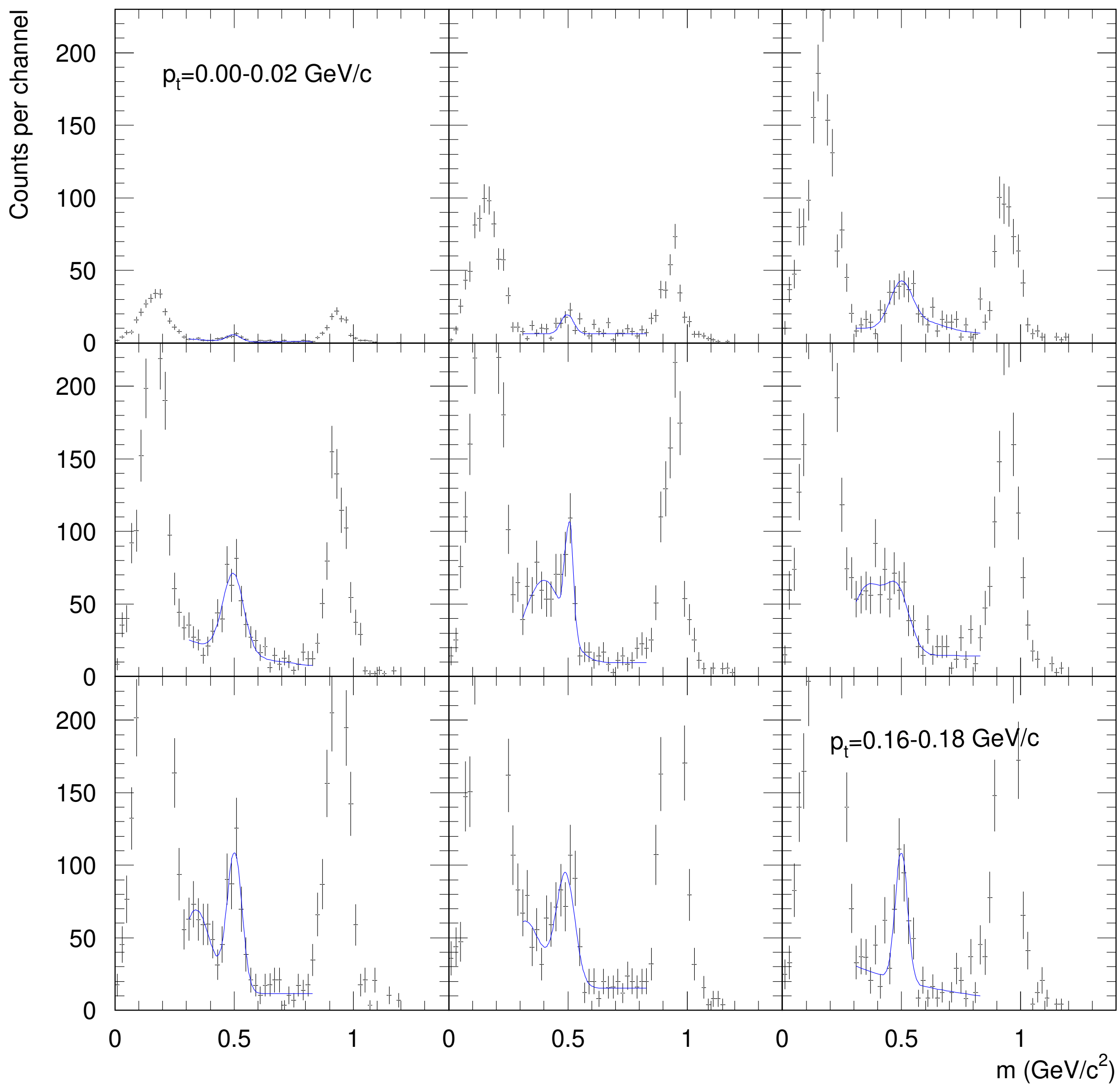

Figure 5.5: Positive-particle measured mass distribution plotted for the first nine 20 MeV p_t bins of the kaon rapidity interval $y = 2.4 - 2.5$. Two Gaussian distributions and an exponential background are fitted (solid line) to the data.

values higher than 0.160 GeV/c, the background subtraction procedure involves only a kaon Gaussian distribution and an exponential background distribution since the background effective mass is under the pion peak.

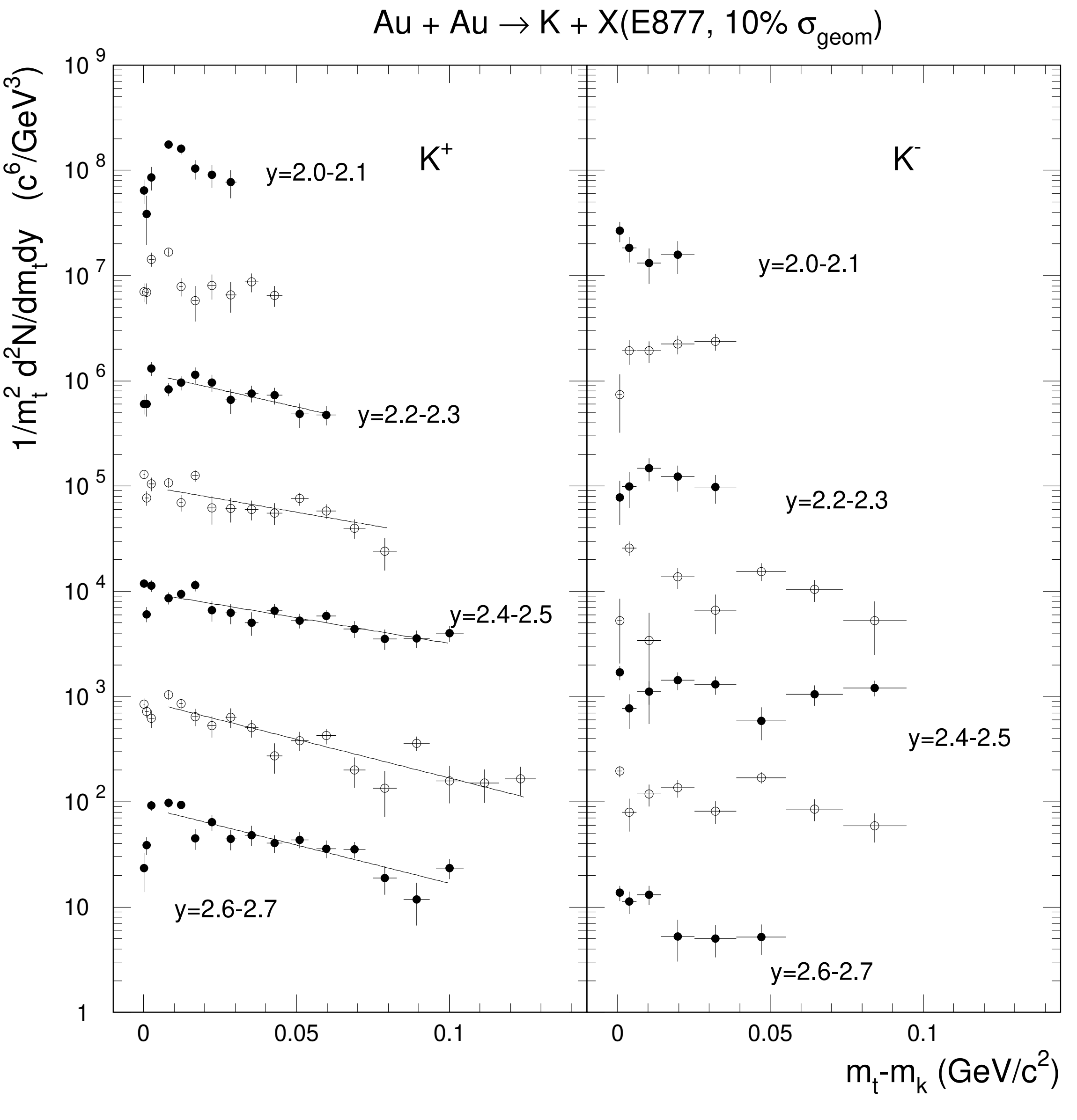

Figure 5.6: Kaon transverse mass spectra for ($\sigma_{top}/\sigma_{geom}$=0.10) Au+Au collisions. Beginning with y=2.6-2.7, the spectra in each successively lower y bin are multiplied by successively increasing powers of ten. Full lines are the results of Boltzmann fits to the data.

The background subtracted kaon transverse mass distributions are given in figure 5.6 for the top 10% of σ_{geom}. The m_t scales are divided into bins equal to 20 MeV/c in p_t for K^+ and 40 MeV/c for K^-. The structures that were visible in the Au+Au K^+ spectra presented at the Quark Matter '95 conference [31] are, within error, no longer present. The distributions seem to still show a dip at the very lowest p_t values. This feature is confirmed by the spectra from data taken in 1994 [109]. Two tracking detectors were added in 1994, in front of the magnet. They allow a better kaon identification by rejecting a large fraction of the smooth kaon background. Care was taken to improve the beam focalization and the statistical sample was improved by a factor of ten. Although these data cover a somewhat narrower range in p_t , they were found to be free of the collimator background.

The exponential inverse slopes that are fitted to the 1993 K^+ spectra have values ranging between 60 to 90 MeV which are consistent with those of figure 5.1, presented at Quark Matter '95 [31]. The fits are performed after excluding the first three points of the spectra but the uncertainties remain rather large. These inverse slope values are somewhat lower than the ones obtained from the E866 data ($T_B \sim 150$ to 170 MeV) in the same rapidity range [14, 110]. The E866 data cover transverse mass values of up to 1 GeV/c^2 whereas our measurement covers only the first 0.1 GeV/c^2. The much better quality data obtained in 1994 [109] lend inverse slope parameters that are consistent with the E866 results. The difference with the 1993 is probably due to the limited statistics and uncertainty on the p_t dependence of the moving background, a complication that is absent from the 1994 data set.

In summary, we have succeeded in identifying the source of the observed low p_t enhancement in the kaon spectra that were presented at the Quark Matter '95 conference. It is attributed to secondary protons that originate at the edge of the spectrometer collimator. Because of the limited quality of the 1993 kaon data set and of the much better quality of the 1994 data sample, we end our discussion of these data here.

Chapter 6

Discussion

The data measured in 1993 are presented and analyzed in terms of rapidity distributions, general shape and inverse slope parameters for the m_t distributions. The evolution of the data as a function of centrality as measured by the TCal is studied. The effects of longitudinal expansion and collective transverse flow are highlighted. The distortion of particle spectra is investigated in terms of Coulomb field. Throughout the present chapter, the data are compared to the calculation results from the RQMD theoretical model. The model is thus presented first, followed by some preliminary considerations that have to be addressed to allow for an accurate comparison to the measured data. A discussion of the proton data set is then presented, followed by that of the pion spectra. A model of the Coulomb distortion of particle spectra is developed last.

6.1 Model filtering

To properly compare results of a theoretical calculation to measured data, it is necessary to duplicate the experimental event selection so that the event sample characteristics of the calculation are as close as possible to that of the data. Depending on the type of measurement performed, the decay channels of long-lived particles have to be accounted for. Model simplifications that introduce unphysical effects need to be understood and removed.

6.1.1 RQMD 1.08

A model commonly referred to as Relativistic Quantum Molecular Dynamics (RQMD) has been developed to study the space-time evolution of heavy-ion collisions with energies ranging from 3 to 200 GeV/c per nucleon [111, 112, 113]. It is an extension of the non-relativistic quantum molecular dynamics developed to study heavy-ion interactions at lower energies [114, 115, 116]. The model has a microscopic approach that includes the cascading of the produced particles in a Lorentz invariant fashion. The model thus explicitly follows the trajectory of all the produced hadrons. It combines multiple two-body elastic and inelastic scattering plus soft many body potential interactions. Efforts are currently being made to integrate nuclear media effects into the model [117]. The model has been successfully used to describe nuclear stopping and particle production in systems that range from 1 A·GeV/c to 200 A·GeV/c [118, 119]. Furthermore, the source sizes that are predicted from the model agree well with measurements [120].

6.1.2 Transverse energy and experimental trigger

In the present work, the event selection is done on the produced transverse energy as measured by the TCal calorimeter. In order to emulate the response of the calorimeter, the amount of transverse energy that is produced in an event is redefined as the summation of the particle effective energies E_{eff} weighted by the sine of their emission angle ($\sin(\theta) = \mathrm{p_t}/\mathrm{p}$)

$$\mathrm{E_t} = \sum E_{\text{eff}} \cdot \frac{\mathrm{p_t}}{\mathrm{p}}. \tag{6.1}$$

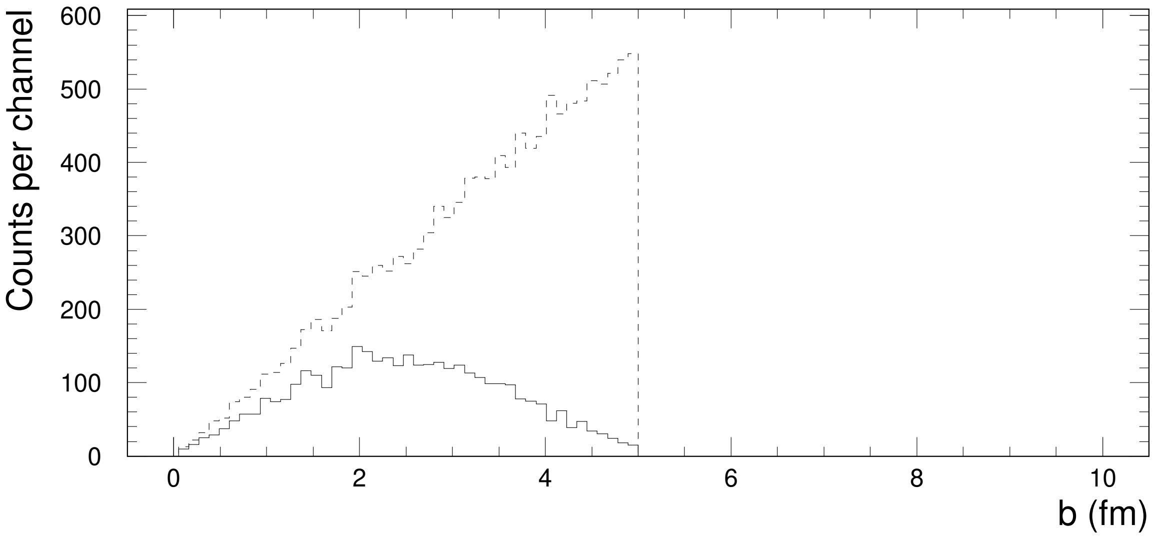

Figure 6.1: Impact parameter distribution of the $\sigma_{\mathrm{top}}/\sigma_{\mathrm{geom}} = 4\%$ TCal centrality trigger.

The summation is performed over the particles that are emitted within the corresponding detector solid angle. The effective energy of a particle corresponds to the amount of energy that is expected to be measured by a calorimeter once the particle rest mass has been taken into account. The rest mass is subtracted from the energy of protons and neutrons. The proton mass is subtracted from Λ energies whereas it is added to the anti-protons total energy. For all other particles, the effective energy is taken to be equal to its total energy.

The distribution of impact parameters for RQMD events that satisfy a calculated TCal E_t cut of $\sigma_{\mathrm{top}}/\sigma_{\mathrm{geom}} = 4\%$ gives some indication as to the effective centrality of the experimental trigger. In figure 6.1, the impact parameter distribution of RQMD events (up to 5 fm) is compared to the events with the top 4% of the calculated TCal transverse energy, obtained with equation 6.1. Because of the fluctuations of the calculated TCal E_t values, the sample of events selected with the TCal centrality trigger of $\sigma_{\mathrm{top}}/\sigma_{\mathrm{geom}} = 4\%$ (solid line), has a mean impact parameter of 2 fm and extends up to 5 fm. A purely geometrical $\sigma_{\mathrm{top}}/\sigma_{\mathrm{geom}} = 4\%$ centrality interval would instead correspond to an impact parameter window of $0 < b < 2.8$. It is interesting to note that even for the most central events, the trigger efficiency is not 100%. Throughout the present work, the model is compared to the data after accounting for the impact parameter dependence of the trigger efficiency, resulting in a smooth cut-off of the impact parameter distribution.

RQMD treats the reaction products as unbound, including the projectile and target, with Fermi energy distributions. Therefore, the spectator nucleons introduce unphysical distortions to the final particle distributions and calculated TCal transverse energy. Here, spectators are defined as initial nucleons (protons and neutrons) that have not interacted and which have rapidities that fall within 3σ (~ 0.3 units of rapidity) of the target and beam rapidity peaks present in large impact parameter calculated events ($8 > b > 10$ fm). When comparing to the data, such particles are removed from both E_t calculation and produced particle spectra. The effect of this cut on the dN/dy distribution of protons that are produced by the model is presented in figure 6.2. Strong peaks of spectator protons at both target and beam rapidity are present in the total RQMD proton dN/dy distribution (dashed line). These peaks are due to the protons that have not interacted in the calculation (dotted line) and their widths are related to the proton initial Fermi momentum distribution assumed in the model. While some of these protons will be ejected by the excited spectator, many will continue to be bound in spectator clusters and, therefore, should not be included in the final particle spectra. Furthermore, protons emitted from the spectator are expected to have energies that are characteristic of the spectator's temperature, *i.e.* that corresponding to the initial Fermi momentum distribution. In the present analysis, the non-interacting protons have been removed from the calculated particle spectra. As a result, the beam and target rapidity peaks are largely suppressed in the calculated proton dN/dy (solid line in figure 6.2).

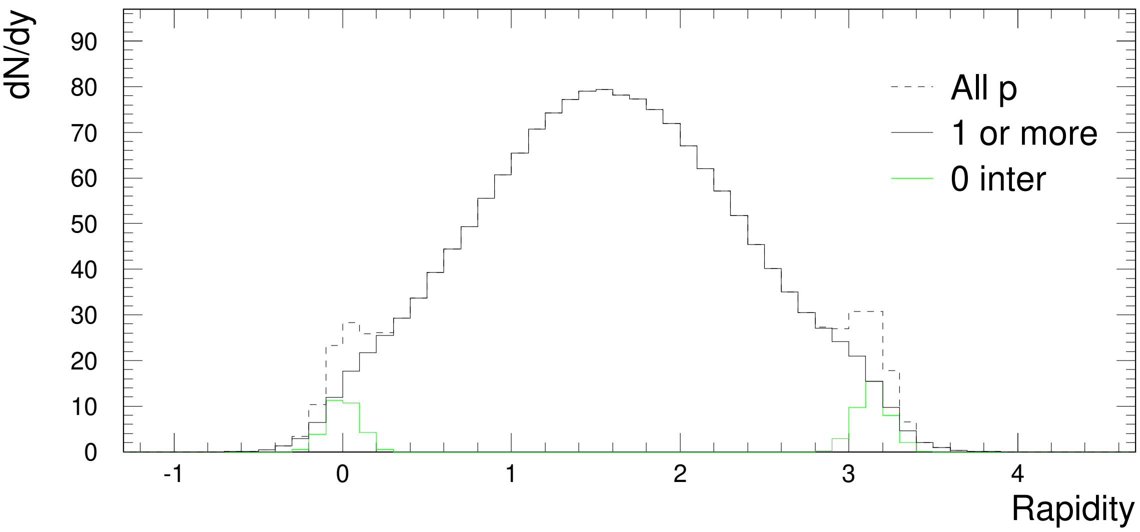

Figure 6.2: RQMD rapidity distributions of participant and spectator protons for $\sigma_{\text{top}}/\sigma_{\text{geom}} = 4\%$. The solid histogram is the proton distribution after non-interacting spectator protons (dotted histogram) are removed from the total distribution (dashed histogram).

6.1.3 Lambda decay

Lambdas are produced in fairly large numbers in central Au+Au collisions at the AGS. Lambdas have a sufficiently long lifetime (2.6×10^{-10} s) to decay as far away as a meter from the target. Since, in 1993, the E877 spectrometer did not provide measurements of the track positions before the spectrometer magnet, there is a finite probability that the decay products will be misidentified by the spectrometer as particles that come from the target and assigned wrong momenta. The Λ rapidity distribution as calculated by RQMD 1.08 for $\sigma_{\text{top}}/\sigma_{\text{geom}} = 4\%$, is shown in figure 6.3. It is compared to the proton (top plot) and pion (bottom plot) calculated rapidity distributions. At mid-rapidity the proton to Λ ratio is about ~ 20 whereas at beam and target rapidities it is ~ 100. The main Λ decay channels are $\mathrm{p} + \pi^-$ (64%) and $\mathrm{n} + \pi^\circ$ (36%). An estimate of the contribution of the decay products to the measured

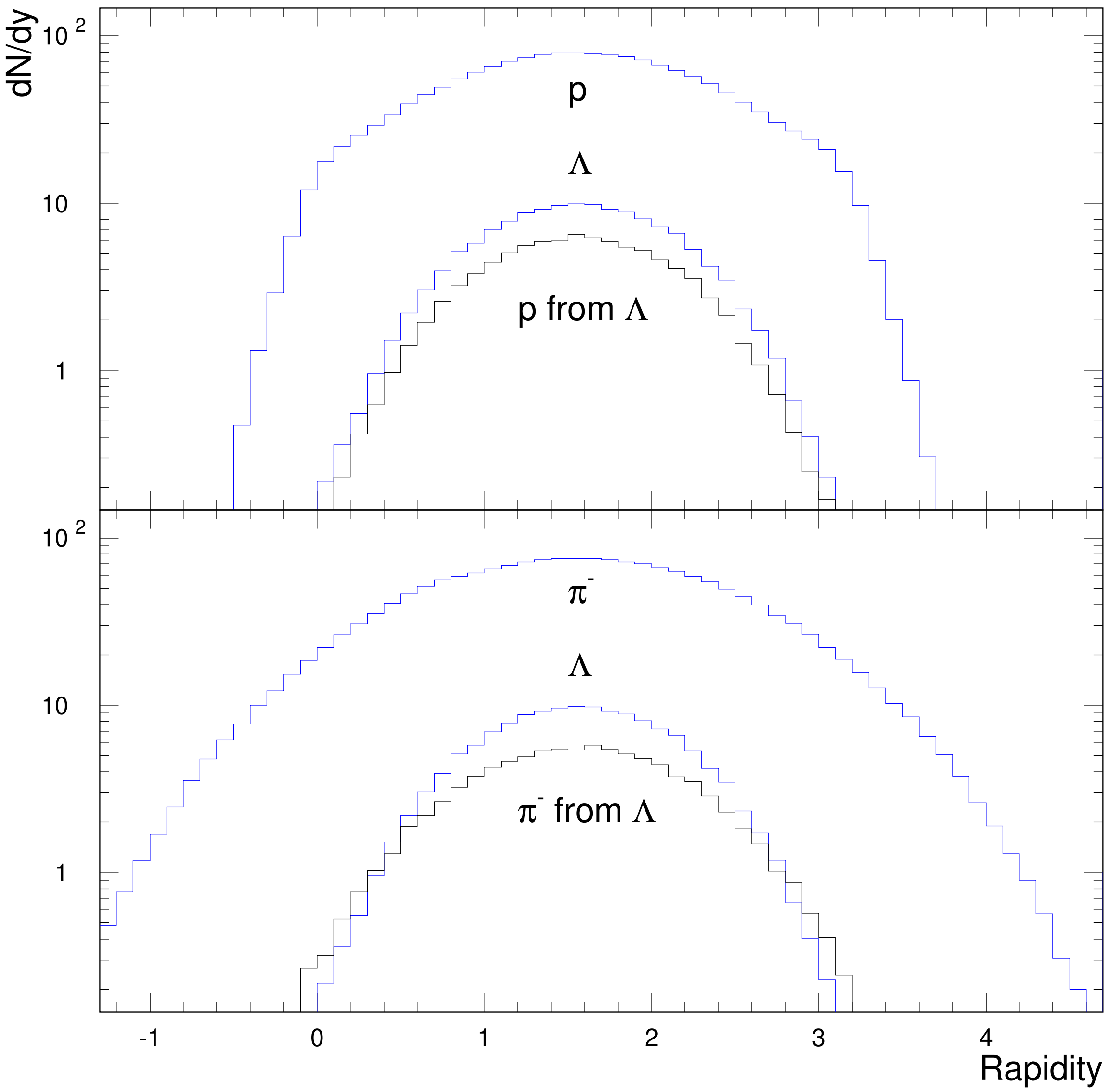

Figure 6.3: RQMD Λ rapidity distribution. Comparison of the calculated Λ rapidity distribution to the calculated distributions of primary protons (top) and pions (bottom). The rapidity distributions of the pion and proton decay products are also shown.

particle spectra is obtained by assuming that the decay of the Λ's occur at the target position and that the decay products are detected with the same efficiency as primary pions and protons. The rapidity distributions of p and π^- resulting from Λ decay are also shown in figure 6.3. The decay products distributions are found to be slightly wider than that of the initial Λ distribution, but remain confined close to center-of-mass rapidities. The effect of the secondary particles on the produced transverse momentum spectra of protons is shown in figure 6.4. The protons from Λ decay are found to contribute most in the lower p_t region of the spectra. However, the Λ decay protons have a spectral shape that is similar to that of the primary protons but with a cross section that is at least 20 times smaller in the studied rapidity range. That is to be expected if one assumes thermalization since the proton and Λ masses are similar, resulting in a relatively small momentum kick of the decay proton.

The Λ decay contribution to the negative pion spectra is shown in figure 6.5. The pions originating from Λ decays are found to contribute to at most 10% of the pion transverse momentum spectra at the very lowest transverse momentum values (p_t $<$ 200 MeV/c) and only for the first three rapidity bins. Because the acceptance of the spectrometer is at forward rapidities, the overall shape of the negative pion spectra is minimaly affected by the Λ decay pions. In the present work, the contributions of the Λ decay products are included in the particle spectra that are compared to the data.

6.2 Hadron spectra

6.2.1 Proton spectra

Very few secondary protons are created during heavy-ion collisions at AGS energies. Because of their relatively large masses, they are ideally suited to study collective

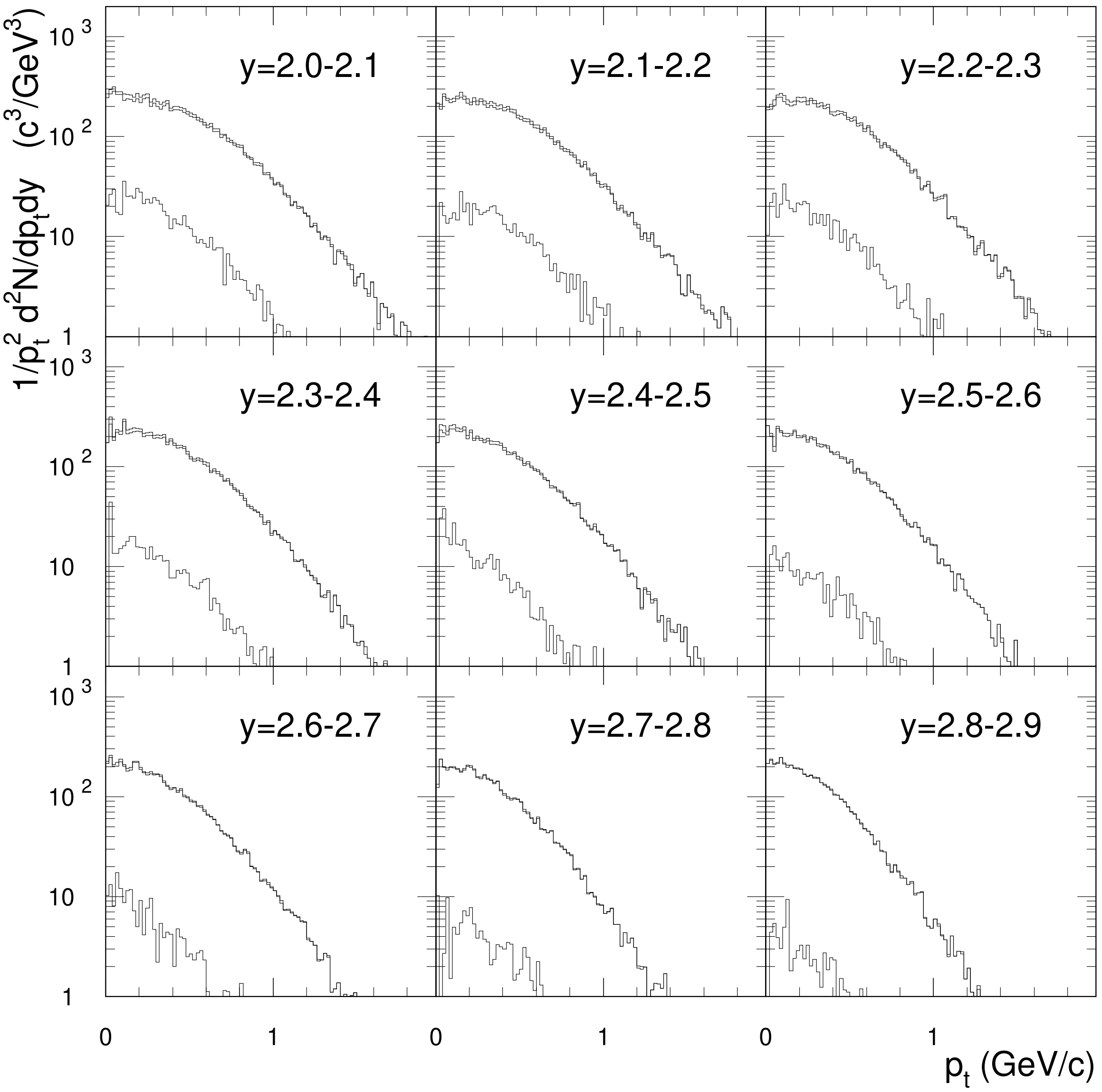

Figure 6.4: Calculated Λ decay contribution to the protons p_t spectra. In each rapidity interval, the top histogram is the sum of the direct protons (middle histogram) and protons from Λ decays (bottom histograms).

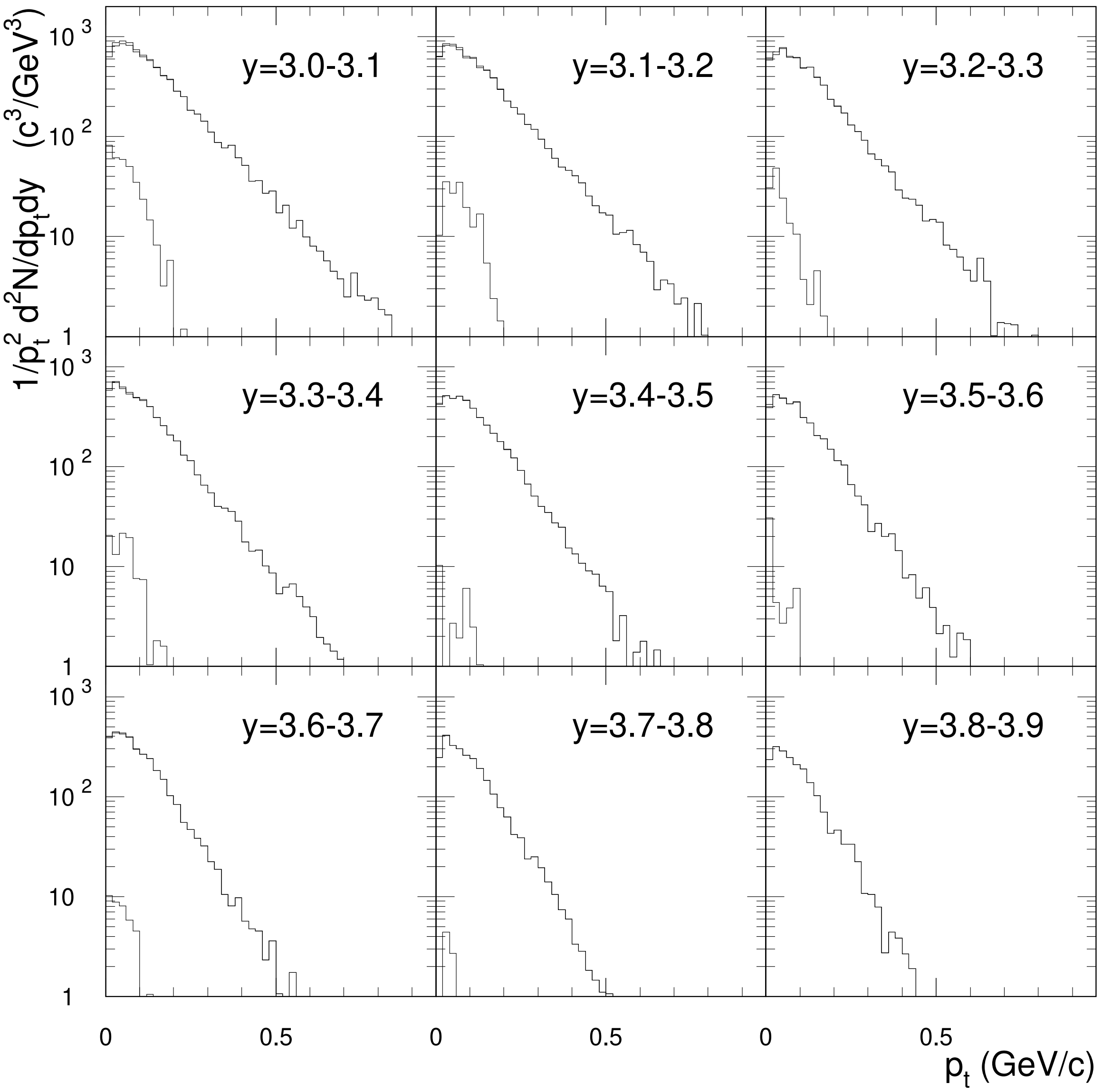

Figure 6.5: Lambda decay contribution to the pions p_t spectra. For each rapidity interval, the top histogram is the sum of the direct pions (middle histogram) and pions from Λ decays (lower histogram).

and directed flow effect. Their study also provides information on the behavior of the original constituents of the nuclei.

The proton transverse mass spectra measured in three centrality intervals are presented in figures 6.6, 6.7 and 6.8 respectively. The measured spectra have progressively larger inverse slope parameters as one approaches center-of-mass rapidities. The overall behavior is well described by exponential Boltzmann fits (solid lines). A second exponential is included in the fit of the spectra in the $2.9 < \mathrm{y} < 3.4$ interval to account for the spectator protons.

The prediction of the RQMD 1.08 model (histogram) is compared to the data. The calculation is found to reproduce all the general features of the spectra. However, close inspection reveals that the predicted slopes are always somewhat smaller than the ones that are measured. In particular, close to mid-rapidities, the lower transverse momentum part of the calculated spectra is systematically steeper than the data.

The rapidity dependence of the inverse slope parameters T_B obtained by fitting each of the spectra, with Boltzmann distribution are presented in figures 6.9, 6.10 and 6.11. The inverse slope parameters are defined by the function:

$$\frac{1}{\mathrm{m_t^2}} \cdot \frac{d^2N}{d\mathrm{m_t}dy} = \frac{C_B}{\mathrm{m_p}} \cdot e^{\frac{\mathrm{m_t}-\mathrm{m_p}}{T_B}} + \frac{C'_B}{\mathrm{m_p}} \cdot e^{\frac{\mathrm{m_t}-\mathrm{m_p}}{T'_B}}, \tag{6.2}$$

where $\mathrm{m_p}$ is the proton mass, C_B and T_B describe the *thermal part* of the spectra and C'_B and T'_B, the *spectator part* (for the rapidities $2.9 < \mathrm{y} < 3.4$)[1]. Since the studied system is symmetric, the measured values (solid symbols) are reflected about mid-rapidity to better visualize the behavior of the data. The values of T'_B (stars) for *spectators* are consistent with an effective source temperature of about ~ 20 MeV similar to what was observed in the 14 A·GeV/c Si beam systems [50, 71]. At the largest rapidity values, the spectator component is relatively small and has a slope

[1] The Boltzmann fit parameters and deduced dN/dy values for each centrality interval are summarized in tables A.2, A.3 and A.4

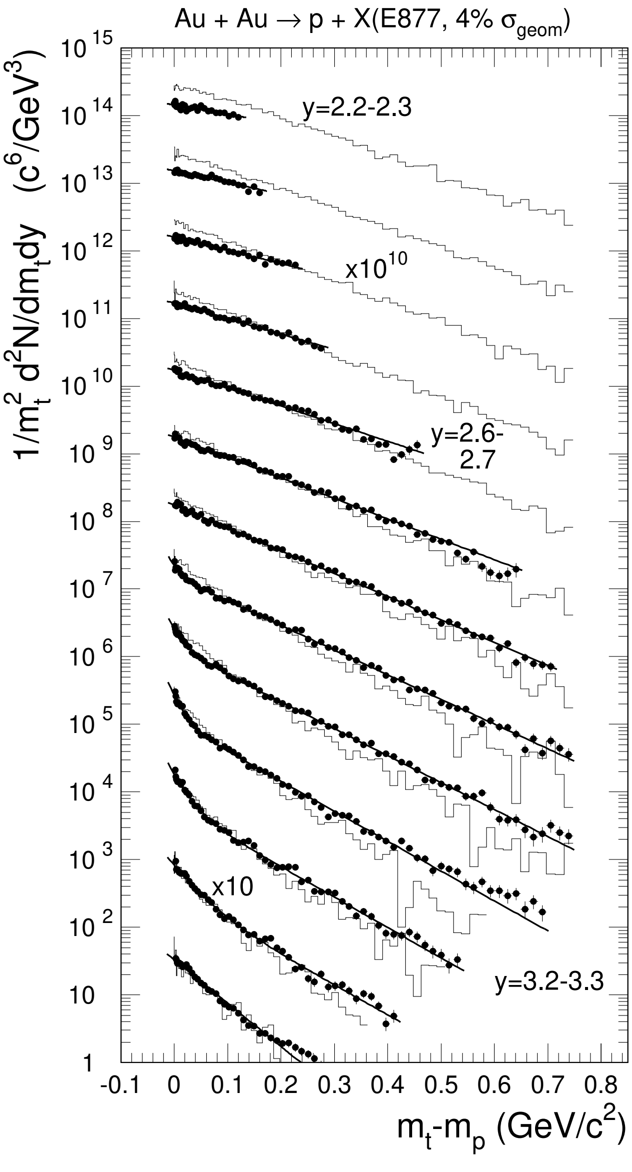

Figure 6.6: Proton transverse mass spectra for $\sigma_{\rm top}/\sigma_{\rm geom} = 4\%$ in $\rm p_t$ bins of 20 Mev, and y bins of 0.1 units of rapidity. Beginning with rapidity bin y=3.3-3.4, spectra have been multiplied by successively increasing powers of ten. Full lines are two-component exponential fits to the data. The histograms are RQMD predictions.

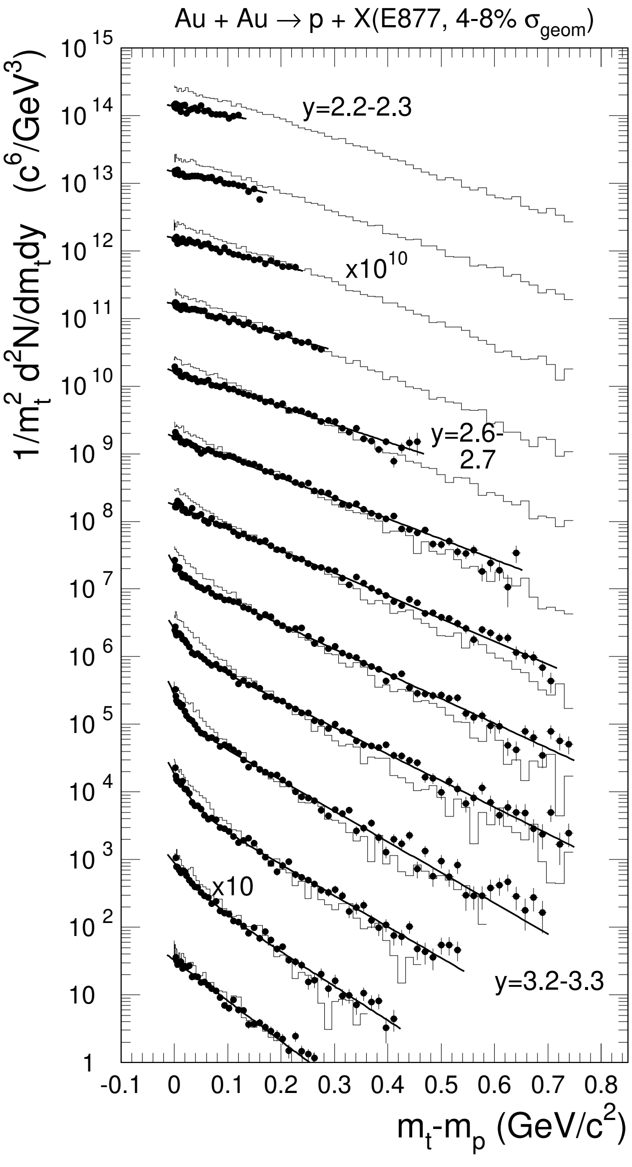

Figure 6.7: Proton transverse mass spectra for $\sigma_{\mathrm{top}}/\sigma_{\mathrm{geom}} = 4-8\%$ in p_t bins of 20 Mev, and y bins of 0.1 units of rapidity. Beginning with rapidity bin y=3.3-3.4, spectra have been multiplied by successively increasing powers of ten. Full lines are two-component exponential fits to the data. The histograms are RQMD predictions.

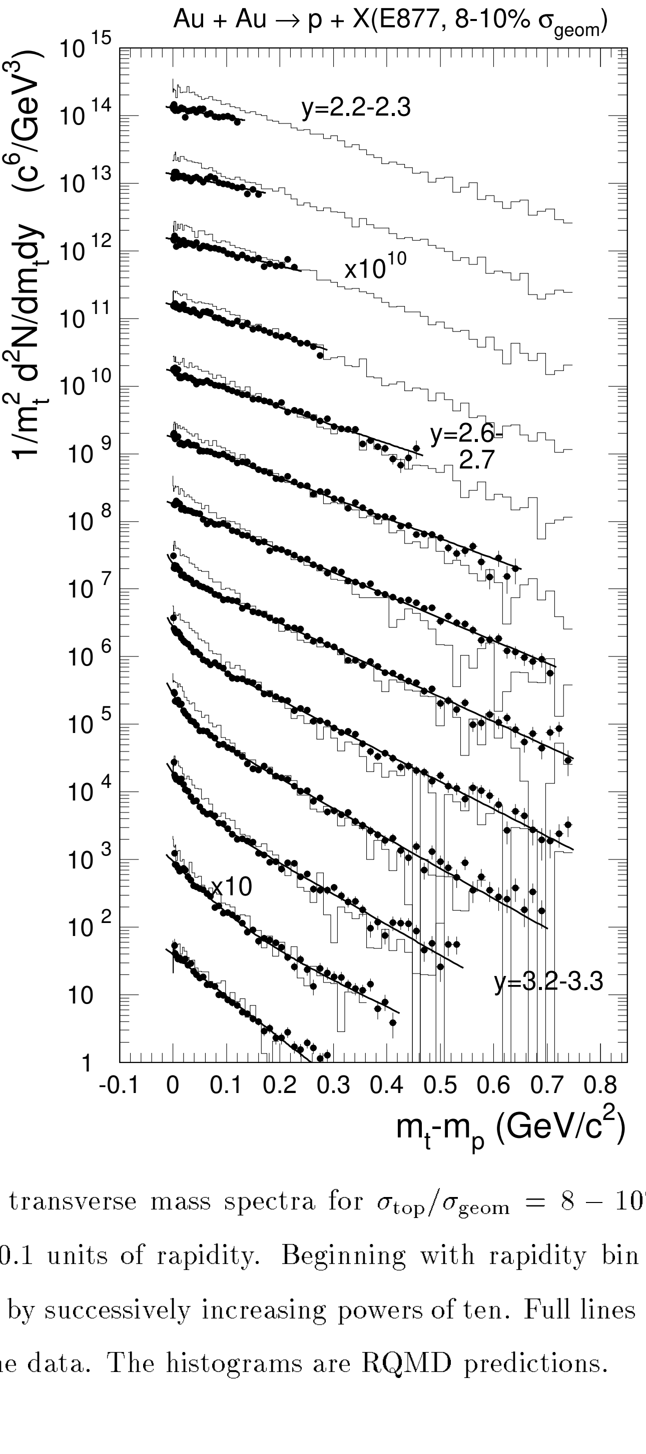

Figure 6.8: Proton transverse mass spectra for $\sigma_{\rm top}/\sigma_{\rm geom} = 8 - 10\%$ in $\rm p_t$ bins of 20 Mev, and y bins of 0.1 units of rapidity. Beginning with rapidity bin y=3.3-3.4, spectra have been multiplied by successively increasing powers of ten. Full lines are two-component exponential fits to the data. The histograms are RQMD predictions.

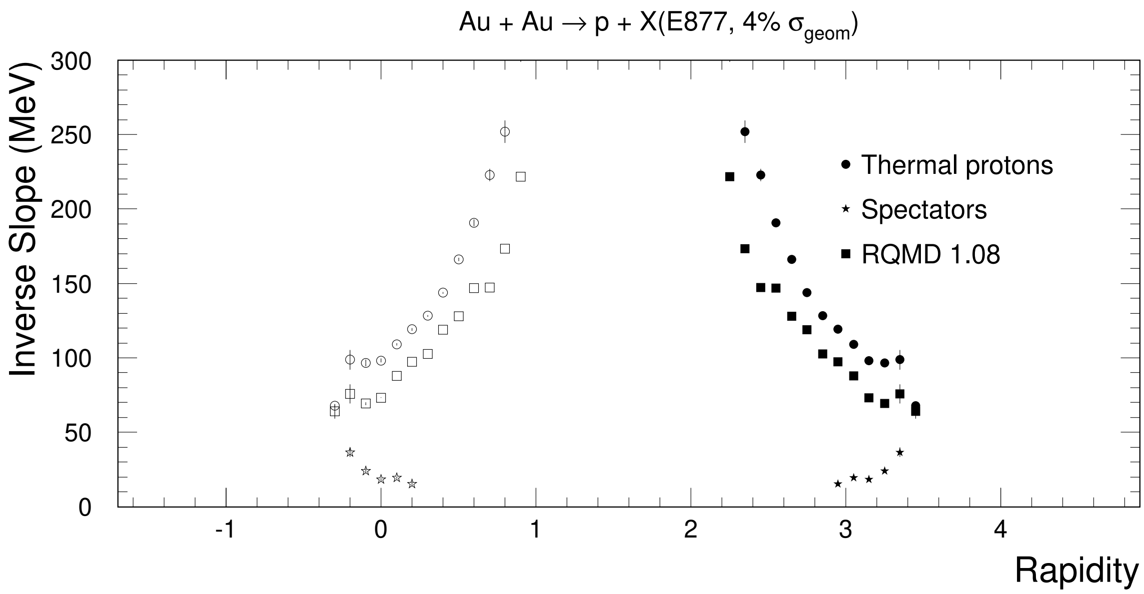

Figure 6.9: Proton inverse slope parameters deduced from fits to the proton m_t spectra for Au+Au collisions in the $\sigma_{top}/\sigma_{geom} = 4\%$ centrality. The data (solid symbols) are reflected (open symbols) about mid-rapidity.

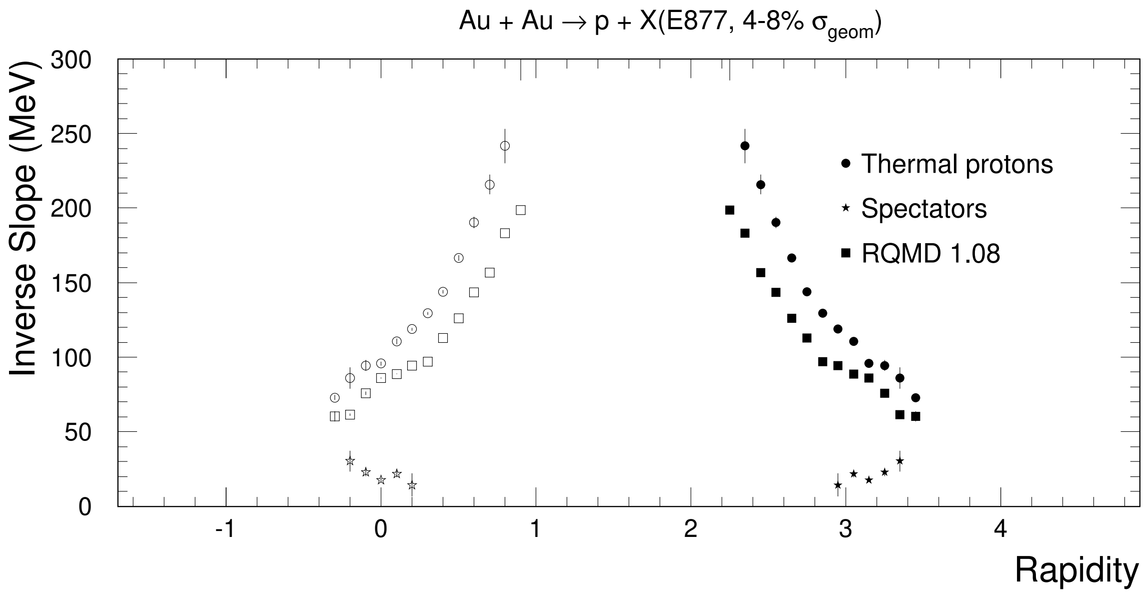

Figure 6.10: Proton inverse slope parameters deduced from fits to the proton m_t spectra for Au+Au collisions in the $\sigma_{top}/\sigma_{geom} = 4 - 8\%$ centrality. The data (solid symbols) are reflected (open symbols) about mid-rapidity.

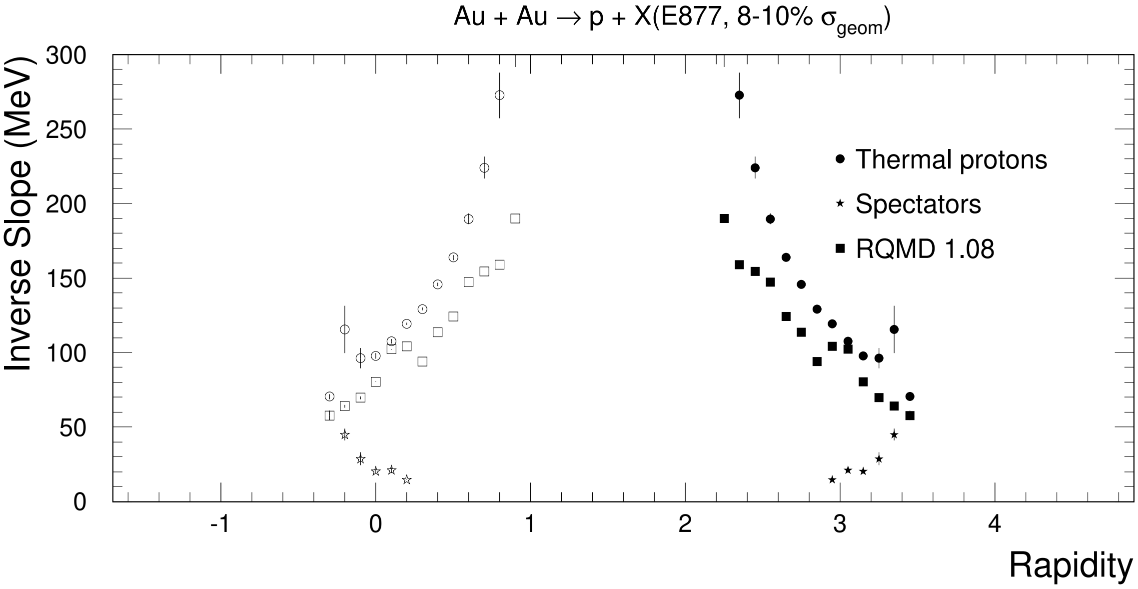

Figure 6.11: Proton inverse slope parameters deduced from fits to the proton m_t spectra of Au+Au collisions in the $\sigma_{\rm top}/\sigma_{\rm geom} = 8 - 10\%$ centrality. The data (solid symbols) are reflected (open symbols) about mid-rapidity.

which is close to that of the thermal component, thereby, increasing the error on the deduced values of T'_B.

T_B values of about 50 MeV are observed near beam rapidity and progressively increase to reach more than 200 MeV near mid-rapidity. Similar high values of proton inverse slope parameters were also observed near mid-rapidity in the Si systems [121, 122]. These large inverse slope parameter values combined with ejectile mass dependence have been discussed in terms of transverse collective flow effects [104, 123, 124]. Similar indications were also found in the 200 A·GeV/c S beam systems [30]. Indications of a flattening of the low transverse momentum part $m_t < 0.2$ GeV/c^2 of the transverse mass spectra are visible for the $2.2 < y < 2.8$ rapidities. Such a flattening is consistent with the presence of a collective transverse flow component in the dynamic evolution of the system before freeze-out. Note that if the spectra are not purely thermal, *i.e.* like in the presence of collective transverse

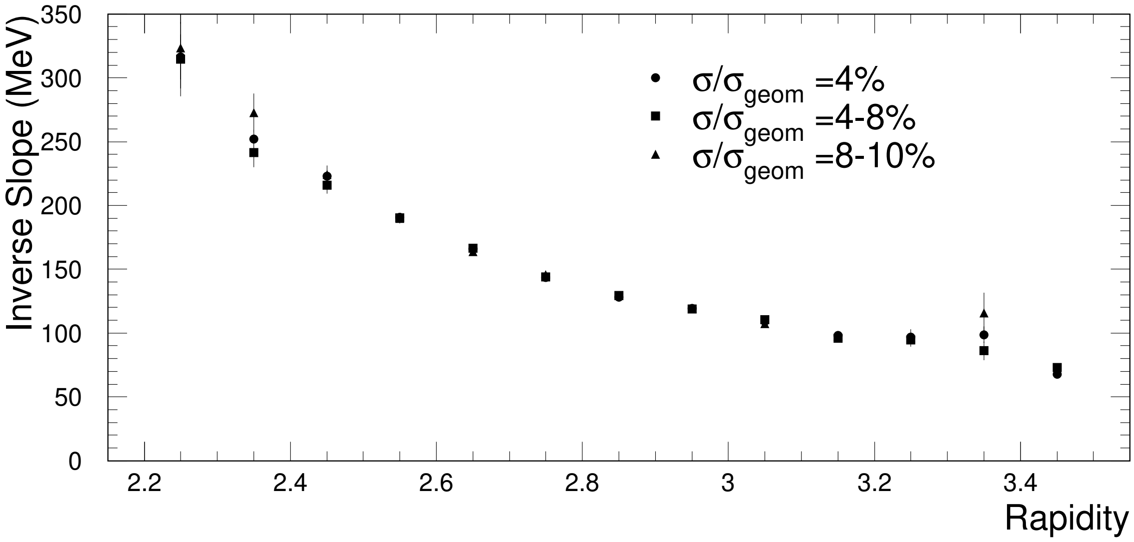

Figure 6.12: Protons inverse slope parameters deduced from fits to the proton m_t spectra for Au+Au collisions for three centrality intervals.

flow, the measured inverse slope parameter will depend on the section of the spectra that is fitted. In our case, the extent of the data is limited by the acceptance of the spectrometer. The inverse slope parameters that are obtained at rapidity values of $y < 2.7$ cannot be directly interpreted as being Boltzmann temperatures. This effect was taken into account when comparing the RQMD results (squares in figures 6.9, 6.10 and 6.11) by fitting the calculated spectra over the same range used for the data. The overall rapidity dependence is well reproduced although the results from the calculation are systematically lower than the experimental values by about 20 to 30 MeV. This is an indication that the model's effective collective transverse flow component is too small.

The inverse slope parameters measured over the three centrality intervals are summarized in figure 6.12. The T_B values are found to vary minimaly over the centrality range covered here.

The measured proton rapidity distributions dN/dy for the three different cen-

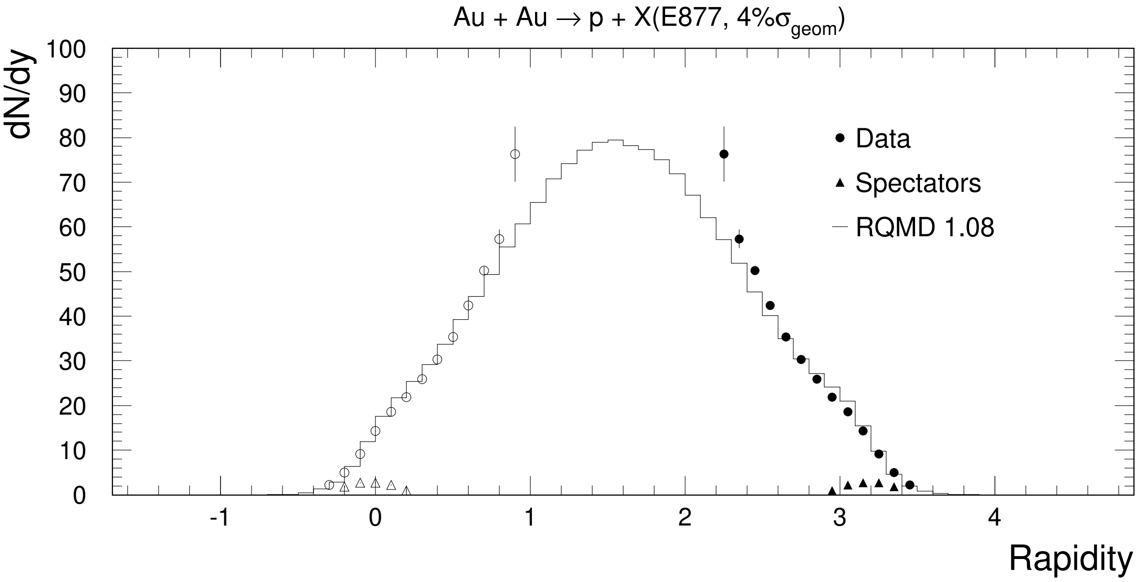

Figure 6.13: Proton rapidity distribution in Au+Au for the $\sigma_{\rm top}/\sigma_{\rm geom} = 4\%$ centrality interval. The data (solid symbols) are reflected (open symbols) about mid-rapidity. The histogram are the results of a RQMD calculation.

trality intervals are presented in figures 6.13, 6.14 and 6.15. The distributions are obtained by integrating the transverse mass spectra where data are available and extrapolating to infinity using the thermal component of the Boltzmann fits (C_B and T_B). The integrals of the *spectator* contributions (triangles) are found to contribute minimaly to the measured rapidity distributions. The *spectator* protons contributions integrate to an average of about 2 *spectator* protons (including target and projectile spectators) for the most central interval $\sigma_{\rm top}/\sigma_{\rm geom} = 4\%$.

The overlaid histograms are the results from RQMD 1.08 calculations computed by simple integration of all the produced protons. The width and shape of the rapidity distributions is well reproduced down to y $\approx$ 2.6. The calculation exhibits a structure attributed to *spectators* at beam and target rapidities that becomes significantly larger than those measured at lower centralities. These structures include protons that originate from the dissociation of spectators that are treated as unbound by

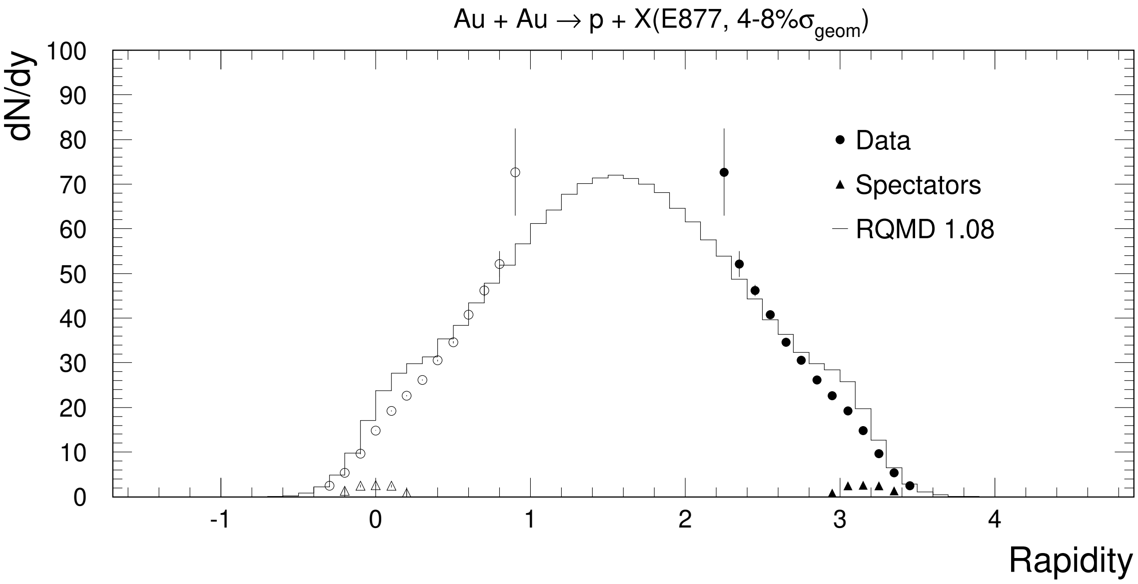

Figure 6.14: Proton rapidity distribution in Au+Au for the $\sigma_{\rm top}/\sigma_{\rm geom} = 4-8\%$ centrality interval. The data (solid symbols) are reflected (open symbols) about mid-rapidity. The histogram are the results of a RQMD calculation.

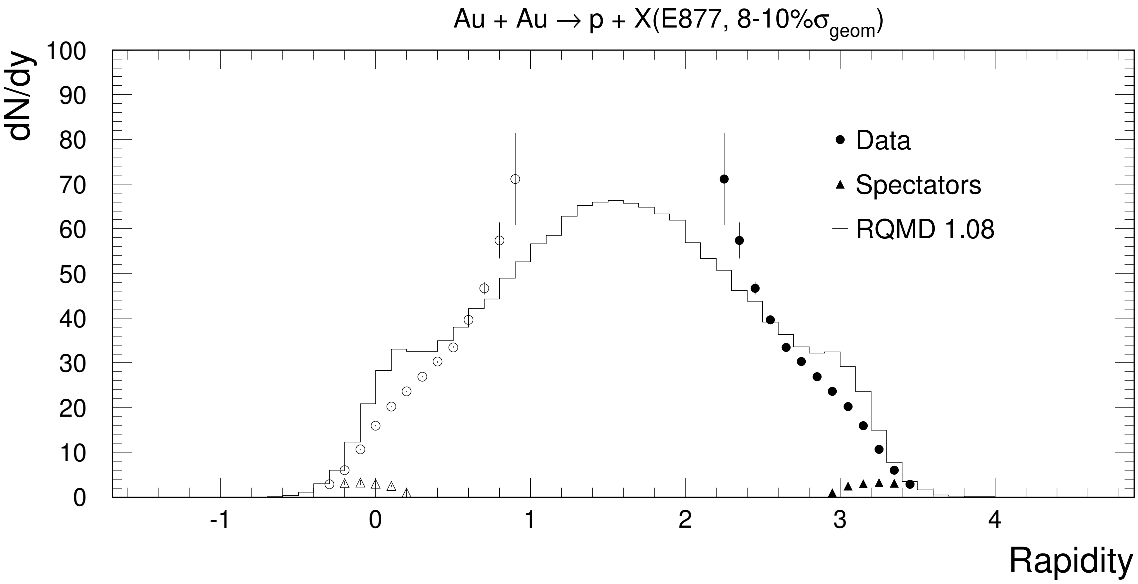

Figure 6.15: Proton rapidity distribution in Au+Au for the $\sigma_{\rm top}/\sigma_{\rm geom} = 8-10\%$ centrality interval. The data (solid symbols) are reflected (open symbols) about mid-rapidity. The histogram are the results of a RQMD calculation.

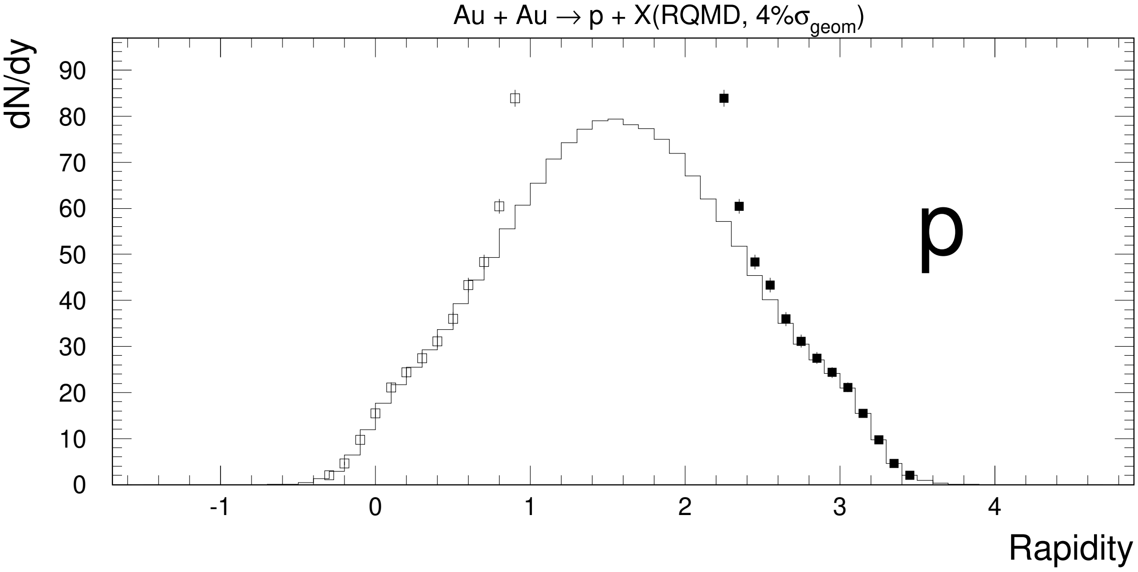

Figure 6.16: RQMD 1.08 extrapolated proton rapidity distribution for the $\sigma_{\mathrm{top}}/\sigma_{\mathrm{geom}} = 4\%$ centrality interval. The extrapolated RQMD calculation (solid symbols) are reflected (open symbols) about mid-rapidity. The histogram is the result of a simple integration of the RQMD calculation.

RQMD. As the calculation is performed for less central interactions, the spectator treatment discrepancies grow larger along with the number of spectators.

The apparent discrepancies between the data and the calculation close to mid-rapidities are attributed to the unreliability of the data extrapolation in that rapidity domain. The result of applying the same extrapolation procedure to the calculated spectra is shown in figure 6.16. The RQMD dN/dy values extrapolated (squares) from the calculated spectra are obtained using the procedure used to extrapolate the data to large transverse mass values over identical ranges in transverse mass. The extrapolation procedure is found to give reliable results down to rapidity values of y ≈ 2.5. At lower rapidities, the limited measured range and the non-thermal shape of the spectra tend to overestimate the actual dN/dy value.

Although the amount of stopping was already shown to be high in Si+Al [50,

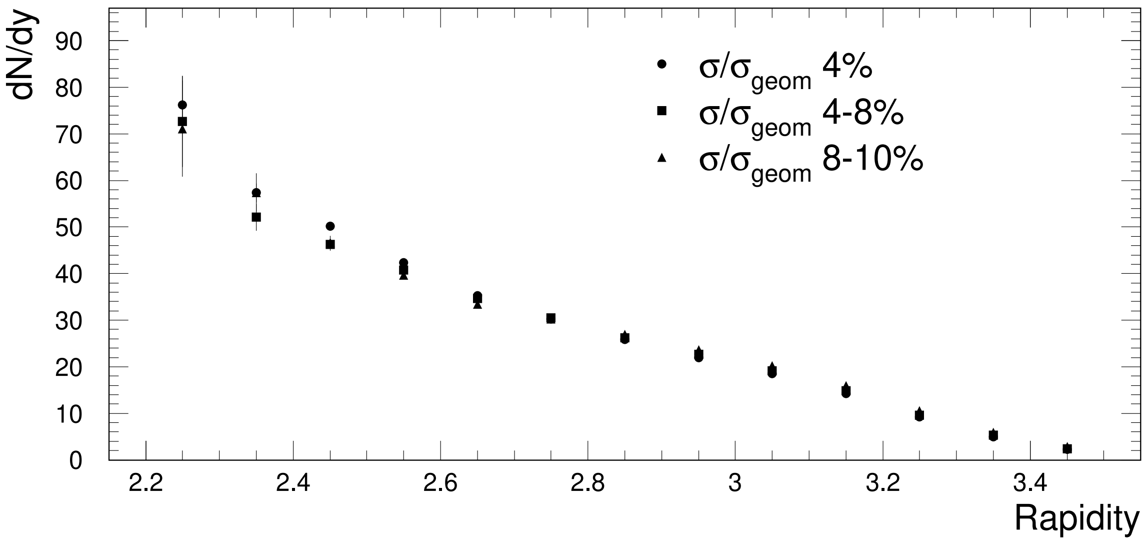

Figure 6.17: Proton rapidity distributions in Au+Au collisions for three centrality intervals.

125], the narrower proton rapidity distributions measured in Au+Au indicate that an even larger amount of stopping is involved [42, 126]. This is understood as being a consequence of the smaller surface to volume ratio and increased average number of rescattering inside the Au+Au system. This interpretation is supported by the fact that the results from the RQMD calculations reproduce both the Si+Al [122] and Au+Au rapidity distribution widths.

The proton rapidity distribution data are summarized in figure 6.17 where all three centrality data sets are overlaid. The proton yields are fairly similar over the considered centrality intervals. The 4% centrality proton yield is higher at low rapidities, consistent with a larger number of participants. The 8-10% centrality proton yield is somewhat higher at beam rapidities consistent with an increased fraction of spectator protons.

6.2.2 Pion spectra

Pions are produced copiously at AGS energies. Because of their small masses and large cross section for interaction in nuclear matter they are expected to thermalize easily. Furthermore, their spectra are not as affected as those of heavier particles by a collective flow effects and thus are a better probe for studying thermal properties of the fireball at freeze-out.

The pion m_t spectra measured in the centrality intervals of $\sigma_{top}/\sigma_{geom}$ = 4, 4-8, 8-10% are presented as a function of rapidity in figures 6.18, to 6.20. The pion data extend to 0.8 GeV/c^2 in $m_t - m_\pi$ and cover the rapidities 2.8 to 4.5. The spectra are found to have thermal shapes with increasing inverse slope values as one approaches center-of-mass rapidities. The lower portion of the pion transverse mass distributions shows a large increase over a simple exponential similar to that of in p+p collisions at the same energies. These effects were also observed in 1 to 2 A·GeV/c Au+Au [127], in Si+Al at 14 A·GeV/c [29] and in the S+S and O+Au at 200 A·GeV/c systems [128, 129, 130]. The origin of this enhancement has generally been attributed to pions originating from Δ resonances [29, 131, 132].

The data are compared to results from RQMD 1.08 calculations (histograms). In contrast to the proton data presented above, the model reproduces very well all of the features of the data over all rapidities and centrality intervals. The rapidity dependence of the shape of the spectra and the magnitude of low p_t enhancements attributed to resonance decay pions are well predicted. The calculation slightly overestimates the yield of negative pions especially at high rapidities.

In order to extract the pion dN/dy rapidity distributions, exponential functions are fitted to the data above $m_t - m_\pi > 0.2$ GeV/c^2 in the rapidity bins where available ($2.8 < y < 3.5$ for π^+ and $2.8 < y < 4.0$ for π^-) and starting from $m_t - m_\pi = 0$ GeV/c^2 at higher rapidities. The rapidity distributions of pions are then

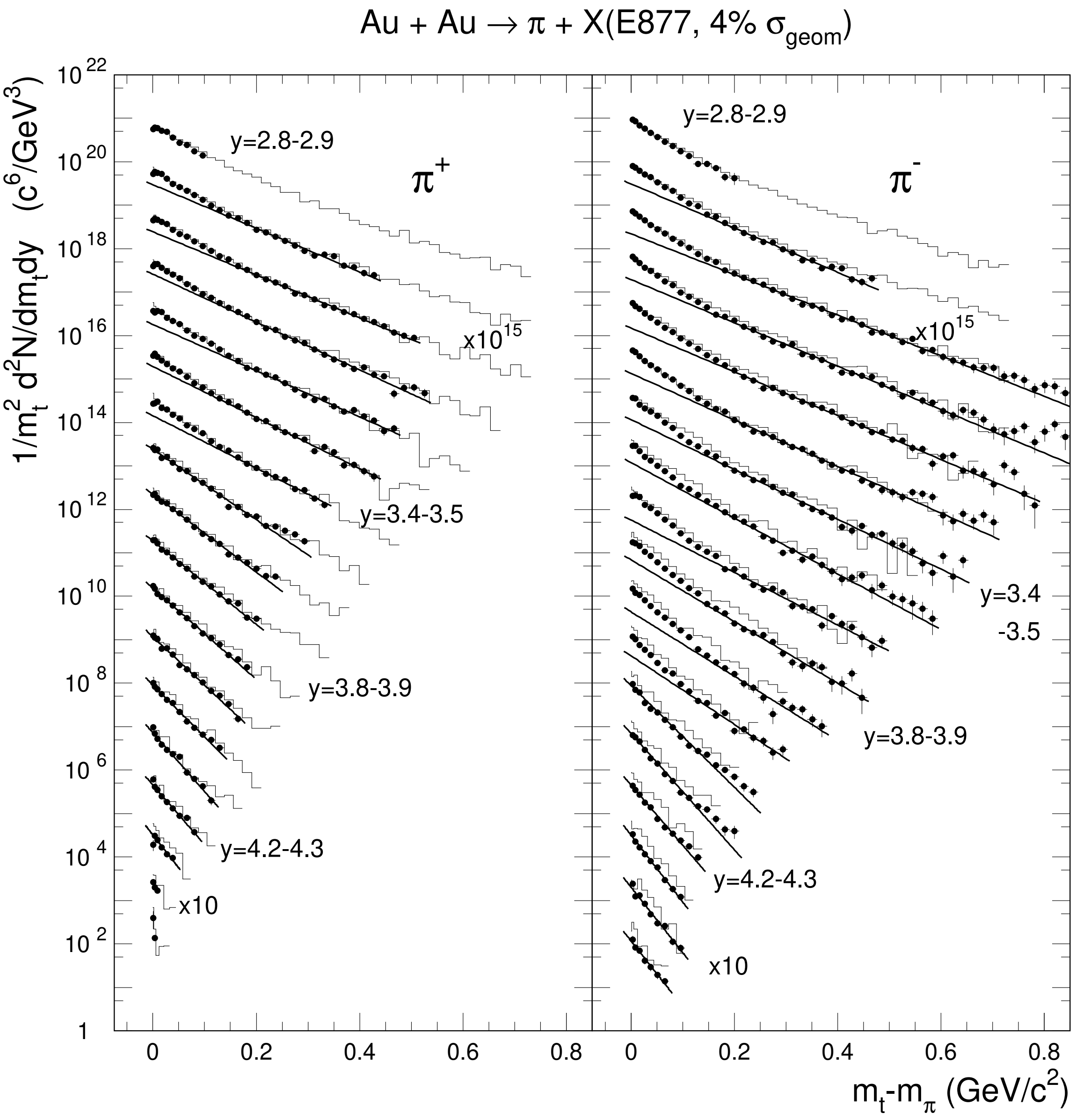

Figure 6.18: π transverse mass spectra for $\sigma_{\rm top}/\sigma_{\rm geom} = 4\%$ in p_t bins of 20 Mev, and y bins of 0.1 units of rapidity. Beginning with y=4.4-4.5, the spectra in each successively lower y bin have been multiplied by successively increasing powers of ten. Full lines are the results of Boltzmann fits to the data. The histograms are RQMD predictions.

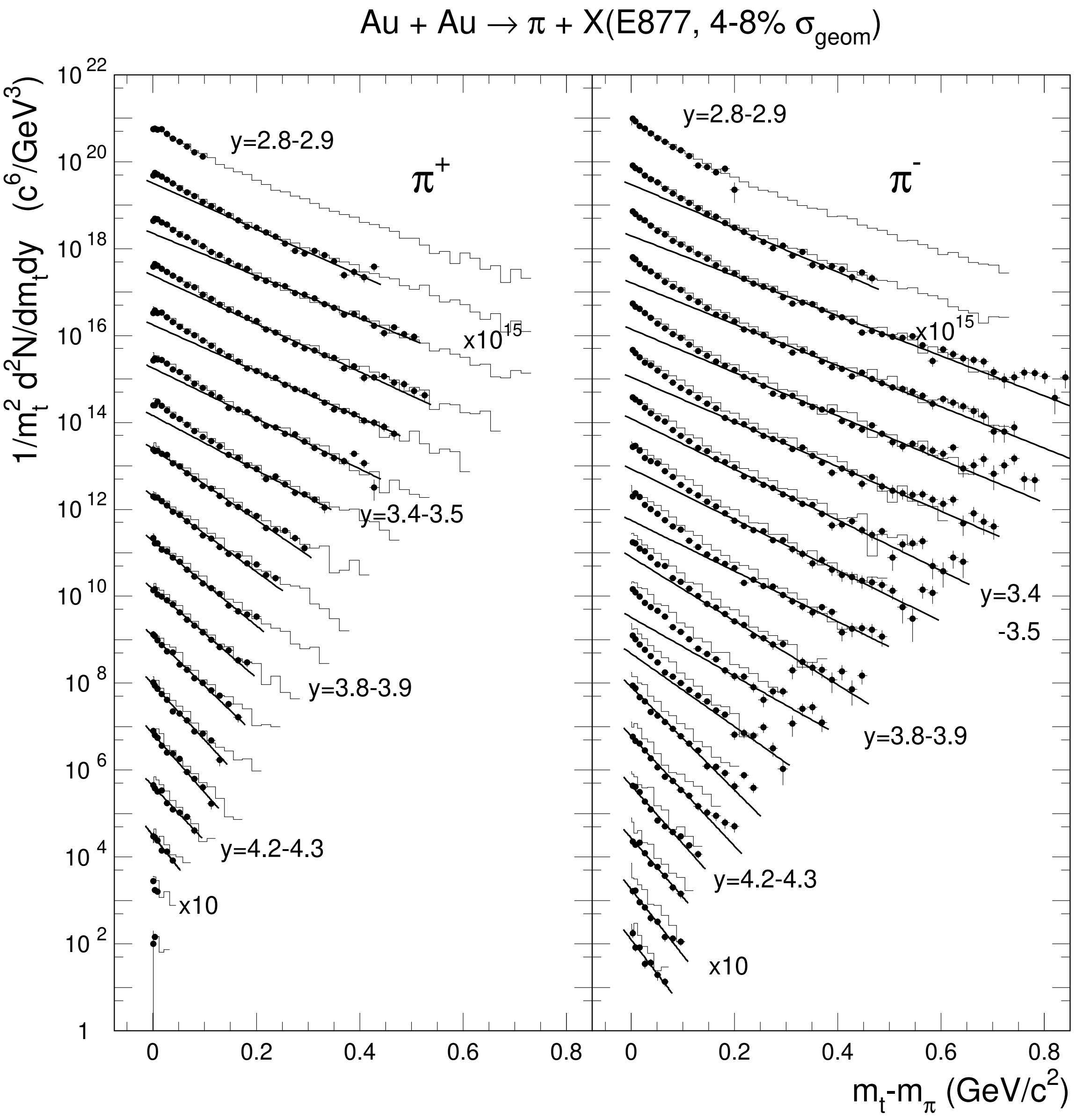

Figure 6.19: π transverse mass spectra for $\sigma_{\mathrm{top}}/\sigma_{\mathrm{geom}} = 4 - 8\%$ in $\mathrm{p_t}$ bins of 20 Mev, and y bins of 0.1 units of rapidity. Beginning with y=4.4-4.5, the spectra in each successively lower y bin have been multiplied by successively increasing powers of ten. Full lines are the results of Boltzmann fits to the data. The histograms are RQMD predictions.

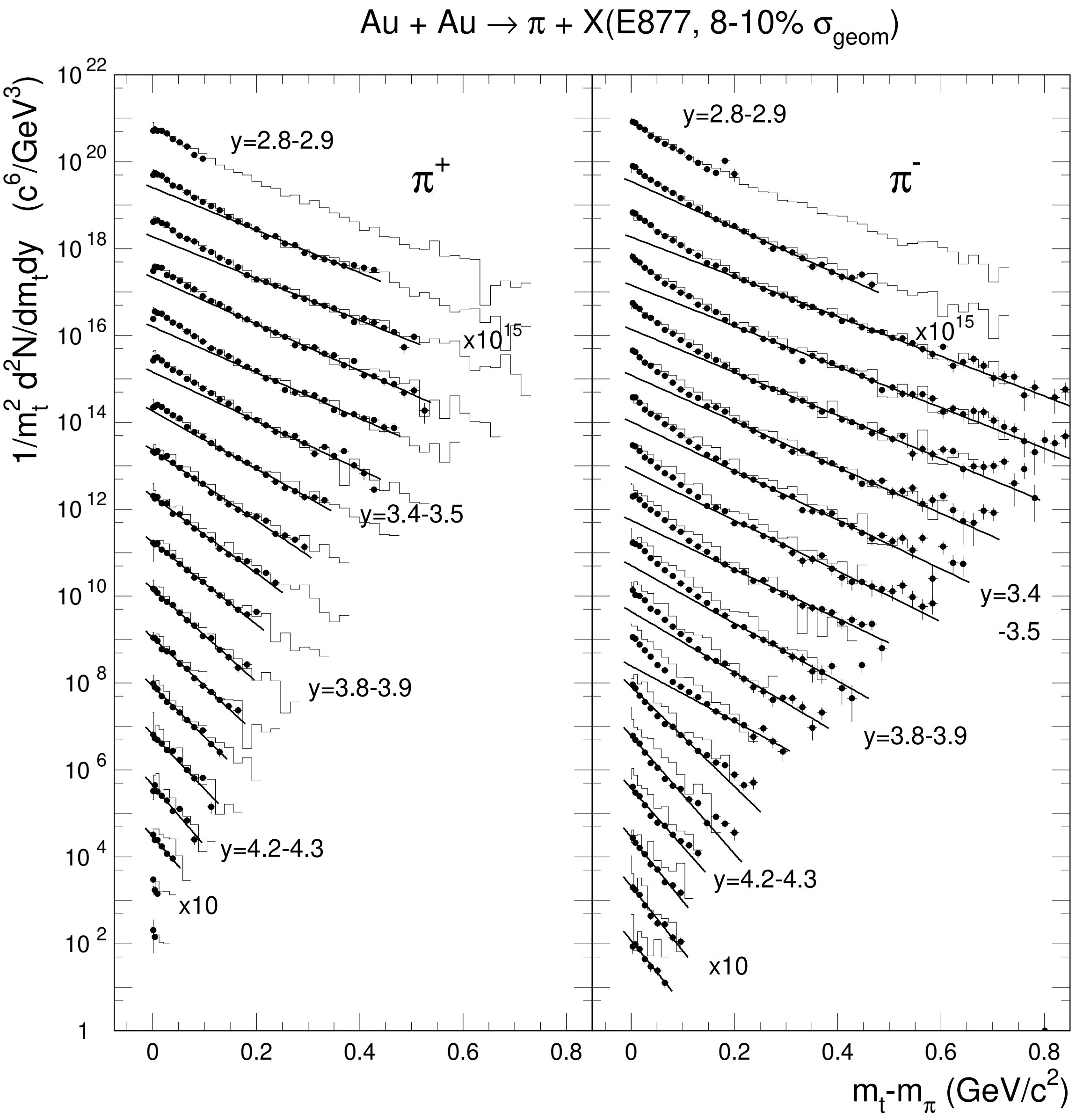

Figure 6.20: π transverse mass spectra for $\sigma_{\rm top}/\sigma_{\rm geom} = 8 - 10\%$ in $\rm p_t$ bins of 20 Mev, and y bins of 0.1 units of rapidity. Beginning with y=4.4-4.5, the spectra in each successively lower y bin have been multiplied by successively increasing powers of ten. Full lines are the results of Boltzmann fits to the data. The histograms are RQMD predictions.

obtained by integrating the transverse mass spectra data and using the results from the exponential fits to extrapolate to infinity. The resulting rapidity distributions are presented in figures 6.21, 6.22 and 6.23, where they are compared to results from an RQMD 1.08 calculation (histograms). The non-exponential shape of the measured pion m_t spectra and the limited coverage in m_t introduce systematic error in the deduced values of dN/dy. This is especially important for the rapidity bins above $y = 3.8$ since the fits are performed on the regions of the spectra that are dominated by pions originating from resonance decay and that have lower inverse slopes.

The shape of the rapidity distribution is very well reproduced over the entire range in rapidity and as a function of centrality. A similar agreement was also observed for the Si+A systems [120, 133]. The quality of the agreement in the tail of the distribution is better visualized in figure 6.24 where the same distributions as in figure 6.21 are shown on a logarithmic scale. The yields of both the positive and negative pions are systematically overpredicted by the RQMD 1.08 model by about 10 to 20%. Additionally, the negative pion yield overprediction seems to be slightly larger than that of the positive pion.

Close inspection of the pions transverse mass spectra shown in figure 6.18, reveals that the deviations from pure exponentials are systematically larger for π^- than for π^+. An obvious difference between the two types of pions is their respective Coulomb interactions with the positively charged fireball. In the following section, we will discuss if such a Coulomb effect can describe the observed difference between the π^+ and π^- spectra.

6.2.3 Coulomb distortion of pion spectra

Anomalously large π^-/π^+ ratios were first observed in low energy proton experiments [134, 135] and were since reported to be of importance at all energy scales.

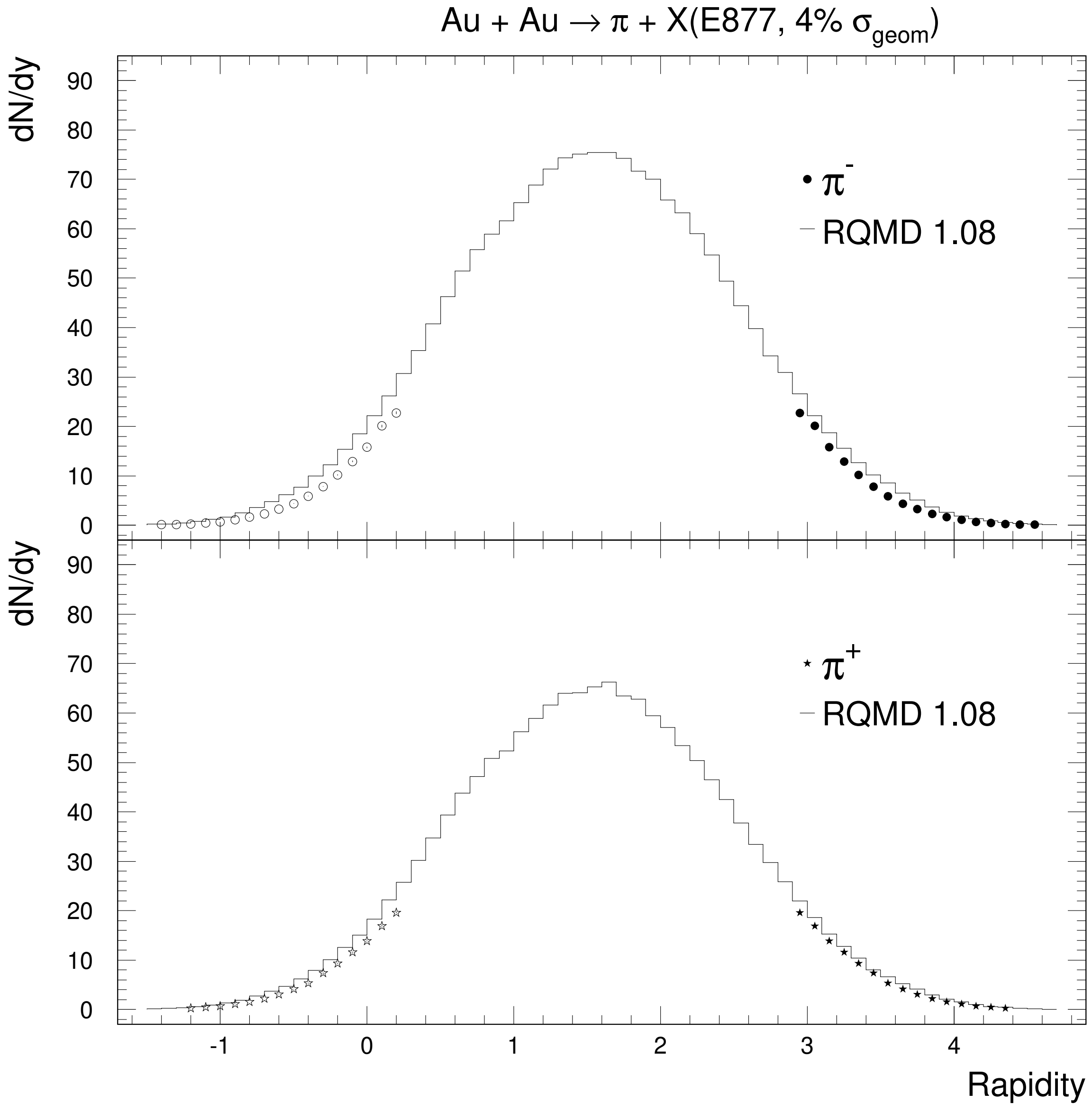

Figure 6.21: π rapidity distributions for $\sigma_{\mathrm{top}}/\sigma_{\mathrm{geom}}$=4%. The data (solid symbols) are reflected (open symbols) about mid-rapidity. The histograms result from RQMD calculations

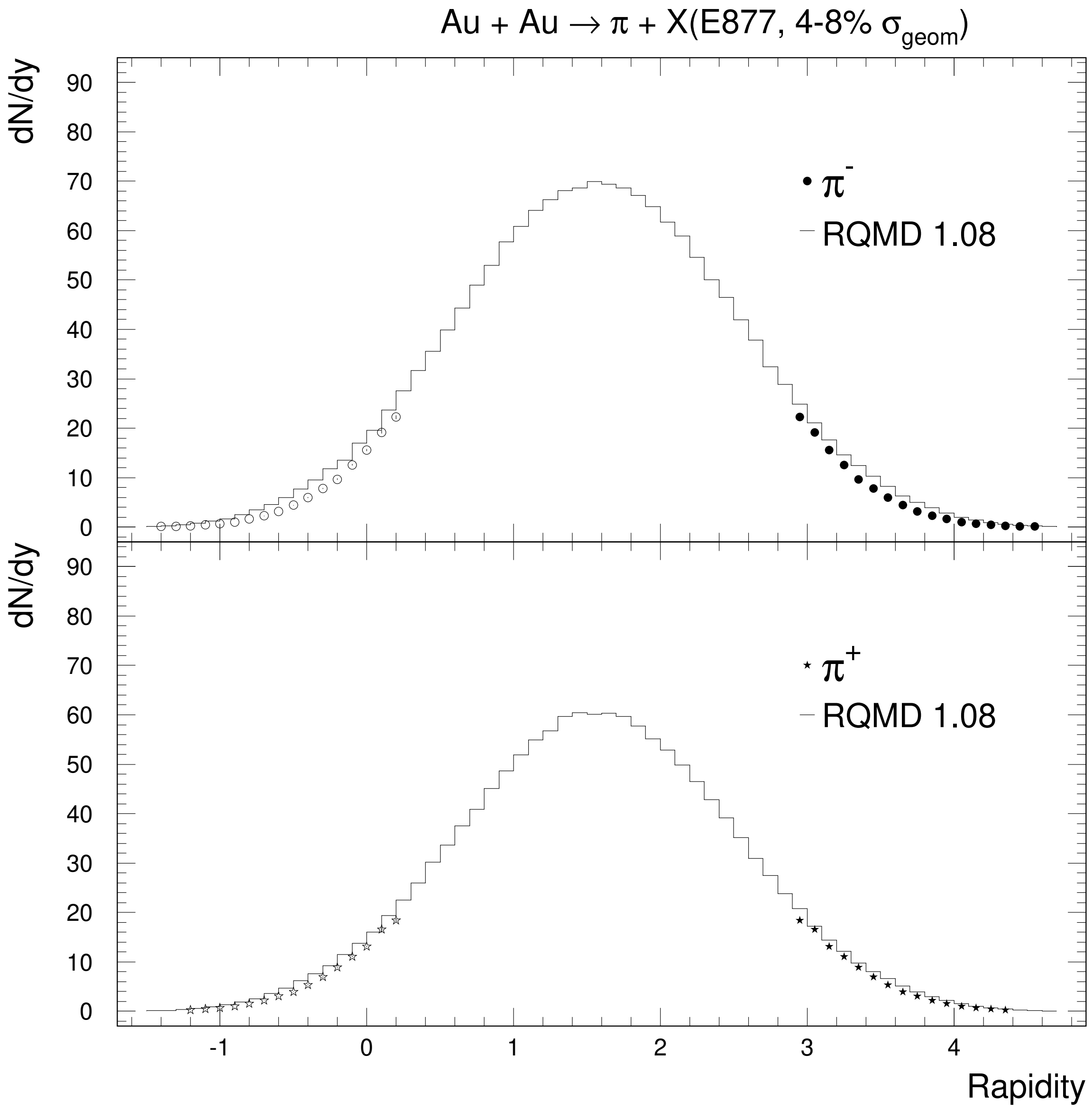

Figure 6.22: π rapidity distributions for $\sigma_{\mathrm{top}}/\sigma_{\mathrm{geom}}$=4-8%. The data (solid symbols) are reflected (open symbols) about mid-rapidity. The histograms result from RQMD calculations

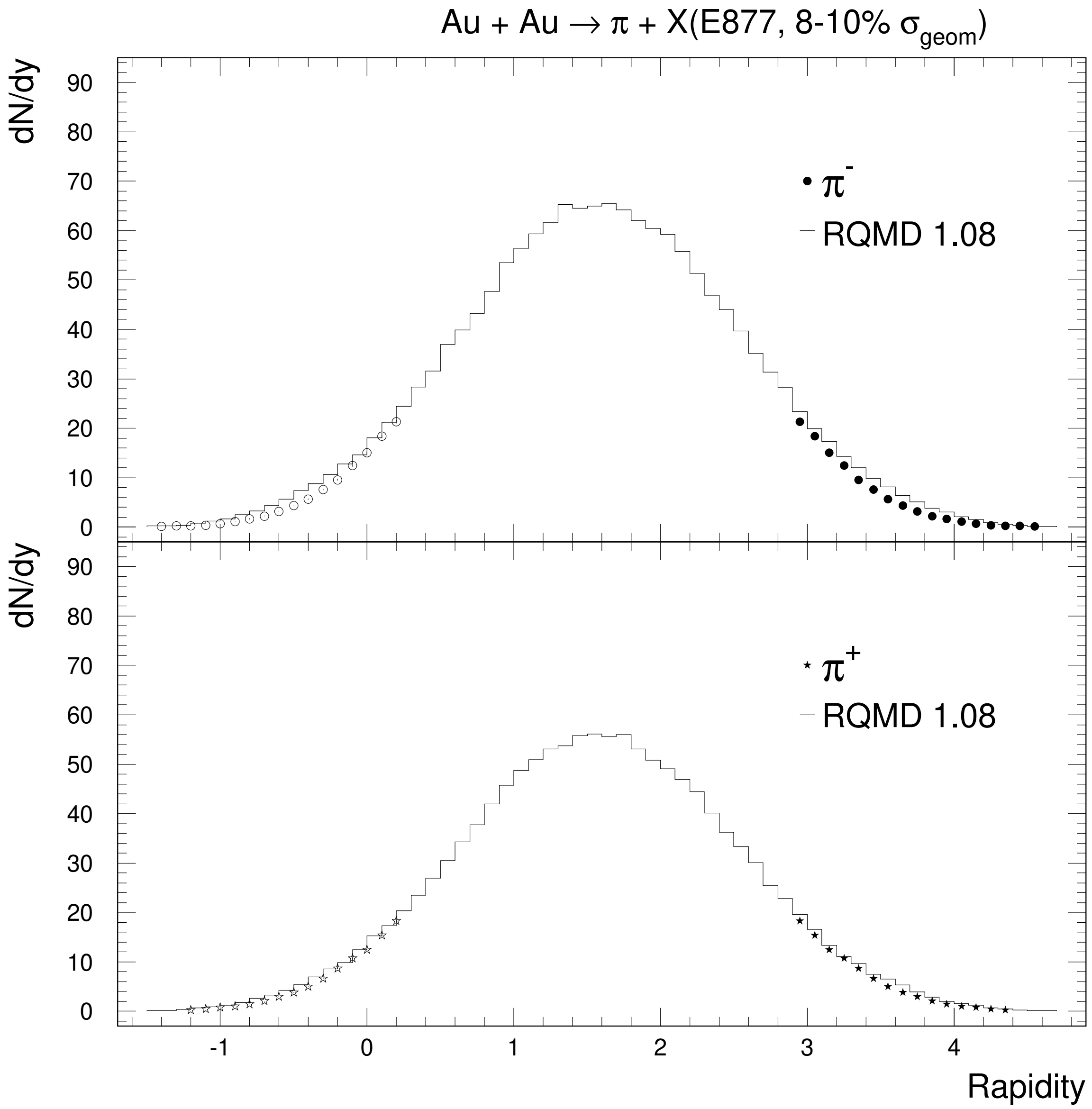

Figure 6.23: π rapidity distributions for $\sigma_{\mathrm{top}}/\sigma_{\mathrm{geom}}$=8-10%. The data (solid symbols) are reflected (open symbols) about mid-rapidity. The histograms result from RQMD calculations

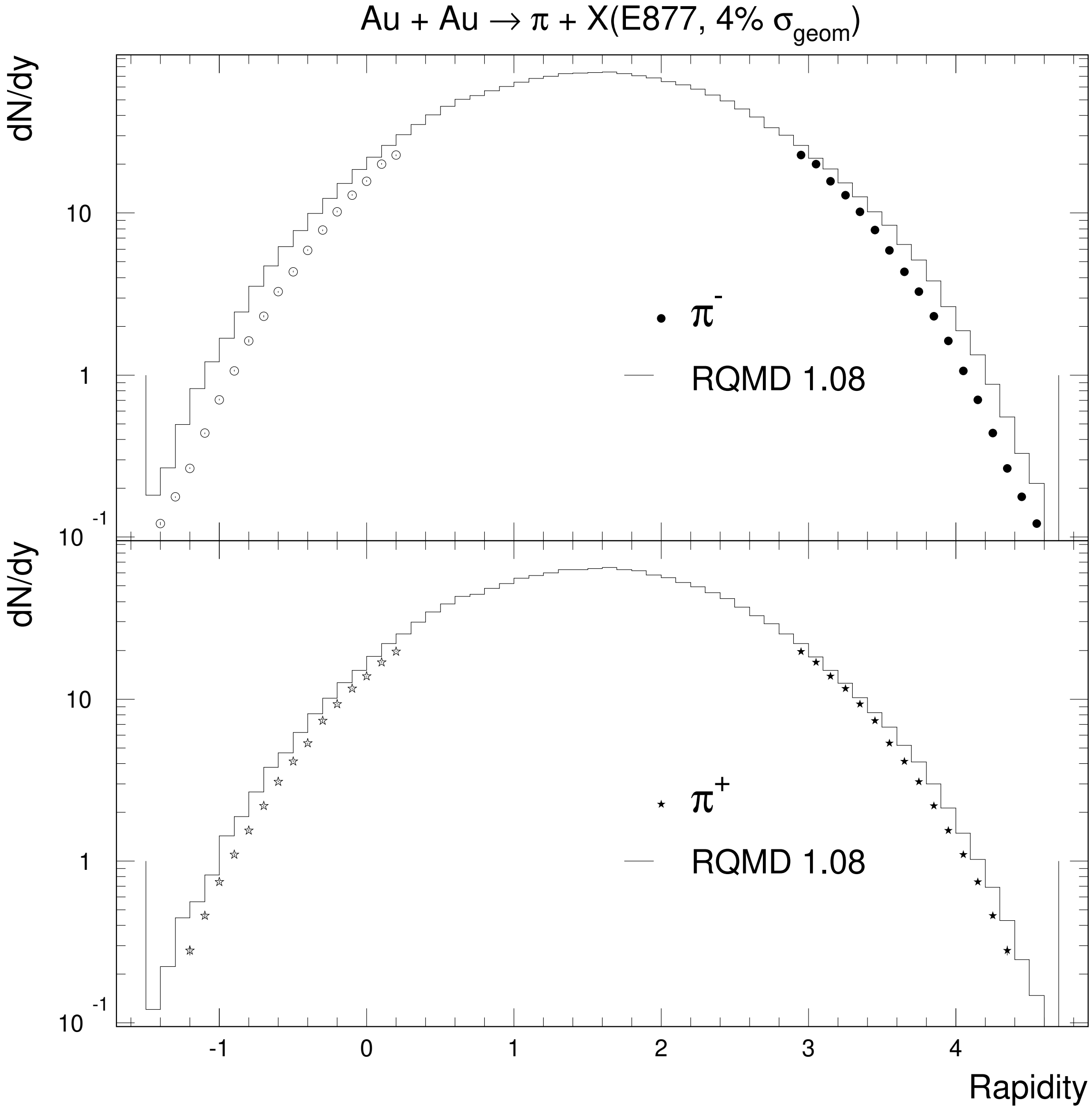

Figure 6.24: Pion rapidity distribution in Au+Au ($\sigma_{\rm top}/\sigma_{\rm geom}$=4%) plotted on a logarithmic scale. The data (solid symbols) are reflected (open symbols) about mid-rapidity. The histograms result from RQMD calculations.

These large ratios of pions were attributed to Coulomb interactions [136]. Medium modifications of the particle spectra in heavier systems have been discussed theoretically since 1979 [137, 138]. The first experimental demonstration of their importance in heavy systems was made in reactions induced by 125 to 400 MeV/nucleon Ne particles [139, 140]. The presence of Coulomb effects was also observed at the intermediate energies of $\sim$ 1 to 2 A·GeV/c [141, 142, 143]. More recently, the effects of the Coulomb potential have been studied in heavy systems at 1 A·GeV/c [144] and have been shown to still be present at 200 A·GeV/c [145, 146]. The Coulomb distortions have also been studied as function of the mass of the system at 800A MeV/c [142] and 200 A·GeV/c [147].

At the AGS, the first evidence of Coulomb effects in heavy systems was reported in 1993 [42, 148]. Since then, the distortion of the pion transverse momentum spectra ratios have been mapped as a function of centrality [149] and rapidity [126]. The pion spectra charge asymmetry is best shown by plotting the ratio of π^- to π^+ spectra as a function of transverse momentum as is presented in the top row of figure 6.25. In order to improve statistical error on the ratio, the data were divided into three large rapidity bins. The measured π^-/π^+ ratios are consistent with unity at large transverse mass values. A strong asymmetry is observed starting at $\mathrm{m_t} - \mathrm{m}_\pi = 0.2$ GeV/c^2 with a maximum value of about 1.5 at $\mathrm{m_t} - \mathrm{m}_\pi = 0$ GeV/c^2 for the $\mathrm{y} = 2.9 - 3.2$ rapidity bin. The asymmetry systematically decreases as one goes to higher rapidity.

The measured ratio is very sensitive to systematic errors since π^+ and π^- of similar rapidity and transverse mass occupy different sections of the spectrometer. The systematic error on the shape of the pion spectra and thus the measured π^-/π^+ ratio can be estimated from figure 6.26. The ratio of the π^+ (top) and π^- spectra (bottom) measured with the two opposite spectrometer magnetic fields (respectively called A and B) are plotted for three rapidity intervals. The ratios of pions measured in each field configuration are found to be consistent with flat distributions for both

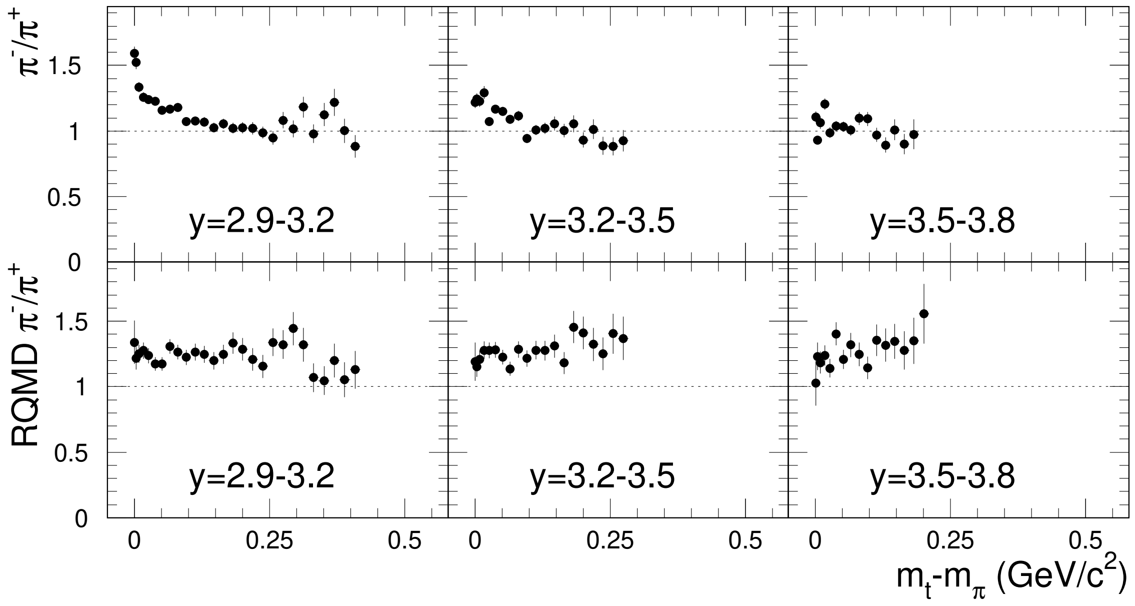

Figure 6.25: Top: measured π^-/π^+ ratio in three rapidity intervals. Bottom: corresponding results from a RQMD 1.08 calculation of the π^-/π^+ ratios.

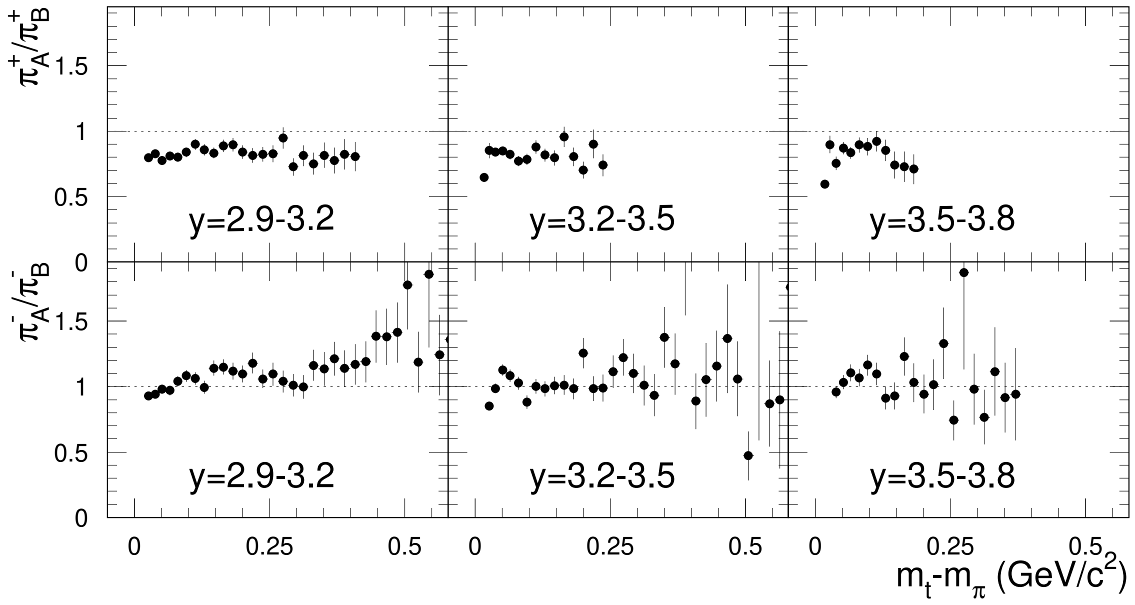

Figure 6.26: Ratios of pion spectra in A and B spectrometer field settings for π^+ (top) and π^- (bottom) measured in three rapidity intervals.

positive and negative pions. Although a slight inconsistency between the absolute normalizations of each field setting for positive pions remains, the shape of the charge asymmetry can not be attributed to a systematic spectrometer bias.

The results from a RQMD 1.08 calculation are shown in figure 6.25. Since the model does not account for final-state interactions of the thermalized products, it is expected to produce m_t and y independent pion ratios. The ratio of calculated spectra are indeed consistent with flat distributions with an overall excess of negative pions of about 20%.

A simple model of the pion Coulomb distortion

We use a simple model to study if the observed magnitude of the rapidity dependence of the π^-/π^+ ratio can be explained by the Coulomb interaction. The model is built along the line of what is presented in [150]. It uses an effective central Coulomb potential to simplify the difficult many-body problem.

Assuming that the *fireball* is at rest and neglecting its time evolution, the effective Coulomb potential V_C seen by a singly-charged test particle is given

$$V_C = \frac{Z_{\text{eff}}}{r_i} \cdot \frac{e^2}{4\pi\epsilon_\circ} \tag{6.3}$$

where the effective charge $Z_{\text{eff}} < Z_A + Z_B$ is expected to be smaller than the total charge present in $A+B$ collisions and r_i is the radius at which the particle leaves the fireball. After exiting from the Coulomb potential well, the measured energy $E(p)$ of a test particle of positive/negative charge becomes

$$E(p) = E(p_i) \pm \frac{Z_{\text{eff}} e^2}{r_a}. \tag{6.4}$$

where p_i and r_a are the initial momentum and position at freeze-out. The number of particles per unit of momentum is then expressed as

$$n(p) = n(p_i)\frac{d^3 p_i}{d^3 p} = \frac{p_i E(p_i)}{p E(p)} n(p_i) \tag{6.5}$$

where $n(p_i)$ is the initial particle distribution and the d^3p_i/d^3p Jacobian deduced from energy conservation [138]. The initial single particle distribution $n(p_i)$ is therefore changed in magnitude as well as distorted by the Coulomb field. The Coulomb field induced distortion $\mathcal{C}$ expands to

$$\mathcal{C}^{\pm} = \frac{p_i E(p_i)}{pE(p)} \tag{6.6}$$

$$= \sqrt{p^2 \mp 2E(p)V_C + V_C^2} \cdot \frac{(E(p) \mp V_C)}{pE(p)} \tag{6.7}$$

for positive/negative charge particles. The Coulomb distortion of the pion ratio is expressed in terms of measured momenta p as

$$\frac{\pi^-}{\pi^+}(p) = \mathrm{R} \cdot \frac{\mathcal{C}^-}{\mathcal{C}^+} \cdot \frac{n(p_i^-)}{n(p_i^+)} \tag{6.8}$$

$$= \mathrm{R} \cdot \frac{\sqrt{p^2 + 2E(p)V_C + V_C^2}}{\sqrt{p^2 - 2E(p)V_C + V_C^2}} \cdot \frac{(E(p) + V_C)}{(E(p) - V_C)} \cdot \frac{n(p_i^-)}{n(p_i^+)} \tag{6.9}$$

where R is an overall normalization constant. The transverse momentum and rapidity dependences are introduced by substituting $E = \mathrm{m_t}\cosh(y)$ and $p = \sqrt{(E^2 - m^2)}$. Thus, the model predicts the shape of the π^-/π^+ ratio as well as its rapidity dependence with only two free parameters: the effective Coulomb potential V_C and the normalization constant R.

The model neglects the deflection of the particle trajectories induced by the Coulomb interaction. It is assumed that the initial angle of the particle ($\mathrm{p_t}/p_z$) is conserved. Possible quantum mechanical effects are ignored and we also neglect the possible contribution from the spectators. Such a contribution has been discussed at lower energies [137, 138]. However, our analysis concerns only the most central collisions where the fraction of the total charge carried by the spectator is relatively small. The model also assumes a static effective potential that is identical for all the particles. This approximation is not valid in general. Here, we discuss mainly high rapidity pions that are in the tail of the dN/dy rapidity distribution. Thus, on the average, these pions see a relatively similar fireball at freeze out. This also justifies the non-treatment of the expansion of the fireball. These approximations are less and less valid as we approach mid-rapidity.

The non-distorted $n(p_i^{\pm})$ distributions are not accessible experimentally. In the present calculation, in agreement with the RQMD prediction, we assume that both distributions are similar. The initial spectra are generated using mean values of the parameters used in the two-exponential description of the data (see figure 6.18).

The model predictions are compared to the measured ratios of pion transverse mass spectra in figure 6.27. The predictions of the Coulomb distortion model (solid lines) are obtained from a fit to the first four measured distributions where the measured effect is the largest. The values of $V_C \sim 31 \pm 22$ MeV and R $\sim 0.92 \pm 0.14$ are found to best describe the shape and rapidity dependences of the pion ratio. These parameters are found to be still in agreement with the data at the larger rapidities. The errors on the fitted values (dotted lines) are rather large, since, as discussed below, there is a strong correlation between the effect of the normalization constant R and that of the effective Coulomb potential value.

The Coulomb induced distortion has two components: a purely Coulomb factor $\mathcal{C}^-/\mathcal{C}^+$ and an amplitude factor $n(p_i^-)/n(p_i^+)$ that is related to the shape of the initial pion spectrum. However, the magnitude of this amplitude distortion is also related to the value of the effective Coulomb potential. The effects of each of the two components are compared in figure 6.28. The two contributions are flat at large $\mathrm{m_t}$ with the Coulomb factor being slightly larger than one. At low $\mathrm{m_t}$, the two factors distort the shape of the pion ratio in a similar way, but most of the distortion is attributable to the Coulomb factor.

The effects of R and V_C can not be distinguished above transverse mass values of about 0.25 GeV/c^2 since the Coulomb distortion is rather flat and affects mainly the magnitude of the ratio. The uncertainty on the value of the R and V_C constants could

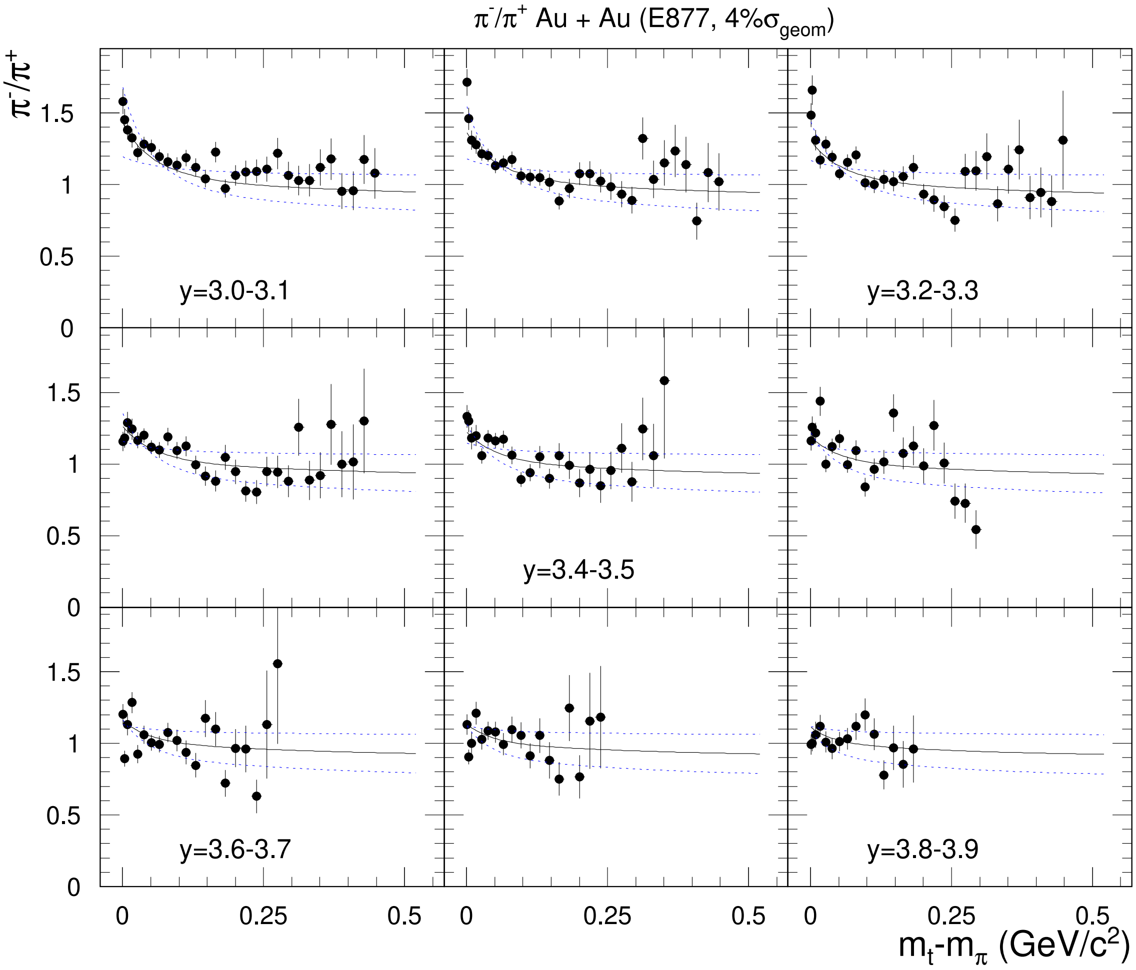

Figure 6.27: The π^-/π^+ ratio as a function of transverse mass for nine rapidity intervals. The solid line is the result from a Coulomb distortion calculation. The dotted lines show the error on the fit.

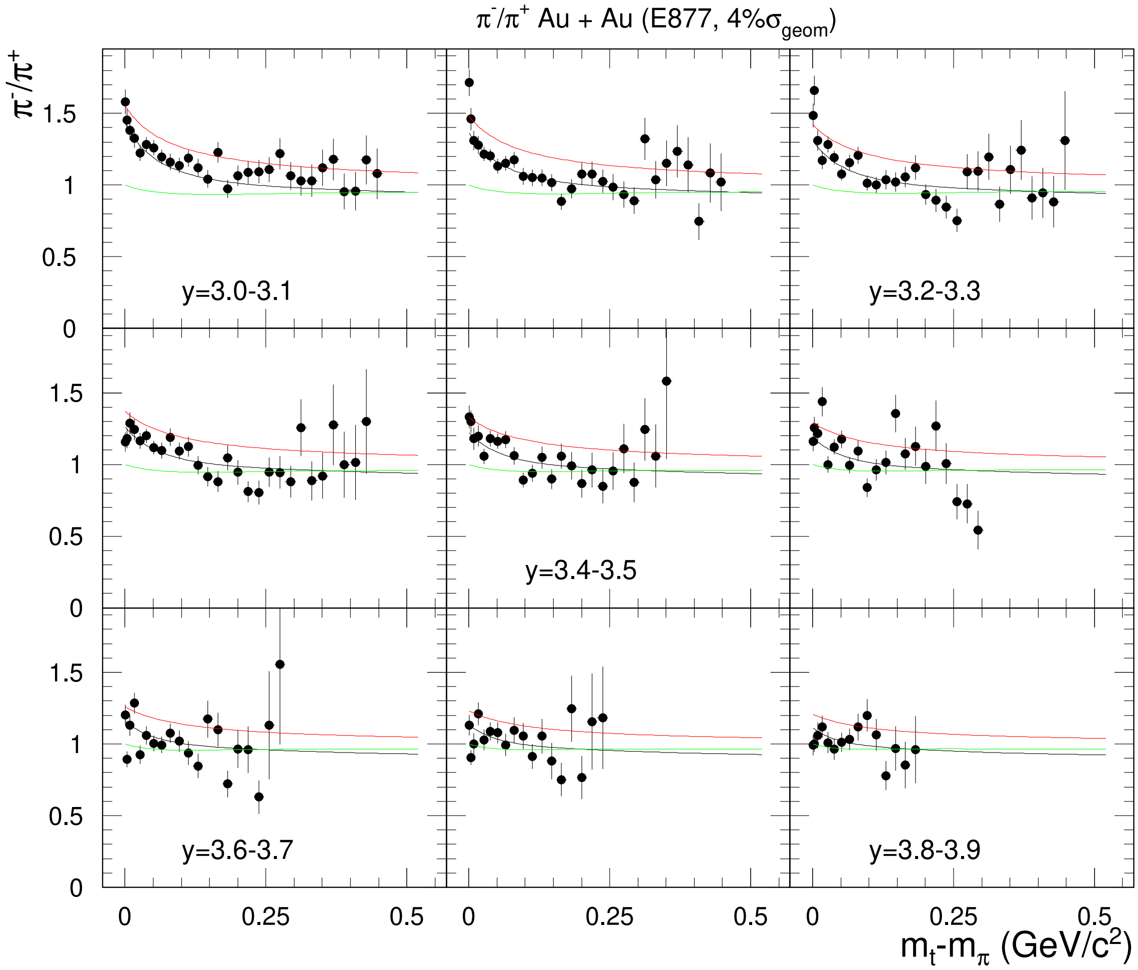

Figure 6.28: The π^-/π^+ ratio as a function of transverse mass is plotted for nine rapidity intervals. The solid line is the result from a Coulomb distortion fit. The dotted lines show effect of the Coulomb factor (dotted lines above the data) and amplitude factor (dotted lines below the data) as a function of m_t .

be greatly improved with a larger data sample, *e.g.* by providing a measurement that would extend to larger values of m_t. This would better fix the relative values of R and V_C at large m_t while the shape at low m_t would fix the magnitude of V_C. Additionally, an independent measurement of the value of R, such as 4π measurement of the pion yields, would allow to dramatically reduce the uncertainty on the value of the effective Coulomb potential.

The pion ratio in Au+Au at the AGS has also been measured at lower rapidities by the E866 collaboration. The results of our Coulomb distortion calculation are compared to these data in figure 6.29 using the parameters deduced above. The center-of-mass rapidity $y = 1.17 - 1.97$ data were presented at the Quark Matter '95 conference [148] while the data at $y = 2.1$ and $y = 2.3$ are from the Quark Matter '96 conference [110] proceedings. The model (solid curves) is found to reproduce the $y = 2.3$ data quite well with the V_C and R values obtained at beam rapidities. The model slightly overpredicts the magnitude of the distortion at $y = 2.1$ and overshoots by about 30% for the lowest rapidity bin.[2] Similar behavior, *i.e.* maximum effect in the π^-/π^+ ratio at large rapidities followed by subsequent suppression near center-of-mass momenta were also observed at the lower energies [139, 141].

Our model is based on the simple assumption that the pion spectra are distorted by static effective Coulomb potential. This assumption is reasonable at forward rapidities where the particles have large energies relative to the bulk of the *fireball*. The present result is an indication that our assumption ceases to be valid at the center-of-mass where the effective charge is expanding at a similar velocity as that of the test particles. A more detailed description of the reaction dynamics would be required to properly compute the magnitude of the effective Coulomb potential near center-of-mass rapidities. Thus, the π^-/π^+ ratio provides an additional mean,

[2] For this calculation, the amplitude factor $n(p_i^-)/n(p_i^+)$ was obtained by extrapolating the spectral shapes obtained in the present work.

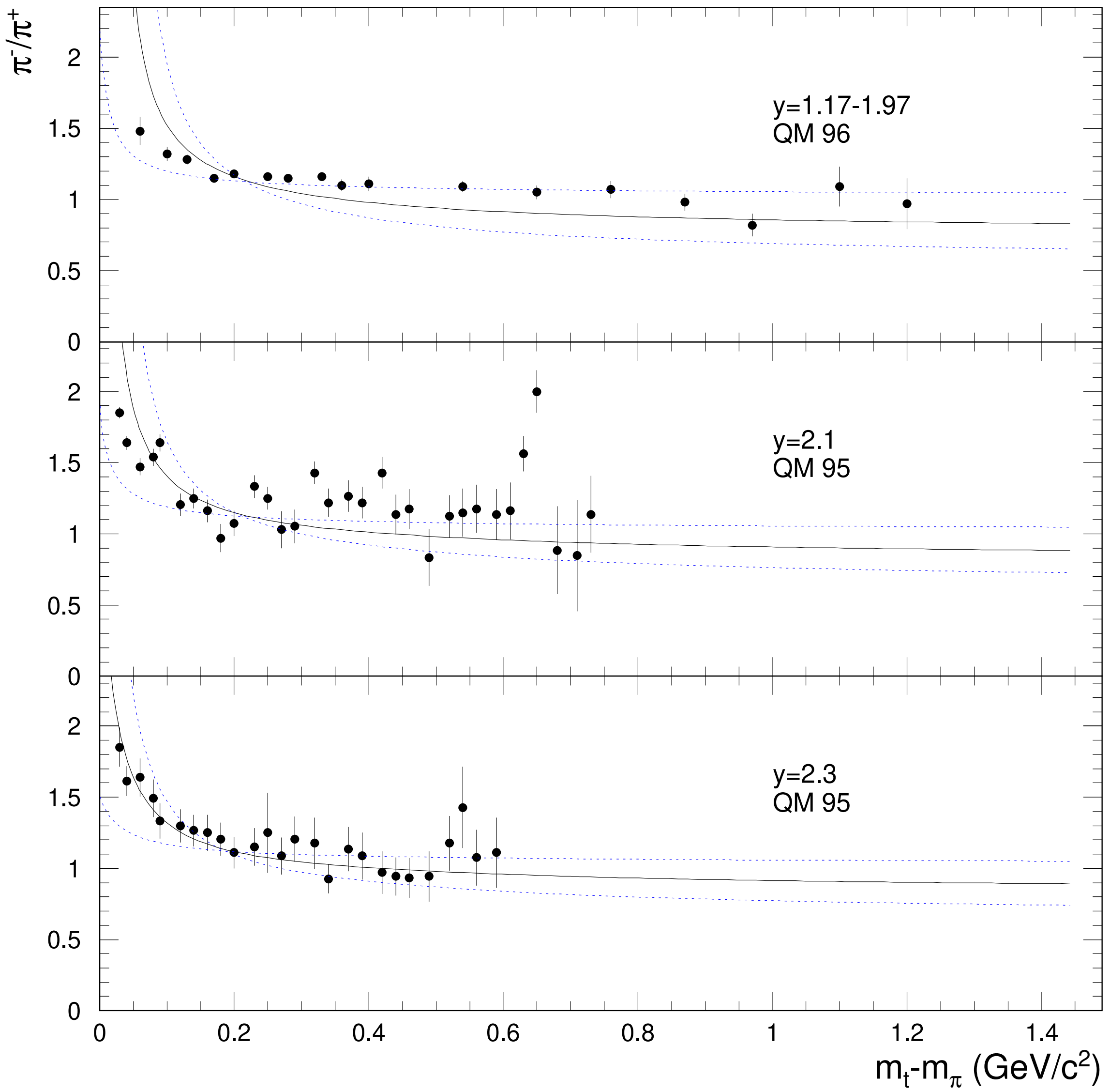

Figure 6.29: Ratios of pion transverse mass spectra measured by the E866 collaboration as presented at the 1995 and 1996 Quark Matter conferences [148, 110]. The lines are the results from our Coulomb distortion calculation performed with the parameters deduced from our measurements at high rapidity.

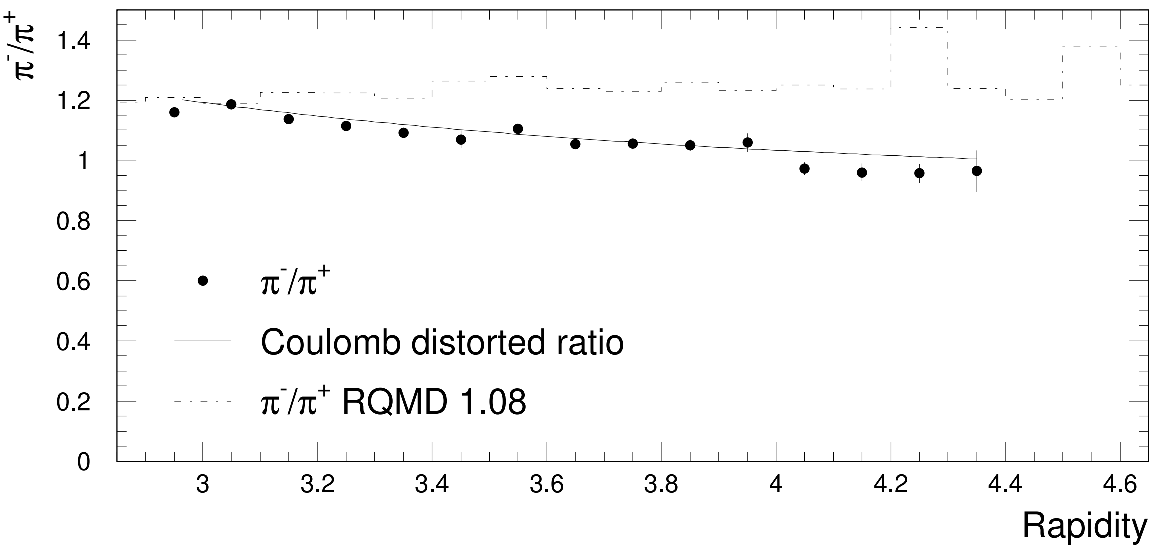

Figure 6.30: π rapidity distribution ratio $dN/d\mathrm{y}(\pi^-)/dN/d\mathrm{y}(\pi^+)$.

complementary to HBT analysis, for studying source sizes and dynamics. Such work is already being pursued [151] where the sensitivity of the π^-/π^+ ratio to the total charge, the transverse expansion velocity and the temporal and spatial extent of the source are investigated.

6.2.4 Coulomb distortion of the pion rapidity distributions

The pion rapidity distribution should also show effects of the Coulomb interaction since this interaction not only affects the transverse momentum but also the final rapidity of the emitted pions. We have shown in section 6.2.2 that the π^+ and π^- have very similar rapidity distributions reasonably well reproduced by RQMD. In figure 6.30, the ratio of the pion distribution $dN/d\mathrm{y}(\pi^-)/dN/d\mathrm{y}(\pi^+)$ is plotted as a function of rapidity. One observes that the ratio is not quite constant but shows a systematic decrease at the highest rapidities.

We have used the Coulomb distortion model developed here to determine if we can provide a consistent description of the effects observed both in the transverse mass

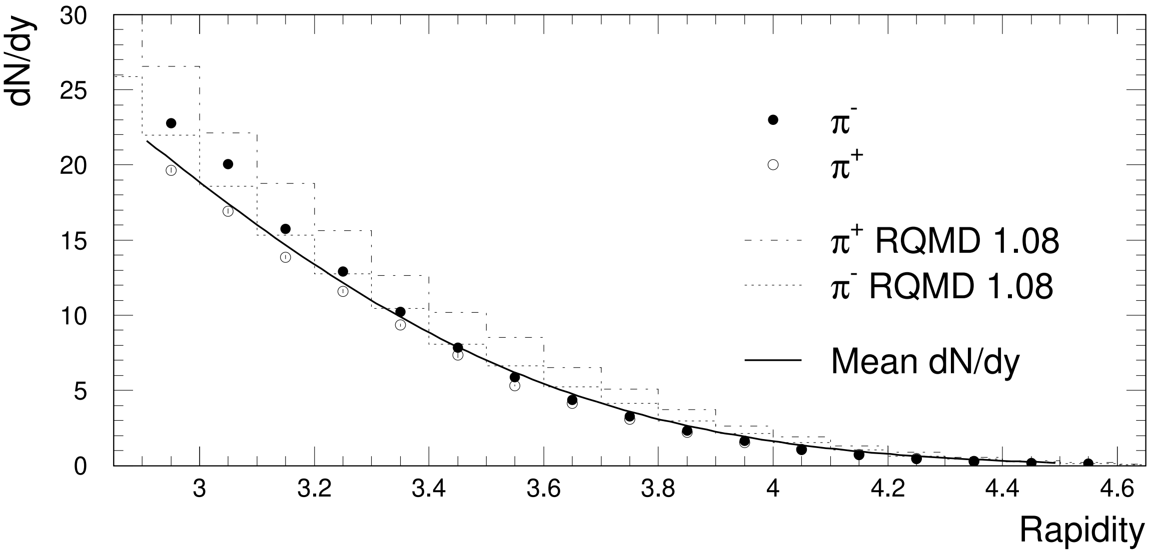

Figure 6.31: Pion dN/dy distributions. The solid line is the undistorted dN/dy distribution used as input in the model calculation.

spectra and in the rapidity dN/dy distribution. The calculated pion dN/dy ratio is obtained by integrating the calculated distorted transverse mass distribution. Since the Coulomb distortion will change the pion rapidity, the first step of the calculation consists in verifying that the integral with $V_C = 0$ lends reasonable dN/dy mean values. The undistorted calculated mean rapidity distributions of pions (solid line) are overlaid on the data in figure 6.31. The mean dN/dy is found to reproduce relatively well the average shape of the experimental dN/dy distribution.

The dN/dy ratio calculated using the parameters V_C and R from the shape of the m_t spectra is shown by the solid line in figure 6.30. The rapidity dependence of the data is very well reproduced by the model over the entire measured rapidity range. This result shows that light particle yield ratios should be interpreted with care. The effective Coulomb field in Au+Au collisions is strong enough to significantly distort the rapidity distributions of light particles *i.e.* the ratio of pion dN/dy can easily vary by more than 20% depending of the rapidity at which it is measured. Comparison of yield ratios from experiments that perform their respective measurements at different rapidities should therefore, account for the effect of the Coulomb field. It is interesting to note that the RQMD 1.08 model (dashed histogram) predicts a much flatter and slight but opposite rapidity dependence.

The effects of the two model parameters, V_C and R, on the pion dN/dy ratio are shown in figure 6.32. The values of each of the two parameters are changed simultaneously in the top figure and independently in the two lower ones. The amplitude of the rapidity dependence of the dN/dy ratio is determined by the magnitude of V_C. The effect of varying V_C is more important at the lower rapidities. The effect of R parameter is independent of rapidity and tends compensate for the change in mean dN/dy ratio from varying V_C. This correlation is responsible for the large uncertainties on the fitted values of V_C and R. The size of the error on the V_C parameter could be improved with measurements closer to the center-of-mass rapidity region. It could also be improved by independently measuring the absolute value of the R parameter, thereby fixing the forward rapidity portion of the distorted dN/dy ratio.

It is interesting to compare the expected Coulomb potential viewed by the first pions that are ejected from the fireball to the effective Coulomb parameter V_C value that was obtained with our simple model. To simplify, we use the Coulomb potential of a uniformly charged sphere as given equation 6.3. The potential is proportional to the total charge Z inside the sphere of radius R and where $e^2/4\pi\epsilon_\circ = 1.4$ MeV·fm [152]. Assuming that the reaction participants are fully stopped, the charge of the fireball is then equal to the total charge of the participants in the Au+Au reaction, thus $Z \approx 158$. Handbury-Brown-Twiss (HBT) analysis of pion correlations provide an estimate of the fireball radius. Values of R from one-dimensional HBT analysis of Au+Au central events are found to vary between $R \sim 5.5$ and 6 fm [23, 153, 154, 155]. These numbers lead to uniformly-charged-sphere Coulomb potential values of $V \sim 36$ to 41 MeV. This simple estimate is consistent with the value of $V_C = 31 \pm 22$ MeV

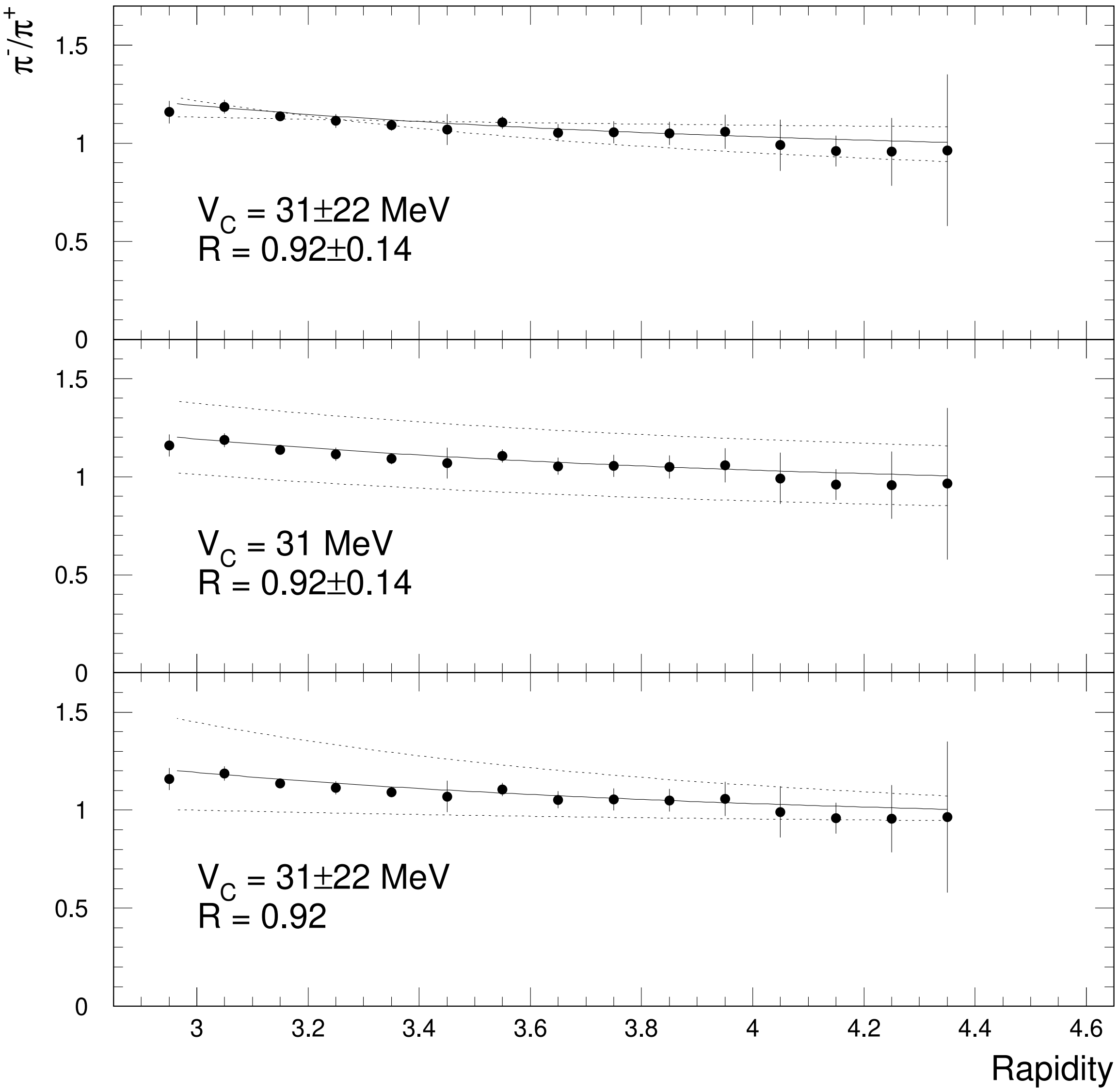

Figure 6.32: Effects of varying the parameters (dotted lines) of the calculated $dN/d\mathrm{y}(\pi^-)/dN/d\mathrm{y}(\pi^+)$ ratio (solid lines).

obtained from our simple model of the Coulomb interaction. Because not all pions see the full charge of the fireball, it is not surprising that the measured value is somewhat smaller than the one obtained from our simple estimate of the uniformly-charged-sphere Coulomb potential. The interpretation of the measured values V_C and R is complicated by the presence of radial flow and break-up time [151] and only provide a qualitative description of the effects of the Coulomb field on the measured pion transverse mass spectra.

Chapter 7

Conclusion and summary

We have studied particle production in Au+Au collisions at 10.8 A·GeV/c in terms of transverse mass, rapidity and centrality. In order to perform the necessary measurements, an existing magnetic spectrometer had to be modified. The present work includes the description of a new high-granularity time-of-flight hodoscope, with excellent time resolution. The hodoscope counters were designed to optimize light collection and thus time resolution. The use of light guides was reduced to a minimum by stacking the counters in an original fashion. A modular holding system was designed to eliminate gaps between counters and allow easy installation and maintenance of the hodoscope. A standard wrapping procedure was developed to obtain reliable and very precise positioning of the counters. A laser monitoring system was also built to allow complete detector-system fault diagnostic, even during downtime. An overall time-of-flight resolution of 85 ps was achieved, 15 ps better than the design value.

During data analysis, it was realized that the large spectrometer occupancy introduced a transverse momentum dependent particle detection inefficiency. This inefficiency was traced to the inability of detectors to reconstruct all the particle tracks that overlap within their finite spatial resolution. A method was developed to correct for the tracks that are missed while accounting for correlated losses in each detector. It proceeds by assigning a multi-detector position dependent weight to all reconstructed tracks. This inefficiency is present in any detector system that is operated in a high occupancy environment, typical in relativistic heavy-ions experiments. Therefore, such occupancy corrections may be important for the future experiments at RHIC and LHC.

We have shown, after a careful re-analysis, that the structures seen at low m_t in the preliminary kaon data presented at the Quark Matter '93 conference were caused by a background source of beam rapidity protons located at the upstream edge of the spectrometer collimator. A method was developed to remove these background protons from the kaon signal. The measured slopes remain unusually steep with large fit errors. Independent analysis of data taken in 1994 has confirmed the overall shape of the spectra and the absence of low m_t structure.

Measured proton transverse mass spectra are very well described by thermal distributions. The narrow rapidity distribution indicates that the the amount of stopping is larger than in Si+A systems. The large values of inverse slope parameters that are obtained from the proton transverse mass spectra indicate that a significant collective transverse flow components will be necessary to properly describe the dynamics of the fireball. A comparison of the data with the RQMD 1.08 model predictions shows that, after a proper treatment of the spectators, the model reproduces the overall shape of the measured transverse mass spectra. However, the predicted values of inverse slope are systematically smaller than the measured ones, indicating that the model does not have a sufficiently large collective transverse flow component. This result emphasizes that comparison of measured inverse slopes that are obtained at identical rapidity but over different transverse mass intervals should be made carefully.

The measured pion transverse mass spectra are observed to have overall thermal shapes. The lower portion of these spectra exhibit a large enhancement over simple exponential distributions. The comparison of RQMD 1.08 calculations to measured pion spectra indicates that the model reproduces the shape of the spectra very well, as it did for the lighter systems, and thus, probably describes the effective temperature of the Au+Au system. However, the calculation slightly overpredicts the negative pion yield, particularly at high rapidities.

A close inspection of the measured pion spectra reveals that the low transverse mass enhancement is systematically larger for negative pions than for positive pions. A simple model of the Coulomb interaction was developed to study the transverse mass dependence of the shape of the pion ratio over a wide range of rapidities. This simple model allowed us to understand a few important points. Firstly, it demonstrates that the low p_t enhancement of the π^-/π^+ ratio can be largely attributed to the effects of an effective Coulomb field. Secondly, the extrapolation of the model predictions to center-of-mass rapidities shows that a detailed description of the reactions dynamics is needed to properly describe the Coulomb distortion over all rapidities. More importantly, our analysis shows that the interpretation of light charged particle yields (and thus yield ratios) is complicated by the rapidity dependence introduced by the Coulomb effect. And finally, special care should be taken when experimental light particle spectra are compared to models that do not account for the interaction of the reaction products with the effective Coulomb field.

Whether the systems produced at the AGS have undergone a phase transition is still an unsettled issue. We have learned a few more details on the way to characterizing the type of media that are achieved in relativistic heavy-ion collisions at the AGS. An experimental program is currently underway at the AGS to look at the most violent collisions in finer details, hoping that some small volumes of QGP are formed but remain undetected [156, 157].

Appendix A

Data Tables

Table A.1: Boltzmann fit parameters for kaons in $\sigma_{\mathrm{top}}/\sigma_{\mathrm{geom}} = 10\%$. $1/\mathrm{m}_\mathrm{t}^2 \cdot d^2N/d\mathrm{m}_\mathrm{t}d\mathrm{y} = C_B/\mathrm{m}_\mathrm{K} \cdot \exp(-1 \cdot (\mathrm{m}_\mathrm{t} - \mathrm{m}_\mathrm{K})/T_B) + C'_B/\mathrm{m}_\mathrm{K} \cdot \exp(-1 \cdot (\mathrm{m}_\mathrm{t} - \mathrm{m}_\mathrm{K})/T'_B)$.

y	C_B (c^4/GeV^2)	T_B (MeV)
2.2-2.3	59.2 ± 7.0	66 ± 20
2.3-2.4	49.8 ± 5.6	86 ± 25
2.4-2.5	48.6 ± 3.9	89 ± 14
2.5-2.6	45.2 ± 3.8	59 ± 4
2.6-2.7	44.3 ± 3.9	60 ± 8

Table A.2: Boltzmann fit parameters for protons in the centrality interval $\sigma_{\rm top}/\sigma_{\rm geom} = 4\%$. $1/\mathrm{m_t}^2 \cdot d^2N/d\mathrm{m_t}dy = C_B/\mathrm{m_p} \cdot \exp(-1 \cdot (\mathrm{m_t} - \mathrm{m_p})/T_B) + C'_B/\mathrm{m_p} \cdot \exp(-1 \cdot (\mathrm{m_t} - \mathrm{m_p})/T'_B)$.

y	C_B (c^4/GeV^2)	T_B (MeV)	C'_B (c^4/GeV^2)	T'_B (MeV)	dN/dy
2.2-2.3	134.13 ± 1.39	316.39 ± 17.50			76.26 ± 6.15
2.3-2.4	142.63 ± 1.28	252.06 ± 7.54			57.33 ± 2.06
2.4-2.5	148.95 ± 1.20	222.90 ± 4.18			50.20 ± 0.86
2.5-2.6	157.21 ± 1.11	190.63 ± 2.19			42.35 ± 0.33
2.6-2.7	159.02 ± 0.98	166.12 ± 1.14			35.32 ± 0.14
2.7-2.8	165.35 ± 0.93	143.72 ± 0.68			30.25 ± 0.12
2.8-2.9	164.05 ± 0.93	128.17 ± 0.55			25.91 ± 0.10
2.9-3.0	145.39 ± 2.04	119.13 ± 0.83	61.96 ± 2.77	15.30 ± 1.55	21.93 ± 0.09
3.0-3.1	126.17 ± 1.92	109.07 ± 0.78	117.34 ± 3.00	19.50 ± 0.88	18.56 ± 0.08
3.1-3.2	102.77 ± 2.65	98.28 ± 1.16	150.49 ± 3.34	18.25 ± 0.86	14.27 ± 0.06
3.2-3.3	58.32 ± 3.39	96.61 ± 2.34	113.56 ± 2.96	24.17 ± 1.29	9.19 ± 0.05
3.3-3.4	27.28 ± 4.93	98.78 ± 6.55	50.41 ± 4.36	36.62 ± 3.28	4.98 ± 0.04
3.4-3.5	30.96 ± 0.50	67.81 ± 1.01			2.26 ± 0.02

Table A.3: Boltzmann fit parameters for protons in the centrality interval of $\sigma_{\mathrm{top}}/\sigma_{\mathrm{geom}} = 4-8\%$. $1/\mathrm{m_t}^2 \cdot d^2N/d\mathrm{m_t}dy = C_B/\mathrm{m_p} \cdot \exp(-1 \cdot (\mathrm{m_t}-\mathrm{m_p})/T_B) + C'_B/\mathrm{m_p} \cdot \exp(-1 \cdot (\mathrm{m_t}-\mathrm{m_p})/T'_B)$.

y	C_B (c^4/GeV^2)	T_B (MeV)	C'_B (c^4/GeV^2)	T'_B (MeV)	dN/dy
2.2-2.3	128.72 ± 2.30	314.73 ± 29.15			72.68 ± 9.79
2.3-2.4	138.05 ± 2.10	241.56 ± 11.48			52.08 ± 2.88
2.4-2.5	143.79 ± 1.96	215.80 ± 6.52			46.21 ± 1.23
2.5-2.6	151.69 ± 1.81	190.32 ± 3.61			40.75 ± 0.52
2.6-2.7	154.38 ± 1.59	166.45 ± 1.89			34.60 ± 0.22
2.7-2.8	165.75 ± 1.54	143.93 ± 1.10			30.51 ± 0.19
2.8-2.9	163.15 ± 1.52	129.33 ± 0.91			26.17 ± 0.17
2.9-3.0	150.57 ± 2.27	118.81 ± 1.02	63.97 ± 5.77	14.29 ± 7.71	22.63 ± 0.15
3.0-3.1	126.48 ± 4.53	110.60 ± 1.74	113.07 ± 5.49	21.84 ± 2.17	19.17 ± 0.13
3.1-3.2	111.72 ± 3.33	95.78 ± 1.34	147.34 ± 5.78	17.70 ± 1.19	14.87 ± 0.11
3.2-3.3	65.84 ± 6.00	94.44 ± 3.63	109.07 ± 5.09	22.79 ± 2.42	9.65 ± 0.08
3.3-3.4	41.11 ± 9.53	86.04 ± 7.24	42.53 ± 7.91	30.43 ± 7.01	5.31 ± 0.06
3.4-3.5	30.29 ± 0.84	72.89 ± 1.73			2.42 ± 0.04

Table A.4: Boltzmann fit parameters for protons in the centrality interval of $\sigma_{\mathrm{top}}/\sigma_{\mathrm{geom}} = 8-10\%$. $1/\mathrm{m_t}^2 \cdot d^2N/d\mathrm{m_t}dy = C_B/\mathrm{m_p} \cdot \exp(-1 \cdot (\mathrm{m_t} - \mathrm{m_p})/T_B) + C'_B/\mathrm{m_p} \cdot \exp(-1 \cdot (\mathrm{m_t} - \mathrm{m_p})/T'_B)$.

y	C_B (c^4/GeV^2)	T_B (MeV)	C'_B (c^4/GeV^2)	T'_B (MeV)	dN/dy
2.2-2.3	120.80 ± 2.25	323.43 ± 31.82			71.13 ± 10.32
2.3-2.4	126.85 ± 2.04	272.66 ± 15.30			57.41 ± 4.07
2.4-2.5	136.92 ± 1.94	224.12 ± 7.28			46.67 ± 1.38
2.5-2.6	148.21 ± 1.82	189.73 ± 3.70			39.65 ± 0.52
2.6-2.7	153.97 ± 1.61	163.71 ± 1.86			33.49 ± 0.22
2.7-2.8	162.07 ± 1.55	145.61 ± 1.15			30.28 ± 0.20
2.8-2.9	168.06 ± 1.57	129.24 ± 0.91			26.90 ± 0.17
2.9-3.0	156.55 ± 1.90	119.38 ± 0.81	63.07 ± 4.71	14.76 ± 0.32	23.62 ± 0.16
3.0-3.1	138.49 ± 4.35	107.61 ± 1.50	119.12 ± 5.82	21.13 ± 1.89	20.20 ± 0.14
3.1-3.2	115.58 ± 5.17	97.73 ± 1.90	145.95 ± 5.98	20.41 ± 1.76	15.90 ± 0.11
3.2-3.3	65.72 ± 12.36	96.19 ± 6.80	113.98 ± 8.70	28.71 ± 4.40	10.64 ± 0.09
3.3-3.4	19.65 ± 7.23	115.60 ± 15.90	67.76 ± 6.56	44.85 ± 4.00	5.94 ± 0.09
3.4-3.5	36.93 ± 0.99	70.43 ± 1.63			2.86 ± 0.04

Table A.5: Boltzmann fit parameters for positive pions in the centrality interval of $\sigma_{\text{top}}/\sigma_{\text{geom}} = 4\%$. $1/\text{m}_\text{t}^2 \cdot d^2N/d\text{m}_\text{t}dy = C_B/\text{m}_\pi \cdot \exp(-1 \cdot (\text{m}_\text{t} - \text{m}_\pi)/T_B) + C_B'/\text{m}_\pi \cdot \exp(-1 \cdot (\text{m}_\text{t} - \text{m}_\pi)/T_B')$.

y	C_B (c^4/GeV^2)	T_B (MeV)	dN/dy
2.9-3.0	413.59 ± 2.85	86.49 ± 1.74	19.64 ± 0.17
3.0-3.1	338.45 ± 11.73	87.75 ± 7.27	16.92 ± 0.18
3.1-3.2	359.53 ± 2.38	78.86 ± 1.23	13.87 ± 0.12
3.2-3.3	250.79 ± 11.58	81.65 ± 8.64	11.60 ± 0.14
3.3-3.4	270.34 ± 3.99	73.92 ± 2.38	9.35 ± 0.09
3.4-3.5	198.80 ± 14.52	72.21 ± 11.65	7.34 ± 0.20
3.5-3.6	336.65 ± 0.87	53.61 ± 0.68	5.33 ± 0.06
3.6-3.7	309.39 ± 0.84	48.58 ± 0.65	4.14 ± 0.05
3.7-3.8	259.64 ± 0.81	45.34 ± 0.77	3.10 ± 0.04
3.8-3.9	213.79 ± 0.70	41.44 ± 0.70	2.20 ± 0.03
3.9-4.0	163.00 ± 0.64	38.95 ± 0.78	1.54 ± 0.03
4.0-4.1	126.98 ± 0.62	36.35 ± 0.96	1.09 ± 0.02
4.1-4.2	100.65 ± 0.59	32.11 ± 1.14	0.74 ± 0.02
4.2-4.3	63.33 ± 0.56	31.69 ± 1.94	0.46 ± 0.01
4.3-4.4	45.03 ± 0.49	28.55 ± 2.85	0.28 ± 0.02

Table A.6: Boltzmann fit parameters for positive pions in the centrality interval of $\sigma_{\mathrm{top}}/\sigma_{\mathrm{geom}} = 4-8\%$. $1/\mathrm{m}_{\mathrm{t}}^2 \cdot d^2N/d\mathrm{m}_{\mathrm{t}}d\mathrm{y} = C_B/\mathrm{m}_\pi \cdot \exp(-1\cdot(\mathrm{m}_{\mathrm{t}}-\mathrm{m}_\pi)/T_B) + C'_B/\mathrm{m}_\pi \cdot \exp(-1\cdot(\mathrm{m}_{\mathrm{t}}-\mathrm{m}_\pi)/T'_B)$.

y	C_B (c^4/GeV^2)	T_B (MeV)	dN/dy
2.9-3.0	441.93 ± 176.78	82.06 ± 10.84	18.43 ± 0.31
3.0-3.1	311.07 ± 31.28	89.16 ± 2.78	16.58 ± 0.17
3.1-3.2	334.16 ± 127.49	78.57 ± 8.58	13.11 ± 0.15
3.2-3.3	245.01 ± 102.70	81.59 ± 10.39	11.10 ± 0.16
3.3-3.4	248.43 ± 119.22	74.91 ± 10.59	8.91 ± 0.14
3.4-3.5	199.35 ± 134.28	69.42 ± 13.85	6.91 ± 0.19
3.5-3.6	341.65 ± 8.01	53.24 ± 0.78	5.34 ± 0.08
3.6-3.7	282.52 ± 7.33	49.93 ± 0.84	3.96 ± 0.06
3.7-3.8	261.72 ± 7.03	44.53 ± 0.86	3.03 ± 0.05
3.8-3.9	203.90 ± 6.13	42.61 ± 0.92	2.22 ± 0.04
3.9-4.0	168.70 ± 5.75	37.97 ± 0.98	1.54 ± 0.03
4.0-4.1	131.13 ± 5.11	33.90 ± 1.05	0.99 ± 0.02
4.1-4.2	95.03 ± 4.35	32.18 ± 1.38	0.71 ± 0.02
4.2-4.3	59.84 ± 3.70	34.50 ± 2.53	0.50 ± 0.02
4.3-4.4	43.59 ± 3.37	28.63 ± 3.49	0.27 ± 0.02

Table A.7: Boltzmann fit parameters for positive pions in the centrality interval of $\sigma_{\rm top}/\sigma_{\rm geom} = 8-10\%$. $1/{\rm m_t^2} \cdot d^2N/d{\rm m_t}dy = C_B/{\rm m_\pi} \cdot \exp(-1 \cdot ({\rm m_t} - {\rm m_\pi})/T_B) + C'_B/{\rm m_\pi} \cdot \exp(-1 \cdot ({\rm m_t} - {\rm m_\pi})/T'_B)$.

y	C_B (c^4/GeV^2)	T_B (MeV)	dN/dy
2.9-3.0	350.84 ± 28.75	88.95 ± 2.66	18.34 ± 0.20
3.0-3.1	260.58 ± 93.76	90.48 ± 10.21	15.40 ± 0.21
3.1-3.2	301.34 ± 118.03	81.14 ± 9.27	12.44 ± 0.15
3.2-3.3	220.58 ± 97.07	82.55 ± 11.23	10.73 ± 0.16
3.3-3.4	200.53 ± 102.43	77.58 ± 11.89	8.74 ± 0.14
3.4-3.5	251.19 ± 168.93	65.71 ± 12.44	6.67 ± 0.17
3.5-3.6	315.92 ± 7.68	53.93 ± 0.81	5.06 ± 0.07
3.6-3.7	276.62 ± 7.37	49.27 ± 0.84	3.82 ± 0.06
3.7-3.8	242.29 ± 6.83	46.13 ± 0.94	3.00 ± 0.05
3.8-3.9	203.61 ± 6.24	40.72 ± 0.88	2.06 ± 0.04
3.9-4.0	154.63 ± 5.42	39.14 ± 1.04	1.48 ± 0.03
4.0-4.1	118.85 ± 4.78	37.15 ± 1.21	1.04 ± 0.03
4.1-4.2	90.79 ± 4.00	34.71 ± 1.36	0.77 ± 0.02
4.2-4.3	61.70 ± 3.69	31.44 ± 2.03	0.45 ± 0.02
4.3-4.4	40.73 ± 3.21	31.86 ± 4.21	0.30 ± 0.03

Table A.8: Boltzmann fit parameters for negative pions in the centrality interval of $\sigma_{\mathrm{top}}/\sigma_{\mathrm{geom}} = 4\%$. $1/\mathrm{m}_{\mathrm{t}}^2 \cdot d^2N/d\mathrm{m}_{\mathrm{t}}d\mathrm{y} = C_B/\mathrm{m}_\pi \cdot \exp(-1 \cdot (\mathrm{m}_{\mathrm{t}} - \mathrm{m}_\pi)/T_B) + C'_B/\mathrm{m}_\pi \cdot \exp(-1 \cdot (\mathrm{m}_{\mathrm{t}} - \mathrm{m}_\pi)/T'_B)$.

y	C_B (c^4/GeV^2)	T_B (MeV)	dN/dy
2.9-3.0	432.65 ± 3.77	85.31 ± 1.85	22.76 ± 0.19
3.0-3.1	305.01 ± 3.47	92.92 ± 2.29	20.07 ± 0.15
3.1-3.2	272.22 ± 5.24	87.03 ± 3.49	15.76 ± 0.13
3.2-3.3	207.68 ± 2.95	86.14 ± 2.42	12.92 ± 0.11
3.3-3.4	188.48 ± 5.54	81.01 ± 4.65	10.21 ± 0.09
3.4-3.5	162.61 ± 4.89	75.74 ± 4.10	7.85 ± 0.08
3.5-3.6	166.32 ± 12.22	67.89 ± 9.01	5.89 ± 0.07
3.6-3.7	79.38 ± 7.43	71.96 ± 11.38	4.36 ± 0.06
3.7-3.8	96.52 ± 11.20	61.19 ± 11.21	3.27 ± 0.05
3.8-3.9	61.41 ± 11.61	58.61 ± 16.27	2.31 ± 0.04
3.9-4.0	59.82 ± 11.82	55.03 ± 16.55	1.63 ± 0.04
4.0-4.1	85.27 ± 20.44	44.55 ± 14.95	1.08 ± 0.04
4.1-4.2	98.76 ± 0.53	32.41 ± 0.78	0.71 ± 0.01
4.2-4.3	63.92 ± 0.48	31.33 ± 1.04	0.44 ± 0.01
4.3-4.4	44.99 ± 0.46	28.20 ± 1.21	0.27 ± 0.009
4.4-4.5	28.41 ± 0.41	28.85 ± 1.53	0.18 ± 0.007
4.5-4.6	16.49 ± 0.44	28.78 ± 3.13	0.12 ± 0.005

Table A.9: Boltzmann fit parameters for negative pions in the centrality interval of $\sigma_{\rm top}/\sigma_{\rm geom} = 4-8\%$. $1/{\rm m_t^2} \cdot d^2N/d{\rm m_t}d{\rm y} = C_B/{\rm m}_\pi \cdot \exp(-1 \cdot ({\rm m_t} - {\rm m}_\pi)/T_B) + C'_B/{\rm m}_\pi \cdot \exp(-1 \cdot ({\rm m_t} - {\rm m}_\pi)/T'_B)$.

y	C_B (c^4/GeV^2)	T_B (MeV)	dN/dy
2.9-3.0	418.97 ± 156.95	86.32 ± 10.91	22.23 ± 0.37
3.0-3.1	277.03 ± 36.30	94.24 ± 3.54	19.16 ± 0.27
3.1-3.2	229.35 ± 37.56	91.22 ± 4.21	15.59 ± 0.22
3.2-3.3	195.82 ± 46.46	86.96 ± 5.73	12.58 ± 0.18
3.3-3.4	153.63 ± 36.52	84.49 ± 5.57	9.69 ± 0.14
3.4-3.5	171.30 ± 87.62	74.46 ± 9.69	7.78 ± 0.11
3.5-3.6	120.15 ± 57.39	74.19 ± 9.44	5.94 ± 0.08
3.6-3.7	77.85 ± 52.64	74.65 ± 13.86	4.42 ± 0.06
3.7-3.8	111.70 ± 102.61	59.07 ± 12.78	3.16 ± 0.05
3.8-3.9	45.96 ± 60.66	64.34 ± 21.81	2.28 ± 0.04
3.9-4.0	67.57 ± 105.02	51.73 ± 19.22	1.64 ± 0.04
4.0-4.1	116.00 ± 4.73	36.58 ± 0.91	0.98 ± 0.01
4.1-4.2	86.70 ± 4.09	34.24 ± 1.07	0.67 ± 0.01
4.2-4.3	62.43 ± 3.67	32.39 ± 1.38	0.46 ± 0.01
4.3-4.4	38.70 ± 2.86	31.93 ± 1.74	0.28 ± 0.009
4.4-4.5	25.56 ± 2.85	28.65 ± 2.23	0.16 ± 0.007
4.5-4.6	17.79 ± 2.84	27.90 ± 3.75	0.11 ± 0.005

Table A.10: Boltzmann fit parameters for negative pions in the centrality interval of $\sigma_{\rm top}/\sigma_{\rm geom} = 8-10\%$. $1/{\rm m}_{\rm t}^2 \cdot d^2N/d{\rm m}_{\rm t}dy = C_B/{\rm m}_\pi \cdot \exp(-1 \cdot ({\rm m}_{\rm t} - {\rm m}_\pi)/T_B) + C'_B/{\rm m}_\pi \cdot \exp(-1 \cdot ({\rm m}_{\rm t} - {\rm m}_\pi)/T'_B)$.

y	C_B (c^4/GeV^2)	T_B (MeV)	dN/dy
2.9-3.0	490.26 ± 189.52	81.46 ± 10.11	21.32 ± 0.35
3.0-3.1	259.36 ± 28.09	94.84 ± 2.93	18.34 ± 0.27
3.1-3.2	201.95 ± 26.61	92.44 ± 3.42	15.02 ± 0.22
3.2-3.3	194.49 ± 32.48	87.57 ± 4.04	12.43 ± 0.18
3.3-3.4	170.78 ± 74.94	81.92 ± 9.92	9.55 ± 0.14
3.4-3.5	144.54 ± 76.62	76.96 ± 10.58	7.63 ± 0.11
3.5-3.6	114.84 ± 74.46	74.47 ± 13.03	5.65 ± 0.08
3.6-3.7	78.26 ± 51.37	76.83 ± 14.11	4.33 ± 0.07
3.7-3.8	71.71 ± 68.21	65.30 ± 15.87	3.11 ± 0.05
3.8-3.9	62.45 ± 77.35	61.87 ± 19.05	2.21 ± 0.04
3.9-4.0	34.98 ± 46.81	68.22 ± 27.94	1.62 ± 0.08
4.0-4.1	118.34 ± 5.08	37.72 ± 1.02	1.05 ± 0.02
4.1-4.2	87.65 ± 4.47	31.94 ± 1.12	0.62 ± 0.01
4.2-4.3	54.01 ± 3.73	32.34 ± 1.67	0.39 ± 0.01
4.3-4.4	40.40 ± 3.27	29.52 ± 1.77	0.26 ± 0.009
4.4-4.5	29.99 ± 3.11	29.22 ± 2.18	0.19 ± 0.009
4.5-4.6	16.92 ± 2.57	29.66 ± 3.92	0.11 ± 0.007

Appendix B

Technical Drawings

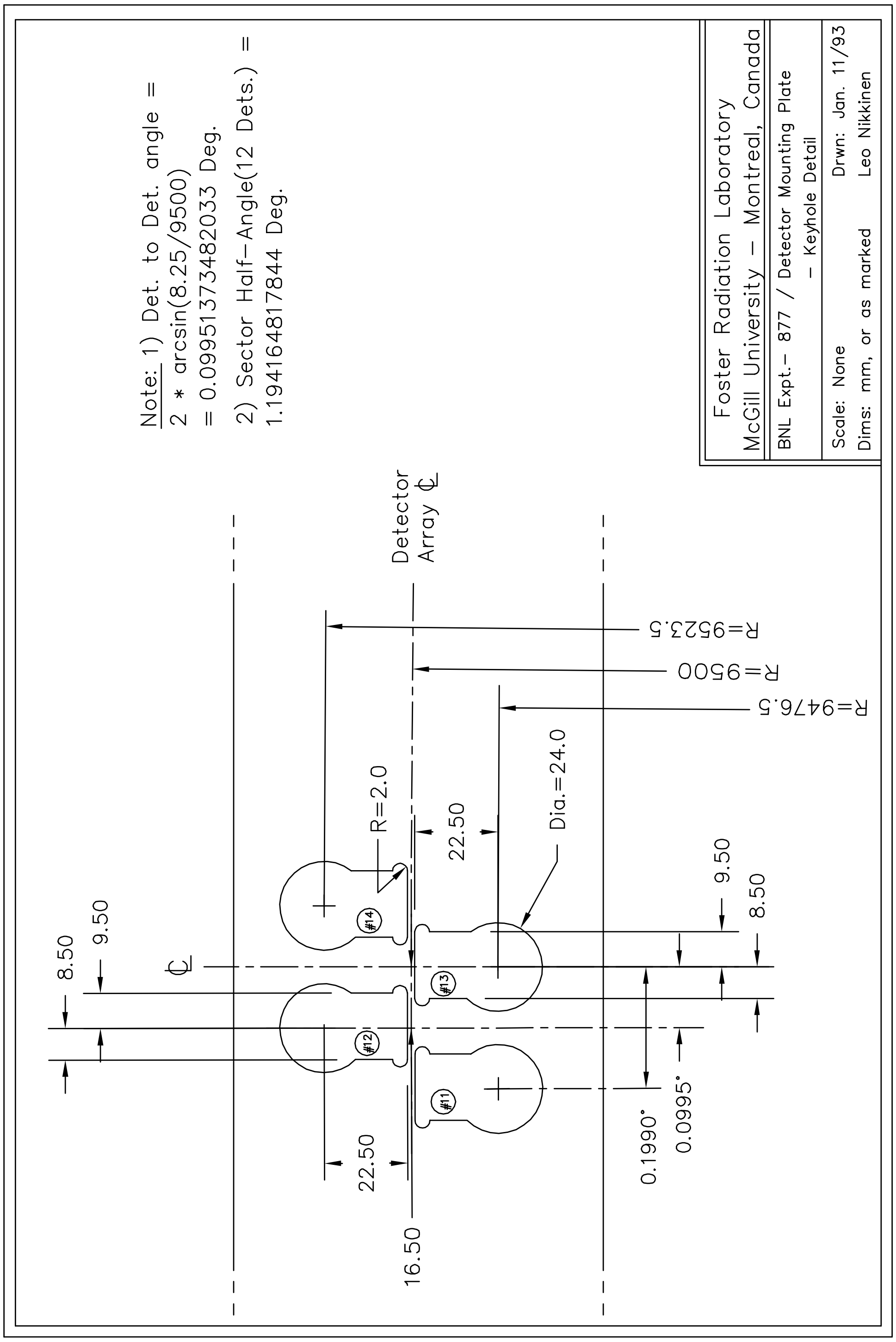

Figure B.1: Large scintillator keyhole.

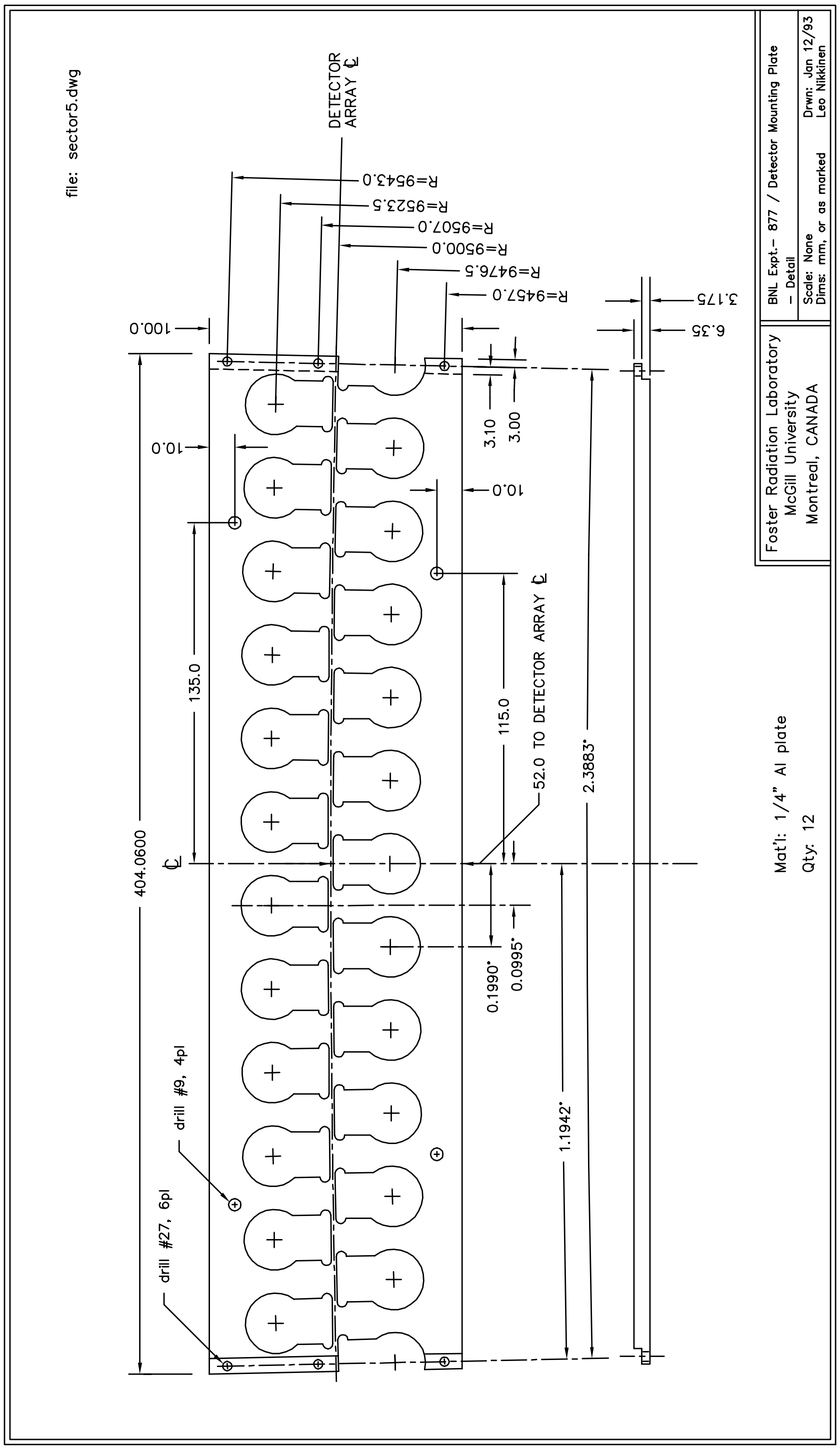

Figure B.2: Large scintillator keyhole positioning plate.

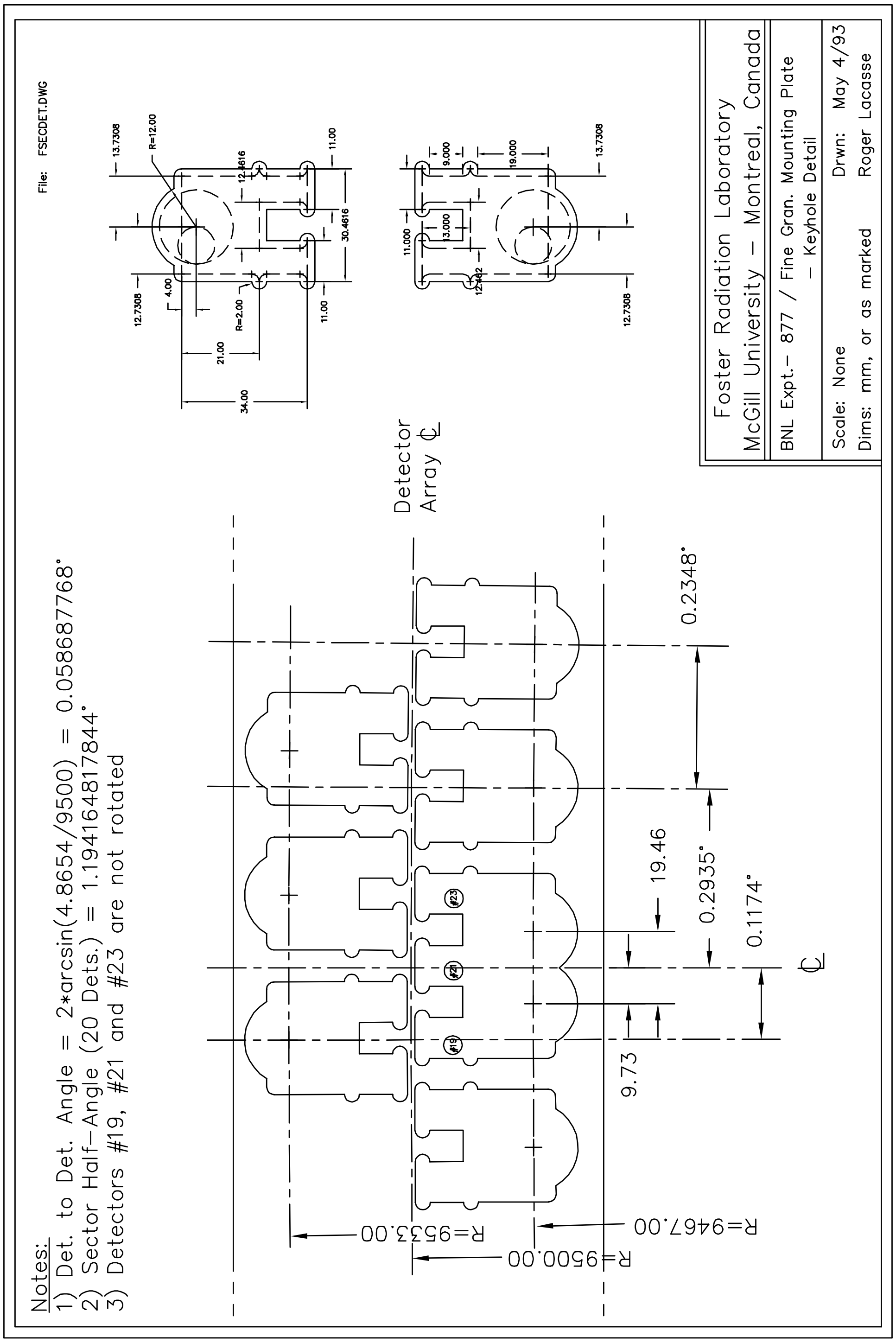

Figure B.3: Narrow scintillator keyhole.

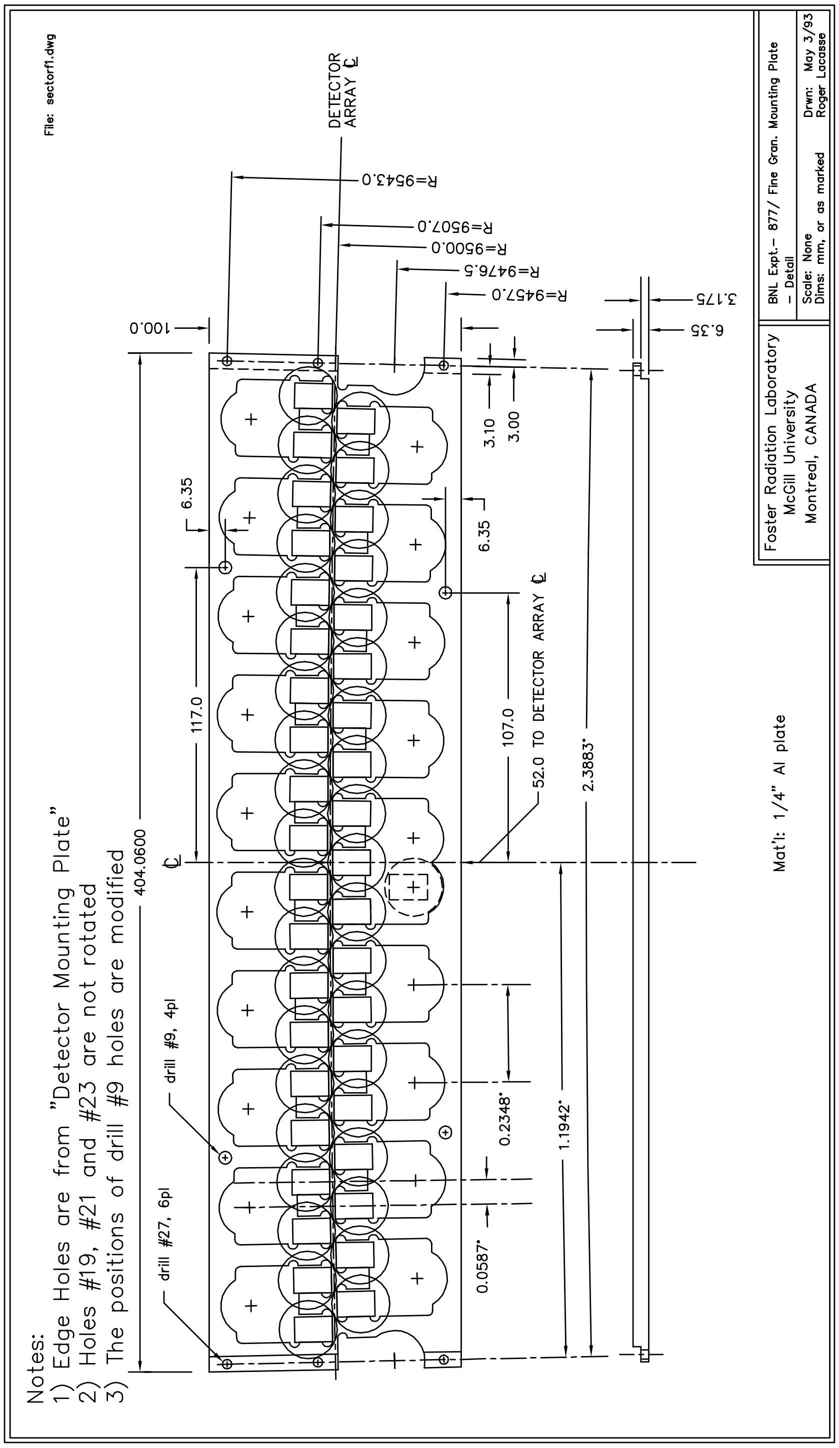

Figure B.4: Narrow scintillator keyhole positioning plate.

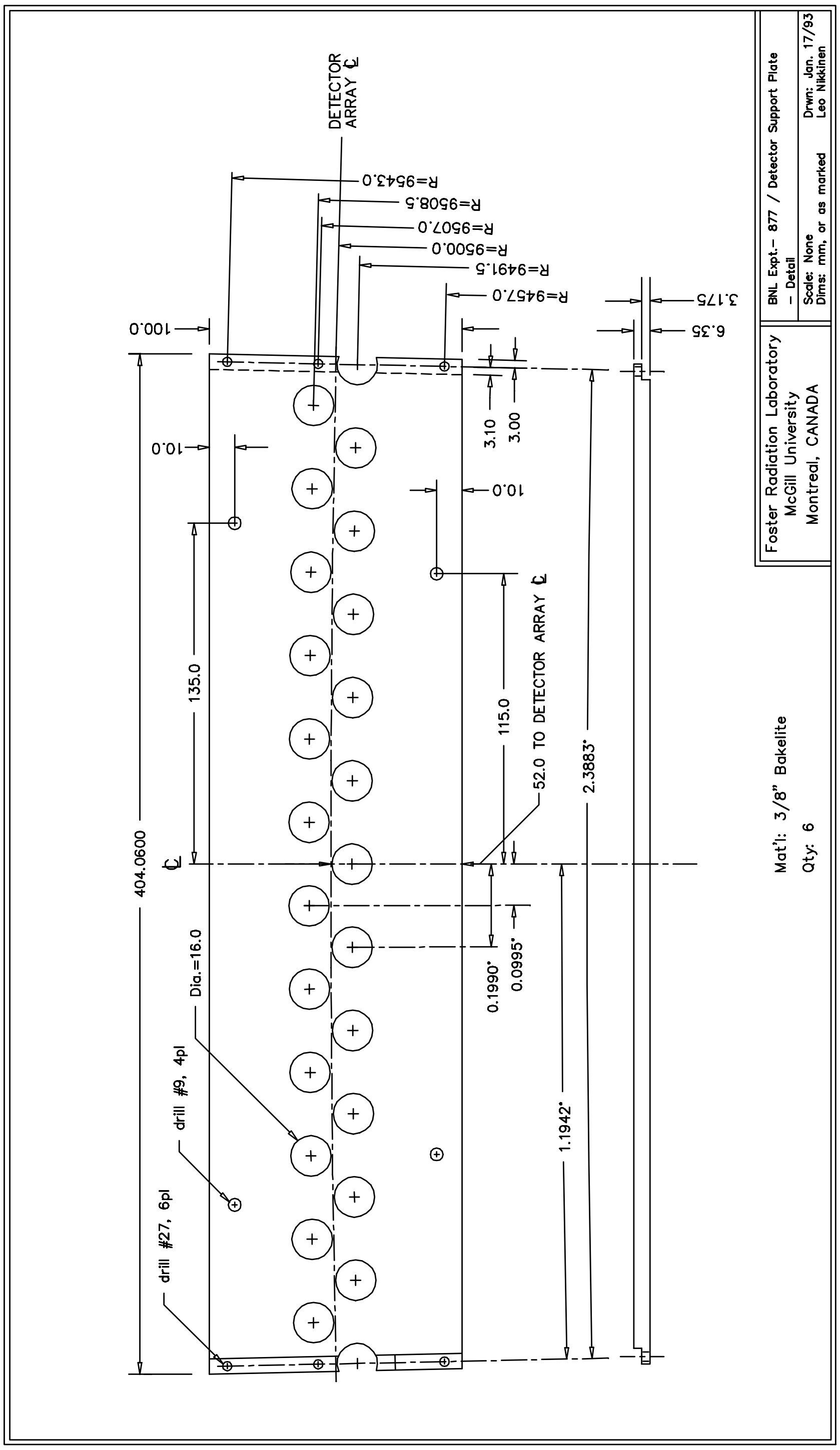

Figure B.5: Large counter support plate.

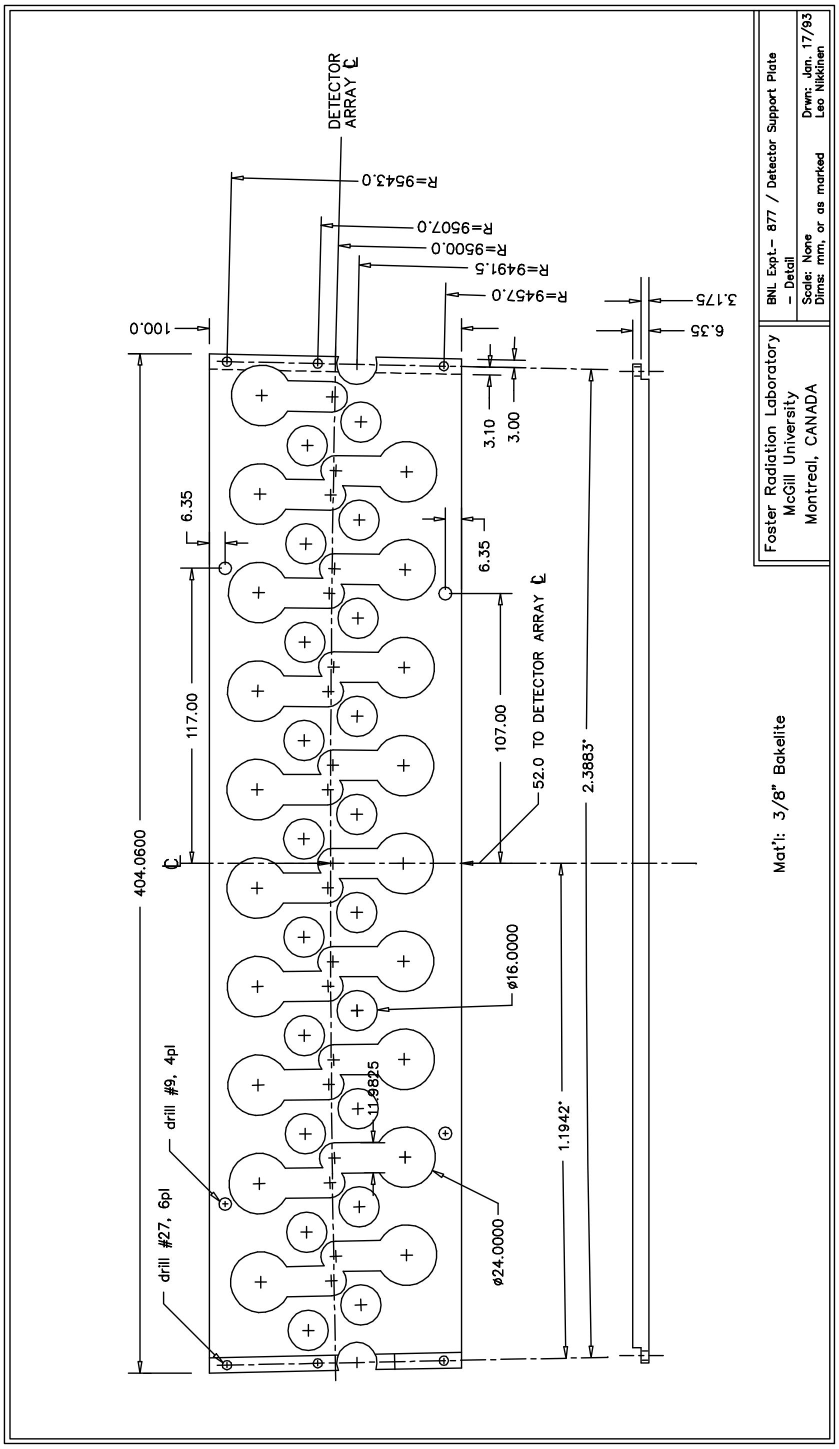

Figure B.6: Narrow counter top support plate.

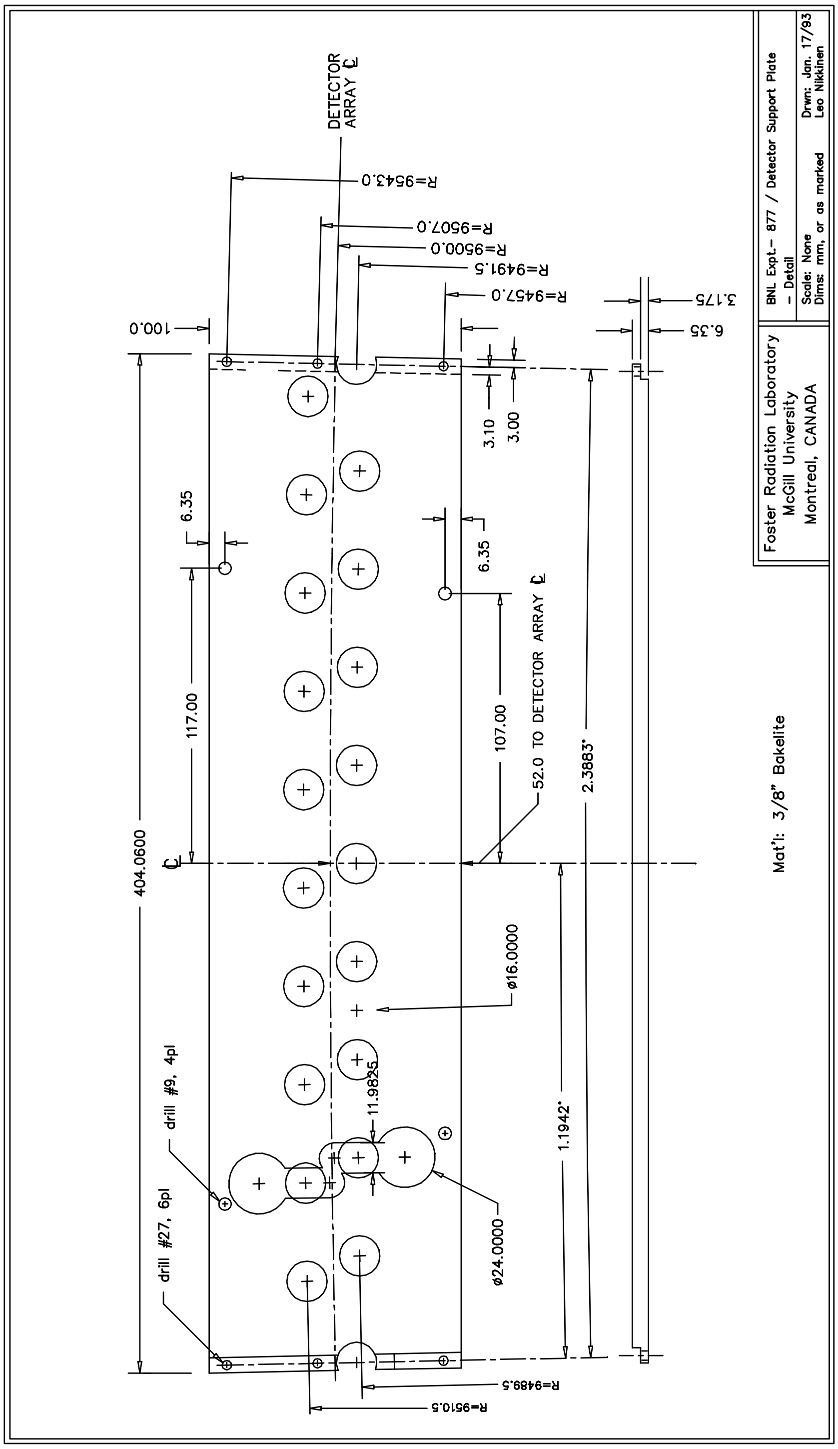

Figure B.7: Narrow counter bottom support plate.

Bibliography

[1] R. Lacasse, M.Sc. thesis, McGill University, 1991.

[2] S. Weinberg, *Les trois premières minutes de l'univers* (Seuil, Paris, 1978).

[3] K. Kajatie, Nucl. Phys. **A498**, 355c (1989).

[4] M. Gell-Mann, Phys. Rev. **125**, 1067 (1962).

[5] M. Gell-Mann and Y. Ne'eman, *The eightfold way* (Benjamin, New York, 1966).

[6] R. M. Barnett *et al.*, Phys. Rev. D **54**, 1 (1996).

[7] T. D. Lee, Nucl. Phys. **A590**, 11c (1995).

[8] J. Rafelski and B. Müller, Phys. Rev. Lett. **42**, 1066 (1982).

[9] E. Witten, Phys. Rev. **D30**, 272 (1984).

[10] G. Alcock, G. M. Fuller, G. J. Mathews, and B. Meyer, Nucl. Phys. **A498**, 301c (1989).

[11] G. Baym, Nucl. Phys. **A590**, 233c (1995).

[12] J. Barrette *et al.*, Phys. Rev. Lett. **70**, 2996 (1993).

[13] J. Barrette for the E814 Collaboration, Nucl. Phys. **A566**, 411c (1994).

[14] J. Stachel, Nucl. Phys. **A610**, 509c (1996).

[15] C.-Y. Wong, *Introduction to High-Energy Heavy-Ion Collisions* (World Scientific, Singapore, 1994).

[16] L. P. Csernai, *Introduction to Relativistic Heavy-Ion Collisions* (John Wiley & Sons, Chichester, 1994).

[17] J. Stachel and G. R. Young, Annu. Rev. Nucl. Part. Sci. **42**, 537 (1992).

[18] J. Barrette for the E814 Collaboration, Phys. Rev. Lett. **64**, 1219 (1990).

[19] T. Abbott *et al.*, Phys. Rev. C **45**, 2933 (1992).

[20] W.A. Zajc for the E805 and E859 Collaboration, Nucl. Phys. **A544**, 237c (1992).

[21] G. Roland for the NA35 Collaboration, Nucl. Phys. **A566**, 527c (1994).

[22] D. Miśkowiec for the E877 Collaboration, Nucl. Phys. **A590**, 473c (1995).

[23] J. Barrette *et al.*, Phys. Rev. Lett. **78**, 2916 (1997).

[24] B. A. Cole for the E802 Collaboration, in *HIPAGS '93* (MIT, Boston, 1993), pp. 313–328.

[25] E. Fermi, Prog. Theor. Phys. **5**, 570 (1950).

[26] L. D. Landau, Izv. Akad. Nauk. SSSR **17**, 51 (1953).

[27] J. Sollfrank, P. Koch, and U. Heinz, Phys. Letts. B **252**, 256 (1990).

[28] G. E. Brown, J. Stachel, and G. M. Welke, Phys. Letts. B **254**, 332 (1991).

[29] J. Barrette for the E814 Collaboration, Phys. Letts. B **351**, 93 (1995).

[30] K. Lee, U. Heinz, and E. Schnedemann, Z. Phys. C **48**, 525 (1990).

[31] J. Barrette for the E877 Collaboration, Nucl. Phys. **A590**, 259c (1995).

[32] J. Barrette *et al.*, Phys. Rev. Lett. **73**, 2532 (1994).

[33] B.-A. Li and C. M. Ko for the E859 Collaboration, in *HIPAGS '96* (Wayne State University, Detroit, 1996), pp. 193–199.

[34] C. Spieles *et al.*, Nucl. Phys. **A590**, 271c (1995).

[35] Y. Pang *et al.*, Nucl. Phys. **A590**, 565c (1995).

[36] B. Müller, Nucl. Phys. **A544**, 95c (1992).

[37] U. Heinz, Nucl. Phys. **A566**, 205c (1994).

[38] M. Abreu *et al.*, Nucl. Phys. **A566**, 77c (1994).

[39] M. Gonin for the NA50 collaboration, Nucl. Phys. **A610**, 404c (1996).

[40] T. Abbott *et al.*, Phys. Rev. Lett. **64**, 847 (1990).

[41] T. Abbott *et al.*, Phys. Rev. Lett. **66**, 1567 (1991).

[42] M. Gonin for the E802/E866 Collaboration, Nucl. Phys. **A566**, 601c (1994).

[43] Y. Wang for the E802 Collaboration, in *HIPAGS '93* (MIT, Boston, 1993), pp. 239–248.

[44] Y. Akiba *et al.*, Phys. Rev. Lett. **76**, 2021 (1996).

[45] T. Abbott *et al.*, Nucl. Phys. **A525**, 455c (1991).

[46] J. Barrette *et al.*, Phys. Rev. Lett. **70**, 1763 (1993).

[47] D. Lissauer *et al.*, Proposal 814 submitted to the AGS program committee, 1986.

[48] J. Barrette *et al.*, Phys. Rev. C **46**, 312 (1992).

[49] J. Barrette *et al.*, Phys. Rev. C **52**, 2028 (1995).

[50] J. Barrette *et al.*, Phys. Rev. C **50**, 1077 (1994).

[51] J. Barrette *et al.*, Phys. Rev. C **52**, 2679 (1995).

[52] J. Barrette *et al.*, Phys. Letts. B **333**, 33 (1994).

[53] D. Lissauer *et al.*, Study of relativistic nuclear collisions with heavy beams using the E814 4π calorimetry and modified forward spectrometer, 1991.

[54] L. Waters, Ph.D. thesis, SUNY at Stony Brook, 1990.

[55] Z. Z. Zhang, Ph.D. thesis, University of Pittsburgh, 1993.

[56] G. Wang, Ph.D. thesis, McGill University, 1994.

[57] Y. Zhang, Ph.D. thesis, SUNY at Stony Brook, 1995.

[58] J. Barrette *et al.*, Phys. Rev. C **51**, 3309 (1995).

[59] J. Barrette *et al.*, Phys. Rev. C **55**, 1420 (1997).

[60] J. Simon-Gillo *et al.*, Nucl. Inst. and Meth. **A309**, 427 (1991).

[61] D. Fox *et al.*, Nucl. Inst. and Meth. **A317**, 474 (1992).

[62] P. Braun-Munzinger *et al.*, Momentum Measurement of the ^{197}Au Beam for the 93 Run and Related Topics, 1994.

[63] J. Dee, Ph.D. thesis, SUNY at Stony Brook, 1995.

[64] B. Hong, Ph.D. thesis, SUNY at Stony Brook, 1995.

[65] N. DaSilva, Ph.D. thesis, Saõ Paulo University, Brazil, 1995.

[66] B. Yu, Ph.D. thesis, University of Pittsburgh, 1991.

[67] R. Debbe *et al.*, IEEE Trans. Nucl. Sci. **37**, 82 (1990).

[68] J. Fischer *et al.*, IEEE Trans. Nucl. Sci. **37**, 88 (1990).

[69] S. V. Green, Ph.D. thesis, Yale University, 1992.

[70] R. Lacasse *et al.*, A time-of-flight hodoscope for the E877 spectrometer, 1997, submitted to Nucl. Inst. and Meth.

[71] J. Barrette *et al.*, Phys. Rev. C **45**, 819 (1992).

[72] J. Barrette *et al.*, Phys. Rev. C **45**, 2427 (1992).

[73] Bicron, catalog, 1991.

[74] Hamamatsu, Photomultiplier Tubes, catalog, 1990.

[75] T. Abbott *et al.*, Nucl. Inst. and Meth. **A290**, 41 (1990).

[76] W. Leo, *Techniques for Nuclear and Particle physics experiments* (Springer-Verlag, Berlin Heidelberg, 1987).

[77] H. Beker *et al.*, Phys. Letts. B **302**, 510 (1993).

[78] T. Kobayashi and T. Sugitate, Nucl. Inst. and Meth. **A287**, 389 (1990).

[79] V. Sum *et al.*, Nucl. Inst. and Meth. **A326**, 489 (1993).

[80] T. Sugitate *et al.*, Nucl. Inst. and Meth. **A249**, 354 (1986).

[81] S. Kobayashi *et al.*, Nucl. Inst. and Meth. **143**, 259 (1977).

[82] T. Fujii *et al.*, Nucl. Inst. and Meth. **215**, 357 (1983).

[83] T. Kishida *et al.*, Nucl. Inst. and Meth. **A254**, 367 (1987).

[84] A. Gobbi *et al.*, Nucl. Inst. and Meth. **A324**, 156 (1993).

[85] J. Benlloch *et al.*, Nucl. Inst. and Meth. **A292**, 319 (1990).

[86] J. Benlloch *et al.*, Nucl. Inst. and Meth. **A290**, 327 (1990).

[87] T. Petrović *et al.*, Nucl. Inst. and Meth. **A273**, 833 (1988).

[88] W. Braunschweig *et al.*, Nucl. Inst. and Meth. **134**, 261 (1976).

[89] T. Tanimori *et al.*, Nucl. Inst. and Meth. **216**, 57 (1983).

[90] EG&G Ortec, Radiation Detection – Measurement – Analysis, Catalog, 1983.

[91] LeCroy, MODEL 1872 and 1875 FASTBUS TDC's, Operator's Manual, 1991.

[92] J. Bauenfeld, 1993, private communication.

[93] J. Fischer *et al.*, IEEE Transactions on nuclear science **37**, 82 (1990).

[94] M. Kurata *et al.*, Nucl. Inst. and Meth. **A349**, 447 (1994).

[95] H. A. Bethe and J. Askin, in *Experimental Nuclear Physics*, edited by E. Segre (Jon Wiley & Sons, New York, 1953), Vol. 1.

[96] P. Braun-Munzinger for the E814 Collaboration, Z. Phys. C **38**, 45 (1988).

[97] T. Abbott *et al.*, Phys. Rev. C **44**, 1611 (1991).

[98] L. Ahle *et al.*, Phys. Letts. B **332**, 258 (1994).

[99] D. G. Cassel and H. Kowalski, Nucl. Inst. and Meth. **185**, 235 (1981).

[100] D. Miśkowiec, Momentum Resolution of the E877 Spectrometer - Calculation, 1996.

[101] T. W. Piazza, Ph.D. thesis, SUNY at Stony Brook, 1997.

[102] S. Voloshin, Occupency correction, method # $n + 1$., 1996.

[103] R. Brun *et al.*, GEANT 3 users guide, 1984.

[104] J. Stachel for the E814 Collaboration, Nucl. Phys. **A566**, 183c (1994).

[105] T. Abbott *et al.*, Phys. Rev. D **45**, 3906 (1992).

[106] R. Mattiello, H. Sorge, H. Stöcker, and W. Greiner, Phys. Rev. Lett. **63**, 1459 (1989).

[107] G. Q. Li and C. M. Ko, Phys. Letts. B **351**, 37 (1995).

[108] V. Koch, Phys. Letts. B **351**, 29 (1995).

[109] M. Pollack, Ph.D. thesis, SUNY at Stony Brook, 1997.

[110] Y. Akiba for the E866 Collaboration, Nucl. Phys. **A610**, 139c (1996).

[111] H. Sorge, H. Stöcker, and W. Greiner, Nucl. Phys. **A498**, 567c (1989).

[112] H. Sorge, H. Stöcker, and W. Greiner, Ann. Phys (N.Y.) **192**, 266 (1989).

[113] H. Sorge, H. Stöcker, and W. Greiner, Z. Phys. C **47**, 629 (1990).

[114] J. Aichelin and H. Stöcker, Phys. Letts. B **176**, 14 (1986).

[115] A. Rosenhauer, J. Aichelin, H. Stöcker, and W. Greiner, J. Phys. **C4**, 395 (1986).

[116] J. Aichelin *et al.*, Phys. Rev. Lett. **58**, 1926 (1987).

[117] H. Sorge, in *HIPAGS '96* (Wayne State University, Detroit, 1996), pp. 184–192.

[118] H. Sorge *et al.*, Phys. Letts. B **B217**, 37 (1991).

[119] M. Hofmann *et al.*, Nucl. Phys. **A566**, 15c (1994).

[120] T.K. Hemmick for the E814 Collaboration, Nucl. Phys. **A566**, 435c (1994).

[121] P. Braun-Munzinger for the E814 Collaboration, Nucl. Phys. **A544**, 137c (1992).

[122] J. Barrette *et al.*, Z. Phys. C **59**, 211 (1993).

[123] S. Nagamiya, Nucl. Phys. **A544**, 5c (1992).

[124] B. A. Cole for the E802 Collaboration, Nucl. Phys. **A544**, 95c (1992).

[125] C. G. Parsons for the E802 Collaboration, in *HIPAGS '93* (MIT, Boston, 1993), pp. 313–328.

[126] R. Lacasse for the E877 Collaboration, Nucl. Phys. **A610**, 153c (1996).

[127] R. Brockmann *et al.*, Phys. Rev. Lett. **53**, 2012 (1984).

[128] H. Ströbele *et al.*, Z. Phys. C **38**, 89 (1988).

[129] J. W. Harris *et al.*, Nucl. Phys. **A498**, 133c (1989).

[130] R. Renfordt *et al.*, Nucl. Phys. **A498**, 385c (1989).

[131] B.-A. Li, Phys. Letts. B **254**, 335 (1991).

[132] J. Sollfrank, P. Kock, and U. Heinz, Phys. Letts. B **252**, 256 (1990).

[133] M. Gonin *et al.*, Phys. Rev. C **51**, 310 (1994).

[134] M. M. Sternheim and R. R. Silbar, Phys. Rev. D **6**, 3117 (1972).

[135] R. R. Silbar and M. M. Sternheim, Phys. Rev. C **8**, 492 (1973).

[136] R. E. Marshak, *Meson Physics* (McGraw-Hill, New York, 1952), pp. 96–117.

[137] K. G. Libbrecht and S. E. Koonin, Phys. Rev. Lett. **43**, 1581 (1979).

[138] M. Gyulassy and S. K. Kauffmann, Nucl. Phys. **A362**, 503 (1981).

[139] W. Beneson *et al.*, Phys. Rev. Lett. **43**, 683 (1979).

[140] G. Bertch, Nature **283**, 280 (1980).

[141] K. L. Wolf *et al.*, Phys. Rev. Lett. **42**, 1448 (1979).

[142] S. Nagamiya *et al.*, Phys. Rev. C **24**, 971 (1981).

[143] K. L. Wolf *et al.*, Phys. Rev. C **26**, 2572 (1982).

[144] B.-A. Li, Phys. Letts. B **346**, 5 (1995).

[145] M. G.-H. Mostafa and C.-Y. Wong, Phys. Rev. C **51**, 2135 (1995).

[146] E. V. Shuryak, Phys. Rev. D **42**, 1764 (1990).

[147] H. Böggild *et al.*, Phys. Letts. B **372**, 339 (1996).

[148] F. Videbæk for the E802 Collaboration, Nucl. Phys. **A590**, 249c (1995).

[149] Z. Chen for the E866 Collaboration, in *HIPAGS '96* (Wayne State University, Detroit, 1996), pp. 5–12.

[150] G. Baym and P. Braun-Munzinger, Nucl. Phys. **A610**, 286c (1996).

[151] H. W. Barz, J. P. Bondroff, J. J. Gaardhoje, and H. Heiselberg, Phys. Rev. C **56**, 1553 (1997).

[152] K. S. Krane, *Introductory nuclear physics* (John Wiley & Sons, New York, 1988).

[153] D. Miśkowiec for the E877 collaboration, Nucl. Phys. **A610**, 227c (1996).

[154] M. D. Baker for the E859/E866 Collaboration, in *HIPAGS '96* (Wayne State University, Detroit, 1996), pp. 159–165.

[155] M. D. Baker for the E802 collaboration, Nucl. Phys. **A610**, 213c (1996).

[156] C. Ogilvie for the E917 collaboration, in *HIPAGS '96* (Wayne State University, Detroit, 1996), pp. 267–273.

[157] E. G. Judd for the E896 collaboration, in *HIPAGS '96* (Wayne State University, Detroit, 1996), pp. 260–266.